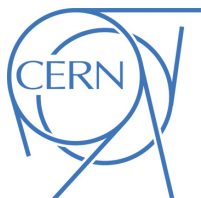




ATLAS Note

ANA-HDBS-2020-09-INT1

23rd January 2023



Draft version 0.1

1

2 Search for $t\bar{b}$ resonance using boosted top-quark 3 topology in the lepton+jets final state at $\sqrt{s} = 13$ 4 TeV with the ATLAS detector

5

De La Torre Perez, Hector^a, Gombas, Jason Peter^a, Schwienhorst, Reinhard^a,
6 Sato, Koji^b, Hirose, Shigeki^b, Yamauchi, Hiroki^b, Salvador Salas, Adrian^c, Riu,
7 Imma^c, Mir Martinez, Lluisa Maria^c

8

^a*Michigan State University (US)*

9

^b*University of Tsukuba (JP)*

10

^c*The Barcelona Institute of Science and Technology (BIST) (ES)*

11

A search for $t\bar{b}$ resonances with a boosted top tagging technique is presented, focusing on a final state consisting of a single charged lepton and multiple jets as well as a top-tagged large- R jet. The analysis is based on the pp collision data at the centre-of-mass energy of 13 TeV collected with the ATLAS detector with an integrated luminosity of 139 fb^{-1} . As a hypothetical particle with spin-0(1), a charged Higgs boson (a W' boson) scenario is searched in the mass range from 1 TeV up to 5 TeV.

17

© 2023 CERN for the benefit of the ATLAS Collaboration.

18 Reproduction of this article or parts of it is allowed as specified in the CC-BY-4.0 license.

19 **Contents**

20	1 Introduction	5
21	2 Data and MonteCarlo Simulated Events	7
22	2.1 Data Sample	7
23	2.2 Signal Samples	7
24	2.2.1 $\bar{t}bH^+$ Samples	8
25	2.2.2 $\bar{t}bW'$ Samples	8
26	2.3 Background Samples	9
27	2.3.1 $t\bar{t}$ +jets	10
28	2.3.2 $t\bar{t}H$	11
29	2.3.3 $t\bar{t}V$	11
30	2.3.4 Single top	11
31	2.3.5 tH	12
32	2.3.6 Rare t processes	13
33	2.3.7 Vector bosons plus jets	13
34	2.3.8 Dibosons	14
35	3 Object Reconstruction	15
36	3.1 Electrons	15
37	3.2 Muons	15
38	3.3 Taus	15
39	3.4 Small- R jets and b -tagging	15
40	3.5 Large- R jets and top-tagging	16
41	3.6 Overlap Removal	16
42	4 Analysis Strategy	18
43	4.1 Analysis strategy at $M_{H^+}, M_{W'} \leq 3$ TeV points	18
44	4.1.1 Event Selection	18
45	4.1.2 Multivariable analysis using BDT	21
46	4.2 Analysis strategy at $M_{H^+}, M_{W'} > 3$ TeV points	30
47	5 Background modeling	34
48	5.1 Blind strategy	34
49	5.2 Data/MC comparison for BDT input variables	34
50	5.3 Data/MC comparison for BDT outputs	37
51	5.4 Reweighting technique	42
52	6 Systematics Uncertainties	50
53	6.1 Luminosity and pile-up modeling	51
54	6.1.1 Luminosity	51
55	6.1.2 Pile-up modeling	51
56	6.2 Reconstructed objects	52
57	6.2.1 Charged leptons	52
58	6.2.2 Small- R jets, Large- R jets	52
59	6.3 Signal modeling	54

60	6.4	Background modeling	55
61	6.4.1	$t\bar{t}$ +jets	55
62	6.4.2	Other backgrounds	57
63	7	Profile Likelihood Fit	59
64	7.1	Method	59
65	7.2	Pruning and smoothing of systematic uncertainties	59
66	7.3	Asimov fit	60
67	7.3.1	Pre-fit plots	60
68	7.3.2	Asimov fit results	76
69	7.3.3	Post-fit plots	133
70	7.3.4	Asimov fit results summary	148
71	7.4	Upper cross-section limits as a function of signal mass	150
72	8	Summary and Conclusions	154
73	Appendices		162
74	A	TOPQ1 DAOD list	162
75	A.1	Data	162
76	A.2	$\bar{t}bH^+$	162
77	A.3	$\bar{t}bW'$	162
78	A.4	$t\bar{t}$ + jets	163
79	A.5	$t\bar{t}H$	164
80	A.6	$t\bar{t}V$	165
81	A.7	Single top	165
82	A.8	tH	166
83	A.9	Rare t processes	166
84	A.10	Vector bosons plus jets	166
85	A.10.1	W + jets	166
86	A.10.2	Z + jets	167
87	A.11	Diboson	169
88	B	Signal/background comparisons	170
89	B.1	BDT input variables	170
90	B.2	BDT outputs	173
91	B.3	Comparison using distributions with binning	173

92 List of contributions

De La Torre Perez, Hector	W' vs H+ comparisons, W' generation
Gombas, Jason Peter	W' NLO model, W' vs H+ comparisons, W' generation
Schwienhorst, Reinhard	W' NLO model, Jason supervision
Sato, Koji	Analysis contact, supervision of Hiroki
Hirose, Shigeki	Analysis contact, ntuple production, BDT training, MC production, supervision of Hiroki
93 Yamauchi, Hiroki	Main analyser: ntuple production, fit studies and limits extraction
Salvador Salas, Adrian	Main analyser of resolved analysis, providing technical support; ntuple production
Riu, Imma	Signal AODs and TOPQ1s production; provision of other technical support from resolved analysis
Mir Martinez, Lluisa Maria	Monte Carlo production

95 1 Introduction

96 The discovery of a neutral boson with a measured mass around 125 GeV at the Large Hadron Collider
 97 (LHC) in 2012 [1–3] opens the question whether this is the Higgs boson of the Standard Model (SM)
 98 or part of an extended scalar sector. Indeed, charged Higgs bosons¹ are predicted in several extensions
 99 of the SM, which add a second doublet [4–7] or triplets [7–11] to its scalar sector. In CP-conserving
 100 Two-Higgs-Doublet Models (2HDMs) H^+ production and decay at tree level depend on its mass and
 101 two parameters: the mixing angle α of the neutral CP-even Higgs bosons, and the ratio of the vacuum
 102 expectation values of the two Higgs doublets ($\tan \beta$).

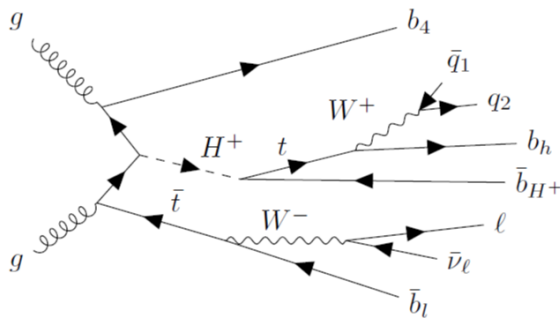


Figure 1: Feynman diagram for $pp \rightarrow tbH^+ \rightarrow tb(tb)$

103 For H^+ masses above the top-quark mass the leading production mode is $gg \rightarrow tbH^+$ and, close to the
 104 alignment limit when $\cos(\beta - \alpha) \approx 0$, the dominant decay mode is $H^+ \rightarrow tb$. For lower H^+ masses, the
 105 dominant decay mode is $H^+ \rightarrow \tau\nu$, as well as for large values of $\tan \beta$ irrespective of the charged Higgs
 106 mass. Therefore, the two decay modes naturally complement each other in searches for charged Higgs
 107 bosons.

108 The ATLAS and CMS collaborations have searched for charged Higgs bosons in pp collisions at $\sqrt{s} = 7, 8$
 109 and 13 TeV, probing the mass range below the top-quark mass in the $\tau\nu$ [12–17], cs [18, 19], and cb [20]
 110 decay modes, as well as above the top-quark mass in the $\tau\nu$ and tb decay modes [14, 16, 17, 21–27]. In
 111 addition, $H^+ \rightarrow WZ$ was searched for in the vector-boson-fusion production mode [28, 29]. No evidence for
 112 charged Higgs bosons was found in any of these searches.

113 This note presents a search for H^+ production in the $H^+ \rightarrow tb$ decay mode using pp collisions at $\sqrt{s} = 13$
 114 TeV. Events with one charged lepton ($l = e, \mu$) and jets in the final state are considered. Compared with the
 115 previous analysis using the same final state and the dataset [24] (so-called ‘resolved analysis’), boosted
 116 top tagging technique is used to identify a hadronically decaying top quark originated from the decay
 117 of the heavy H^+ . This technique allows to improve sensitivities in the high mass regions, where all top
 118 decay products are merged into a single large-R jet, and therefore cannot be reconstructed in the resolved
 119 analysis [24]. To separate signal from SM background, multivariate discriminants are employed in the
 120 regions where the signal rate is expected to be the largest. Limits on the $H^+ \rightarrow tb$ production cross-section
 121 are set by a simultaneous fit of BDT distributions.

¹ Charge-conjugate is implied elsewhere in this note.

¹²² Furthermore, the analysis technique is extended to a search for the $W' \rightarrow tb$ decay, where W' is produced in
¹²³ association with tb .

¹²⁴ The analysis replies on ATLAS official background as well as requested H^+ and W' signal samples, as
¹²⁵ detailed in Section 2, with the TOPQ1 derivation. The ntuples are produced using the TTHbbAnalysis
¹²⁶ software package.² These ntuples are used as inputs to TRExFitter to perform statistical analysis.³

² https://gitlab.cern.ch/atlasHTop/TTHbbAnalysis/-/tree/user/hyamauch/pflow_dev_HplusBoosted

³ <https://gitlab.cern.ch/hyamauch/TRExFitter>

127 2 Data and MonteCarlo Simulated Events

128 2.1 Data Sample

129 This analysis uses pp collision data collected from 2015 to 2018 by the ATLAS detector at $\sqrt{s} = 13$ TeV.
 130 Selected events are recorded using unprescaled triggers, as detailed in Table 1. Only runs with stable
 131 colliding beams and all ATLAS subsystems operational are used. These are summarized in the Good
 132 Run Lists (GRL) shown in Table 2, together with the integrated luminosity collected each year. The total
 133 integrated luminosity is 139 fb^{-1} [30].

Year		Single-electron triggers
2015	e24_lhmedium_L1EM20VH_OR_e60_lhmedium_OR_e120_lhloose	
2016-2018	e26_lhtight_nod0_ivarloose_OR_e60_lhmedium_nod0_OR_e140_lhloose_nod0	
<hr/>		
(a)		
Year		Single-muon triggers
2015	mu20_iloose_L1MU15_OR_mu50	
2016-2018	mu26_ivarmedium_OR_mu50	
<hr/>		
(b)		

Table 1: Single-electron (a) and single-muon (b) trigger menus used depending on the year of data-taking.

Year	Luminosity (pb^{-1})	GRL
2015	3219.6	data15_13TeV/20170619/physics_25ns_21.0.19.xml
2016	32988.1	data16_13TeV/20180129/physics_25ns_21.0.19.xml
2017	44307.4	data17_13TeV/20180619/physics_25ns_Triggerno17e33prim.xml
2018	58450.1	data18_13TeV/20190318/physics_25ns_Triggerno17e33prim.xml

Table 2: Integrated luminosity for each year of data-taking, computed with the OffLumi-13TeV-010 luminosity tag [31], together with the corresponding GRLs [32].

134 2.2 Signal Samples

135 This paragraph describes MC samples used for each signal event's estimation. The summary is shown in
 136 Table 3.

Physics process	Generator	PS generator	Normalisation	PDF set
$t b H^+$ ($M_{H^+} \leq 3.0$ TeV)	MG5_aMC 2.6.2	Pythia 8.212	NLO	NNPDF2.3NLO
$t b H^+$ ($M_{H^+} = 4.0, 5.0$ TeV)	MG5_aMC 2.8.1	Pythia 8.244	NLO	NNPDF3.0NLO
$t b W'$	MG5_aMC 2.9.9	Pythia 8.307	NLO	NNPDF3.0NLO

Table 3: Nominal simulated signal event samples. The generator, parton shower generator and cross-section used for normalization are shown together with the applied PDF set.

137 2.2.1 $\bar{t}bH^+$ Samples

138 The H^+ signal samples are generated with MadGraph5_aMCatNLO (MG5_aMC) [33], which is a generator
 139 based on a four-flavor scheme (4FS) next-to-leading order (NLO) in QCD [34]. The NNPDF2.3NLO
 140 [35] parton distribution function (PDF) set is used.⁴ The width of the H^+ is set to zero. Dynamic QCD
 141 factorisation and renormalisation scales (μ_f and μ_r) are set to $\frac{1}{3} \sum_i \sqrt{m(i)^2 + p_T(i)^2}$, where i runs over the
 142 final state particles (H^+ , t and b) used in the generation. The events are showered with Pythia 8.212 [37]
 143 with the A14 [38] set of underlying-event related parameters tuned to ATLAS. Ten different H^+ mass points
 144 between 1000 and 5000 GeV are generated as detailed in Table 4. The table also shows cross sections from
 145 MG5_aMC and Santander-matched cross sections for 2HDM type-II (a la MSSM), but without SUSY
 146 QCD corrections [33, 39–41]. All samples are fully simulated with the proportions of mc16a, mc16d,
 147 and mc16e corresponding to the amount of data recorded in the 2015-2016, 2017, and 2018 data-taking
 148 years.

DSID	H^+ mass [GeV]	Size	$\sigma^{\text{MG5_aMC}}$ [fb]	$\sigma_{\tan\beta=1}^{\text{MSSM}}$ [fb]	$\sigma_{\tan\beta=60}^{\text{MSSM}}$ [fb]
450004	1000	1.0M	3.28	40.9	37.8
450598	1200	1.0M	1.31	16.4	15.1
450599	1400	1.0M	5.62×10^{-1}	7.1	6.5
450600	1600	1.2M	2.54×10^{-1}	3.2	3.0
450601	1800	1.3M	1.21×10^{-1}	1.5	1.4
450602	2000	1.9M	5.90×10^{-2}	0.8	0.7
451490	2500	1.9M	1.11×10^{-2}	<i>Not available</i>	
451491	3000	1.9M	2.34×10^{-3}	<i>Not available</i>	
508710	4000	1.9M	9.75×10^{-5}	<i>Not available</i>	
508711	5000	1.9M	4.28×10^{-6}	<i>Not available</i>	

Table 4: List of the generated H^+ samples. All samples are simulated with FullSim and available in the appropriate proportions of mc16a, mc16d, and mc16e. The cross-section values for $\tan\beta = 1$ or $\tan\beta = 60$ take into account the production of H^\pm .

149 2.2.2 $\bar{t}bW'$ Samples

150 The left- and right-handed W' (W'_L and W'_R) signal samples are generated with the same options (QCD
 151 scales, PDF, NLO, and 4FS) as the H^+ signal sample generations. Nine different W' mass points between
 152 1000 and 4000 GeV are generated as same as the H^+ signal samples as detailed in Table 5⁵. The table also
 153 shows cross-sections from MG5_aMC. All samples are fully simulated with the proportions of mc16a,
 154 mc16d, and mc16e corresponding to the amount of data recorded in the 2015-2016, 2017, and 2018
 155 data-taking years.

⁴ The samples with masses of 4 and 5 TeV are generated using NNPDF3.0NLO [36] PDF set.

⁵ Only 5000 GeV mass sample aren't generated, because it is difficult technically due to its very narrow mass width.

DSID	W'_L mass [GeV]	Size	$\sigma^{\text{MG5_aMC}}$ [fb]
510889	1000	0.5M	22.54
510890	1200	0.5M	8.56
510891	1400	0.5M	3.50
510892	1600	0.5M	1.53
510893	1800	0.5M	7.03×10^{-1}
510894	2000	0.5M	3.33×10^{-1}
510895	2500	0.5M	5.98×10^{-2}
510896	3000	0.5M	1.19×10^{-2}
510897	4000	0.5M	5.50×10^{-4}

(a)

DSID	W'_R mass [GeV]	Size	$\sigma^{\text{MG5_aMC}}$ [fb]
510898	1000	0.5M	22.66
510899	1200	0.5M	8.52
510900	1400	0.5M	3.50
510901	1600	0.5M	1.52
510902	1800	0.5M	6.98×10^{-1}
510903	2000	0.5M	3.33×10^{-1}
510904	2500	0.5M	5.94×10^{-2}
510905	3000	0.5M	1.19×10^{-2}
510906	4000	0.5M	5.48×10^{-4}

(b)

Table 5: List of the generated W'_L (a) and W'_R (b) samples. All samples are simulated with FullSim and available in the appropriate proportions of mc16a, mc16d, and mc16e.

156 2.3 Background Samples

157 This paragraph describes MC samples used for each background event's estimation. The summary is shown
 158 in Table 6.

Physics process	Generator	PS generator	Normalisation	PDF set
$t\bar{t}$ + jets	PowhegBox v2	Pythia 8.230	NNLO+NNLL	NNPDF3.0NLO
$t\bar{t}H$	PowhegBox v2	Pythia 8.230	NNLO	NNPDF3.0NLO
$t\bar{t}V$	MG5_aMC 2.3.3	Pythia 8.210	NLO	NNPDF3.0NLO
Single top t-chan.	PowhegBox v2	Pythia 8.230	aNNLO	NNPDF3.0NLOnf4
Single top s-chan.	PowhegBox v2	Pythia 8.230	aNNLO	NNPDF3.0NLO
Single top tW	PowhegBox v2	Pythia 8.230	aNNLO	NNPDF3.0NLO
$tHjb$	MG5_aMC 2.6.X	Pythia 8.230	NLO	NNPDF3.0NLOnf4
tHW	MG5_aMC 2.6.2	Pythia 8.235	NLO	NNPDF3.0NLO
tZq	MG5_aMC 2.3.3	Pythia 8.212	NLO	CTEQ6L1LO
tZW	MG5_aMC 2.3.3	Pythia 8.212	NLO	NNPDF3.0NLO
4 tops	MG5_aMC 2.3.3	Pythia 8.230	NLO	NNPDF3.1NLO
V + jets	Sherpa 2.2.1	Sherpa 2.2.1	NNLO	NNPDF3.0NLO
Diboson	Sherpa 2.2	Sherpa 2.2	NLO	NNPDF3.0NLO

Table 6: Nominal simulated background event samples. The generator, parton shower generator and cross-section used for normalisation are shown together with the applied PDF set.

2.3.1 $t\bar{t}$ +jets

The production of $t\bar{t}$ events is modeled using the PowhegBox [42–45] v2 generator, which provides matrix element (ME) at NLO in the strong coupling constant (α_S) with the NNPDF3.0NLO PDF set [36] and the h_{damp} parameter⁶ set to $1.5m_{\text{top}}$ [46]. The functional form of μ_f and μ_r is set to the default scale $\sqrt{m_t^2 + p_{T,t}^2}$. The events are showered with Pythia 8.230 [47].

The uncertainty due to initial-state-radiation (ISR) is estimated using weights in the ME and in the parton shower (PS). To simulate higher parton radiation μ_f and μ_r are varied by a factor of 0.5 in the ME while using the *Var3c* upward variation from the A14 tune. For lower parton radiation, μ_f and μ_r varied by a factor of 2.0 while using the *Var3c* downward variation in the PS. The impact of final-state-radiation (FSR) is evaluated using PS weights which vary μ_r for QCD emission in the FSR by a factor of 0.5 and 2.0, respectively. The impact of the PS and hadronisation model is evaluated by changing the showering of the nominal PowhegBox events from Pythia to Herwig 7.04 [48, 49].

To assess the uncertainty due to the choice of the matching scheme, the Powheg sample is compared to a sample of events generated with MG5_aMC v2.6.0 and the NNPDF3.0NLO PDF set showered with Pythia 8.230. The shower starting scale has the functional form $\mu_q = H_T/2$ [50], where H_T is defined as the scalar sum of the p_T of all outgoing partons. Choice of μ_f and μ_r is the same as that for the Powheg setup.

To enhance the statistics in the phase-space relevant for this analysis, for all the samples described above, dedicated filtered samples were produced, requiring b - or c -hadrons in addition to those arising from the decays of the top quarks, as follows:

- One sample was produced with at least two additional b -hadrons with $p_T > 15$ GeV.

⁶ The h_{damp} parameter controls the transverse momentum of the first additional emission beyond the LO Feynman diagram in the parton shower and therefore regulates the high- p_T emission against which the $t\bar{t}$ system recoils.

- One sample was produced with at least one additional b -hadron with $p_T > 5$ GeV and failing the previous requirement.
- One sample was produced with at least one additional c -hadron with $p_T > 15$ GeV and failing the previous two requirements.

The combined use of the unfiltered and filtered samples is done by assuring no overlap between them (by the use of the heavy flavour filter flag, *TopHeavyFlavorFilterFlag*) and weighted with the appropriate cross-section and filter efficiencies.

2.3.2 $t\bar{t}H$

The production of $t\bar{t}H$ events is modeled in the 5F scheme using PowhegBox [51] at NLO in α_S with the NNPDF3.0NLO PDF set. The h_{damp} parameter is set to $3/4 \times (m_t + m_{\bar{t}} + m_H) = 352.5$ GeV. The events are showered with Pythia 8.230. The uncertainties due to ISR, FSR, PS and hadronisation model, as well as that due to the matching scheme, are evaluated with the same procedures used for the $t\bar{t}$ + jets background.

2.3.3 $t\bar{t}V$

The production of $t\bar{t}V$ events is modeled using the MG5_aMC v2.3.3 generator, which provides ME at NLO in α_S with the NNPDF3.0NLO PDF set. The functional form of μ_f and μ_r is set to the default scale $0.5 \times \sum_i \sqrt{m_i^2 + p_{T,i}^2}$ where the sum runs over all the particles generated from the ME calculation. The events are showered with Pythia 8.210.

Additional $t\bar{t}V$ samples are produced with Sherpa 2.2.0 [52] at LO accuracy, using the MEPS@LO setup [53, 54] with up to one additional parton for the $t\bar{t}V$ sample and two additional partons for the others. A dynamic μ_r is used, defined similarly to that of the nominal MG5_aMC+Pythia samples. The CKKW matching scale of the additional emissions is set to 30 GeV. The default Sherpa 2.2.0 PS is used along with the NNPDF3.0NNLO PDF set.

2.3.4 Single top

t -channel

Single-top t -channel production is modeled using the PowhegBox v2 generator, which provides ME at NLO in α_S in the 4F scheme with the NNPDF3.0NLOnf4 PDF set. The functional form of μ_f and μ_r is set to $\sqrt{m_b^2 + p_{T,b}^2}$, following the recommendation of Ref. [55]. The events are showered with Pythia 8.230.

The impact of the PS and hadronisation model is evaluated by comparing the nominal generator setup with a sample produced with the PowhegBox v2 generator at NLO in QCD in the 4FS using the NNPDF3.0NLOnf4 PDF set. The same events produced for the nominal PowhegBox+Pythia8 sample are used. The events are showered with Herwig 7.04.

212 To assess the uncertainty due to the choice of the matching scheme, the nominal sample is compared
 213 to a sample generated with the MG5_aMC v2.6.2 generator at NLO in QCD in the 4FS, using the
 214 NNPDF3.0NLOnf4 PDF set. Top quarks are decayed at LO using MadSpin [56, 57] to preserve all
 215 spin correlations. The events are showered with Pythia 8.230.

216 **s-channel**

217 Single-top *s*-channel production is modeled using the PowhegBox v2 generator, which provides ME
 218 at NLO in α_S in the 5F scheme with the NNPDF3.0NLO PDF set. The functional form of μ_f and μ_r
 219 is set to the default scale, which is equal to the top quark mass. The events are showered with Pythia
 220 8.230.

221 The impact of the PS and hadronisation model is evaluated by comparing the nominal generator
 222 setup with a sample produced with the PowhegBox v2 generator at NLO in QCD in the 5FS using the
 223 NNPDF3.0NLO PDF set. The same events produced for the nominal PowhegBox+Pythia8 sample
 224 are used. The events are showered with Herwig 7.04.

225 To assess the uncertainty due to choice of the matching scheme, the nominal sample is compared
 226 to a sample generated with the MG5_aMC v2.6.2 generator at NLO in QCD in the 5FS, using
 227 the NNPDF3.0NLO PDF set. Top quarks are decayed at LO using MadSpin to preserve all spin
 228 correlations. The events are showered with Pythia 8.230.

229 ***tW***

230 Single-top *tW* associated production is modeled using the PowhegBox v2 generator, which provides ME
 231 at NLO in α_S in the 5F scheme with the NNPDF3.0NLO PDF set. The functional form of μ_f
 232 and μ_r is set to the default scale, which is equal to the top quark mass. The diagram removal scheme
 233 [58] is employed to handle the interference with $t\bar{t}$ production [46]. The events are showered with
 234 Pythia 8.230.

235 The nominal Powheg+Pythia8 sample is compared to an alternative sample generated using the
 236 diagram subtraction scheme [46, 58] to estimate the uncertainty due to the interference with $t\bar{t}$
 237 production.

238 The impact of the PS and hadronisation model is evaluated by comparing the nominal generator
 239 setup with a sample produced with the Powheg v2 generator at NLO in QCD in the 5FS using the
 240 NNPDF3.0NLO PDF set. The same events produced for the nominal Powheg+Pythia8 sample are
 241 used. The events are showered with Herwig 7.04.

242 To assess the uncertainty due to the choice of the matching scheme, the nominal sample is compared
 243 to a sample generated with the MG5_aMC v2.6.2 generator at NLO in QCD in the 5FS, using the
 244 NNPDF2.3NLO PDF set. The events are showered with Pythia 8.230.

245 **2.3.5 *tH***

246 ***tHjb* production**

247 The production of *tHjb* events is modeled in the 4F scheme using the MG5_aMCv2.6.0 with
 248 the NNPDF3.0NLOnf4 PDF set. The functional form of μ_f and μ_r is set to the default scale
 249 $1/2 \times \sum_i \sqrt{m_i^2 + p_{T,i}^2}$, where the sum runs over all the particles generated from the ME calculation.

250 The shower starting scale has the functional form $\mu_q = H_T/2$, where H_T is defined as the scalar sum
 251 of the p_T of all outgoing partons. The events are showered with Pythia 8.230.

252 ***tHW* production**

253 The production of *tHW* events is modeled in the 5F scheme using the MG5_aMCv2.6.2 with the
 254 NNPDF3.0NLO PDF set. The functional form μ_f and μ_r is set to the default scale $1/2 \times \sum_i \sqrt{m_i^2 + p_{T,i}^2}$
 255 where the sum runs over all the particles generated from the ME calculation. The shower starting
 256 scale has the functional form $\mu_q = H_T/2$, where H_T is defined as the scalar sum of the p_T of all
 257 outgoing partons. The events are showered with Pythia 8.235.

258 **2.3.6 Rare *t* processes**

259 ***tZq***

260 The *tZq* MC samples [59] are generated at LO in α_S using MG5_aMC 2.3.3 in the 4F scheme,
 261 with the CTEQ6L1 [60] LO PDF set. Following the recommendations taken from Ref. [55], the
 262 renormalisation and factorisation scales are set to $4 \times \sum_b \sqrt{m_i^2 + p_{T,b}^2}$, where the *b*-quark is the one
 263 coming from the gluon splitting. The events are showered with Pythia 8.212.

264 ***tZW***

265 The *tZW* sample is simulated using the MG5_aMC v2.3.3 generator at NLO in α_S with the
 266 NNPDF3.0NLO PDF set. The top quark is decayed inclusively while the *Z* boson decays to a pair of
 267 leptons, by means of Pythia 8.212. The 5F scheme is used where all the quark masses are set to zero,
 268 except for the top quark. μ_f and μ_r are set to the top quark mass. The DR1 scheme [58] is employed
 269 to handle the interference between *tWZ* and *ttZ*, and is applied to the *tWZ* sample.

270 **4 tops**

271 The production of 4 tops events is modeled using the MG5_aMC v2.3.3 generator, which provides
 272 ME at NLO in α_S with the NNPDF3.1NLO PDF set. The functional form of μ_f and μ_r is set to
 273 $0.25 \times \sum_i \sqrt{m_i^2 + p_{T,i}^2}$, where the sum runs over all the particles generated from the ME calculation,
 274 following the Ref.[61]. The events are showered with Pythia 8.230.

275 **2.3.7 Vector bosons plus jets**

276 QCD vector bosons plus jets production is simulated with the Sherpa v2.2.1 PS Monte Carlo generator. In
 277 this setup, NLO-accurate ME for up to two jets, and LO-accurate ME for up to four jets are calculated with
 278 the Comix [62] and OpenLoops [63, 64] libraries. The default Sherpa PS [65] based on Catani-Seymour
 279 dipoles and the cluster hadronisation model [66] are used. They employ the dedicated set of tuned
 280 parameters developed by the Sherpa authors for this version based on the NNPDF3.0nnlo set. The NLO ME
 281 of a given jet-multiplicity are matched to the PS using a colour-exact variant of the MC@NLO algorithm
 282 [67]. Different jet multiplicities are then merged into an inclusive sample using an improved CKKW
 283 matching procedure [53, 54], which is extended to NLO accuracy using the MEPS@NLO prescription
 284 [68]. The merging cut is set to $Q_{\text{cut}} = 20$ GeV.

285 QCD scale uncertainties are evaluated on-the-fly [69] using 7-point variations of μ_f and μ_r in the ME. The
 286 scales are varied independently by factors of 0.5 and 2 but avoiding opposite factors. PDF uncertainties for
 287 the nominal PDF set are evaluated using the 100 variation replicas, as well as ± 0.001 shifts of α_S .

288 2.3.8 Dibosons

289 Diboson samples are simulated with the Sherpa v2.2 generator. In this setup multiple ME are matched
290 and merged with the Sherpa PS based on Catani-Seymour dipole using the MEPS@NLO prescription.
291 For semileptonically and fully leptonically decaying diboson samples, as well as loop-induced diboson
292 samples, the virtual QCD correction for ME at NLO accuracy are provided by the OpenLoops library.
293 For electroweak $VVjj$ production, the calculation is performed in the G_μ scheme, ensuring an optimal
294 description of pure electroweak interactions at the electroweak scale. All samples are generated using
295 the NNPDF3.0nnlo set, along with the dedicated set of tuned PS parameters developed by the Sherpa
296 authors.

297 3 Object Reconstruction

298 3.1 Electrons

299 Electrons are reconstructed from energy clusters in the electromagnetic calorimeter matched to tracks
 300 reconstructed in the inner detector (ID) [70, 71], and are required to have $p_T > 10$ GeV and $|\eta| < 2.47$.
 301 Candidates in the barrel–endcap transition region of the calorimeter ($1.37 < |\eta| < 1.52$) are excluded.
 302 Electrons must satisfy the *tight* identification criterion based on a likelihood discriminant described in
 303 Ref. [71] and the following constraints in the longitudinal and transverse impact parameters: $|z_0| < 0.5$ mm
 304 and $|d_0|/\sigma_{d_0} < 5$. The impact parameters are defined with respect to the beamline. Electrons are required
 305 to satisfy the *FCTight* isolate criteria [72].

306 3.2 Muons

307 Muons are reconstructed from either track segments or full tracks in the muon spectrometer which are
 308 matched to tracks in the ID [73]. Tracks are then re-fitted using information from both detector systems.
 309 Muons are required to have $p_T > 10$ GeV and $|\eta| < 2.5$ and the following constraints in the longitudinal
 310 and transverse impact parameters: $|z_0| < 0.5$ mm and $|d_0|/\sigma_{d_0} < 3$. Muons should satisfy the *medium*
 311 identification and the *FCTightTrackOnly* isolation criteria [72].

312 3.3 Taus

313 Hadronically decaying tau leptons (τ_{had}) are distinguished from jets using the track multiplicity and the
 314 τ_{had} identification algorithm based on a recurrent neural network [74]. This algorithm exploits the track
 315 collimation, jet substructure, kinematic information and so son. These τ_{had} candidates are required to have
 316 $p_T > 25$ GeV, $|\eta| < 2.5$ and pass the *Medium τ* -identification working point. Although taus are not used in
 317 the analysis, the consistent configuration with the resolved analysis as well as the $t\bar{t}H(\rightarrow bb)$ analysis is
 318 kept.

319 3.4 Small- R jets and b -tagging

320 Jets are reconstructed using the anti- k_t clustering algorithm [75] on particle-flow objects [76] with a radius
 321 of $R = 0.4$. Jets are calibrated using the standard jet calibration procedure, which corrects the jet energy to
 322 match on average the true jet energy at the particle level and applies an in-situ correction for data [77]. The
 323 jet collection name in ATLAS is `AntiKt4EMPFflowJets_BTagging201903`. Jets are required to have
 324 $|\eta| < 2.5$ such that they are within the acceptance of the ID and the recommended jet vertex tagging (JVT)
 325 requirement [78] is applied to jets with $p_T < 60$ GeV in order to remove jets originating from the pile-up.

326 Small- R jets originating from the hadronization of b -quarks (referred to as b -jets hereafter) are identified
 327 using an algorithm based on multivariate techniques to combine information from the impact parameters
 328 of displaced tracks as well as properties of secondary and tertiary decay vertices reconstructed within the
 329 jets. In this analysis, b -tagging relies on the *DL1r* tagger [79], trained on simulated $t\bar{t}$ events, and the event
 330 selection makes use of jets b -tagged with the *DL1r* algorithm at the 70% efficiency working point.

331 3.5 Large- R jets and top-tagging

332 Top quarks with high transverse momentum ($p_T \gtrsim 2m_t$) are expected to result in decay products that are
 333 collimated. For top quarks decaying hadronically (bqq'), the three quarks may not be resolved as three
 334 separate jets. In order to reconstruct these boosted hadronically-decaying top quarks, large-radius (large- R)
 335 jets are used. The large- R jets are formed from the topological clusters of calorimeter cells which are
 336 calibrated to the hadronic energy scale using the local calibration weighting method [80] and reconstructed
 337 using the anti- k_t algorithm with radius parameter of $R = 1.0$. The jet collection name in ATLAS is
 338 `AntiKt10LCTopoTrimmedPtFrac5SmallR20Jets`. These jets are further trimmed to remove the effects
 339 of pile-up and underlying events. The trimming [81] is done by reclustering the original constituents of a
 340 large- R jet into a collection of R_{sub} subjets using k_t algorithm [82]. The subjets are then discarded if they
 341 carry less than a specific fraction (f_{cut}) of the p_T of the original large- R jet. In this analysis, the optimized
 342 values ($R_{\text{sub}} = 0.2$, $f_{\text{cut}} = 5\%$) are used [83]. The large- R jet energy and mass scale are then calibrated
 343 using correction factors derived from simulation. The mass of the large- R jets is calculated using tracking
 344 and calorimeter information, the so-called combined mass technique [84]. Only the large- R jets that satisfy
 345 $200 < p_T < 3000 \text{ GeV}$, $|\eta| < 2.0$ and $40 < m_{\text{comb}} < 600 \text{ GeV}$ are considered in this analysis.

346 The identification of hadronically decaying top quarks that are reconstructed as large- R jets is performed
 347 using a multivariate classification algorithm employed in a deep neural network [85]. In the kinematic
 348 region of interest in this search, a single large- R jet captures the top quark decay products, resulting in a
 349 characteristic multi-core structure within the jet, in contrast to a typical single-core structure associated with
 350 jets in multijet. In order to exploit this characteristic behavior for top quark identification, a multivariate
 351 top-tagging classifier was developed. The tagger uses multiple jet-level discriminants as inputs, such as
 352 calibrated jet p_T and mass, information about the dispersion of the jet constituents such as N -subjettiness
 353 [86], splitting scales [87] and energy correlation functions [88]. Top-tagging, associated scale factors, and
 354 uncertainties are only provided for jets with $350 < p_T < 2500 \text{ GeV}$. The tagger used is optimized for the
 355 contained top definition, in which the signal category is defined using jets matched to a truth top quark. In
 356 addition, a truth jet matched to the reconstructed jet is required to have a mass above 140 GeV and at least
 357 one b -hadron ghost matched to it.

358 In this analysis, large- R jets which pass the 80% efficiency working point of the contained top-tagging
 359 criterion ($J_{\text{top-tagged}}$) are chosen as the boosted top candidates. Especially, the leading boosted top candidate
 360 out of them is represented by $J_{\text{top-tagged}}^{\text{1st}}$ in the following sections.

361 3.6 Overlap Removal

362 In order to avoid counting a single detector response as more than one lepton or jet, the following overlap
 363 removal procedure is applied.

364 To prevent double-counting of electron energy deposits as jets, the small- R jet within $\Delta R_y = \sqrt{(\Delta y)^2 + (\Delta\phi)^2} =$
 365 0.2 of a selected electron is removed. Here, the rapidity is defined as $y = \frac{1}{2} \ln \frac{E+p_z}{E-p_z}$, where E is the energy
 366 and p_z is the longitudinal component of the momentum along the beam pipe. If the nearest small- R jet
 367 surviving that selection is within $\Delta R_y = 0.4$ of the electron, the electron is discarded. In the case that a
 368 large- R jet is found within $\Delta R = 1.0$ of the electron, the large- R jet is removed.⁷

⁷ Following the recommendation for ATLAS analyses in Run 2 [89], the overlap removal implemented in the `AssociationUtils` package [90] is based on ΔR_y . It is found more appropriate in the case of non-massless objects [91]. However, overlap removal

- 369 Muons are removed if their distance from the nearest small- R jet is within $\Delta R_y < 0.4$. This treatment
 370 reduces the background from heavy-flavor decays inside small- R jets. However, if this small- R jet has
 371 fewer than three associated tracks, the muon is kept and the small- R jet is removed instead. This avoids an
 372 inefficiency for high-energy muons undergoing significant energy loss in the calorimeter.
- 373 A τ_{had} candidate is rejected if it is within $\Delta R_y < 0.2$ from any selected electron or muon. Also, small- R
 374 jets with $\Delta R_y < 0.2$ around a τ_{had} candidate are rejected. The overlap removal with τ_{had} is applied in order
 375 to keep consistency with the $t\bar{t}H(\rightarrow bb)$ analysis as well as the $H^+ \rightarrow tb$ analysis.
- 376 Small- R jets within $\Delta R < 1.0$ of a leading top-tagged large- R jet are removed⁶ to prevent double-counting
 377 of jet energy deposits. All of the above overlap removal procedures are summarized in Table 7.

Reject	Against	Criteria
Small- R jet	Electron	$\Delta R_y < 0.2$
Electron	Small- R jet	$0.2 < \Delta R_y < 0.4$
Small- R jet	Muon	$N_{\text{track}} < 3$ in jet and $\Delta R_y < 0.4$
Muon	Small- R jet	$\Delta R_y < 0.4$
τ_{had}	Electron	$\Delta R_y < 0.2$
τ_{had}	Muon	$\Delta R_y < 0.2$
Small- R jet	τ_{had}	$\Delta R_y < 0.2$
Large- R jet	Electron	$\Delta R < 1.0$
Small- R jet	Leading top-tagged large- R jet	$\Delta R < 1.0$

Table 7: Summary of overlap removal procedures in this analysis.

for large- R jets is performed in the ttHOffline software and is computed based on ΔR .

378 4 Analysis Strategy

379 We take different analysis approaches between the under and above 3 TeV signal mass points. In the
 380 analyses at the under 3 TeV mass points, we adopt the multivariable analyses by training boosted decision
 381 tree (BDT) on every mass point. On the other hand, at the above 3 TeV mass points, we adopt the method
 382 based on cut-and-counting. We describe these strategies below.

383 **4.1 Analysis strategy at $M_{H^+}, M_{W'} \leq 3$ TeV points**

384 **4.1.1 Event Selection**

385 In the analysis below 3 TeV signal mass points, two signal regions, “SR1” and “SR2”, are defined according
 386 to the numbers of leptons, top tagged large- R jets, and b -tagged small- R jets.

387 Figure 2 shows the schematic of boosted event topology of an $H^+ \rightarrow tb$ event. A signal event is expected
 388 to have one $J_{\text{top-tag}}$, three b -jets, and one lepton+MET. However, the b -jet originated from the gluon is
 389 typically not detectable because it tends to fly in the forward directions and outside the detector acceptance.
 390 Therefore, at least two b -jets are required in this analysis.

391 Events in the SR1 are required to have exactly one lepton (e or μ) that is matched to the one firing one of
 392 the single lepton triggers to be consistent with the signal event as shown in Figure 2. Events must also have
 393 at least one top-tagged large- R jet, at least two small- R jets, and exactly two b -tagged small- R jets. These
 394 small- R jets must additionally satisfy $\Delta R(J_{\text{top-tag}}^{\text{1st}}, \text{jet}) > 1.0$ to ensure these small- R jets are not constituent
 395 of the leading top-tagged jet. This analysis does not require missing E_T . The SR1 becomes enriched in
 396 $t\bar{t}$ + light events after these selections as shown in Figure 3. Therefore, SR1 is used to control $t\bar{t}$ + light in
 397 the final data fittings.

398 Events in the SR2 are required to have one more small- R jet and one more b -tagged small- R jet in addition
 399 to the requirements of SR1. This region is enriched in $t\bar{t}$ + heavy flavor jets (HF) events (i.e., $t\bar{t}+ \geq 1b$,
 400 $t\bar{t}+ \geq 1c$).

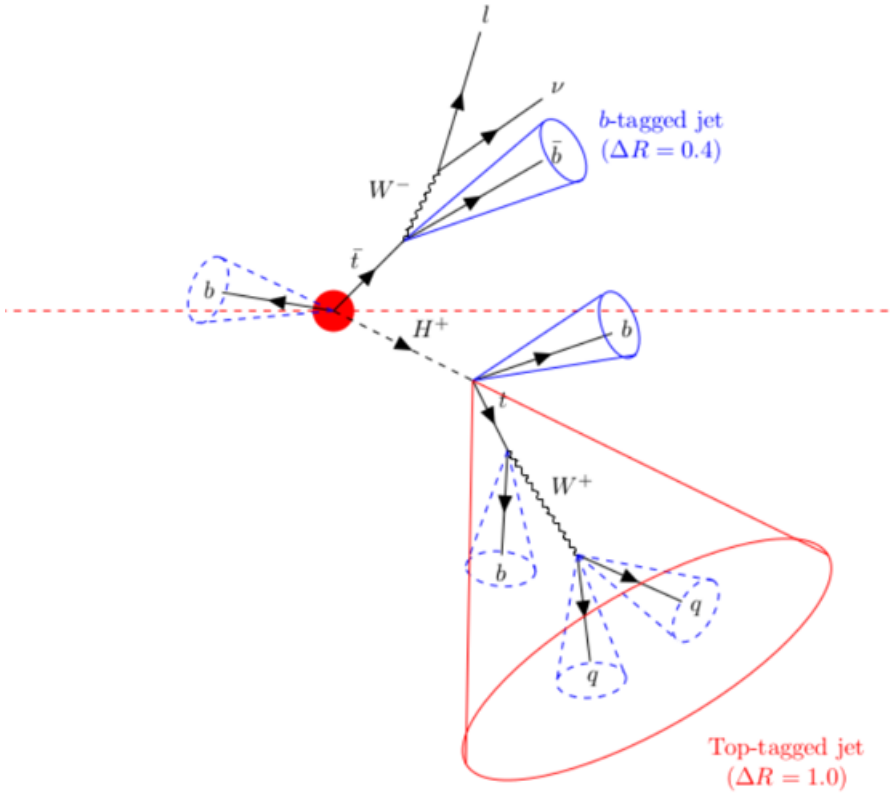


Figure 2: Schematic of boosted event topology. Signal event has one $J_{\text{top-tag}}$ and at least two b -tagged small- R jets.

Cut	SR1	SR2
leptons	$\mathbf{N_{lepton}=1}$ <u>Electron</u> - $p_T > 27 \text{ GeV}$ - $ \eta < 1.37$ or $1.52 < \eta < 2.47$ <u>Muon</u> - $p_T > 27 \text{ GeV}$ - $ \eta < 2.5$	Same as SR1
Top-tagged large- R jets	$\mathbf{N_{J_{\text{top-tag}} \geq 1}}$ - $350 \text{ GeV} < p_T < 2500 \text{ GeV}$ - $m > 40 \text{ GeV}$	Same as SR1
Small- R jets	$\mathbf{N_{jet} \geq 2}$ - $p_T > 25 \text{ GeV}$ - $ \eta < 2.5$ - $\Delta R(J_{\text{top-tag}}, jet) > 1.0$	$\mathbf{N_{jet} \geq 3}$ (Kinematic requirements are same as SR1)
b -tagged small- R jets	$\mathbf{N_{b-jet} = 2}$	$\mathbf{N_{b-jet} \geq 3}$

Table 8: Event selections in the SR1 and SR2. After these selections, SR1 becomes enriched in $t\bar{t} + \text{light}$, and SR2 becomes enriched in $t\bar{t} + \text{HF}$.

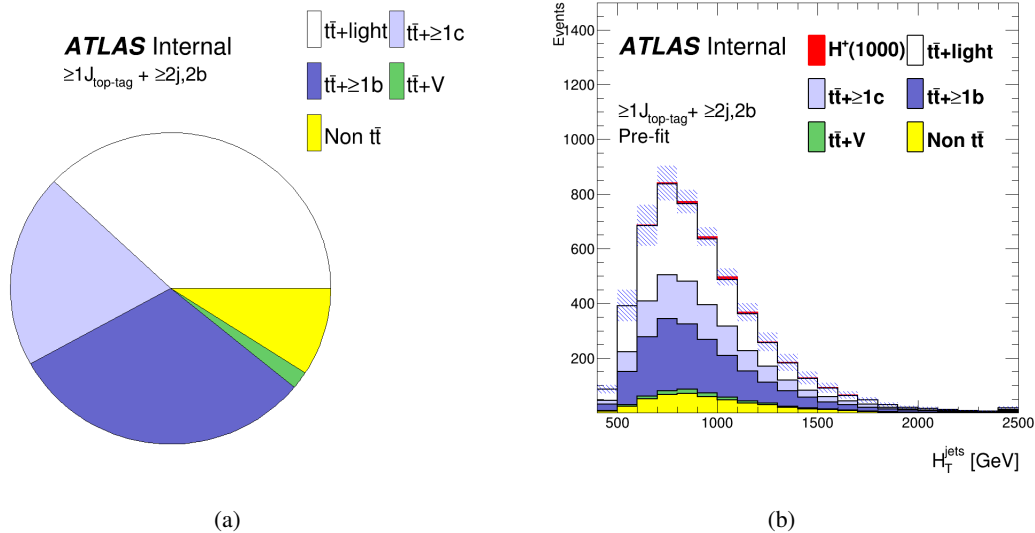


Figure 3: Background composition in the SR1 is shown in the pie chart (a) and the H_T^{jets} distributions (b).

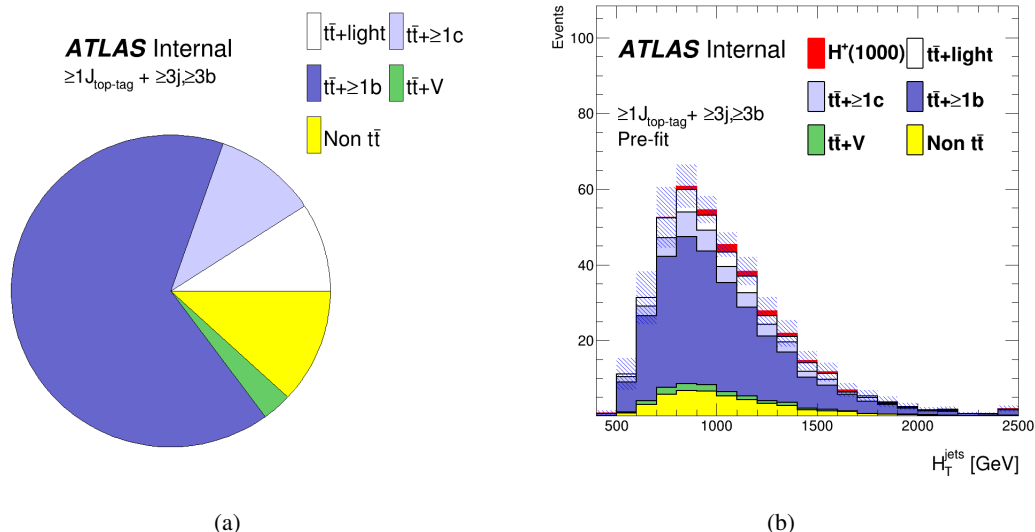


Figure 4: Background composition in the SR2 is shown in the pie chart (a) and the H_T^{jets} distributions (b).

401 The number of expected signal and background events in the SR1 and SR2 are shown in Table 9. The
 402 predicted number of H^+ signal events for the 1000 and 3000 GeV mass hypothesis assume
 403 $\sigma(pp \rightarrow tbH^+) \times Br(H^+ \rightarrow tb) = 0.046$ pb. This is the upper limit at $M_{H^+} = 1000$ GeV obtained from the
 404 resolved analysis, which is the largest upper limit in the mass range
 405 $1000 \geq M_{H^+} \geq 2000$ GeV where both the resolved and the boosted analyses search for H^+ . We use the signal
 406 $\sigma \times Br$ to define the blinded regions.

	SR1	SR2
$t\bar{t}$ + light	1943 ± 87	35 ± 4
$t\bar{t} + \geq 1c$	1029 ± 54	41 ± 5
$t\bar{t} + \geq 1b$	1588 ± 69	253 ± 15
$t\bar{t} + W$	36 ± 19	52 ± 27
$t\bar{t} + Z$	57 ± 9	2 ± 1
Wt channel	176 ± 89	9 ± 2
t channel	36 ± 3	1 ± 0
Other top sources	30 ± 11	9 ± 4
$VV, V+jets$	147 ± 53	5 ± 2
$t\bar{t}H$	79 ± 3	24 ± 1
Total	5120 ± 230	387 ± 24
H^+ 1000 GeV	46 ± 5	9 ± 2
H^+ 3000 GeV	60 ± 14	13 ± 3

Table 9: Number of expected and selected events split according to the analysis region. The quoted uncertainties include both statistical and systematic uncertainties before fitting.

407 4.1.2 Multivariable analysis using BDT

408 In this search, the most important background is $t\bar{t}$ + jets as discussed in Section 4.1. To enhance the
 409 separation between signal and background, multivariable analysis is performed using Boosted Decision
 410 Trees (BDT) technique of TMVA [92]. Obtained BDT score distribution is used in the profile likelihood fit
 411 as a final discriminant (Section 7).

412 Signal and background definition in BDT training

413 To classify signal (H^+ and W') and $t\bar{t}$ + jets background events, BDTs are trained using the simulated
 414 H^+ signal and $t\bar{t}$ + jets background samples. This analysis under 3 TeV mass points considers eight
 415 different mass hypotheses, and the training is performed on each mass hypothesis. On the other
 416 hand, the $t\bar{t}$ + jets background samples are common in each training. Since kinematics of H^+ signals
 417 become harder in higher mass hypotheses, the BDTs trained using the higher H^+ mass samples
 418 typically have greater separation power. These signal events and background events used in training
 419 are required to pass either SR1 or SR2 criteria. These BDTs optimized using H^+ signal samples can
 420 be also used in $W' \rightarrow tb$ analysis because the difference between a H^+ and W' is only their spin and
 421 the kinematic characteristics of $W' \rightarrow tb$ events are similar to the ones of $H^+ \rightarrow tb$ events. This
 422 validation is done in the section below. BDTs are also trained using 4 and 5 TeV mass point samples.
 423 These BDT outputs are only used for the study in Section 5.4.

424 BDT training settings

425 To fully use the simulation samples' statistics, we adopt the 4-fold cross-validation method in the
 426 BDT training (Figure 5). Each simulation sample is divided into four sub-datasets (Fold1, Fold2,
 427 Fold3, and Fold4). For each MC event, a random number is generated with the MC event number as
 428 a seed, and the event is categorized into one of the sub-datasets according to the generated number.
 429 Two of the four sub-datasets are labeled "TRAIN," which are used for BDT training. One of the other
 430 sub-datasets is labeled "VALID" and is used to optimize the BDT performance. The last sample,
 431 "TEST" is used to construct a fit template. Four combinations of sub-dataset usage (Split1 to Split4

432 in Figure 5) are tried, and we obtain four statistically-independent BDTs and fit templates. They are
 433 combined into one fit template used in the profile likelihood fit (Section.7).

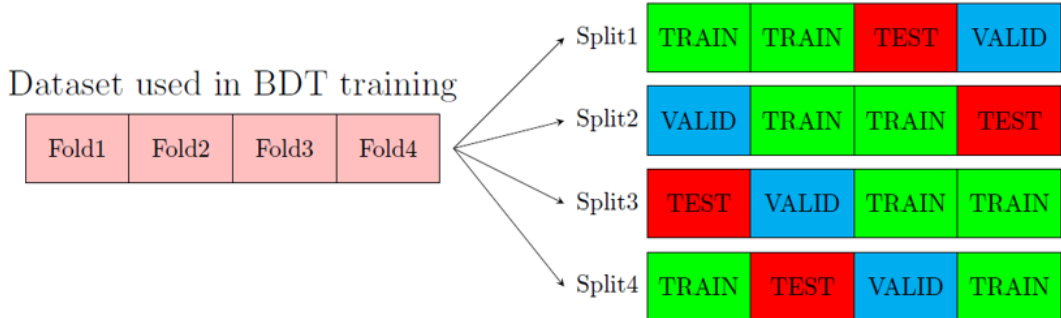


Figure 5: Scheme of 4-fold cross-validation of BDT in this analysis.

434 Hyperparameters for the BDTs are summarized in Table. 10. Those hyperparameters are chosen to
 435 obtain the best sensitivity.

Configuration	
Algorithm	Gradient boosting
<i>Hyperparameters</i>	
NTrees	100
MinNodeSize	2.5
MaxDepth	3
nCuts	20

Table 10: List of hyperparameters used in the training of a BDT

436 Input variables in BDT

437 Jets originating from a H^+ (W') decay have higher p_T comparing with $t\bar{t}$ + jets events due to its
 438 heavy mass. Additionally, angular and kinematics correlation among jets are different between H^+
 439 (W') and $t\bar{t}$ + jets events because these bosons create a resonance. The BDT is trained to exploit
 440 these kinematic characteristics fully. The variables used in BDT training are summarized in Table
 441 11. Any variables for missing E_T are not used in BDT training. In Figure 6, each distribution in the
 442 H^+ sample with a mass of 3000 GeV is compared with the $t\bar{t}$ + jets background. Table 12 shows the
 443 ranking of these variables.

Symbol	Description
HT_jets	Scalar sum of the transverse energy of all jets
LeadingJet_pt	Leading jet p_T
Mjjj_MaxPt	Invariant mass of the jet triplet with maximum p_T
Mbb_MaxPt	Invariant mass of the b-jet pair with maximum p_T
Muu_MindR	Invariant mass of the untagged jet-pair with minimum ΔR
dRlepb_MindR	ΔR between the lepton and the pair of b -jets with smallest ΔR
dRbb_avg	Average ΔR between all b -jet pairs in the event
Centrality_all	Centrality calculated using all jets and leptons
H1_all	Second Fox-Wolfram moment calculated using all jets and lepton
LeadingTop_pt	Leading top-tagged jet p_T
LeadingTop_m	Invariant mass of leading top-tagged jet
Pt_tb	p_T of the pair of leading top-tagged jet and leading b -jet
M_tb	Invariant mass of the pair of leading top-tagged jet and leading b -jet
PtAsymm_tb	p_T asymmetry between leading top-tagged jet and leading b -jet

Table 11: List of variables included in the training of the BDT

Ranking	Variable	Importance				
		Fold1	Fold2	Fold3	Fold4	Avg.
1	HT_jets	9.509E-02	1.118E-01	1.216E-01	1.073E-01	1.089E-01
2	Centrality_all	1.053E-01	9.995E-02	1.126E-01	1.012E-01	1.048E-01
3	M_tb	9.192E-02	9.473E-02	8.282E-02	8.014E-02	8.740E-02
4	LeadingTop_pt	8.710E-02	8.107E-02	6.472E-02	7.292E-02	7.645E-02
5	Pt_tb	7.944E-02	7.816E-02	7.888E-02	6.795E-02	7.611E-02
6	LeadingJet_pt	6.180E-02	7.860E-02	6.628E-02	7.577E-02	7.061E-02
7	dRlepb_MindR	6.997E-02	7.842E-02	6.968E-02	6.393E-02	7.050E-02
8	dRbb_avg	6.236E-02	6.435E-02	5.331E-02	7.843E-02	6.461E-02
9	Mbb_MaxPt	5.348E-02	6.657E-02	7.339E-02	5.552E-02	6.224E-02
10	PtAsymm_tb	5.209E-02	6.526E-02	5.843E-02	6.620E-02	6.050E-02
11	Mjjj_MaxPt	6.439E-02	6.248E-02	5.503E-02	5.577E-02	5.942E-02
12	H1_all	6.316E-02	4.577E-02	4.876E-02	6.291E-02	5.515E-02
13	LeadingTop_m	5.868E-02	3.864E-02	5.567E-02	5.748E-02	5.262E-02
14	Muu_MindR	4.438E-02	3.422E-02	5.889E-02	5.439E-02	4.797E-02

Table 12: Importance ranking of variables used in BDT training on 3000 GeV H+ mass hypothesis. Importance values are output from TMVA.

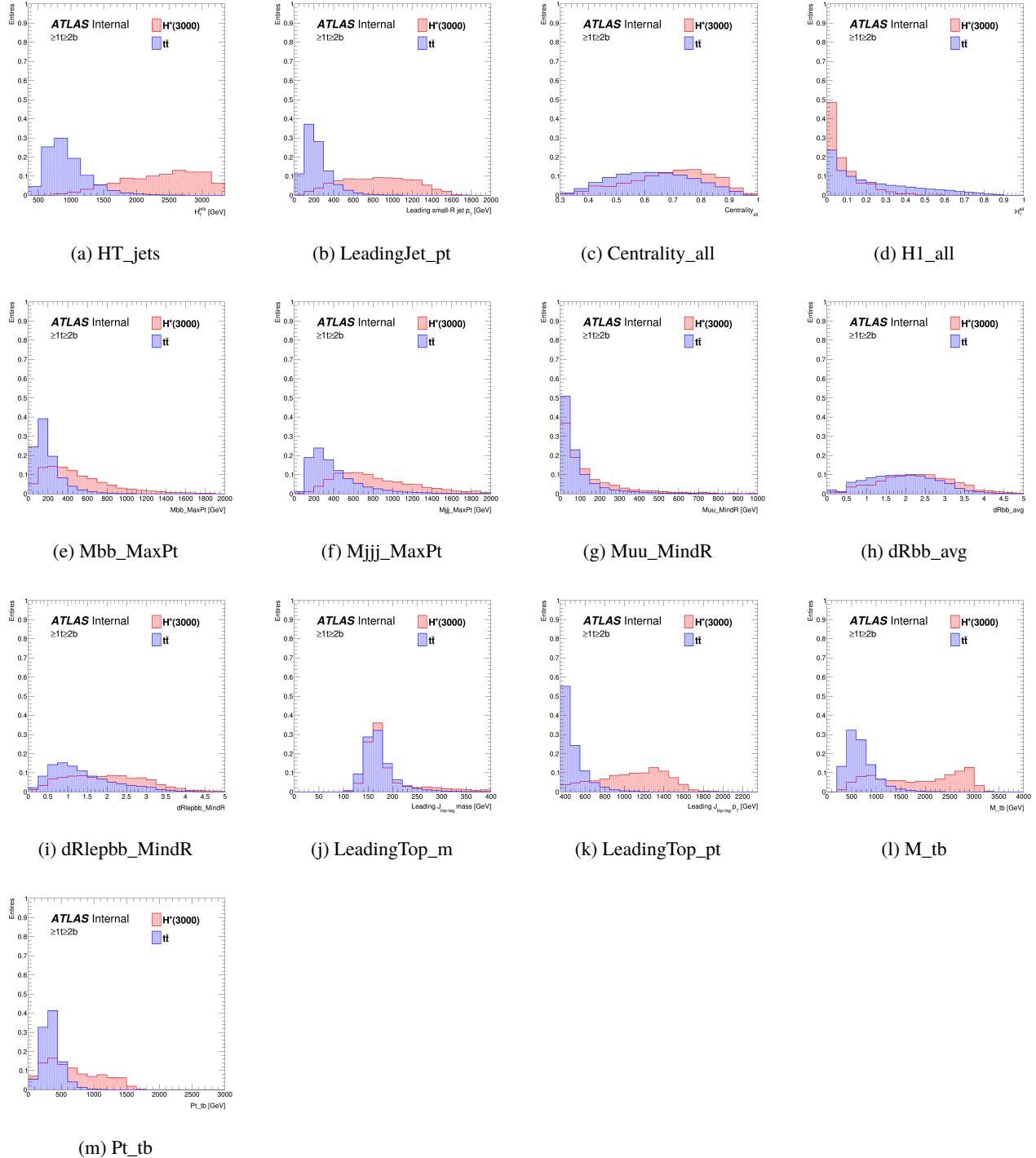


Figure 6: Comparison of input variables for BDT training between H^+ and $t\bar{t} + \text{jets}$ events under 3000 GeV H^+ mass hypothesis in the inclusive SR (i.e., SR1 + SR2).

Results of BDT training

The BDT output distributions for H^+ signal and background events in the inclusive SR region (i.e.,

444

445

446 SR1+SR2) for different values of the H^+ mass are shown in Figure 7 to 14, together with receiver
 447 operating characteristic (ROC) curves.

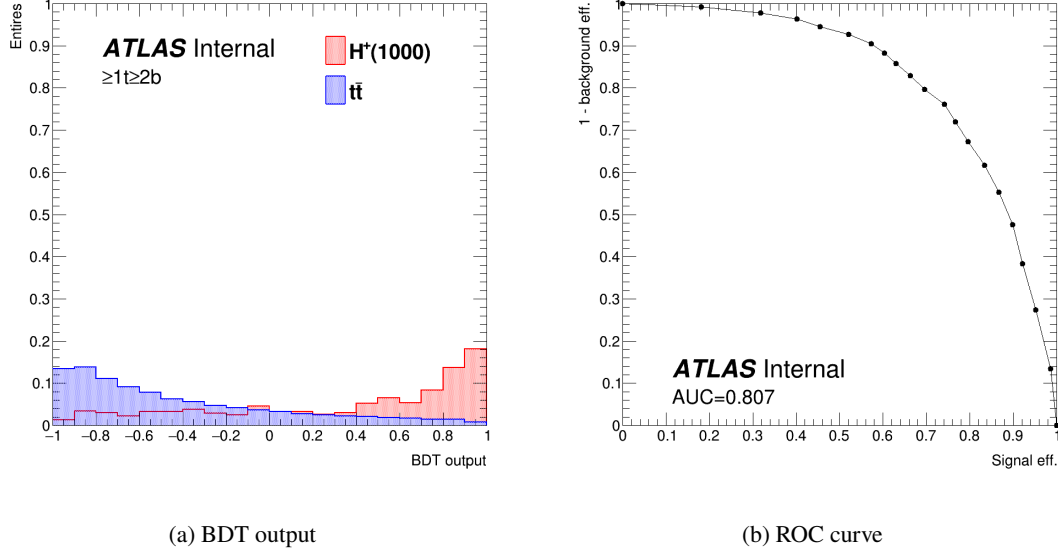


Figure 7: BDT distribution and ROC curve for the 1000 GeV H^+ mass hypothesis.

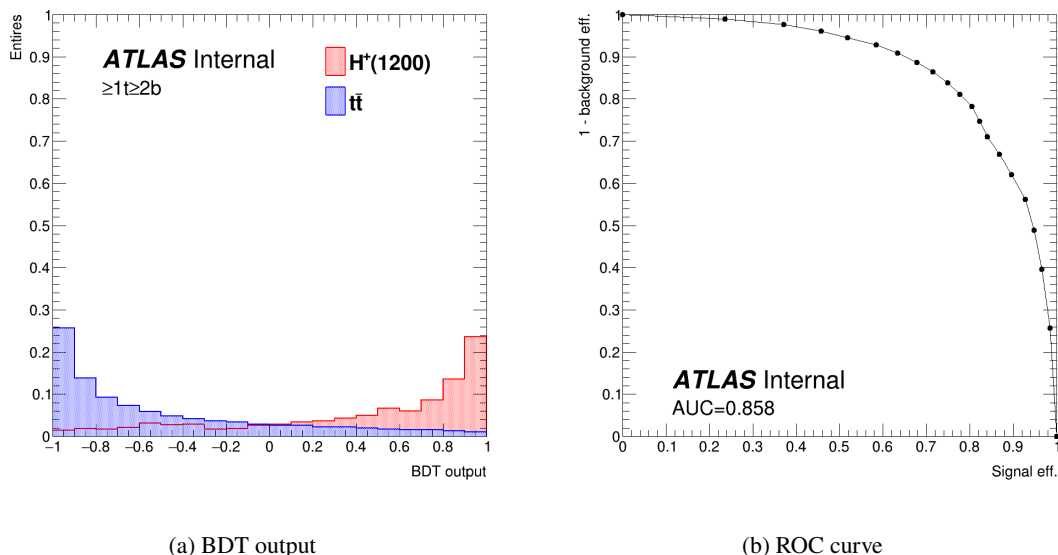


Figure 8: BDT distribution and ROC curve for the 1200 GeV H^+ mass hypothesis.

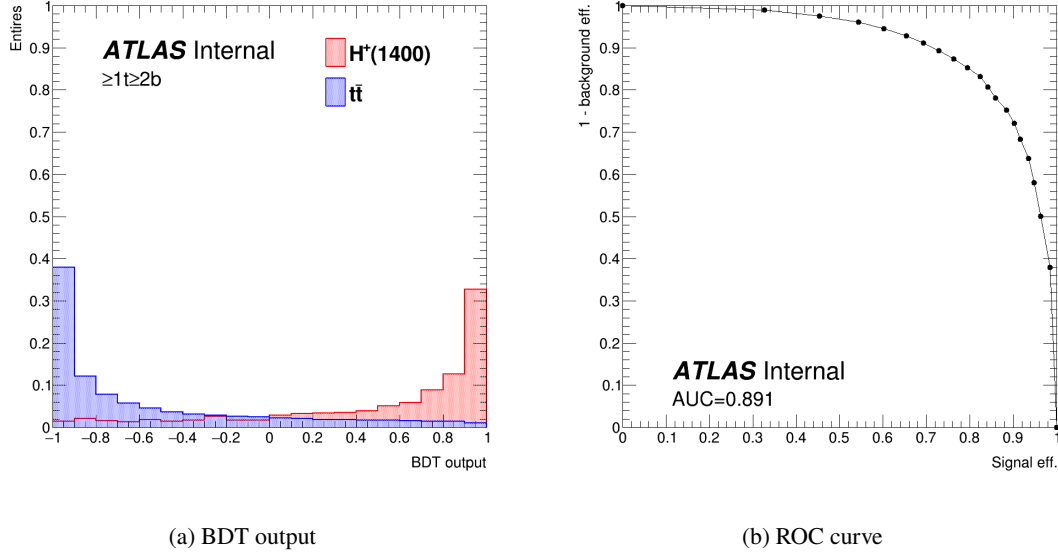


Figure 9: BDT distribution and ROC curve for the 1400 GeV H^+ mass hypothesis.

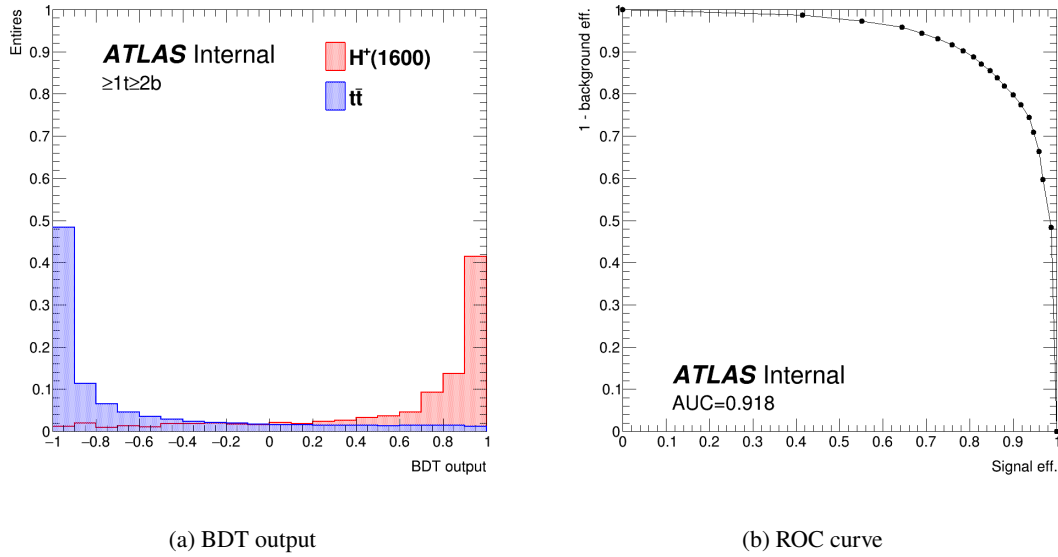


Figure 10: BDT distribution and ROC curve for the 1600 GeV H^+ mass hypothesis.

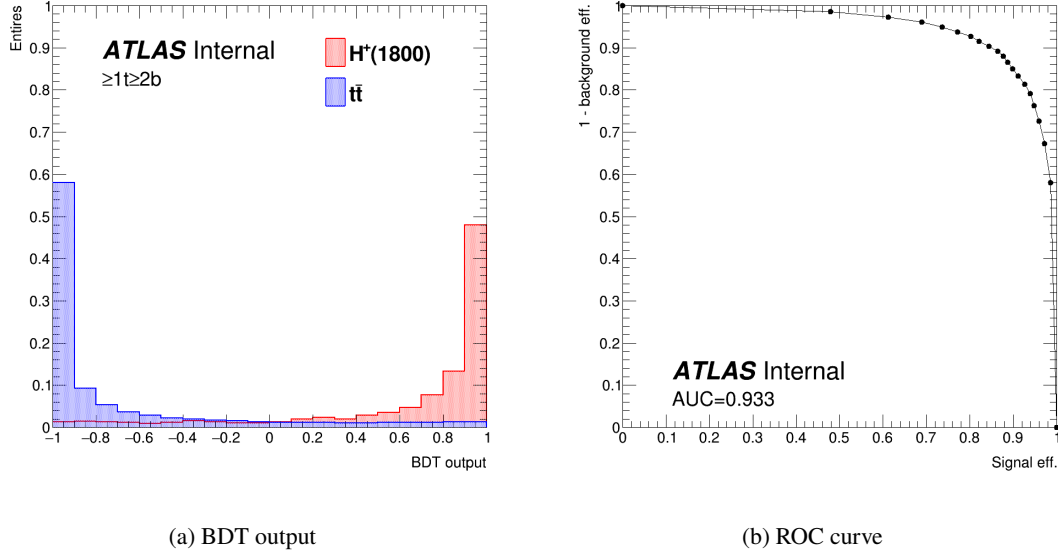


Figure 11: BDT distribution and ROC curve for the 1800 GeV H^+ mass hypothesis.

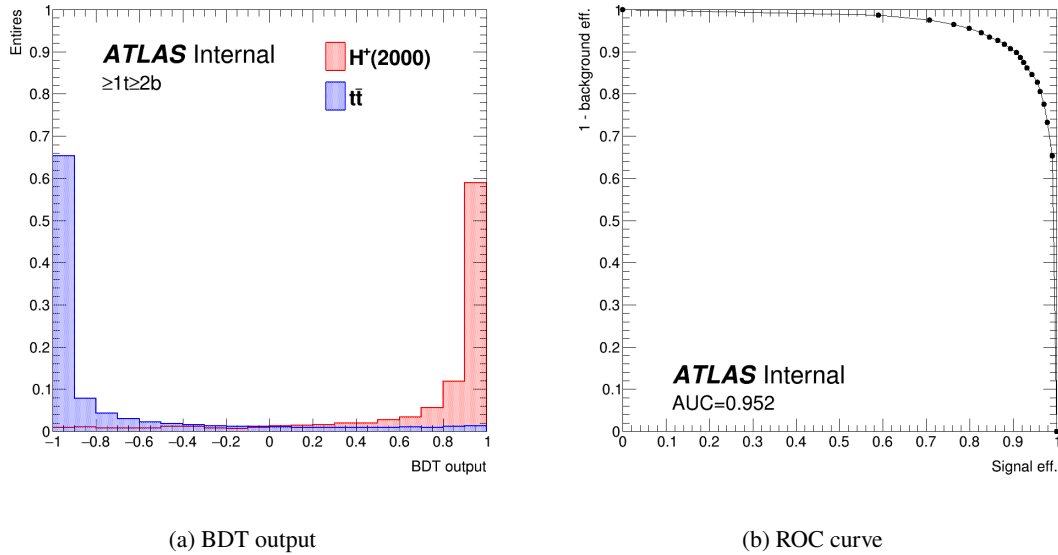


Figure 12: BDT distribution and ROC curve for the 2000 GeV H^+ mass hypothesis.

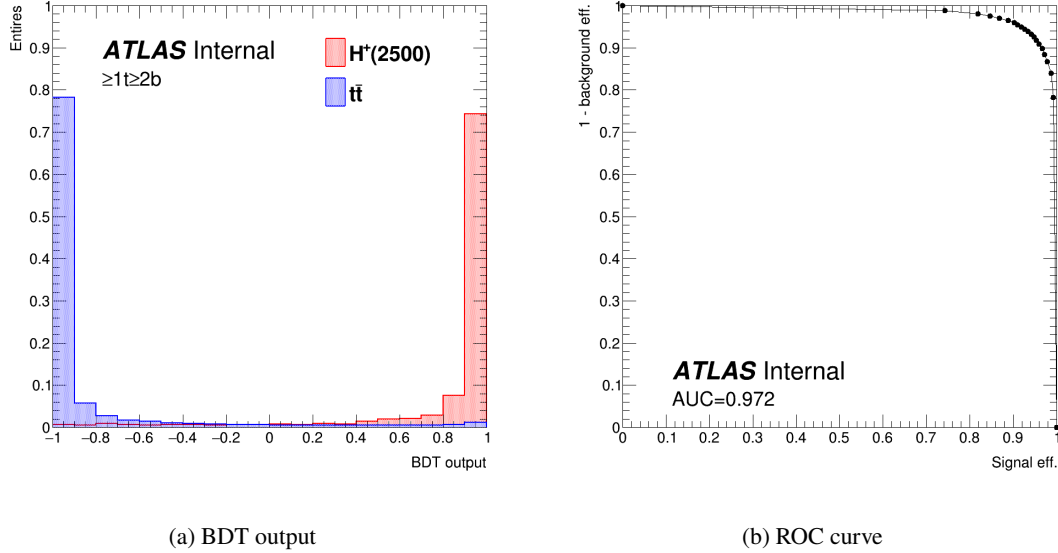


Figure 13: BDT distribution and ROC curve for the 2500 GeV H^+ mass hypothesis.

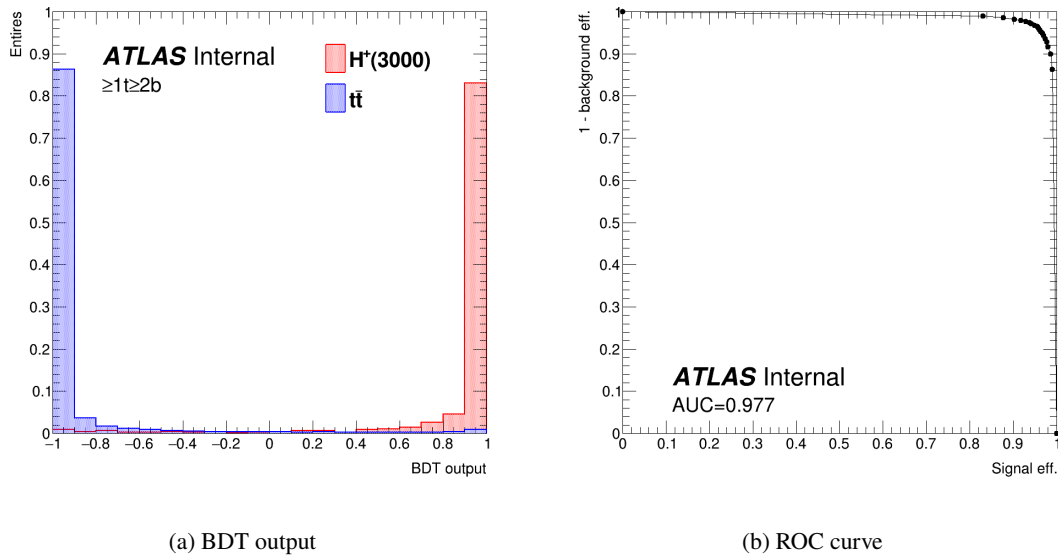
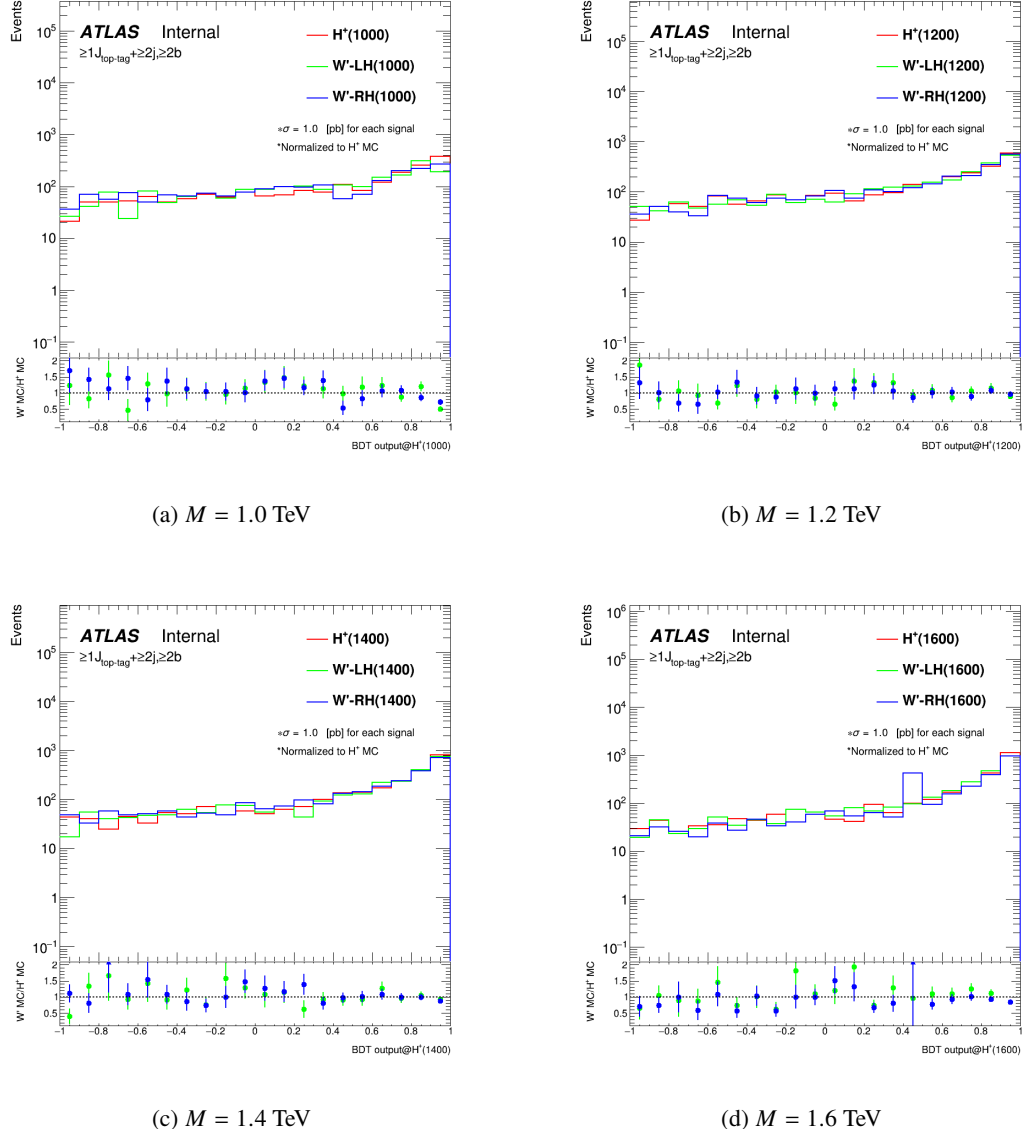


Figure 14: BDT distribution and ROC curve for the 3000 GeV H^+ mass hypothesis.

Comparison of BDT distributions between $H^+ \rightarrow tb$ and $W' \rightarrow tb$ events

BDT distributions for $W' \rightarrow tb$ events are compared with the ones for $H^+ \rightarrow tb$ events in Figure 14. The large differences above their statistic uncertainty aren't observed. Therefore, it is expected to obtain comparable sensitivity with $H^+ \rightarrow tb$ analysis without optimizing BDTs using $W' \rightarrow tb$ samples.



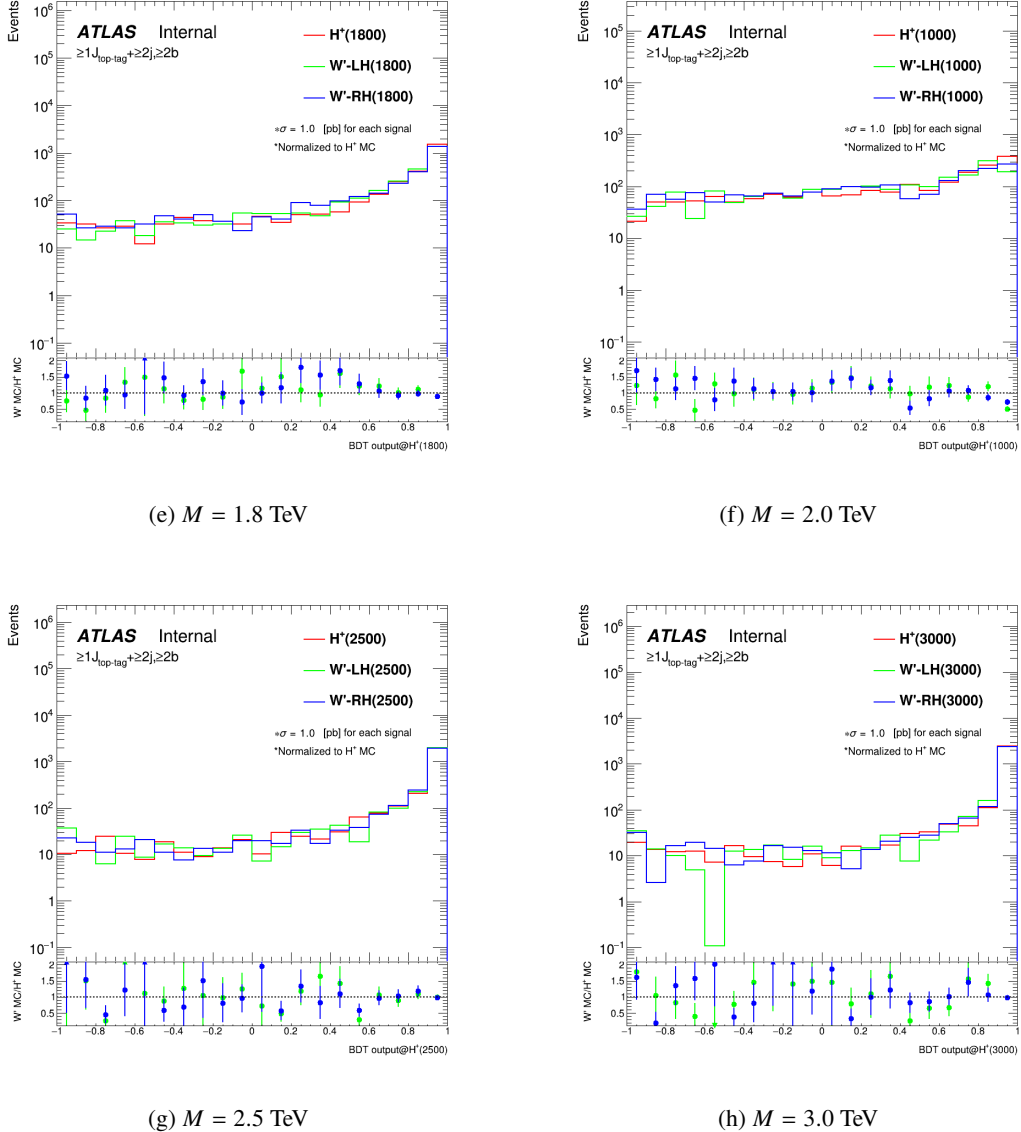


Figure 14: Comparison of BDT distributions between $H^+ \rightarrow tb$ and $W' \rightarrow tb$ events in the inclusive SR (i.e., SR1+SR2).

453 4.2 Analysis strategy at $M_{H^+}, M_{W'} > 3 \text{ TeV}$ points

454 In analyzing the above 3 TeV mass points, we take a different approach from the above. This is because it is
 455 difficult to estimate $t\bar{t} + \text{jets}$ events reliably in the signal region. In Section 5.4, we describe the correction
 456 method of $t\bar{t} + \text{jets}$ MC prediction to improve the data/MC disagreement. This is performed by data-driven
 457 reweighting using the shape of H_T^{jets} distribution. The reweighting factors have considerable uncertainties
 458 in the $H_T^{\text{jets}} > 2000 \text{ GeV}$ region due to the meager statistics in this region, as shown in Figure ???. The
 459 signal events for the above 3 TeV mass hypotheses distribute in such high H_T^{jets} region as shown in Figure

460 15. Therefore, we adopt a conservative approach without relying on the template shapes for signal vs.
 461 background separation.

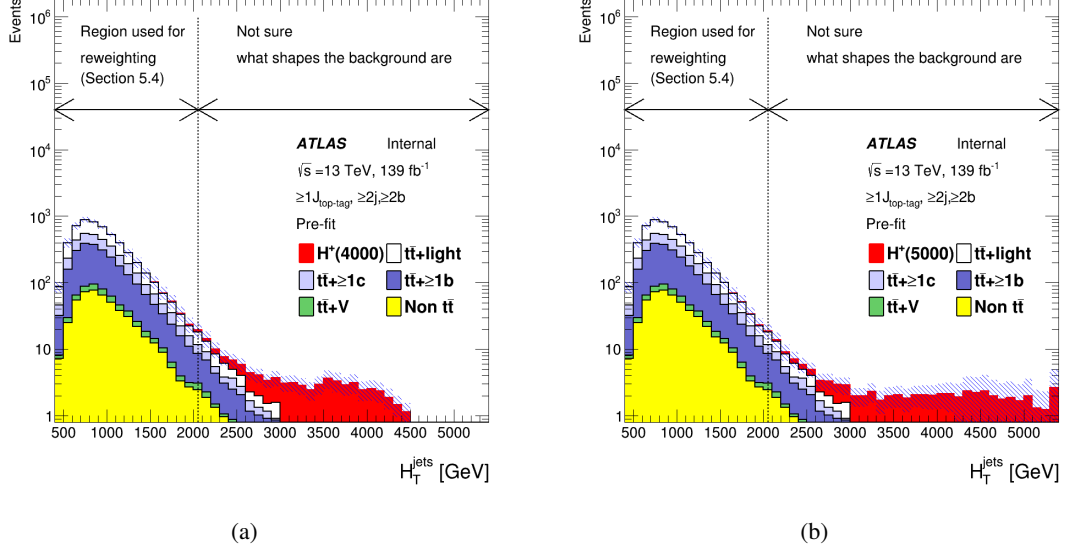


Figure 15: Signal and background comparison for 4000 (a) and 5000 (b) GeV mass hypotheses. These signal events distribute mostly in $H_T^{\text{jets}} > 2000 \text{ GeV}$. These regions don't have enough shape information to perform reweighting in Section 5.4.

462 One signal region (SR) and two control regions (CR1, CR2) are defined according to the H_T^{jets} and the
 463 number of b -jets. The events categorized in the SR are required to have $H_T^{\text{jets}} > 2000 \text{ GeV}$, while events
 464 categorized in the CR1 and CR2 are required $H_T^{\text{jets}} \leq 2000 \text{ GeV}$. Moreover, $N_{b-\text{jets}} \geq 2$, $N_{b-\text{jets}} = 2$,
 465 and $N_{b-\text{jets}} \geq 3$ are imposed on events categorised in the SR, CR1, and CR2, respectively. After these
 466 selections, the CR1 becomes enriched in $t\bar{t} + \text{light}$ events, while the CR2 becomes enriched in $t\bar{t} + \text{HF}$.
 467 Therefore, CR1 and CR2 are expected to control $t\bar{t} + \text{jets}$ events. The event selections in these regions are
 468 summarized in Table 13. H_T^{jets} distributions in these regions are used as final discriminates in the final
 469 fitting in Section ???. The number of bins of H_T^{jets} distribution in the SR is set to one exactly; the analyses
 470 of these mass points are performed based on the cut-and-counting (C&C) method. These distributions and
 471 the composition ratio of backgrounds for these regions are shown in Figure 16 to Figure 18.

Cut	SR	CR1	CR2
leptons	Same requirements as Table 8		
Top-tagged large- R jets	Same requirements as Table 8		
Small- R jets	$N_{\text{jet}} \geq 2$ (Kinematic requirements are the same as Table 8)	$N_{\text{jet}} \geq 3$ (Kinematic requirements are the same as Table 8)	
b -tagged small- R jets	$N_{b-\text{jet}} \geq 2$	$N_{b-\text{jet}} = 2$	$N_{b-\text{jet}} \geq 3$
H_T^{jets}	$> 2000 \text{ GeV}$		$\leq 2000 \text{ GeV}$

Table 13: Event selections in the SR, CR1, and CR2. After these selections, CR1 becomes enriched in $t\bar{t} + \text{light}$, and CR2 becomes enriched in $t\bar{t} + \text{HF}$.

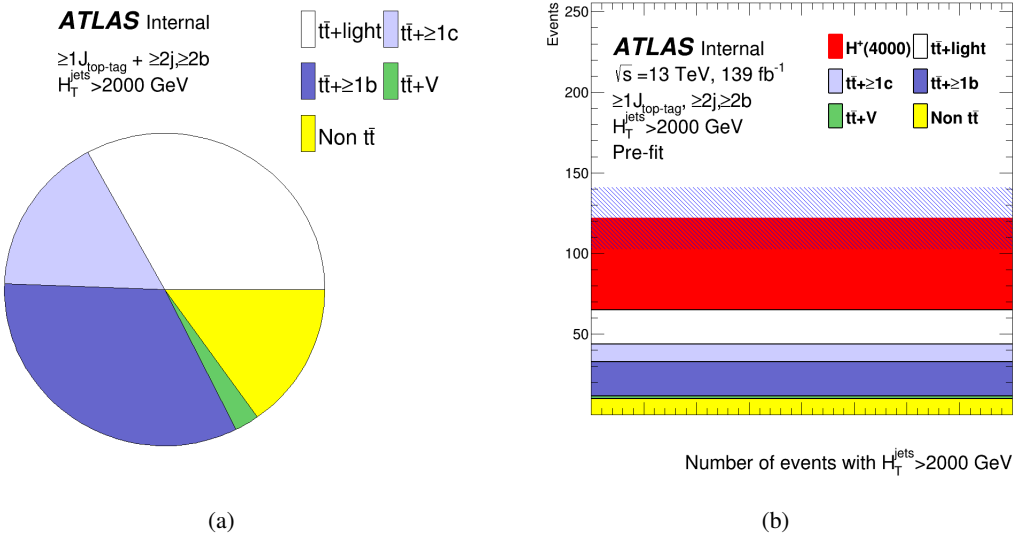


Figure 16: Background composition in the SR is shown in the pie chart (a) and the H_T^{jets} distributions (b). The number of bins of H_T^{jets} distribution is set to exactly one.

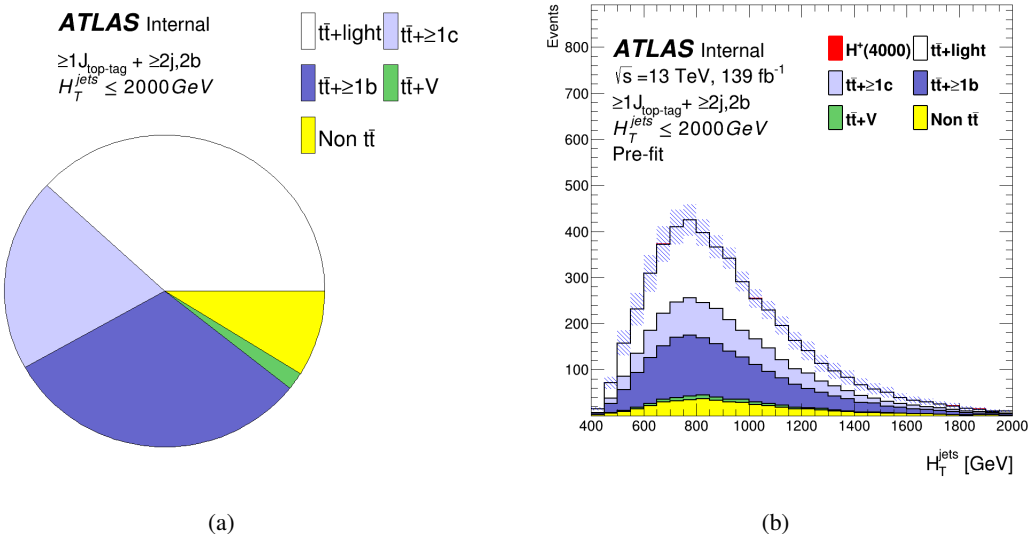


Figure 17: Background composition in the CR1 is shown in the pie chart (a) and the H_T^{jets} distributions (b).

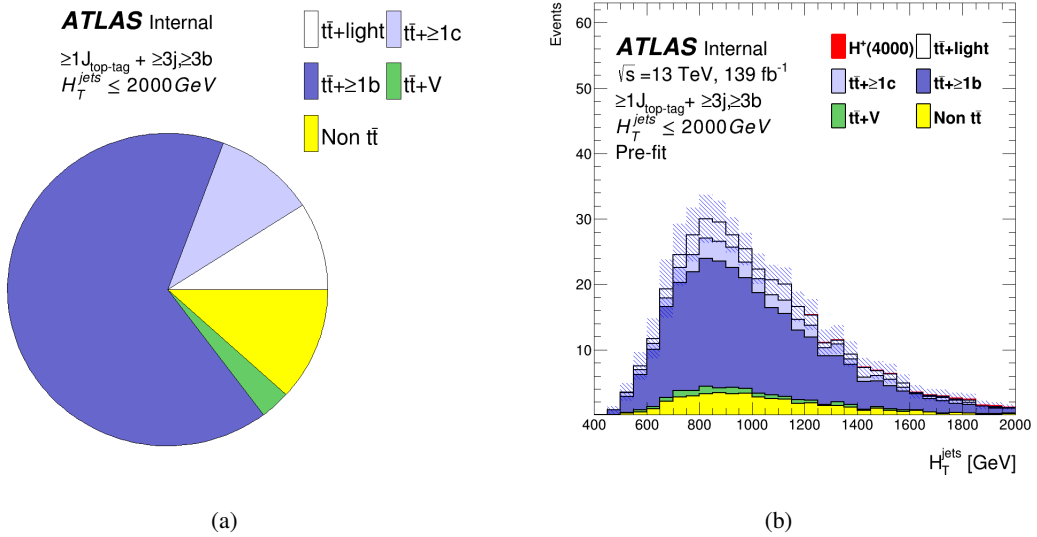


Figure 18: Background composition in the CR2 is shown in the pie chart (a) and the H_T^{jets} distributions (b).

⁴⁷² The number of expected signal and background events in the SR, CR1, and CR2 are shown in Table 14.
⁴⁷³ The predicted number of H^+ and W' signal events for the 4000 and 5000 GeV mass hypothesis assume
⁴⁷⁴ $\sigma \times Br = 0.046 \text{ pb}$ as same as Table 9.

	SR	CR1	CR2
$t\bar{t} + \text{light}$	21 ± 3	1920 ± 162	34 ± 5
$t\bar{t} + \geq 1c$	11 ± 9	1007 ± 782	39 ± 37
$t\bar{t} + \geq 1b$	21 ± 10	1568 ± 794	249 ± 46
$t\bar{t} + W$	1 ± 0	35 ± 6	2 ± 0
$t\bar{t} + Z$	1 ± 0	57 ± 8	9 ± 2
Wt channel	3 ± 3	173 ± 101	7 ± 4
t channel	1 ± 0	35 ± 16	16 ± 1
Other top sources	1 ± 0	28 ± 12	8 ± 4
$VV, V+\text{jets}$	5 ± 2	132 ± 53	4 ± 2
$t\bar{t}H$	1 ± 0	78 ± 3	24 ± 1
Total	65 ± 7	5033 ± 308	377 ± 33
$H^+ 4000 \text{ GeV}$	57 ± 18	5 ± 2	2 ± 0
$H^+ 5000 \text{ GeV}$	55 ± 27	3 ± 1	1 ± 0

Table 14: Number of expected and selected events split according to the SR, CR1, and CR2. The quoted uncertainties include both statistical and systematic uncertainties before fitting.

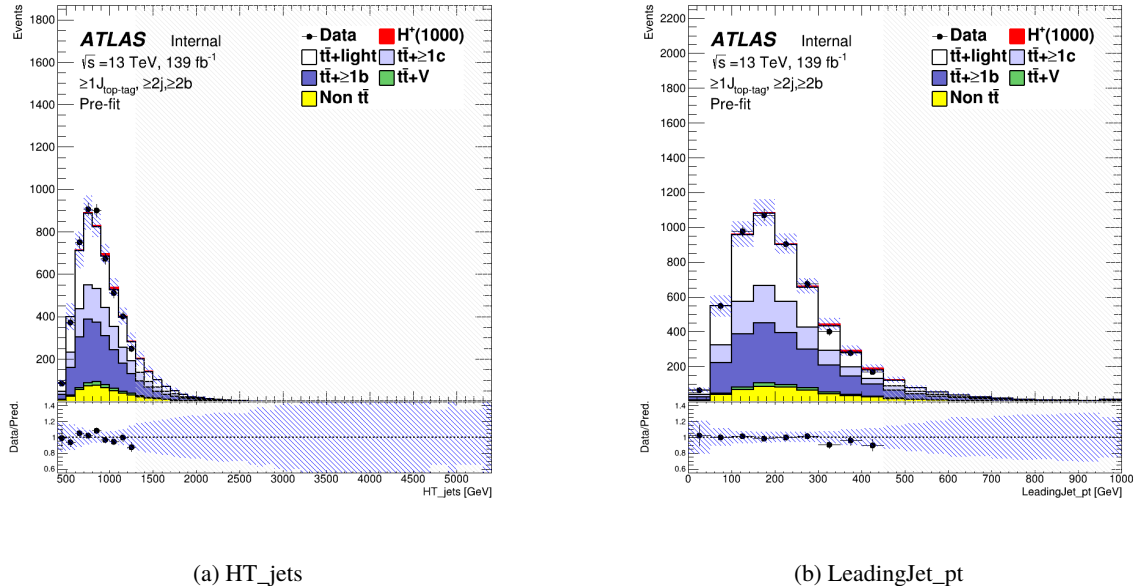
475 5 Background modeling

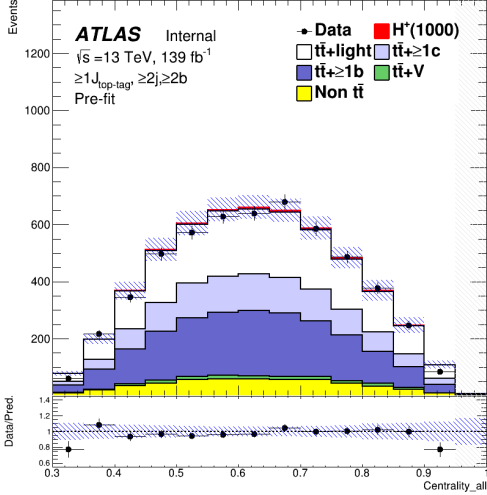
476 5.1 Blind strategy

477 In the following sections, the modeling of kinematic distributions, particularly those used for BDT training,
 478 of the $t\bar{t}$ + jets background is checked by comparing the data and MC. In order to avoid observing signals
 479 or any other biases before fixing the analysis procedure, the following blinding strategy is applied. The
 480 signal-to-noise ratio (S/B) is calculated in each bin of each distribution for all mass hypotheses (more
 481 details in Appendix B). The signal cross section (σ_{signal}) on each mass hypothesis is set to 0.046 pb, which
 482 is the upper limit at 1 TeV H^+ mass point obtained from the resolved $H^+ \rightarrow tb$ search [24]. Therefore, it can
 483 be considered the most conservative assumption. The data in bins with $S/B > 0.05$ in at least one mass
 484 hypothesis are blinded when the data is compared with MC.

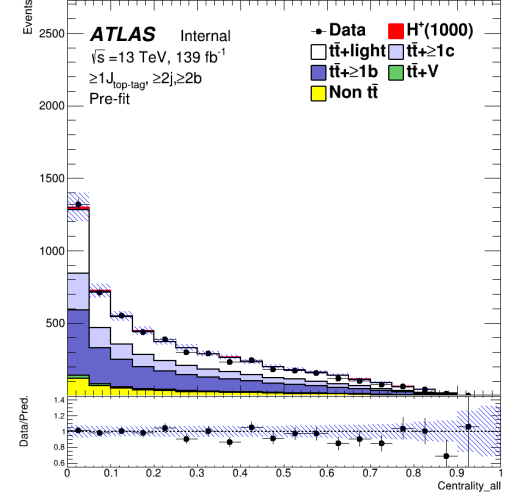
485 5.2 Data/MC comparison for BDT input variables

486 Figures 13 show the distributions of input variables for BDT training in the inclusive SR region (i.e.,
 487 SR1+SR2). Data are blinded according to the blind strategy in Section 5.1. No significant difference
 488 between the data and MC is found in each variable.

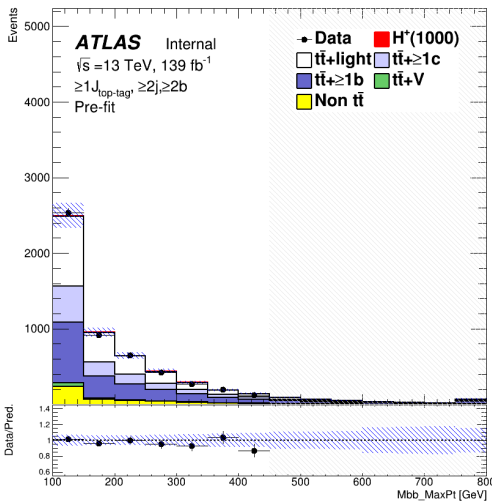




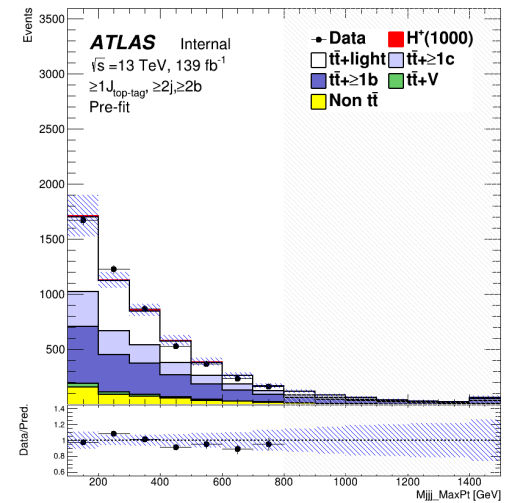
(c) Centrality_all



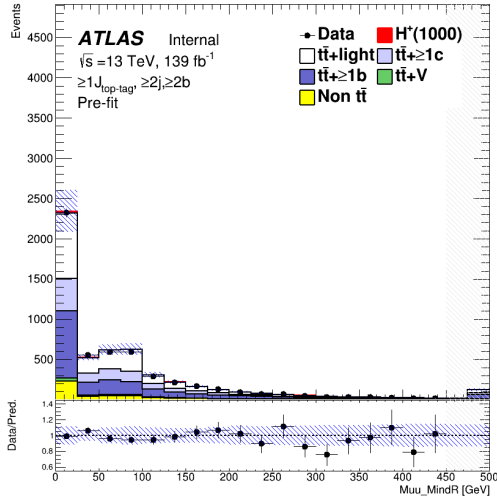
(d) H1_all



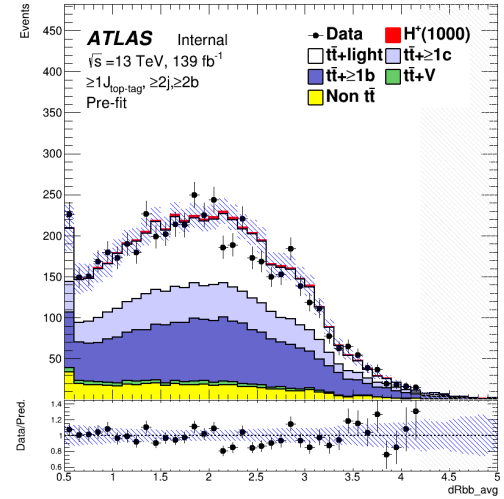
(e) Mbb_MaxPt



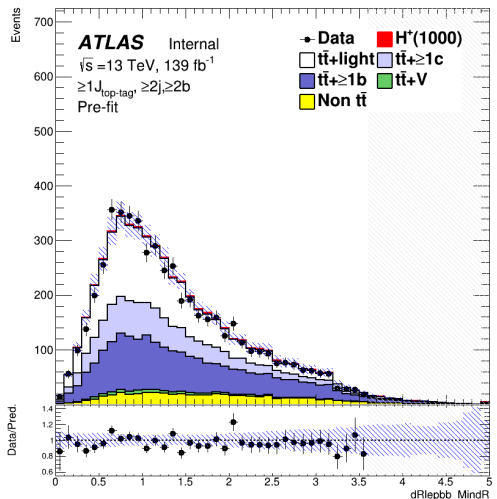
(f) Mjjj_MaxPt



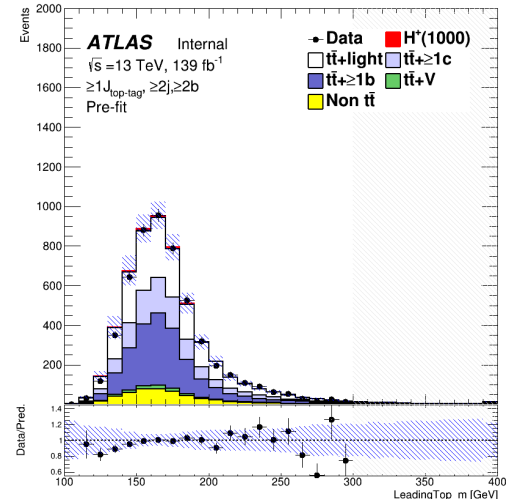
(g) Muu_MindR



(h) dRbb_avg



(i) dRlepb_MindR



(j) LeadingTop_m

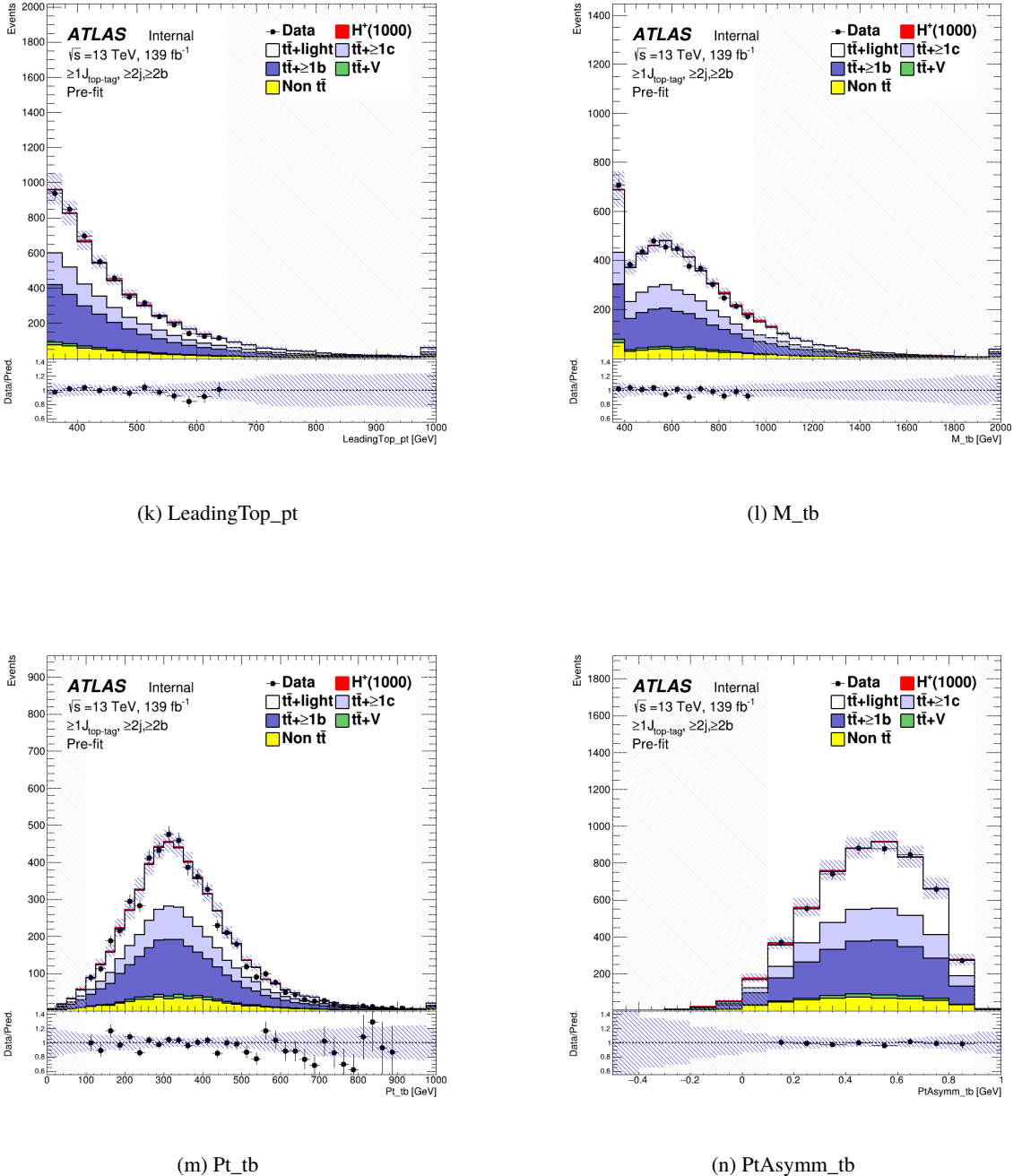


Figure 13: Comparison of the kinematic variables included in the BDT in the SR for the data and MC.

5.3 Data/MC comparison for BDT outputs

Figures 14 to 21 show the distributions of BDT output in the SR1 and SR2. The binning of each BDT output is optimized for the search sensitivity by *TransfoD* algorithm [93]. Such binning results in extremely narrow bins towards high BDT scored, and makes the plot hard to see as shown in Figure ?? in Appendix

493 B.2 when plotted in a usual manner. We rather show the distribution with an equal interval for each bin.
 494 The distributions are input into the profile likelihood fit on each H^+ mass hypothesis as shown in Section 7.
 495 It is observed that the data/MC ratio tends to be lower for the high BDT score regions, which may bias
 496 the search for the signal in the highest BDT bins. The reweighting to correct for the slope is discussed in
 497 Section 5.4. Data in the SR2 tends to be higher as a whole. This cause should be due to the mismodeling
 498 of the $t\bar{t}$ + jets event's cross-section. Therefore, $t\bar{t}$ + light and $t\bar{t}$ + HF yields are determined by floating
 499 them in the fit.

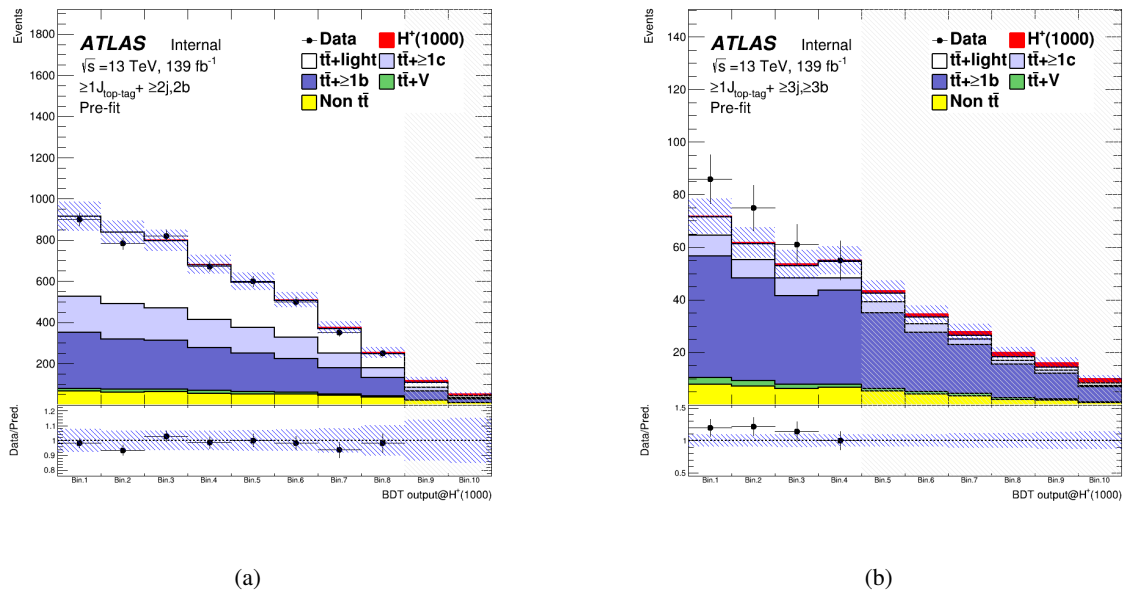


Figure 14: Pre-fit distribution of BDT output trained using 1000 GeV H^+ samples in the SR1 (a) and SR2 (b).

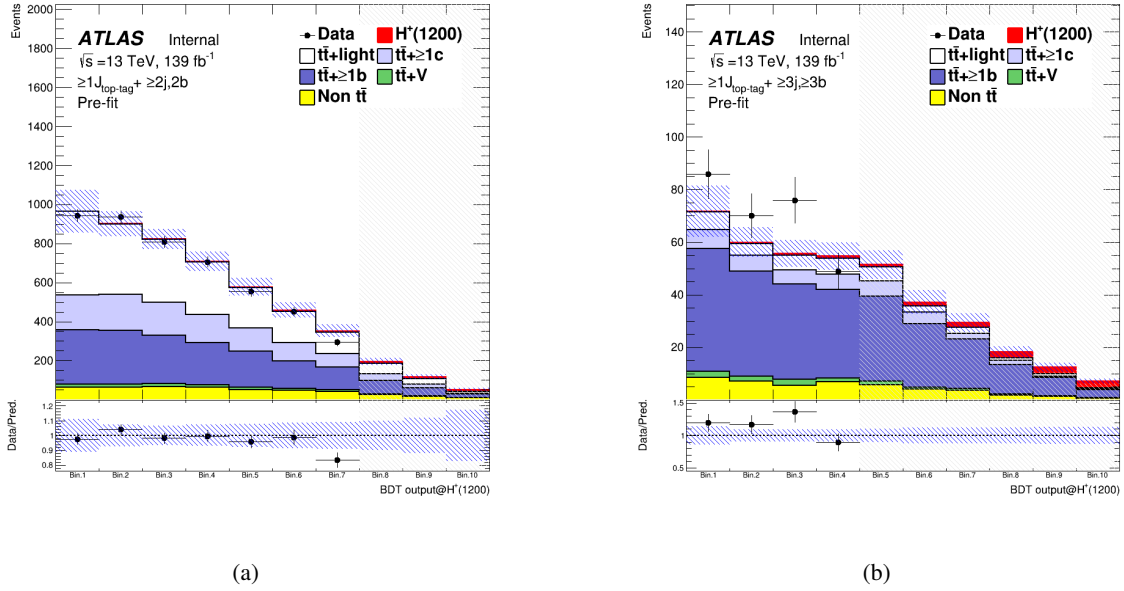


Figure 15: Pre-fit distribution of BDT output trained using 1200 GeV H^+ samples in the SR1 (a) and SR2 (b).

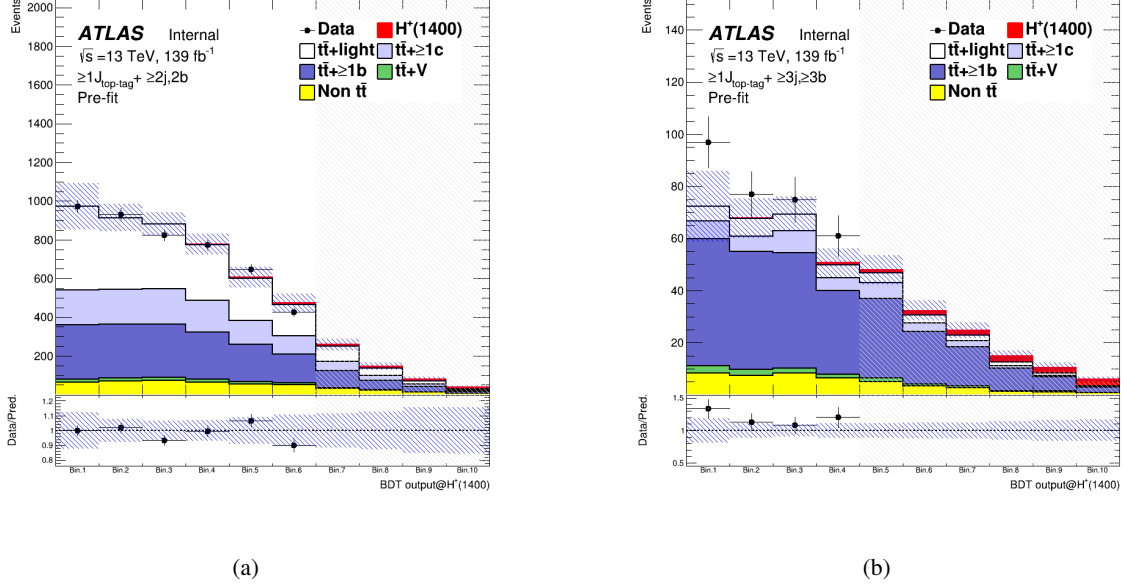


Figure 16: Pre-fit distribution of BDT output trained using 1400 GeV H^+ samples in the SR1 (a) and SR2 (b).

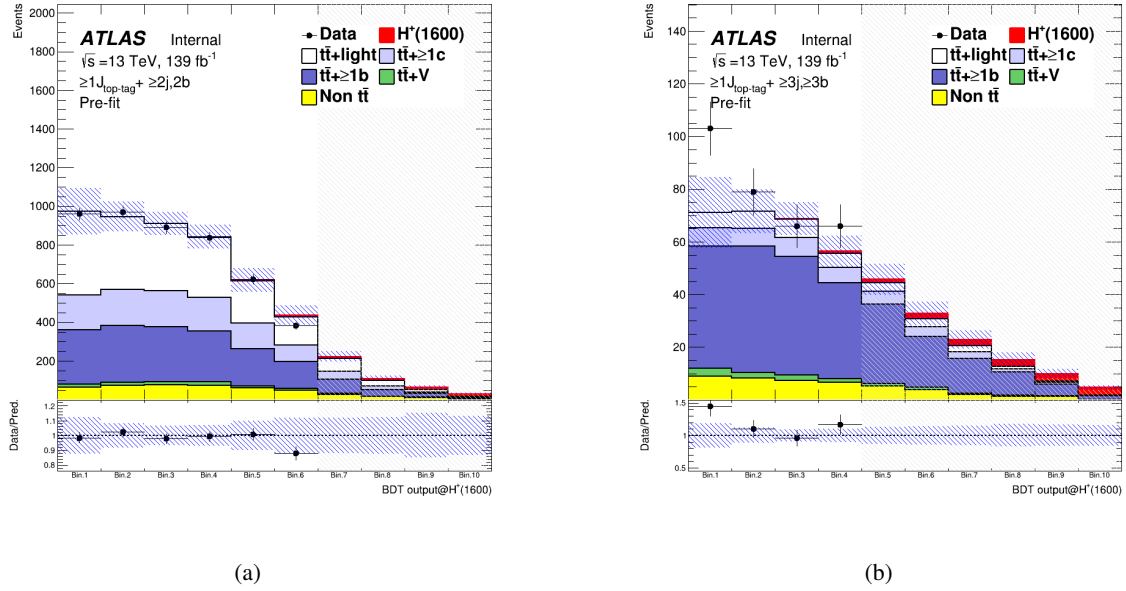


Figure 17: Pre-fit distribution of BDT output trained using 1600 GeV H^+ samples in the SR1 (a) and SR2 (b).

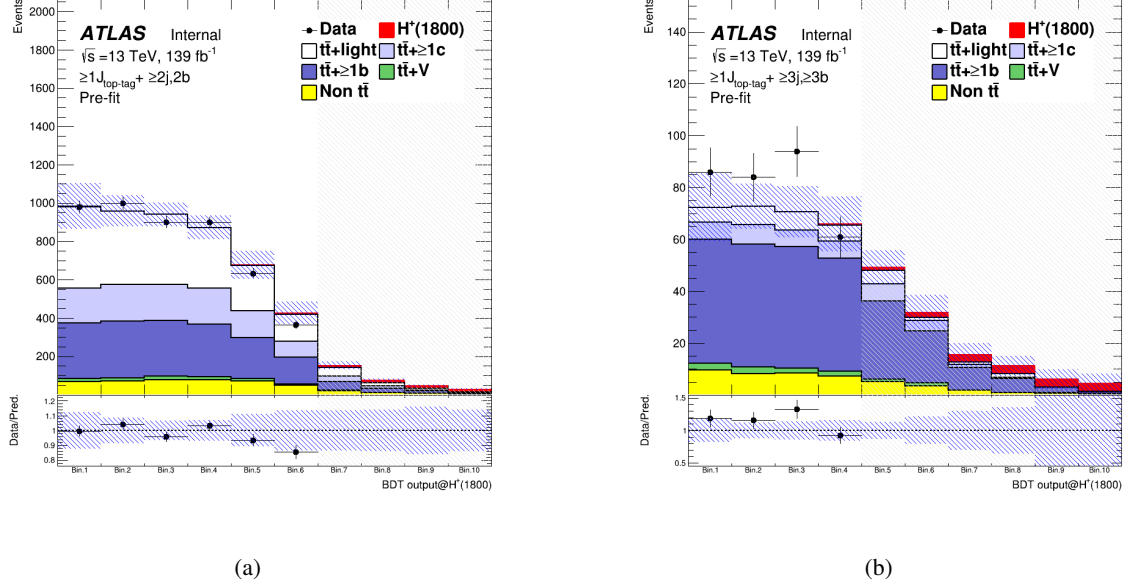


Figure 18: Pre-fit distribution of BDT output trained using 1800 GeV H^+ samples in the SR1 (a) and SR2 (b).

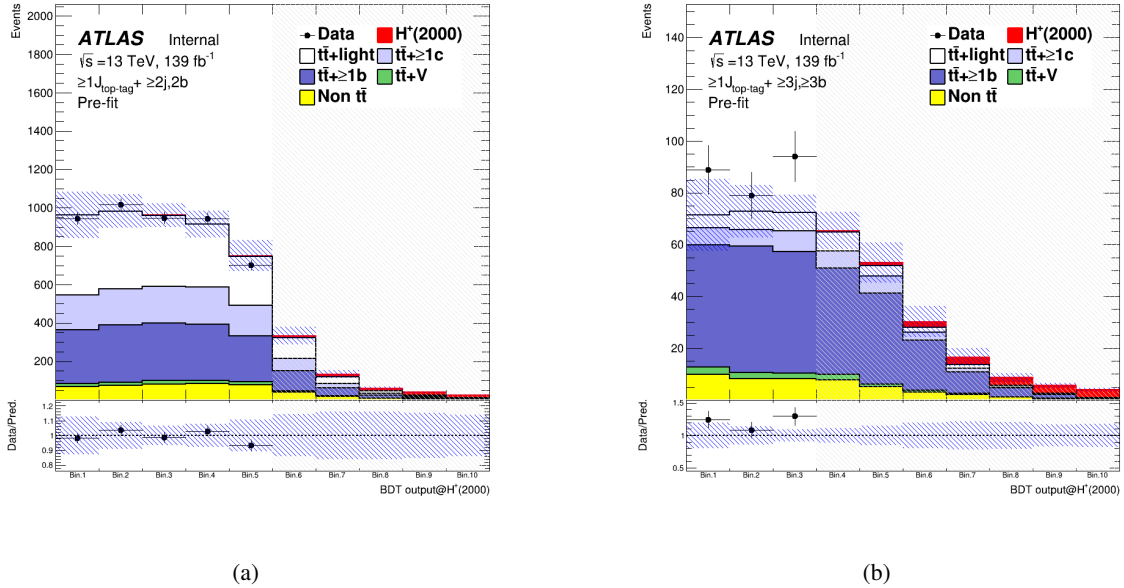


Figure 19: Pre-fit distribution of BDT output trained using 2000 GeV H^+ samples in the SR1 (a) and SR2 (b).

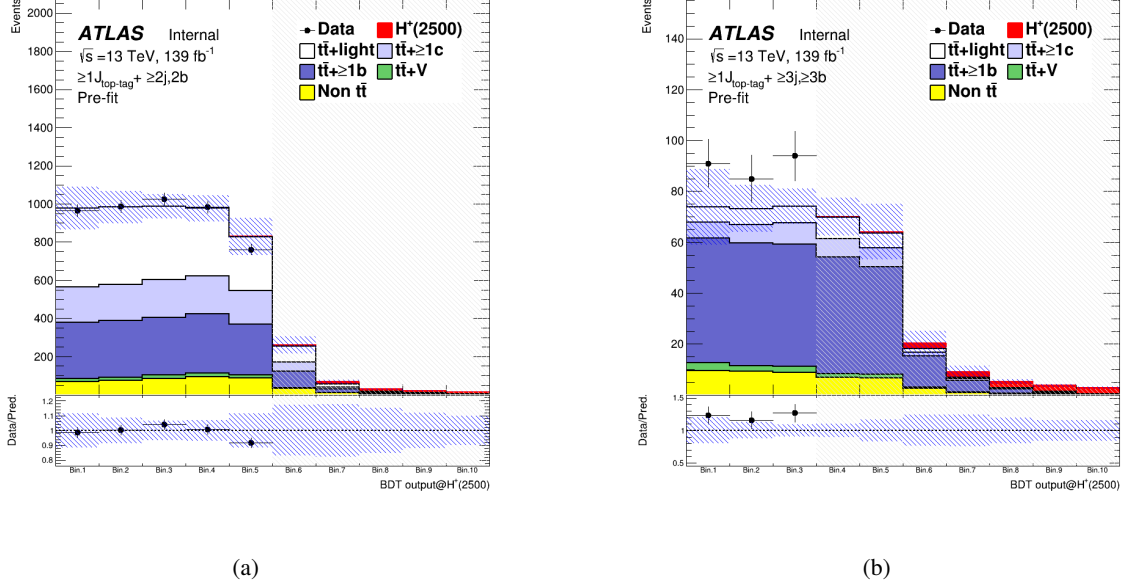


Figure 20: Pre-fit distribution of BDT output trained using 2500 GeV H^+ samples in the SR1 (a) and SR2 (b).

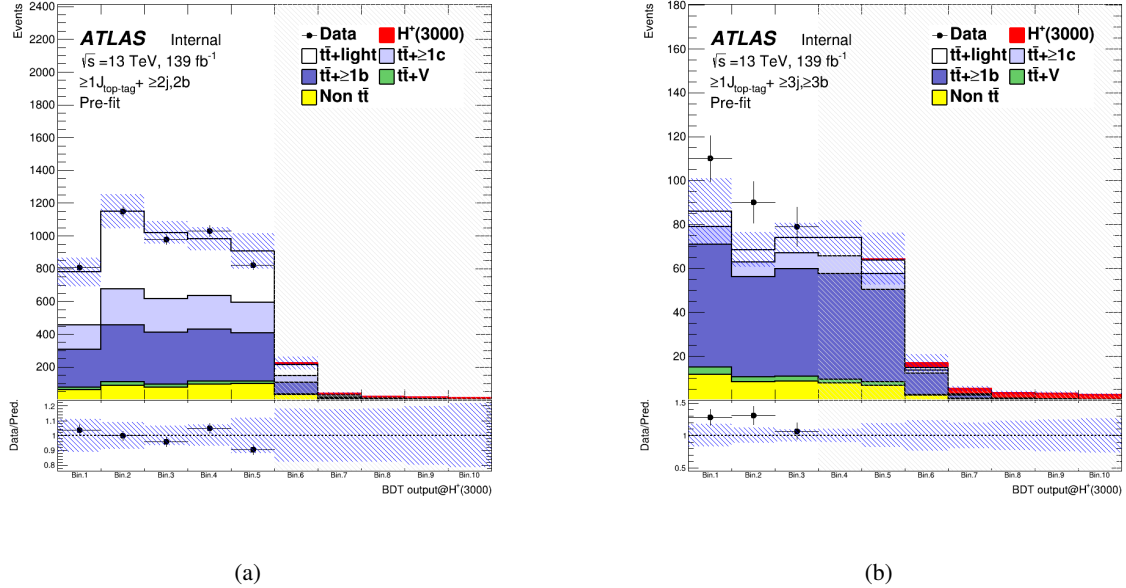


Figure 21: Pre-fit distribution of BDT output trained using 3000 GeV H^+ samples in the SR1 (a) and SR2 (b).

500 5.4 Reweighting technique

501 It is known that the $t\bar{t}$ Powheg+Pythia generator does not properly model data as observed in Figure 14
 502 to 21. This is due to the mismodeling of the hard and soft jets. These mismodelings appear in the p_T
 503 distribution of the leading top-tagged large-R jet (LeadingTop_pt) and the invariant mass distribution of
 504 small-R jet triplet with maximum p_T (Mjjj_MaxPt) (these small-R jets are mainly QCD jets) as shown in
 505 Figure 22, which are plotted for events in the low BDT score regions.

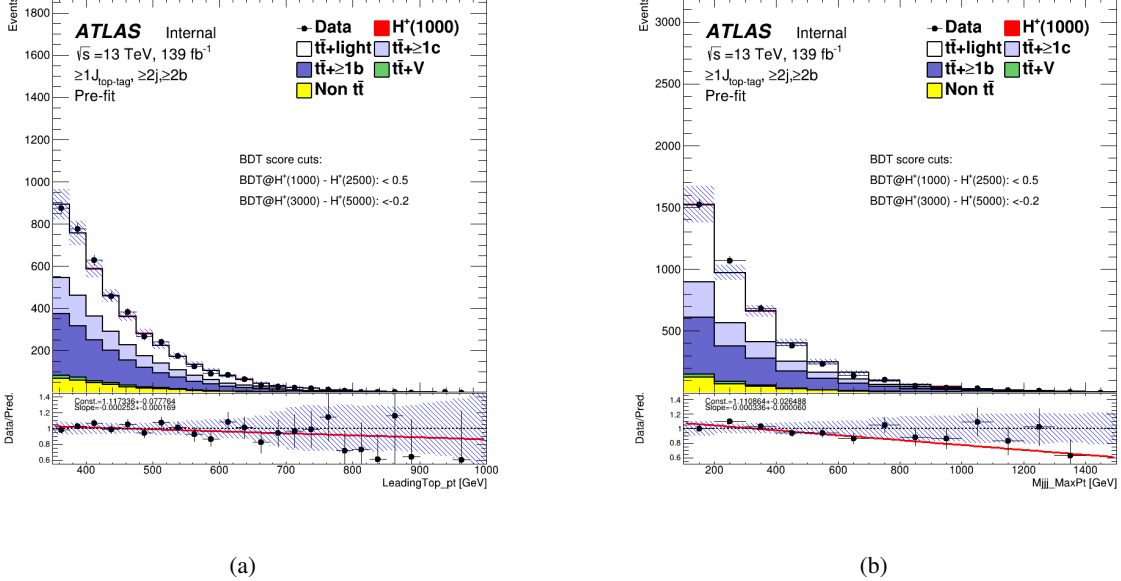


Figure 22: p_T distribution of the leading top-tagged large-R jet (a) and invariant mass distribution of small-R jet triplet with maximum p_T (b) in the low BDT score regions. Each data/MC ratio plot has a slope.

To improve the poor prediction of $t\bar{t} +$ jets, data-based corrections are applied to the MC prediction. The reweighting factors are derived by comparing the H_T^{jets} distribution between data and MC prediction in the inclusive SR region (i.e., SR1+SR2) because H_T^{jets} has both hard and soft jet information. For deriving reweighting factors, events in the only low BDT score region are selected to avoid being reweighted signal events. These events are required to pass all BDT cuts under different mass hypotheses, as shown in Table 15. Firstly, the data/MC ratios R are derived according to the following definition:

$$R = \frac{\text{Data} - \text{MC}^{\text{non-}t\bar{t}+\text{jets}}}{\text{MC}^{t\bar{t}+\text{jets}}} \quad (1)$$

$t\bar{t} +$ jets includes the $t\bar{t} +$ light, $t\bar{t} + \geq 1c$ and $t\bar{t} + \geq 1b$. The obtained R distribution is fitted with a quadratic function ($f(H_T^{\text{jets}}) = a + b \cdot H_T^{\text{jets}} + c \cdot (H_T^{\text{jets}})^2$), and the function is used for reweighting. Figure 23(a) shows the H_T^{jets} distribution with BDT score cuts applied as indicated in Table 15. Figure 23(b) shows the distribution of the weights derived from the H_T^{jets} distribution and the obtained reweighting function. The function values are applied to $t\bar{t} +$ light, $t\bar{t} + \geq 1c$ and $t\bar{t} + \geq 1b$. Table 16 includes the fitted values for all the parameters. The statistical errors of fitted parameters are included as systematic uncertainties in the final fitting. The reweighting factors in $H_T^{\text{jets}} > 2057$ GeV region are used the value at $H_T^{\text{jets}} = 2057$ GeV because the weight value of -1σ become negative at the point.

Mass point [GeV]	BDT score cut
1000	< 0.5
1200	< 0.5
1400	< 0.5
1600	< 0.5
1800	< 0.5
2000	< 0.5
2500	< 0.5
3000	< -0.2
4000	< -0.2
5000	< -0.2

Table 15: Events used for deriving weight factors are selected by cutting with BDT score under different mass hypotheses according to criteria in this table.

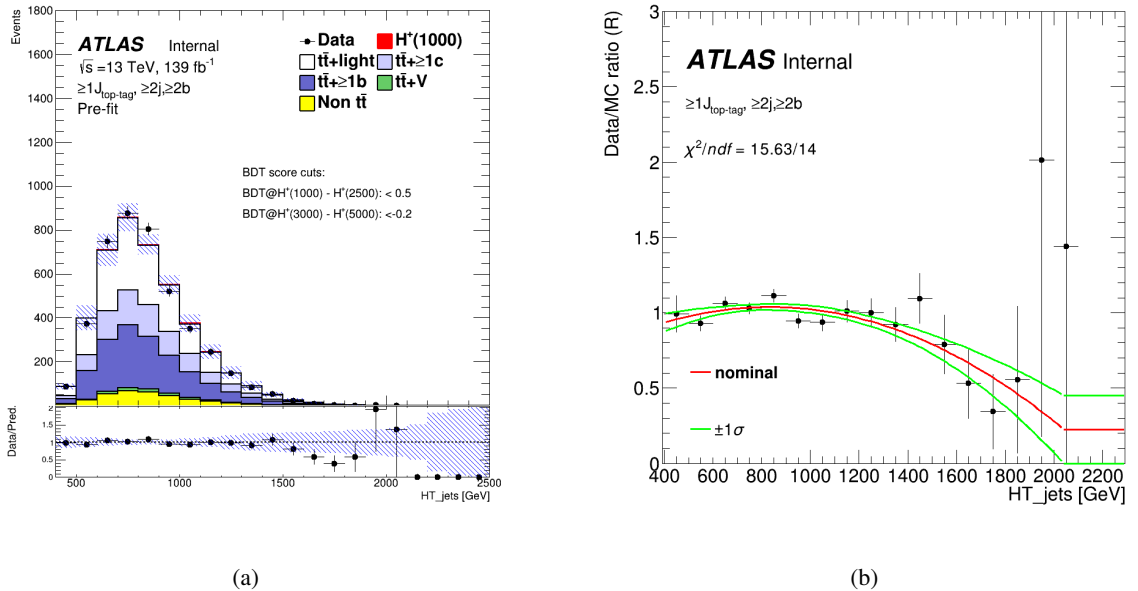


Figure 23: H_T^{jets} distribution with BDT score cuts applied (left) and the data/MC ratio distribution derived from the H_T^{jets} distribution (right). The red function in Figure (b) is the reweighting function obtained by fitting to R distribution with a quadratic function. The green ones are the stat. uncertainty ($\pm 1\sigma$) of the red function. They are included as systematic uncertainties in the final fitting. The reweighting factors in $H_T^{\text{jets}} > 2057$ GeV region are assigned the value at $H_T^{\text{jets}} = 2057$ GeV because the weight value of -1σ become negative at the point.

Parameter	Value
a	$(6.51 \pm 1.85) \times 10^{-1}$
b	$(9.30 \pm 3.93) \times 10^{-4}$
c	$(-5.58 \pm 1.99) \times 10^{-7}$

Table 16: Summary of parameters obtained by fitting to the weight distribution with a quadratic function ($f(H_T^{\text{jets}}) = a + b \cdot H_T^{\text{jets}} + c \cdot (H_T^{\text{jets}})^2$). The error of each parameter is from stat. uncertainty.

520 Figure 26 to Figure 31 show BDT output distributions applied to reweighting in the SR1 and SR2 region.
521 The data/MC disagreements in the high BDT score regions have improved.

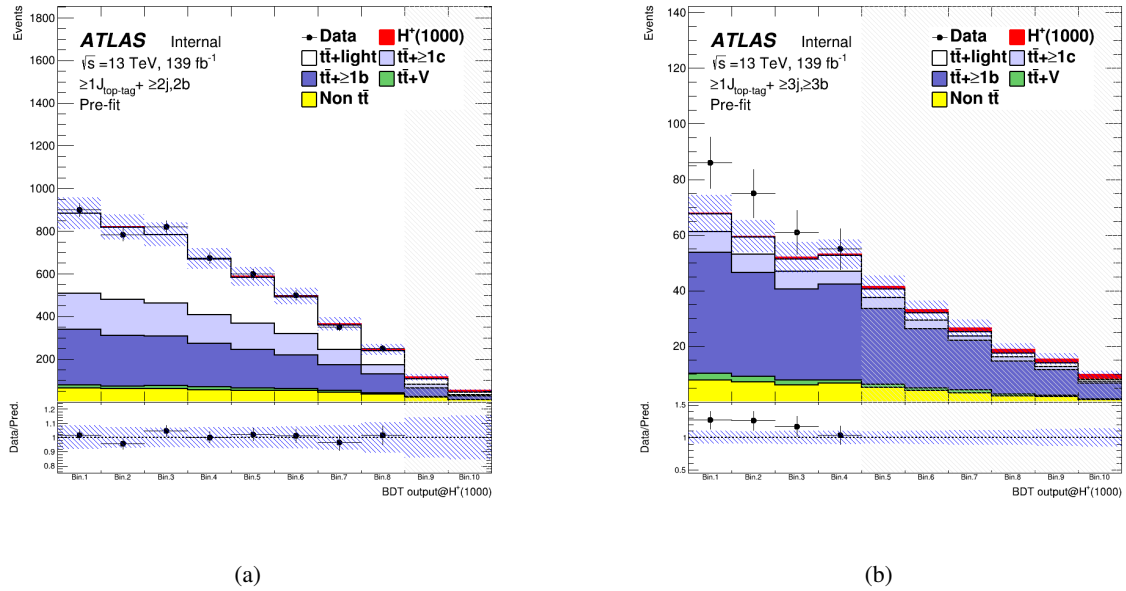


Figure 24: Pre-fit distributions of BDT output trained using 1000 GeV H^+ in the SR1 (a) and SR2 (b) after reweighting.

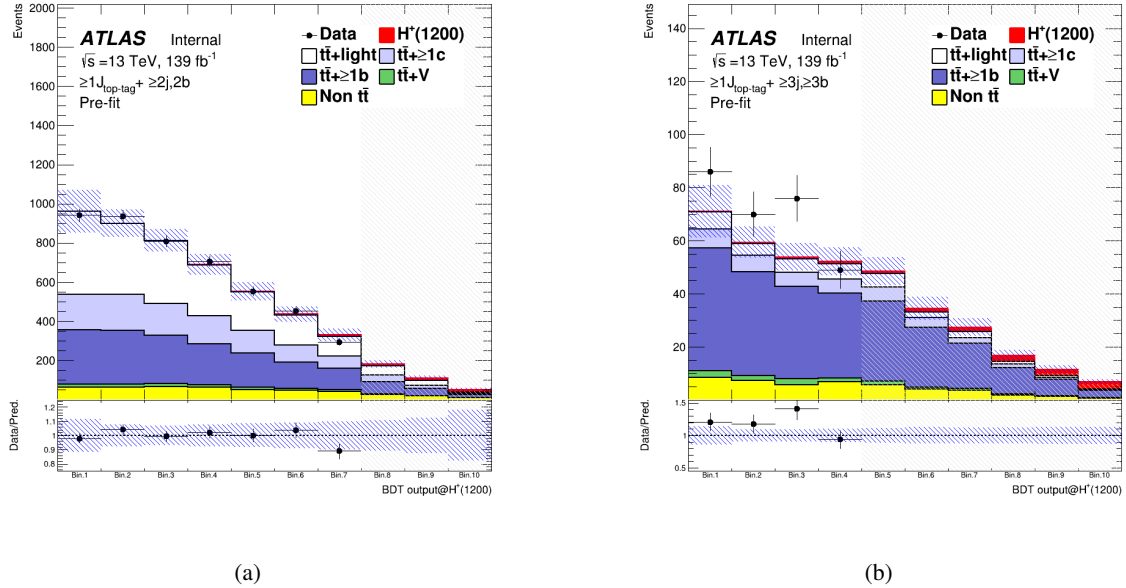


Figure 25: Pre-fit distributions of BDT output trained using 1200 GeV H^+ in the SR1 (a) and SR2 (b) after reweighting.

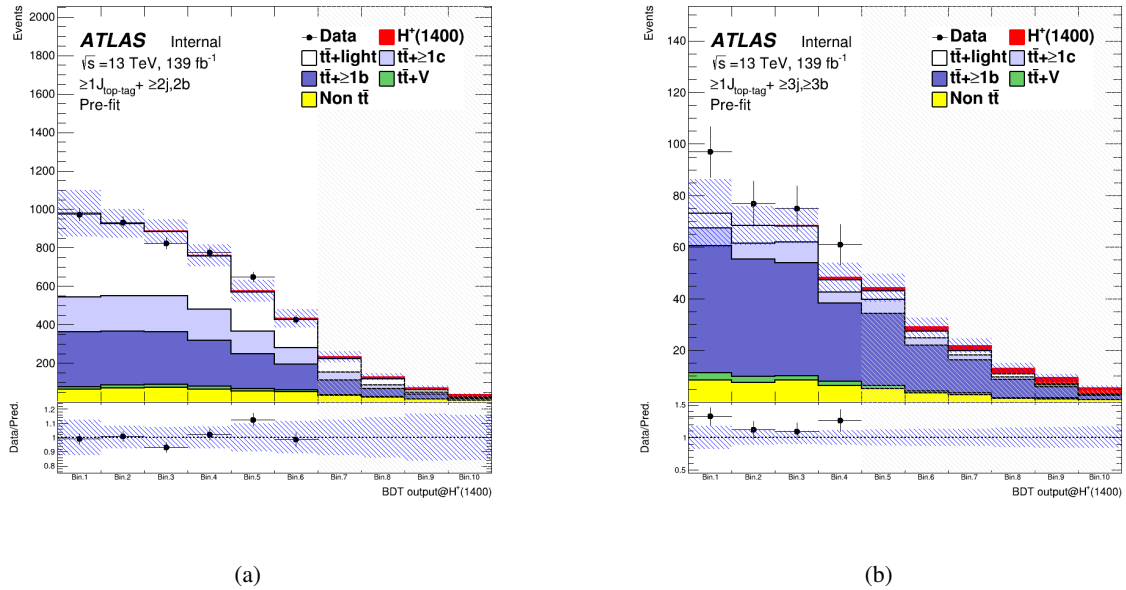


Figure 26: Pre-fit distributions of BDT output trained using 1400 GeV H^+ in the SR1 (a) and SR2 (b) after reweighting.

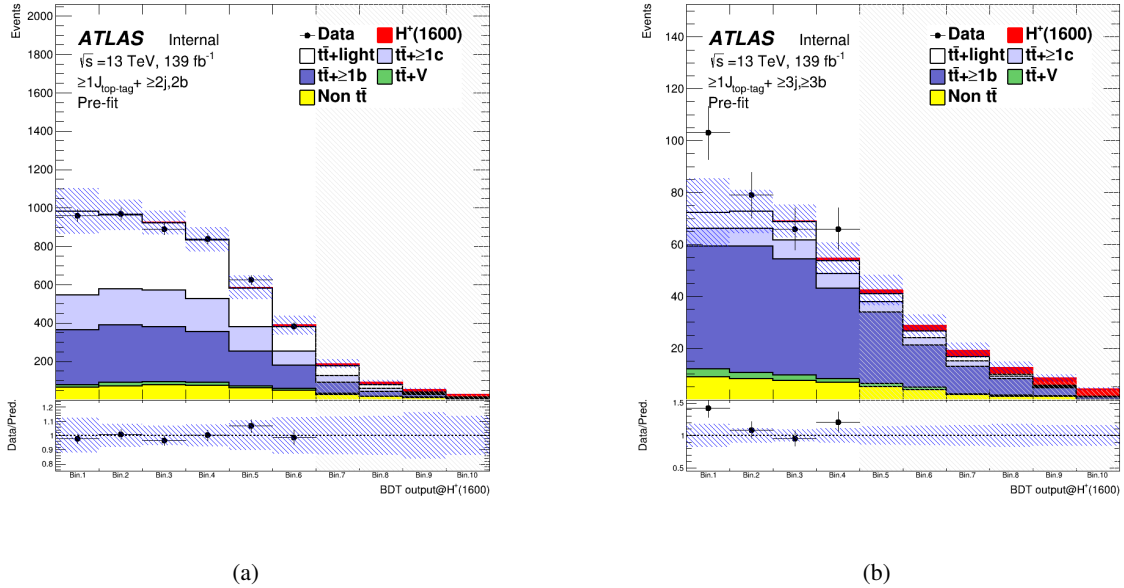


Figure 27: Pre-fit distributions of BDT output trained using 1600 GeV H^+ in the SR1 (a) and SR2 (b) after reweighting.

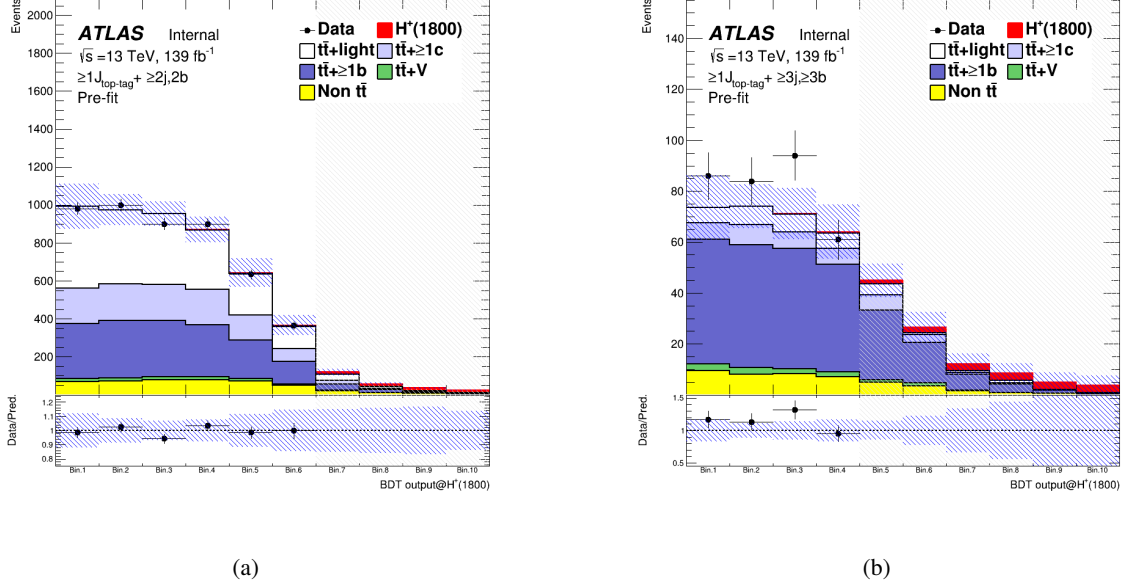


Figure 28: Pre-fit distributions of BDT output trained using 1800 GeV H^+ in the SR1 (a) and SR2 (b) after reweighting.

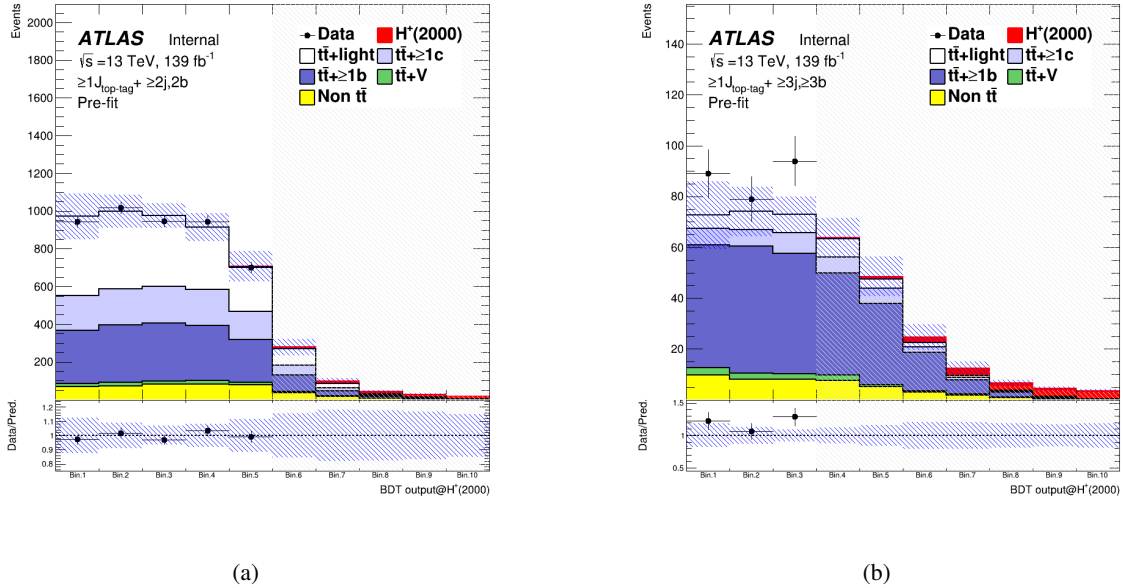


Figure 29: Pre-fit distributions of BDT output trained using 2000 GeV H^+ in the SR1 (a) and SR2 (b) after reweighting.

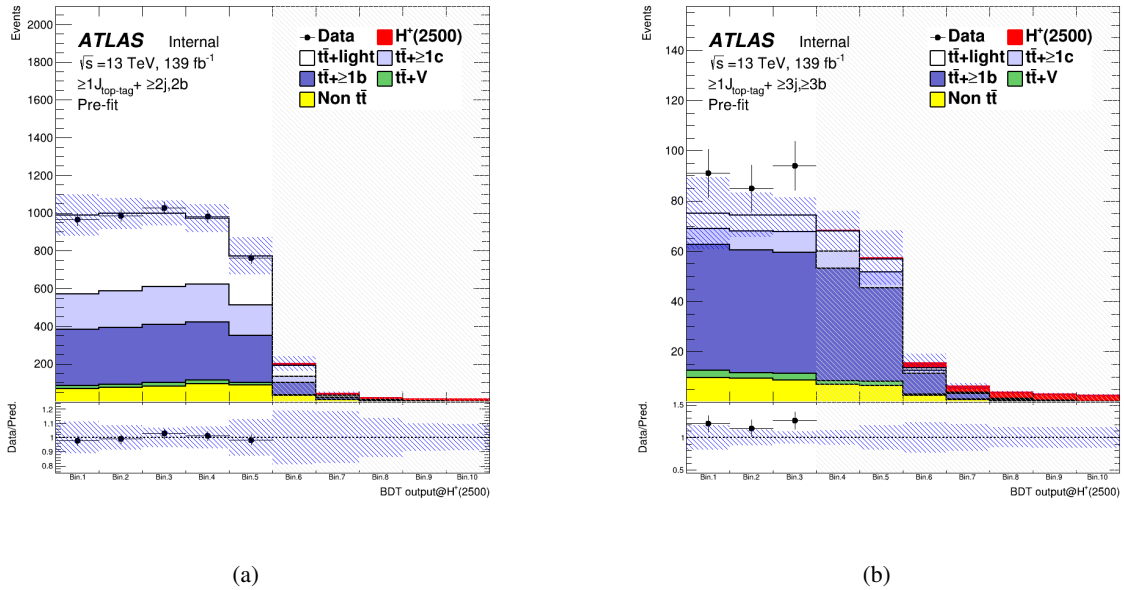


Figure 30: Pre-fit distributions of BDT output trained using 2500 GeV H^+ in the SR1 (a) and SR2 (b) after reweighting.

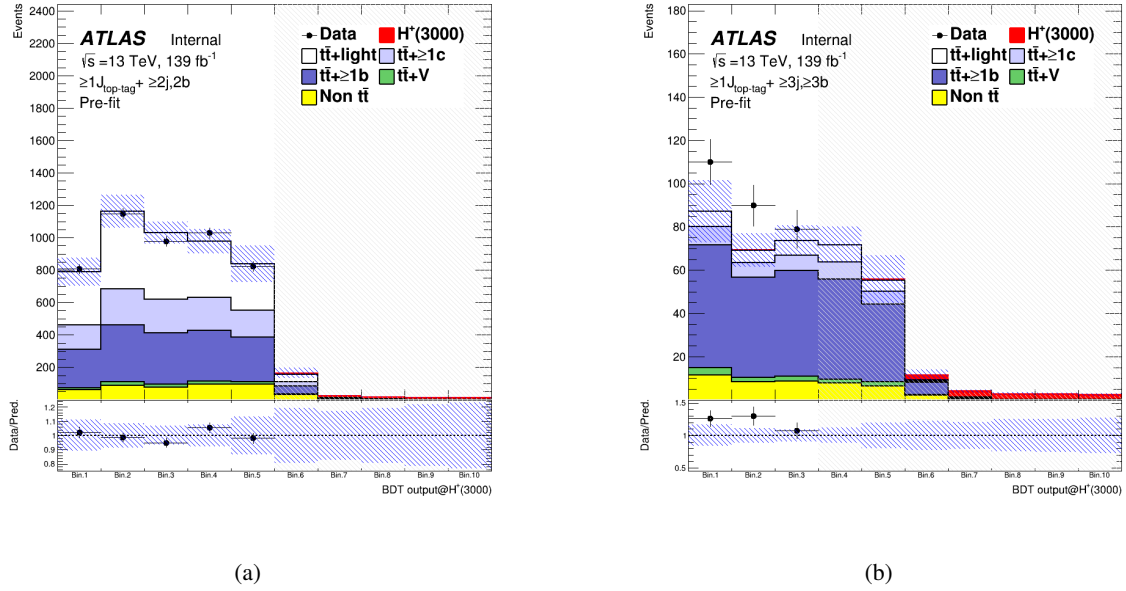


Figure 31: Pre-fit distributions of BDT output trained using 3000 GeV H^+ in the SR1 (a) and SR2 (b) after reweighting.

522 6 Systematics Uncertainties

523 The uncertainties considered in the following may affect the overall normalization of the process, the
 524 shapes of the templates, or both. All the experimental uncertainties considered, with the exception of
 525 that in the luminosity, affect both normalization and shape in all the simulated samples. Uncertainties
 526 related to the modeling of the signal and background affect both normalization and shape, with the
 527 exception of cross-section and $t\bar{t}$ modeling uncertainties. The former only affects the normalization of the
 528 considered sample, while the latter only affects the shape of $t\bar{t}$ samples. Nevertheless, the normalization
 529 uncertainties modify the relative fractions of the different samples, leading to a shape uncertainty in the
 530 final distributions.

531 A single independent nuisance parameter is assigned to each source of systematic uncertainty in the
 532 statistical analysis. Some of the systematic uncertainties, in particular most of the experimental ones, are
 533 decomposed into several independent sources, as specified in the following. Each individual source then
 534 has a correlated effect across all analysis regions and signal and background samples. Table 17 presents a
 535 list of all systematic uncertainties considered and indicates for each category the number of independent
 536 components and whether they affect the normalization or shape.

Systematic uncertainty	Type	Components
Experimental uncertainties		
Luminosity	N	1
Pileup modeling	SN	1
<i>Physics objects</i>		
Electrons	SN	7
Muons	SN	15
Small-R jet energy scale	SN	31
Small-R jet energy resolution	SN	9
Small-R jet mass scale	SN	8
Large-R jet energy scale	SN	24
Large-R jet energy resolution	SN	12
Large-R jet mass scale	SN	18
Large-R jet mass resolution	SN	10
Jet vertex tagger	SN	1
<i>b-tagging</i>		
Efficiency	SN	9
Mis-tag rate (c)	SN	4
Mis-tag rate (light)	SN	4
p_T extrapolation efficiency	SN	2
<i>top-tagging</i>		
Signal efficiency	SN	9
p_T extrapolation signal efficiency	SN	1
background efficiency	SN	5
inefficiency	SN	3
Signal and background modeling		
<i>Signal</i>		
PDF variations	SN	30

Scales	SN	2
<i>t̄t background</i>		
PDF variations	SN	90
<i>t̄t + HF normalization</i>	N (free-floating)	1
<i>t̄t + light normalization</i>	N (free-floating)	1
<i>t̄t + light modeling</i>	S	6
<i>t̄t+ ≥ 1c modeling</i>	S	6
<i>t̄t+ ≥ 1b modeling</i>	S	7
<i>t̄t + jets reweighting</i>	SN	1
<i>t̄t+ ≥ 1b fraction</i>	N	1
<i>Other backgrounds</i>		
<i>t̄W cross-section</i>	N	2
<i>t̄Z cross-section</i>	N	2
<i>t̄W modeling</i>	SN	1
<i>t̄Z modeling</i>	SN	1
Single top cross-section	N	3
Single top modeling	SN	6
W+jets normalization	N	3
Z+jets normalization	N	1
Diboson normalization	N	1
<i>t̄t̄t̄ cross-section</i>	N	3

Table 17: List of systematic uncertainties included in the analysis. Each "S" and "N" of type means that the systematic source is considered the "Shape" and "Normalization" effect, respectively. When the type of systematic source is "SN", both "Shape" and "Normalization" effects are considered.

537 6.1 Luminosity and pile-up modeling

538 6.1.1 Luminosity

539 The uncertainty on the integrated luminosity for the full Run-2 dataset is 1.7% [30], obtained using
 540 LUCID-2 detector [94] for the primary luminosity measurement.

541 6.1.2 Pile-up modeling

542 A variation in the pile-up reweighting of the simulated events is included to cover the uncertainties in the
 543 ratio of the predicted and measured inelastic cross-sections in the fiducial volume defined by $M_X > 13$
 544 GeV, where M_X is the mass of the hadronic system [95]

545 **6.2 Reconstructed objects**

546 **6.2.1 Charged leptons**

547 Uncertainties associated with charged leptons arise from the trigger selection, the object reconstruction,
 548 identification and isolation criteria, as well as the lepton momentum scale and resolution. The reconstruction,
 549 identification, and isolation efficiency of electrons and muons, as well as the efficiency of the trigger used
 550 to record the events, differ slightly between data and simulation, which is compensated for by dedicated
 551 scale factors (SFs). Efficiency SFs are measured using tag-and-probe techniques on $Z \rightarrow l^+l^-$ data and
 552 simulated samples [73, 96], and are applied to the simulation to correct for the differences. The effect of
 553 these SFs as well as of their uncertainties are propagated as corrections to the MC event weight. In total,
 554 four independent components are considered for electrons and ten for muons.

555 Additional sources of uncertainty originate from the corrections applied to adjust the lepton momentum
 556 scale and resolution in the simulation to match those in data, measured using reconstructed distributions of
 557 the $Z \rightarrow l^+l^-$ and $J/\psi \rightarrow l^+l^-$ masses, as well as the E/p ratio measured in $W \rightarrow e\nu$ events, where E and p
 558 are the electron energy and momentum measured by the calorimeter and the tracker, respectively [73, 97].
 559 To evaluate the effect of momentum scale uncertainties, the event selection is redone with the lepton energy
 560 or momentum varied by $\pm 1\sigma$. For the momentum resolution uncertainties, the event selection is redone
 561 by smearing the lepton energy or momentum. In total, three independent components are considered for
 562 electrons and five for muons.

563 **6.2.2 Small- R jets, Large- R jets**

564 Uncertainties associated with jets arise from the efficiency of pile-up rejection by the JVT, from the jet
 565 energy scale (JES) and resolution (JER), from the jet mass scale (JMS) and resolution (JMR), and from b -
 566 and top-tagging.

567 **Jet vertex tagging:**

568 Scale factors are applied to correct discrepancies between data and MC for JVT efficiencies. These
 569 SFs are estimated using $Z \rightarrow \mu^+\mu^-$ with tag-and-probe techniques similar to those in Ref.[78], and
 570 the effect of these SFs as well as of their uncertainties are propagated as corrections to the MC event
 571 weight.

572 **Small- R jet:**

573 The *R4_CategoryReduction_FullJER.config* jet uncertainties configuration is used. The JES and
 574 its uncertainty for small- R jets are derived by combining information from test-beam data, LHC
 575 collision data and simulation [98]. The uncertainties from these measurements are factorized into
 576 several independent sources. Additional uncertainties are considered, related to jet flavor (using the
 577 conservative default value of $50 \pm 50\%$ for the quark/gluon fraction for all MC samples), pile-up
 578 corrections, η dependence, high- p_T jets, and differences between full and fast simulation, yielding a
 579 total of 31 independence sources.

580 The JER was measured in Run-2 data and simulation as a function of jet p_T and rapidity using dijet
 581 events, using a similar method as that in Ref. [99]. The combined uncertainty is propagated by
 582 smearing the jet p_T in MC, yielding to nine independent sources.

583 The JMS uncertainties for small- R jets are derived using the RTrk uncertainties that compare the
 584 ratio of the jet mass for calorimeter jets to the jet mass of track-based jets in data and MC simulation
 585 [100]. The six NPs are provided, which are related to baseline, modeling, tracking, and total statistics.
 586 The technique takes advantage of two independent measures of the jet's mass (in the calorimeter
 587 and using the ID), however, this assumption breaks in the case of particle flow jets which uses both
 588 calorimeter and tracking information. For PFlow jets, the uncertainties derived for EMTopo jets are
 589 used and two additional uncertainties are provided. These uncertainties are derived by comparing
 590 the jet mass of EMTopo and PFlow jets in data and MC. Two NPs are provided similarly to the RTrk
 591 uncertainties related to baseline and modeling. The JMS uncertainties are intentionally derived after
 592 the application of the JES and JER smearing. This is different compared to large- R jets where no
 593 nominal JER smearing is applied. The JES corrects the overall energy scale, which impacts the
 594 mass as it is applied to the full four-vector. The JMS correction and uncertainties are then a residual
 595 correction accounting for the distribution of energy within the jet. For this reason, the JES and JMS
 596 uncertainties are to first order uncorrelated effects.

597 **Large- R jet:**

598 The *R10_CategoryJES_FullJER_FullJMS.config* jet uncertainties configuration is used for JES, JER,
 599 and JMS variation. JES uncertainties for large- R jets are derived using a similar approach as for
 600 small- R jets [100]. The correlation between these two objects is taken into account in uncertainty
 601 evaluation. Additional uncertainties related to a topology of an event are included.

602 The JER uncertainties for large- R jets are derived in the same way as the small- R jets uncertainties.
 603 The dijet balance asymmetry is used to evaluate the JER, which is sufficient to cover the fully
 604 supported kinematic regime for large- R jet usage. The nominal data/MC difference is found to
 605 be consistent with 1 within uncertainty. For this reason, no nominal JER smearing is applied.
 606 Instead, the nominal data/MC difference from 1 is taken as an additional uncertainty on top of the
 607 uncertainties related to limited statistics, detector effects, or modeling. The FullJER model with 12
 608 NPs is used. Both data and MC events are smeared to cover properly the correlations between jets in
 609 different regions of the detector.

610 The JMS uncertainties for large- R jets are derived from the forward folding technique (FF) in the
 611 limited region of $200 \text{ GeV} < p_T < 1000 \text{ GeV}$ around the W and top mass peaks [100, 101]. The RTrk
 612 technique is used to extend this region to $200 \text{ GeV} < p_T < 3000 \text{ GeV}$, $m < 600 \text{ GeV}$ and $|\eta| < 2.0$.
 613 The forward folding method is used to fit the W and top mass peaks in $t\bar{t}$ semileptonic events.
 614 The RTrk method uses the double ratio of data/MC for calorimeter-only quantities and track-only
 615 quantities. This technique can cover a wider range in p_T , η , and mass. However, the forward folding
 616 technique is more precise in the lower p_T region and the mass around the top and W masses. The
 617 uncertainties from the two approaches are combined and fitted as a function p_T in a given mass bin.
 618 Interpolation between mass bins is used to provide smooth uncertainties. The full set of JMS NPs is
 619 used in the analysis in order to allow possible combinations with other measurements. The NPs are
 620 related to limited statistics of measurements, detector effects, modeling, and selections. In addition,
 621 uncertainties related to interpolation between mass bins and uncertainties related to a difference
 622 between QCD and hadronic decay jet mass response are included.

623 Measurements of the JMR in the $t\bar{t}$ semileptonic events are also used to constrain the JMR
 624 uncertainties by using the forward folding method [100, 101]. Measurements are performed in
 625 two mass regions to cover W boson and top quark mass peaks. The W boson mass peak is fitted
 626 in a region of $50 \text{ GeV} < m_{\text{jet}} < 120 \text{ GeV}$ and $200 \text{ GeV} < p_{T,\text{jet}} < 350 \text{ GeV}$. The top mass peak is

627 fitted in a region of $120 \text{ GeV} < m_{\text{jet}} < 300 \text{ GeV}$ and $350 \text{ GeV} < p_{\text{T,jet}} < 1000 \text{ GeV}$. Relative JMR
 628 uncertainty of 20% is used outside these regions. FullJMR uncertainty model with 10 nuisance
 629 parameters is used to cover uncertainties related to the measurement of JMR using the FF method,
 630 interpolation between bins, and the comparison between different MC models for events outside the
 631 two regions. This measurement is within the top mass interval. However, $p_{\text{T,jet}}$ exceeds the p_{T} range
 632 provided by the FF method.

633 ***b*-tagging:**

634 *b*-tagging efficiencies in simulated samples are corrected to match efficiencies in data. Scale factors
 635 are derived as a function of p_{T} for jets containing *b*-jets, *c*-jets and for jets containing neither *b*- nor
 636 *c*-hadrons (light-jets) separately, in dedicated calibration analysis. For *b*-jets efficiencies, $t\bar{t}$ events in
 637 the dilepton topology are used, exploiting the very pure sample of *b*-jets arising from the decays of
 638 the top quarks [79]. For *c*-jet mistag rates, $t\bar{t}$ events in single-lepton topology are used, exploiting
 639 the *c*-jets from the hadronically decaying W bosons, using techniques similar to those in Ref. [102].
 640 For light-jets mistag rates, the so-called negative-tag method similar to that in Ref. [103] is used, but
 641 using $Z + \text{jets}$ events instead of di-jet events. In the three calibration analyses, a large number of
 642 uncertainty components are considered, and a principal component analysis is performed, yielding in
 643 45, 20, and 20 eigenvariations, respectively, for *b*-, *c*, and light-jets, which are taken as uncorrelated
 644 sources of uncertainties. The number of these eigenvariations corresponds to the number of p_{T} bins
 645 (9, 4, and 4, respectively, for *b*-, *c*- and light-jets). The calibration used in this analysis is stored in
 646 the following "CDI file":
 647 `/cvmfs/atlas.cern.ch/repo/sw/database/GroupData/xAODTaggingEfficiency/13TeV/2020-21-13TeV-`
 648 `MC16-CDI-2021-04-16_v1.root.`

649 **Top-tagging:**

650 Uncertainties related to the top-tagging calibration are provided for the signal and the background
 651 jets [85, 104]. Jets are called signals if they pass contained top criteria. Otherwise, they are called
 652 background jets. Uncertainties for background jets are measured in two-phase spaces containing
 653 QCD multijet and gamma+jet processes. The signal jets uncertainties are measured in the boosted
 654 $t\bar{t}$ lepton+jets channel in the range of leading large- R jet $p_{\text{T}} \leq 1 \text{ TeV}$, because there are too few $t\bar{t}$
 655 events to extract scale factors for $p_{\text{T}} \geq 1 \text{ TeV}$. Therefore, additional uncertainties are assigned to
 656 cover signal modeling effects and extrapolation beyond the phase spaces. These uncertainties were
 657 released as part of the consolidated large- R jet uncertainties.

658 **6.3 Signal modeling**

659 The H^+ and W' signal uncertainty is modeled in two ways: by using the PDF uncertainties and through
 660 the variation of μ_f and μ_r . The uncertainties from the modeling of the PDF, which is done with the
 661 NNPDF2.3 or NNPDF3.0 PDF set for datasets simulated, are made using a symmetrized Hessian set,
 662 PDF4LHC15_nlo_30, following the PDF4LHC recommendations for LHC Run II [105]. The signal scale
 663 uncertainty is modeled by varying μ_f and μ_r up (and down) by a factor of 2 (or 0.5).

664 6.4 Background modeling

665 6.4.1 $t\bar{t}$ +jets

666 $t\bar{t}$ + heavy flavor classification

667 The $t\bar{t}$ + jets background is categorized according to the flavor of additional jets in the event, using the
 668 same procedure as described in Ref. [23]. Generator-level particle jets are reconstructed from stable
 669 particles (mean lifetime $\tau > 3 \times 10^{-11}$ seconds) using the anti- k_t algorithm with a radius parameter
 670 $R = 0.4$, and are required to have $p_T > 15$ GeV and $|\eta| < 2.5$. The flavor of a jet is determined by
 671 counting the number of b - or c -hadrons within $\Delta R < 0.4$ of the jet axis. Jets matched to exactly
 672 one b -hadron, with p_T above 5 GeV, are labeled single- b -jets, while those matched to two or more
 673 b -hadrons are labeled b -jets (with no p_T requirement on the second hadron); single- c - and c -jets are
 674 defined analogously, only considering jets not already defined as single- b - or b -jets. Events that have
 675 at least one single- b - or b -jet, not counting heavy-flavor jets from top-quark or W -boson decays, are
 676 labeled as $t\bar{t} + \geq 1b$; those with no single- b - or b -jet but at least one single- c - or c -jet are labeled
 677 as $t\bar{t} + \geq 1c$. Finally, events not containing any heavy-flavor jets aside from those from top-quark
 678 or W -boson decays are labeled as $t\bar{t}$ + light. This classification is used to define the background
 679 categories in the likelihood fit.

680 Systematic uncertainties

681 The systematic uncertainties affecting the $t\bar{t}$ + jets background modeling are summarized in Table
 682 18. The normalization of $t\bar{t}$ + light, $t\bar{t} + \geq 1c$ and $t\bar{t} + \geq 1b$ are allowed to vary freely in the fit. The
 683 normalization factors of $t\bar{t} + \geq 1c$ and $t\bar{t} + \geq 1b$ are estimated with a common parameter in the fit.
 684 However, since these distribution's shapes are different slightly from each other in the high BDT
 685 score region as shown in Figure 32. Therefore, the uncertainty of the $t\bar{t} + \geq 1b$ fraction to the whole
 686 of $t\bar{t}$ + HF can be a systematic source because it changes the whole template shape of $t\bar{t} + \geq 1c$ and
 687 $t\bar{t} + \geq 1b$. Referring to the post-fit results of the resolved analysis [24], the observed fraction (R_{ttb}^{Data})
 688 differs from the expected one (R_{ttb}^{MC}) by about 12% as follows:

$$689 R_{ttb}^{\text{MC}} = \frac{N_{ttb}^{\text{MC}}}{N_{ttb}^{\text{MC}} + N_{ttc}^{\text{MC}}} \sim 0.64, \quad R_{ttb}^{\text{Data}} = \frac{N_{ttb}^{\text{Data}}}{N_{ttb}^{\text{Data}} + N_{ttc}^{\text{Data}}} \sim 0.72, \quad \frac{R_{ttb}^{\text{Data}}}{R_{ttb}^{\text{MC}}} \sim 0.88$$

690 In this analysis, the fraction uncertainty is assumed conservatively enough to be $\pm 50\%$, and an NP is
 691 introduced. The total amount of $t\bar{t}$ + HF is kept the same after changing the fraction.

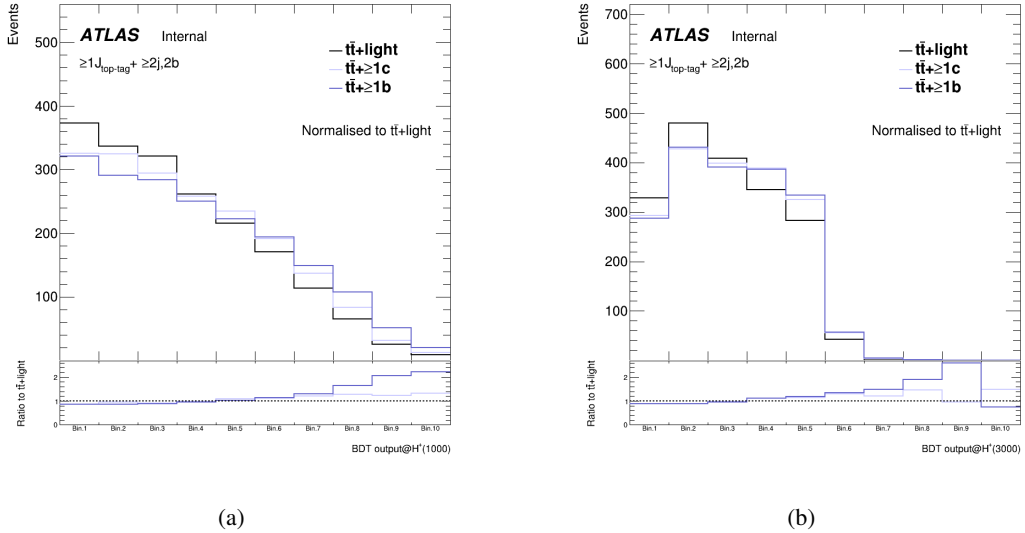


Figure 32: Comparison of the shape of BDT distributions in the SR1 among $t\bar{t} + \text{jets}$ events, where (a) is BDT output trained using 1000 GeV H^+ samples, and (b) is the one trained using 3000 GeV. $t\bar{t} + \geq 1c$ and $t\bar{t} + \geq 1b$ distributions are normalised to the distribution of $t\bar{t} + \text{light}$. And the ratios to $t\bar{t} + \text{light}$ distribution are shown at the bottom.

Besides normalization, the $t\bar{t} + \text{light}$, $t\bar{t} + \geq 1c$ and $t\bar{t} + \geq 1b$ processes are affected by different types of uncertainties: $t\bar{t} + \text{light}$ has additional diagrams and profits from relatively precise measurements in data; $t\bar{t} + \geq 1c$ and $t\bar{t} + \geq 1b$ can have similar or different diagrams depending on the flavor scheme used for the PDF, and different mass of the c - and b -quark contribute to additional differences between these two processes. For these reasons, all uncertainties in the $t\bar{t} + \text{jets}$ background modeling are assigned independent nuisance parameters for the $t\bar{t} + \text{light}$, $t\bar{t} + \geq 1c$ and $t\bar{t} + \geq 1b$ processes.

Systematic uncertainties on the reweighting are extracted according to the reweighting functions derived in Section 5.4. The differences between the BDT output distribution reweighted with the nominal reweighting function and the one reweighted with $\pm 1\sigma$ functions are included in the fit for each $t\bar{t} + \text{jets}$ as an NP.

Systematic uncertainties on the acceptance and shapes are extracted from the comparison between the nominal and different MC samples and settings. For ISR and FSR the settings of the nominal Powheg+Pythia sample are varied, resulting in different event weights; the uncertainty due to ISR is estimated by changing μ_r and μ_f in the ME and α_S^{ISR} in the PS, while the uncertainty due to FSR is estimated by changing α_S^{FSR} in the PS. For the ISR, the amount of radiation is increased (decreased) by scaling μ_r and μ_f by a factor 0.5 (2.0) and by using the Var3cUp (Var3cDown) variation from the A14 tune [38], corresponding to $\alpha_S^{\text{ISR}} = 0.140(0.115)$ instead of the nominal $\alpha_S^{\text{ISR}} = 0.127$. For the FSR, the amount of radiation is increased (decreased) varying μ_r for QCD emission in the FSR by a factor of 0.5 (2.0), corresponding to $\alpha_S^{\text{FSR}} = 0.1423(0.1147)$ instead of the nominal $\alpha_S^{\text{FSR}} = 0.127$. The nominal Powheg+Pythia sample is compared to the Powheg+Herwig sample to access the effect of the PS and hadronization models, and to the MG5_aMC sample to access the effect of the NLO matching technique.

The nominal prediction for the dominant $t\bar{t} + \geq 1b$ background, based on the Powheg+Phytia $t\bar{t}$ (5FS) sample in which all the additional partons are produced by the PS, is compared to the alternative

716 Powheg+Phythia $t\bar{t}$ (4FS) sample, in which the $b\bar{b}$ pair is generated in addition to the $t\bar{t}$ pair at the
 717 ME level at NLO in QCD. A uncertainty resulting from the comparison of the shape of the two
 718 models is included.

Uncertainty source	Description	Components
$t\bar{t}$ + light normalization	Free-floating	$t\bar{t}$ + light
$t\bar{t}$ + HF normalization	Free-floating	$t\bar{t}+ \geq 1b$ and $t\bar{t}+ \geq 1c$
$t\bar{t}+ \geq 1b$ fraction	Fraction to the whole of $t\bar{t}$ + HF	$t\bar{t}+ \geq 1b$ and $t\bar{t}+ \geq 1c$
$t\bar{t}$ + jets reweighting	Statistical uncertainties of weights	All $t\bar{t}$ + jets
$t\bar{t}+ \geq 1b$ flavor scheme	5FS vs 4FS	$t\bar{t}+ \geq 1b$
NLO matching	MG5_aMC+Pythia	vs. Powheg+Pythia
PS & hadronisation	Powheg+Herwig	vs. Powheg+Pythia
α_S^{ISR}	$Var3cUp$ ($Var3cDown$)	in Powheg+Pythia
μ_f	scaling by 0.5 (2.0)	in Powheg+Pythia
μ_r	scaling by 0.5 (2.0)	in Powheg+Pythia
FSR	Varying α_S^{FSR} (PS)	in Powheg+Pythia

Table 18: Summary of the sources of systematic uncertainty for $t\bar{t}$ + jets modeling. The systematic uncertainties listed in the second section of the table are evaluated in such a way to have no impact on the normalization of the three, $t\bar{t}$ + light, $t\bar{t}+ \geq 1c$ and $t\bar{t}+ \geq 1b$ components in the phase-space selected in the analysis. The last column of the table indicates the $t\bar{t}$ + jets components to which a systematic uncertainty is assigned. All systematic uncertainty sources are treated as uncorrelated across the three components.

719 6.4.2 Other backgrounds

720 The predicted $t\bar{t}H$ signal cross-section uncertainty is $^{+5.8\%}_{-9.2\%}$ (QCD scale) $\pm 3.6\%$ (PDF + α_S) [106–111].
 721 These two components are treated as uncorrelated in the fit. The effect of QCD scale and PDF variations
 722 on the shape of the distributions is found to be negligible. Uncertainties in the Higgs-boson branching
 723 fractions are also considered; these amount to 2.2% for the $b\bar{b}$ decay mode [106]. Uncertainties associated
 724 to the modeling of $t\bar{t}H$ by the Powheg+Phythia sample are also considered, for a total of four independent
 725 components. The uncertainty due to ISR is estimated by simultaneously changing μ_f and μ_r in the ME and
 726 α_S^{ISR} in the PS, while the uncertainty due to ISR is estimated by changing α_S^{FSR} in the PS. For the ISR and
 727 FSR, the amount of radiation is varied following the same procedure as for $t\bar{t}$. The nominal Powheg+Pythia
 728 sample is compared to the Powheg+Herwig sample to access the uncertainty due to PS and hadronization,
 729 and to the MG5_aMC+Phythia sample for the uncertainty due to the NLO matching.

730 A $\pm 5\%$ uncertainty is considered for the cross-sections of the three single-top production modes [112–116].
 731 Uncertainties associated with the PS and hadronisation model, and with the NLO matching scheme are
 732 evaluated by comparing, for each process, the nominal Powheg+Pythia sample to a sample produced using
 733 Powheg+Herwig and MG5_aMC+Pythia, respectively. The uncertainty associated to the interference
 734 between Wt and $t\bar{t}$ production at NLO [58] is assessed by comparing the nominal Powheg+Pythia sample
 735 produced using the "diagram removal" scheme to an alternative sample produced with the same generator
 736 but using the "diagram subtraction" scheme.

737 The uncertainty of the $t\bar{t}V$ NLO cross-section prediction is 15% [117, 118], split into PDF and scale
 738 uncertainties as for $t\bar{t}H$. An additional $t\bar{t}V$ modeling uncertainty, related to the choice of PS and

739 hadronisation model and NLO matching scheme is assessed by comparing the nominal MG5_aMC+Pythia
740 samples with alternative ones generated with Sherpa.

741 A total 50% normalization uncertainty is considered for the 4 tops background, covering effects from
742 varying μ_f and μ_r , PDFs and α_S [34, 119]. The small backgrounds from tZq and tWH are each assigned
743 cross-section uncertainties: $\pm 7.9\%$ and $\pm 0.9\%$ for tZq , accounting for μ_f and μ_r variations, and for PDFs,
744 respectively, and $\pm 50\%$ for tWZ [34].

745 An uncertainty of 40% is assumed for the $W +$ jets cross-section, with an additional 30% normalization
746 uncertainty used for $W +$ heavy-flavor jets, taken as uncorrelated between events with two and more than
747 two heavy-flavor jets. These uncertainties are based on variations of the μ_f and μ_r and of the matching
748 parameters in the Sherpa samples. An uncertainty of 35% is then applied to the $Z +$ jets normalization,
749 uncorrelated across jet bins, to account for both the variations of the scales and matching parameters in the
750 Sherpa samples and the uncertainty in the extraction from data of the correction factor for the heavy-flavor
751 component. Finally, a total 50% normalization uncertainty in the diboson background is assumed, which
752 includes uncertainties in the inclusive cross-section and additional jet production [120].

7 Profile Likelihood Fit

7.1 Method

In order to test for the presence of an $H^+ \rightarrow tb$ ($W' \rightarrow tb$) signal, a binned maximum-likelihood fitting to the data is performed simultaneously in all analysis regions, and each mass hypothesis is tested separately.

The inputs to the fit are BDT distributions in the SR1 and SR2 for the under 3 TeV mass hypothesis tests. On the other hand, they are H_T^{jets} distributions in the SR, CR1, and CR2 on the above 3 TeV mass hypothesis tests. Two initially unconstrained fit parameters are used to model the normalization of the $t\bar{t}$ + light and $t\bar{t} + \geq 1$ HF jets background. The procedures used to quantify the level of agreement with the background-only or background-plus-signal hypothesis, and to determine exclusion limits, are based on the profile likelihood ratio test and the CL_s method. The parameter of interest is the signal strength, μ . The signal MC cross-sections are assumed to be 0.046 pb in the fittings.

To estimate the signal strength, a likelihood function, $\mathcal{L}(\mu, \theta)$, is constructed as the product of Poisson probability terms. One Poisson term is included for every bin of distributions in the analysis regions. The binning of each BDT output distribution is defined by an automatic binning algorithm, *TransfoD*, implemented in TRexFitter [93]. The expected number of events in the Poisson terms is a function of μ , and a set of nuisance parameters, θ . The nuisance parameters encode effects from the normalization of backgrounds, including two free normalization factors for the $t\bar{t}$ + light and $t\bar{t} + \geq 1$ HF jets backgrounds, the systematic uncertainties, and one parameter per bin to model statistical uncertainties in the simulated samples. All nuisance parameters are constrained with Gaussian or log-normal terms. There are about 340 nuisance parameters considered in the fit, the number varying slightly across the range of mass hypotheses.

To extract the exclusion limit on μ , the following test statistic is used:

$$\tilde{t}_\mu = \begin{cases} -2 \ln \frac{\mathcal{L}(\mu, \hat{\theta}(\mu))}{\mathcal{L}(0, \hat{\theta}(0))} & \mu < 0 \\ -2 \ln \frac{\mathcal{L}(\mu, \hat{\theta}(\mu))}{\mathcal{L}(\hat{\mu}, \hat{\theta})} & \mu \geq 0 \end{cases} \quad (2)$$

The values of the signal strength and nuisance parameters that maximize the likelihood function are represented by $\hat{\mu}$ and $\hat{\theta}$, respectively. For a given value of μ , the values of the nuisance parameters that maximize the likelihood function are represented by $\hat{\theta}(\mu)$.

7.2 Pruning and smoothing of systematic uncertainties

In the fits, pruning is applied at the threshold of 1%, meaning that if the effect of a nuisance parameter is smaller than 1% before fitting (separately for shape and normalization) it is excluded from the fit. This pruning procedure reduces the CPU time and helps the fit to converge. Appendix ?? shows the systematic uncertainties that are pruned in Asimov fits.

Smoothing is applied for systematic uncertainties on $t\bar{t}$ modeling by *MaxVariation* algorithm implemented in TRexFitter because these uncertainties are typically computed by comparing two different MC samples, or by applying MC generator weights on an MC sample, which dilutes the MC statistics and increases the fluctuations. No smoothing is applied for modeling systematic uncertainties on small backgrounds — given their small impact on the final result — or for experimental systematics — which are obtained either

788 by applying SFs typically close to unity (e.g. b -tagging), or by using the same simulated events but with
 789 different calibrations of the objects (e.g. JES).

790 7.3 Asimov fit

791 7.3.1 Pre-fit plots

792 The following section performs data fitting tests using Asimov datasets from nominal simulated samples.
 793 The signal events aren't injected into these Asimov datasets. Figure 33 to 42 show the pre-fit plots for each
 794 H^+ mass hypotheses. Similarly, Figure 43 to 51 and Figure 52 to 60 show the pre-fit plots for each W'_L and
 795 W'_R mass hypotheses, respectively.

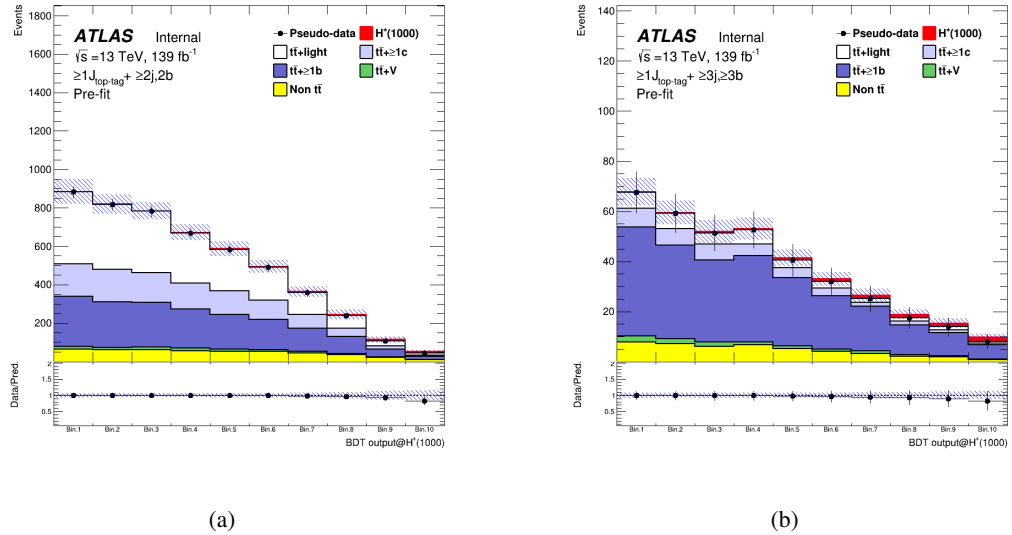


Figure 33: Pre-fit plots in the SR1 (left) and SR2 (right) for 1000 GeV mass hypothesis of H^+ signal.

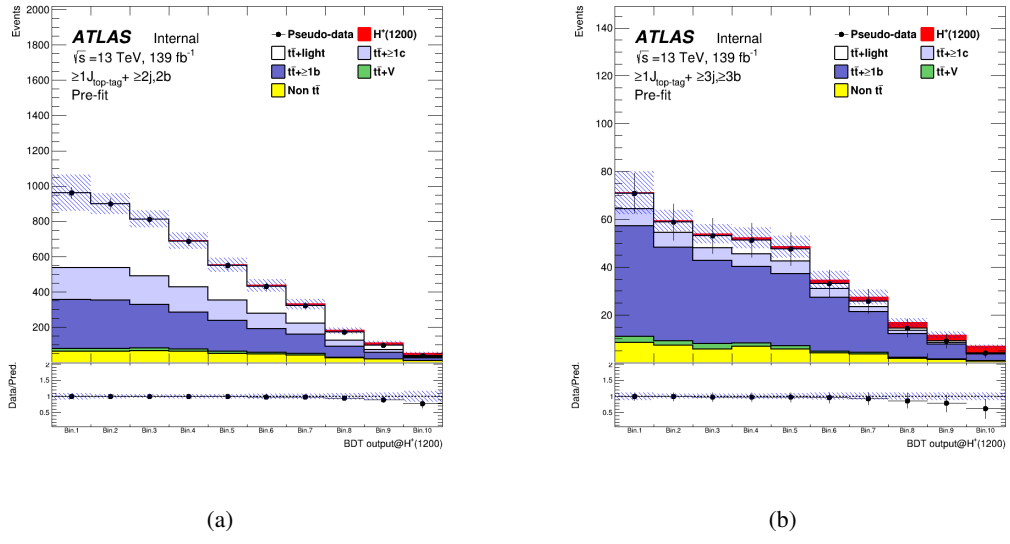


Figure 34: Pre-fit plots in the SR1 (left) and SR2 (right) for 1200 GeV mass hypothesis of H^+ signal.

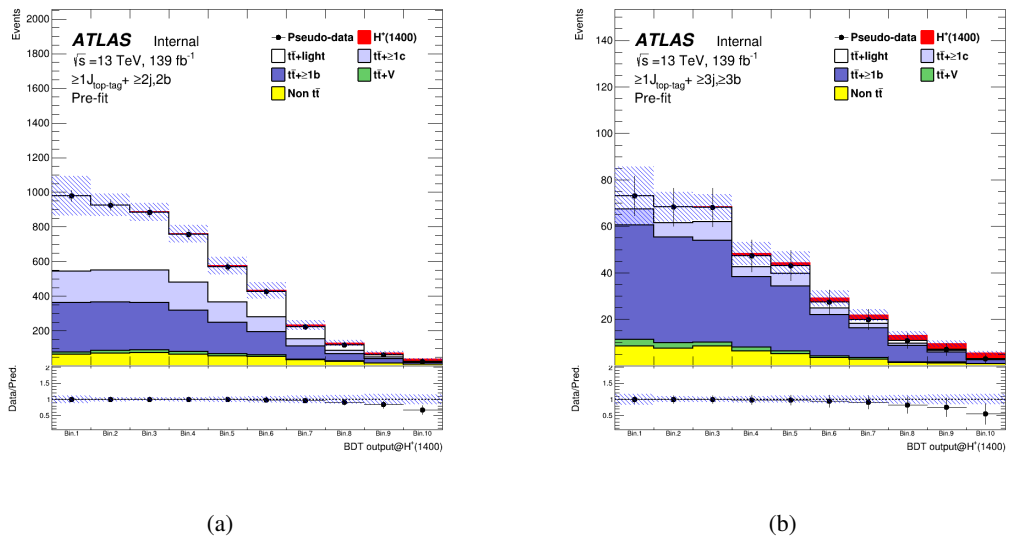


Figure 35: Pre-fit plots in the SR1 (left) and SR2 (right) for 1400 GeV mass hypothesis of H^+ signal.

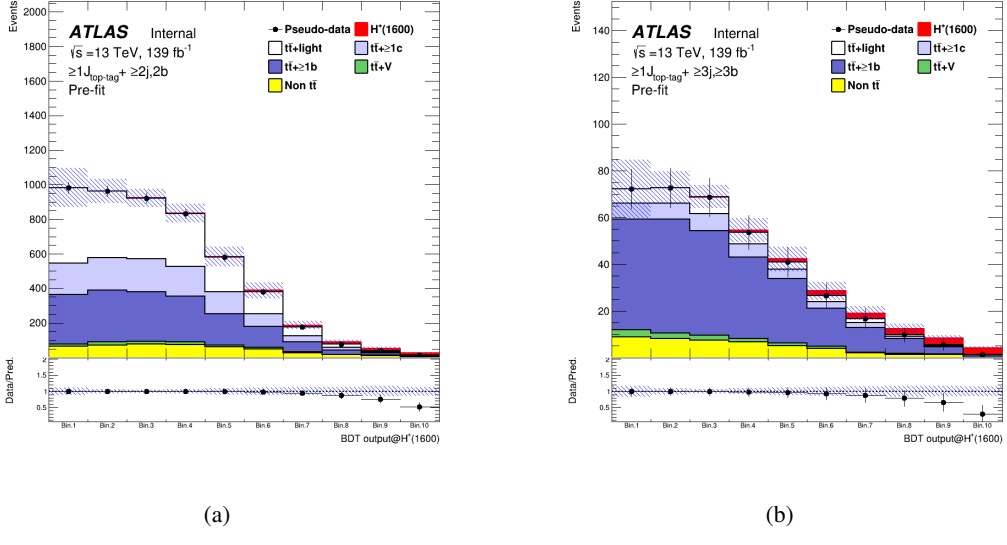


Figure 36: Pre-fit plots in the SR1 (left) and SR2 (right) for 1600 GeV mass hypothesis of H^+ signal.

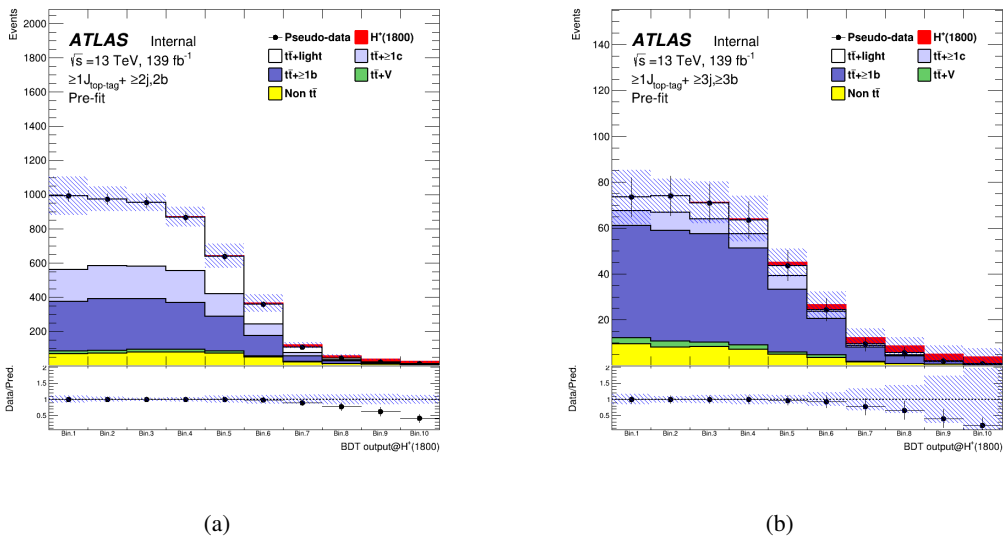


Figure 37: Pre-fit plots in the SR1 (left) and SR2 (right) for 1800 GeV mass hypothesis of H^+ signal.

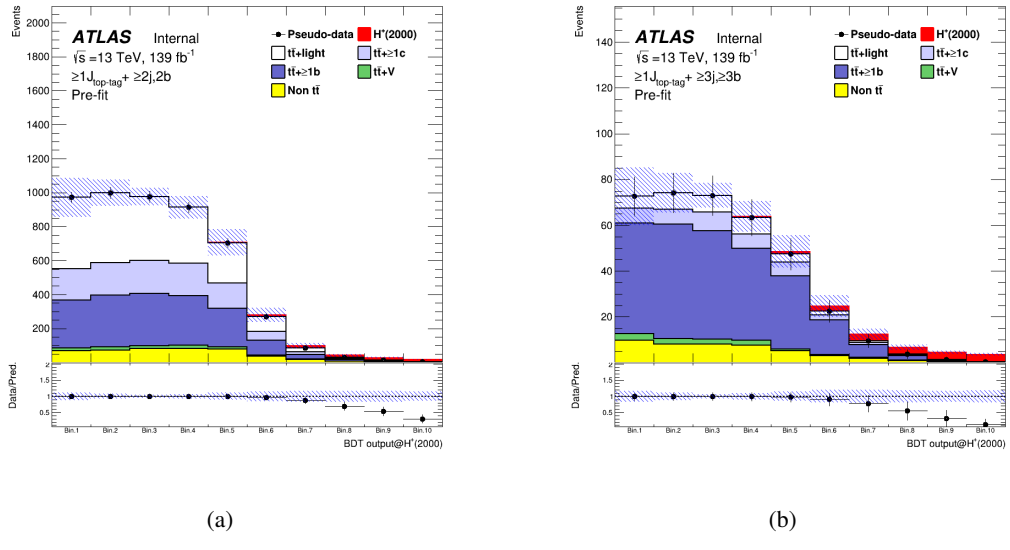


Figure 38: Pre-fit plots in the SR1 (left) and SR2 (right) for 2000 GeV mass hypothesis of H^+ signal.

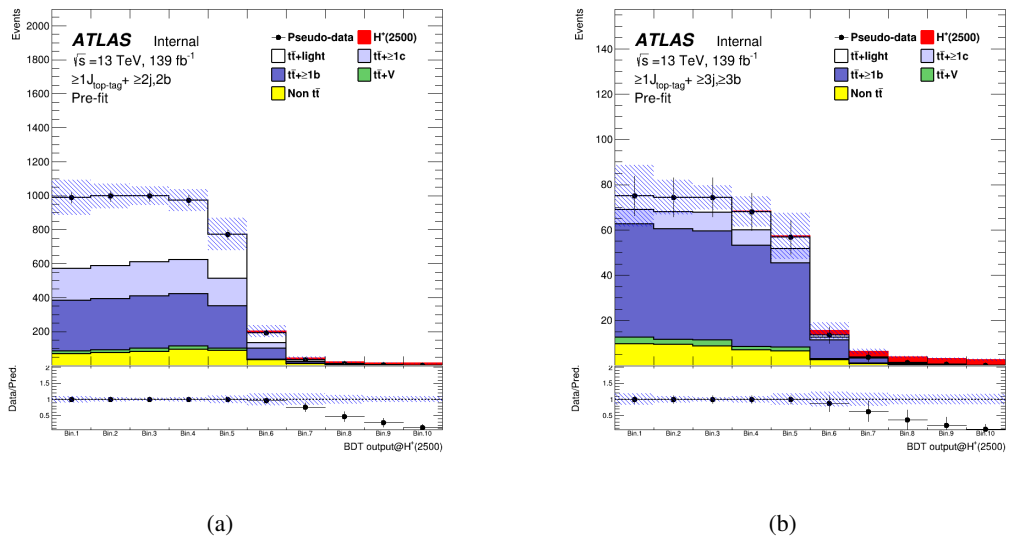


Figure 39: Pre-fit plots in the SR1 (left) and SR2 (right) for 2500 GeV mass hypothesis of H^+ signal.

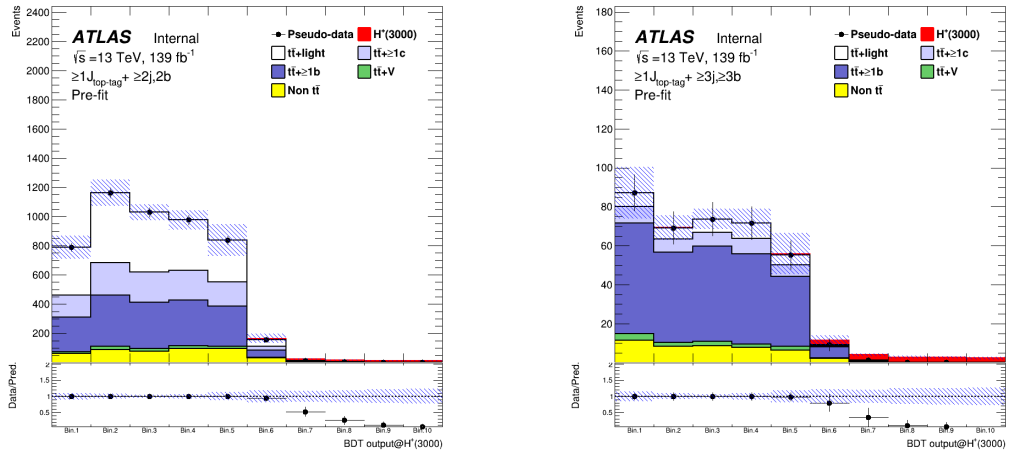


Figure 40: Pre-fit plots in the SR1 (left) and SR2 (right) for 3000 GeV mass hypothesis of H^+ signal.

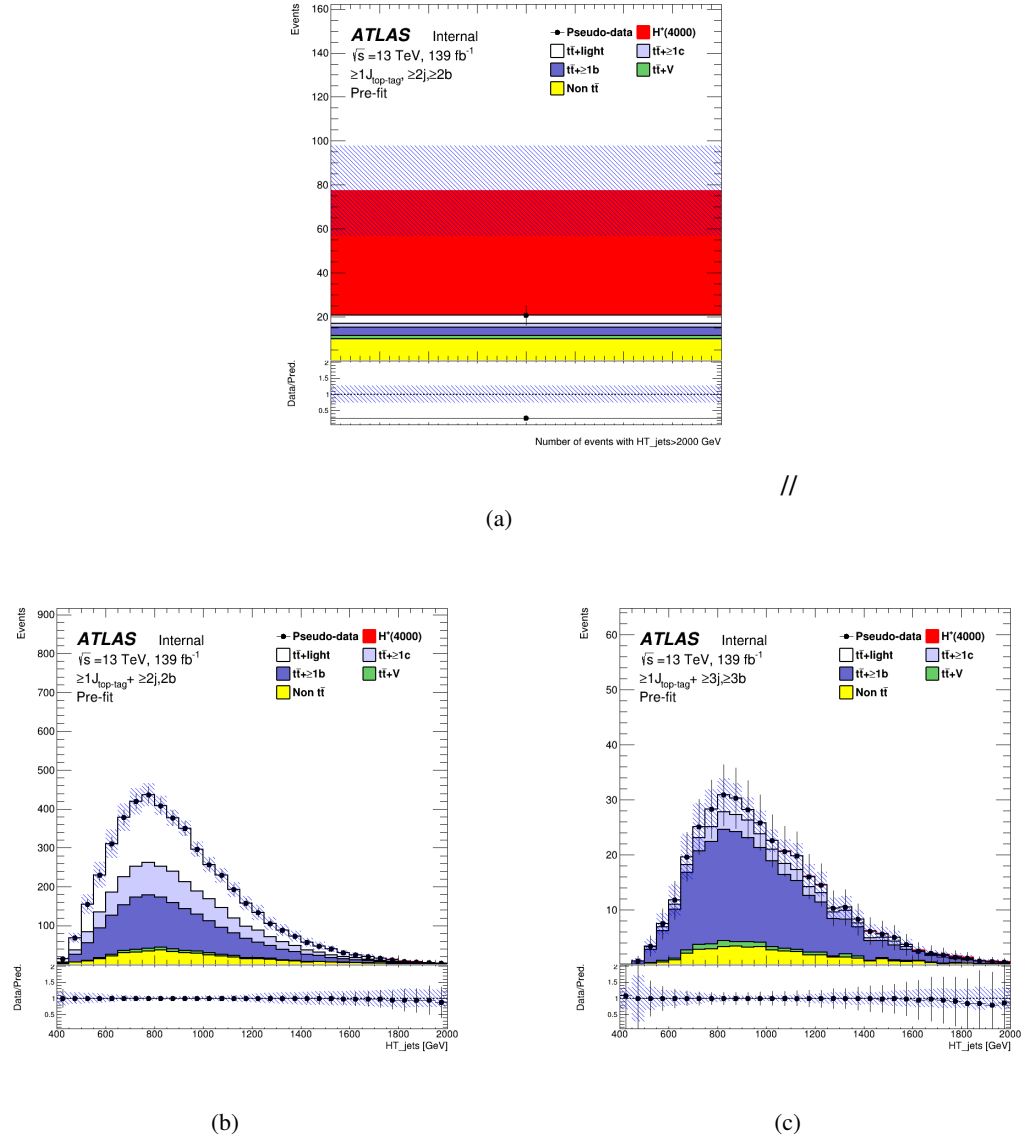


Figure 41: Pre-fit plots in the SR (top), CR1 (bottom-left), and CR2 (bottom-right) for 4000 GeV mass hypothesis of H^+ signal.

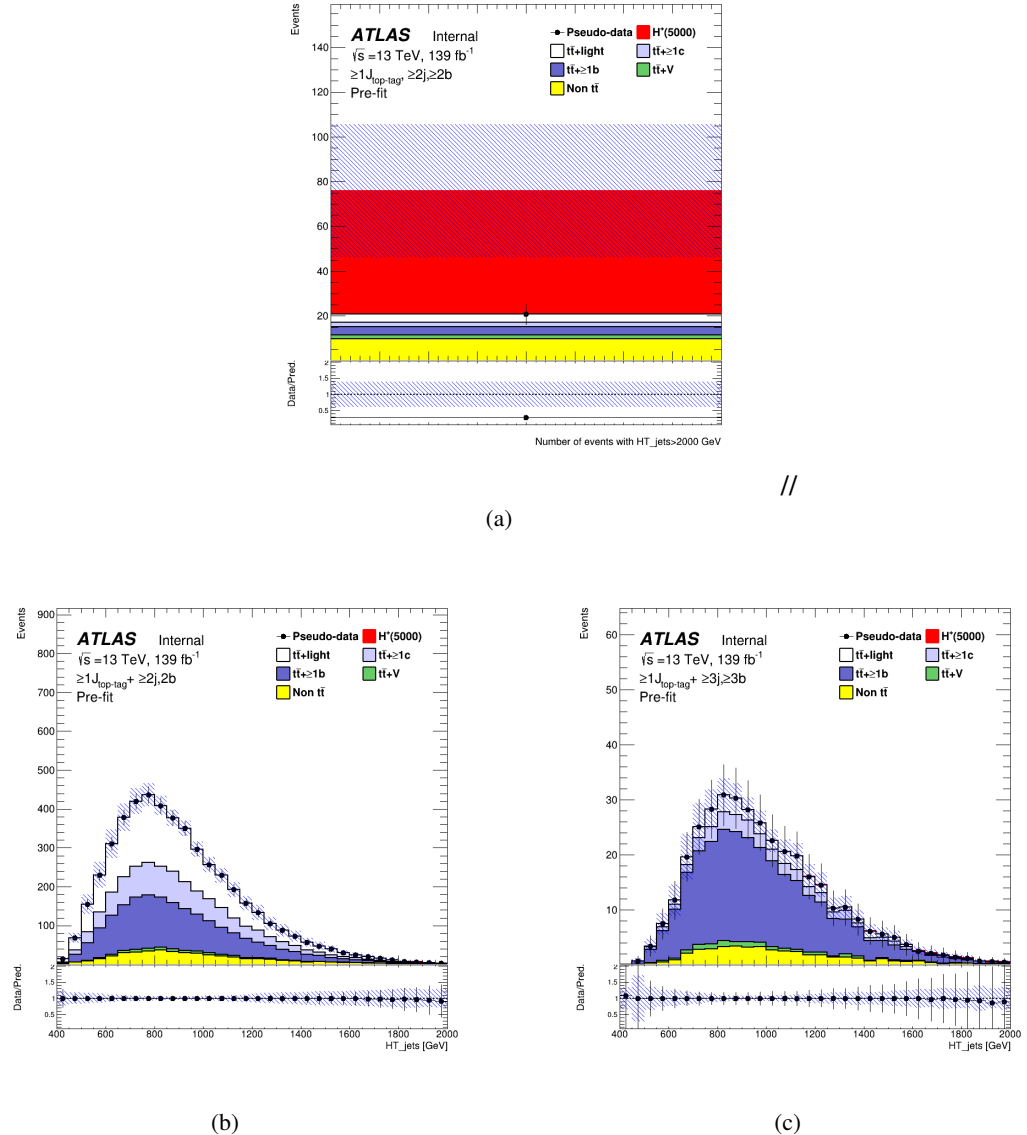


Figure 42: Pre-fit plots in the SR (top), CR1 (bottom-left), and CR2 (bottom-right) for 5000 GeV mass hypothesis of H^+ signal.

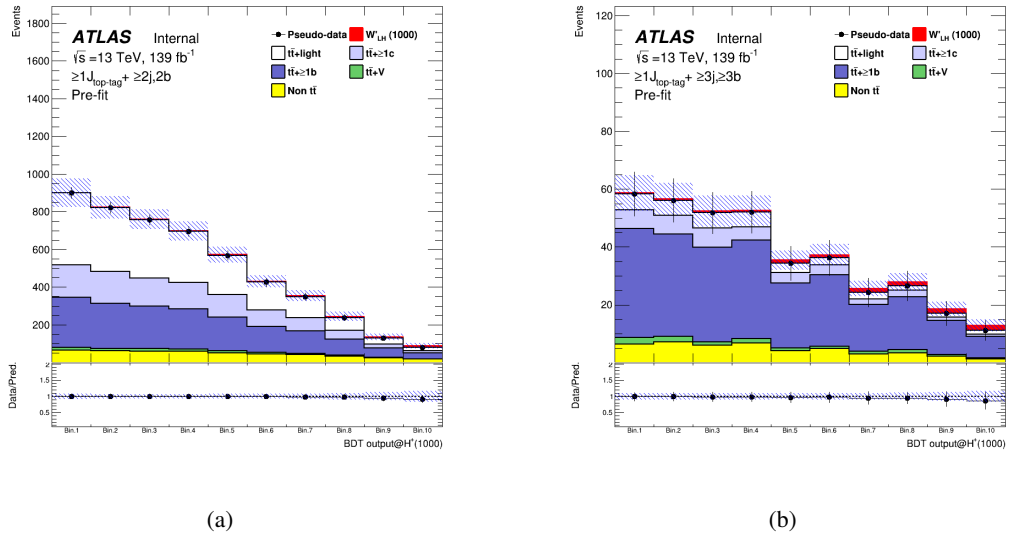


Figure 43: Pre-fit plots in the SR1 (left) and SR2 (right) for 1000 GeV mass hypothesis of W'_L signal.

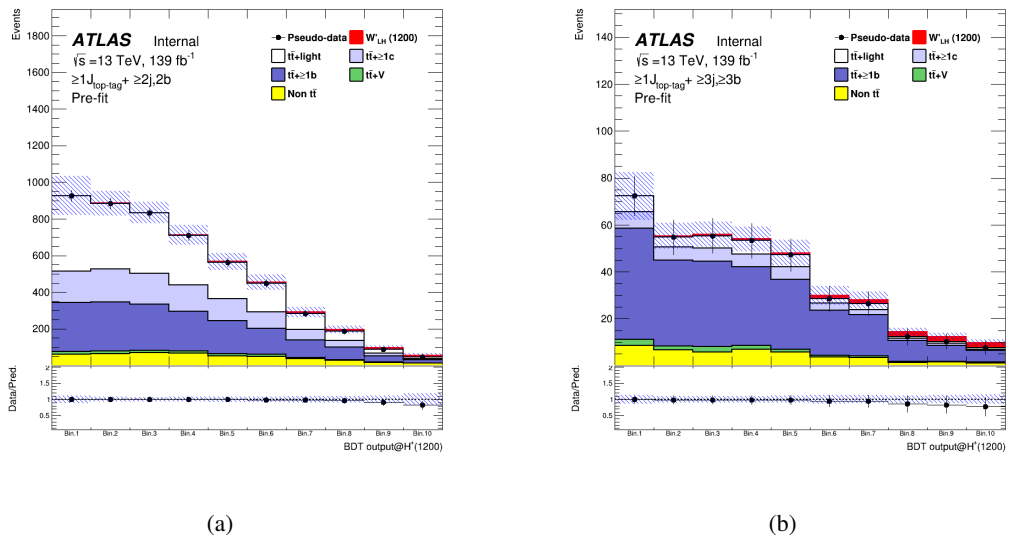


Figure 44: Pre-fit plots in the SR1 (left) and SR2 (right) for 1200 GeV mass hypothesis of W'_L signal.

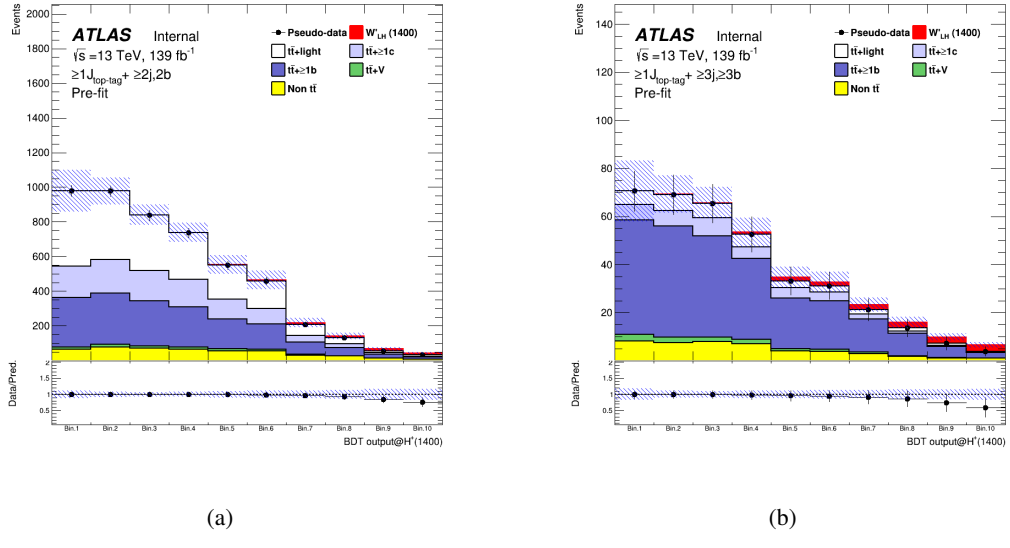


Figure 45: Pre-fit plots in the SR1 (left) and SR2 (right) for 1400 GeV mass hypothesis of W'_L signal.

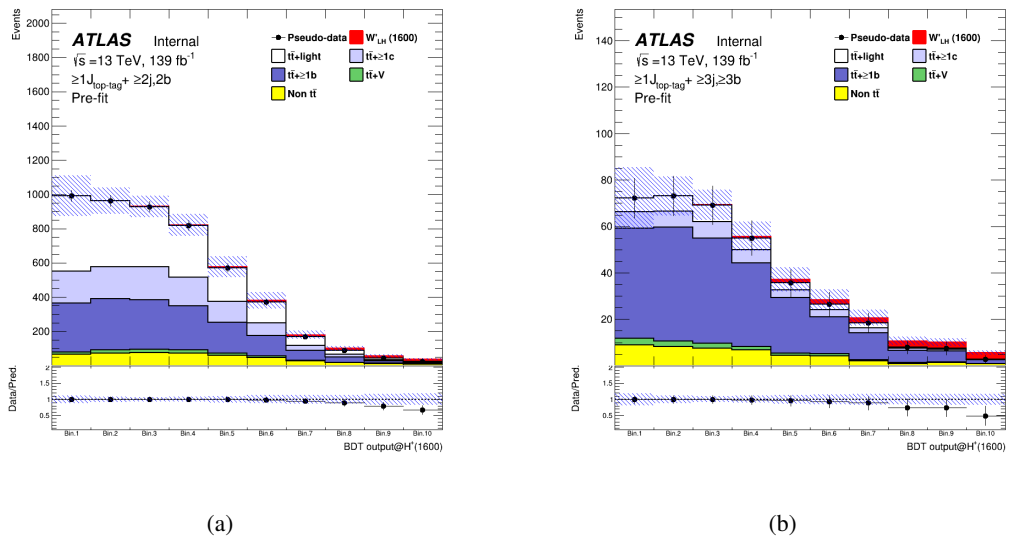


Figure 46: Pre-fit plots in the SR1 (left) and SR2 (right) for 1600 GeV mass hypothesis of W'_L signal.

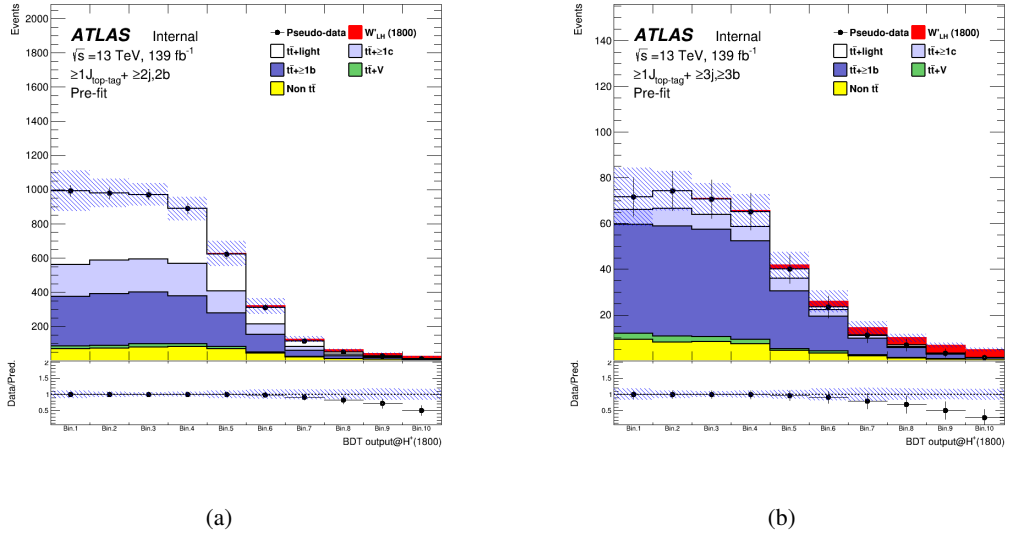


Figure 47: Pre-fit plots in the SR1 (left) and SR2 (right) for 1800 GeV mass hypothesis of W'_L signal.

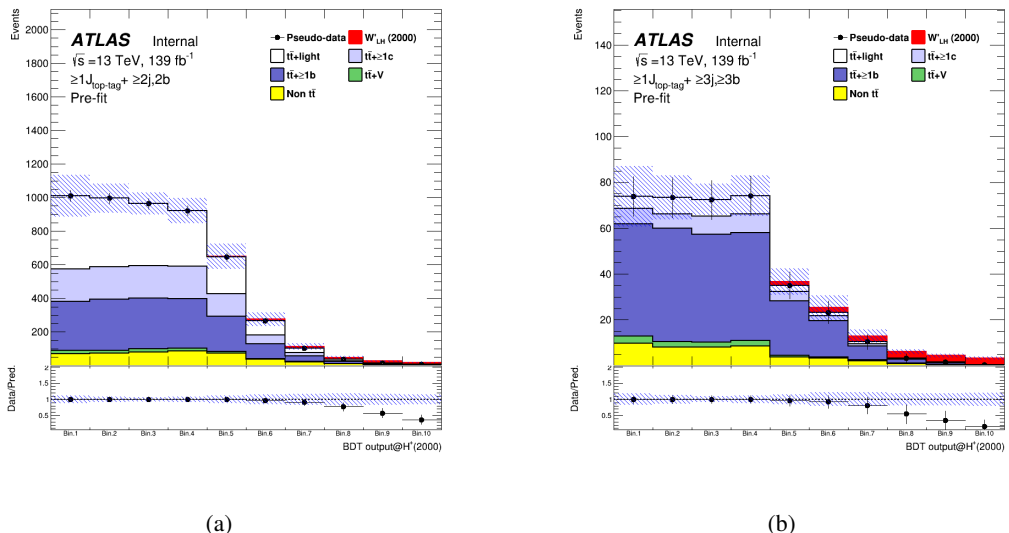


Figure 48: Pre-fit plots in the SR1 (left) and SR2 (right) for 2000 GeV mass hypothesis of W'_L signal.

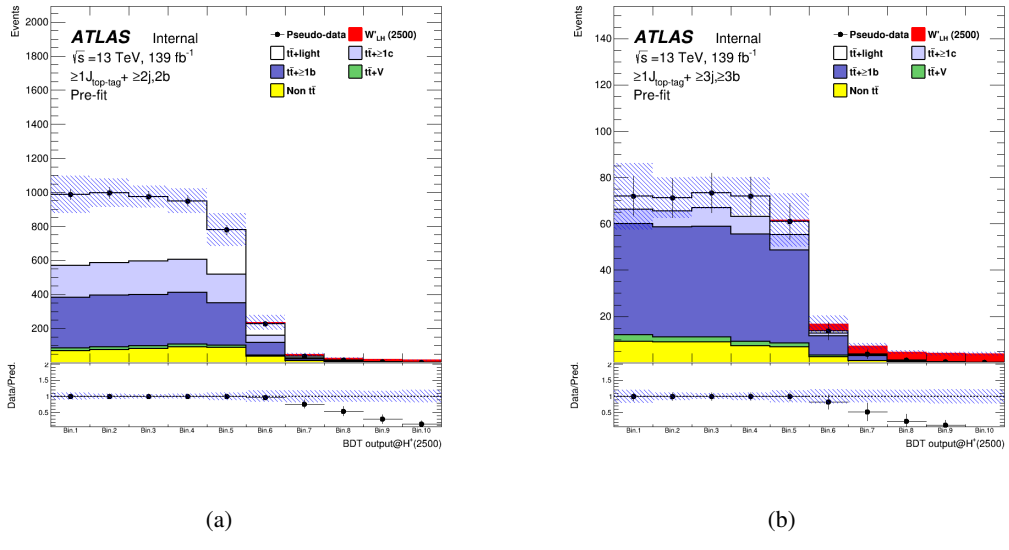


Figure 49: Pre-fit plots in the SR1 (left) and SR2 (right) for 2500 GeV mass hypothesis of W'_{L} signal.

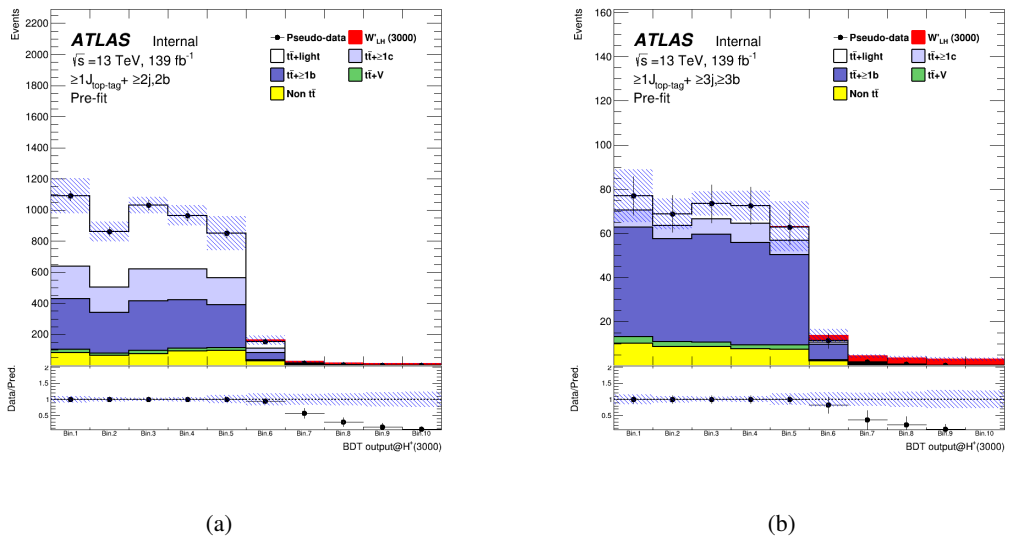


Figure 50: Pre-fit plots in the SR1 (left) and SR2 (right) for 3000 GeV mass hypothesis of W'_{L} signal.

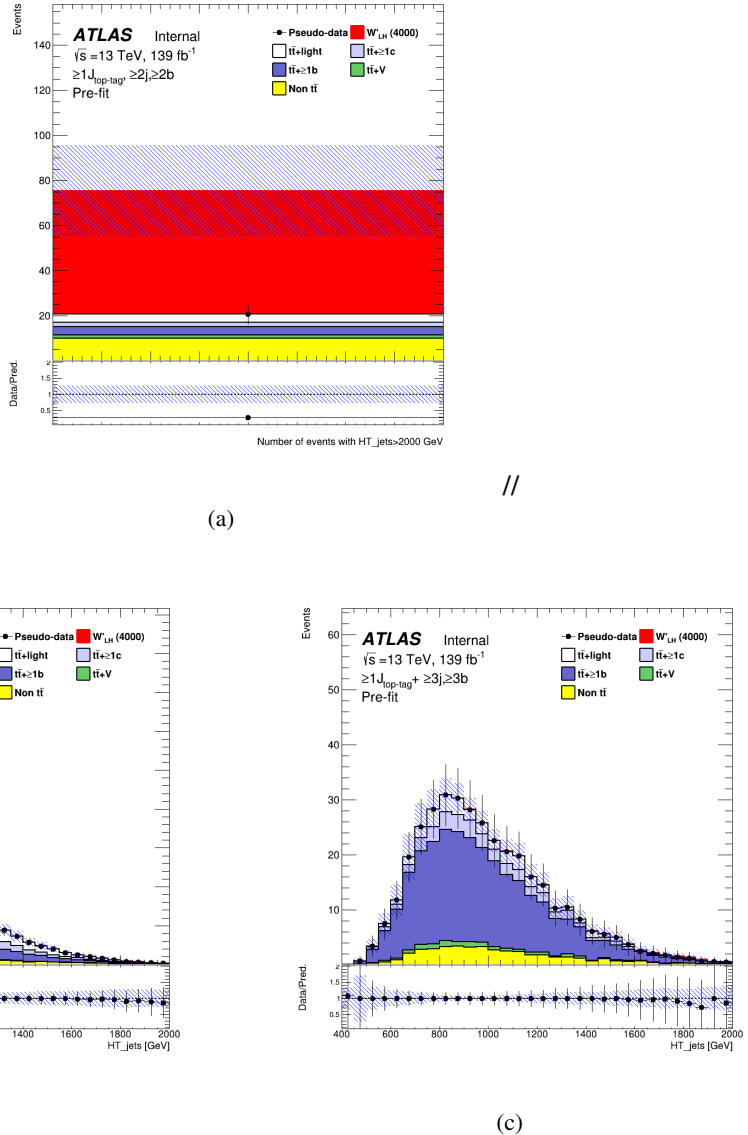


Figure 51: Pre-fit plots in the SR (top), CR1 (bottom-left), and CR2 (bottom-right) for 4000 GeV mass hypothesis of W'_L signal.

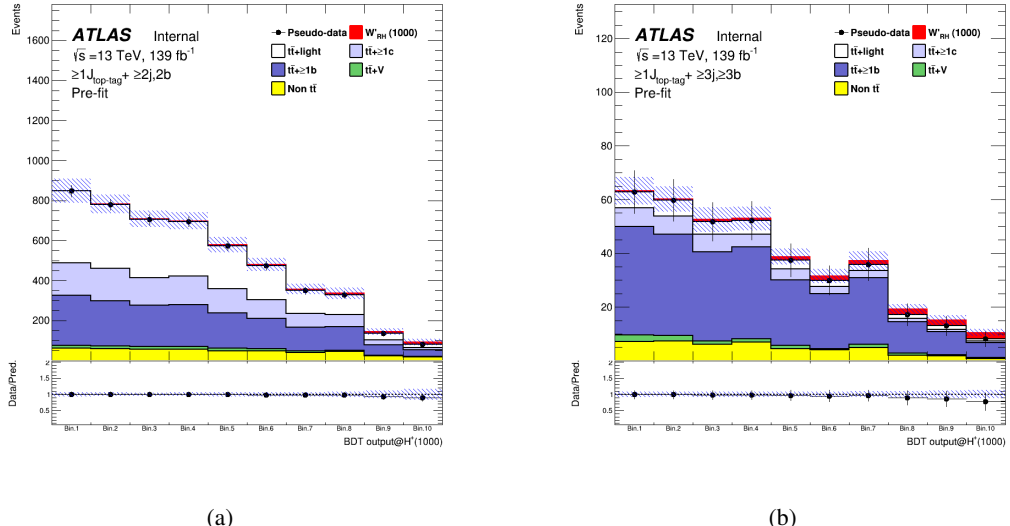


Figure 52: Pre-fit plots in the SR1 (left) and SR2 (right) for 1000 GeV mass hypothesis of W'_R signal.

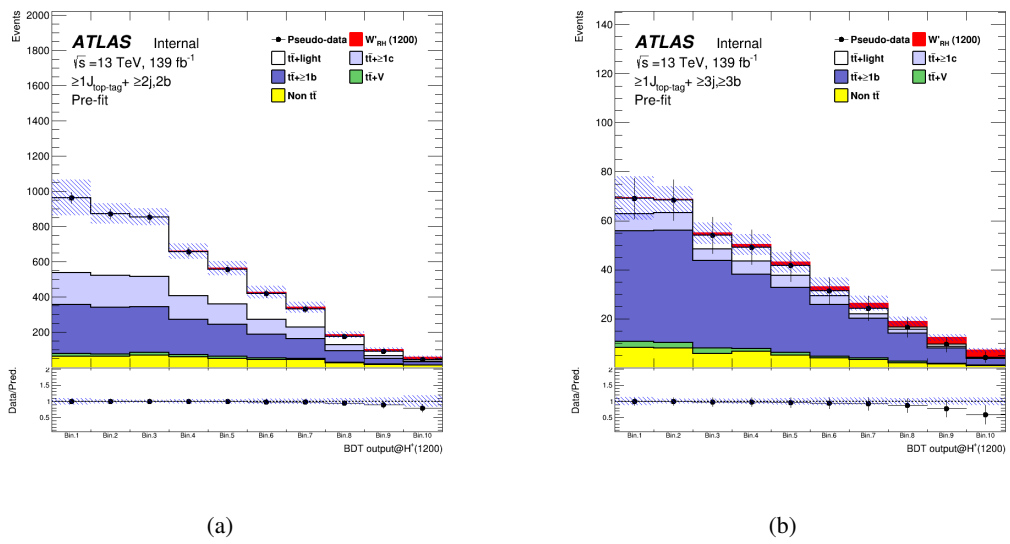


Figure 53: Pre-fit plots in the SR1 (left) and SR2 (right) for 1200 GeV mass hypothesis of W'_R signal.

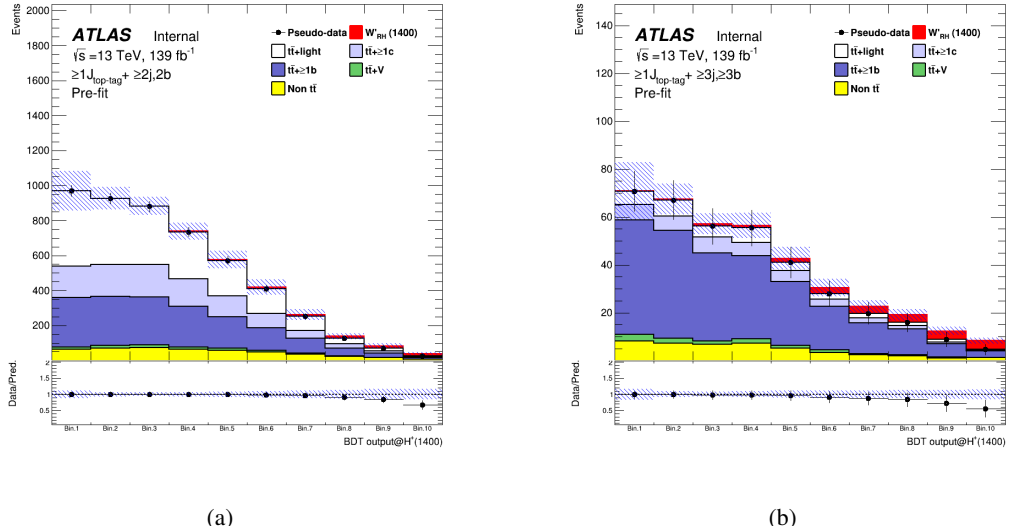


Figure 54: Pre-fit plots in the SR1 (left) and SR2 (right) for 1400 GeV mass hypothesis of W'_R signal.

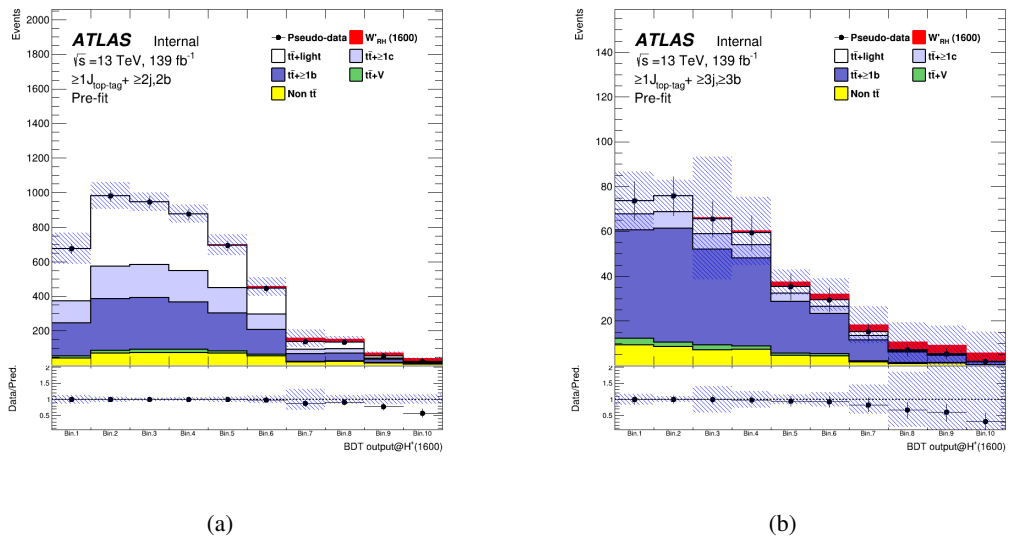


Figure 55: Pre-fit plots in the SR1 (left) and SR2 (right) for 1600 GeV mass hypothesis of W'_R signal.

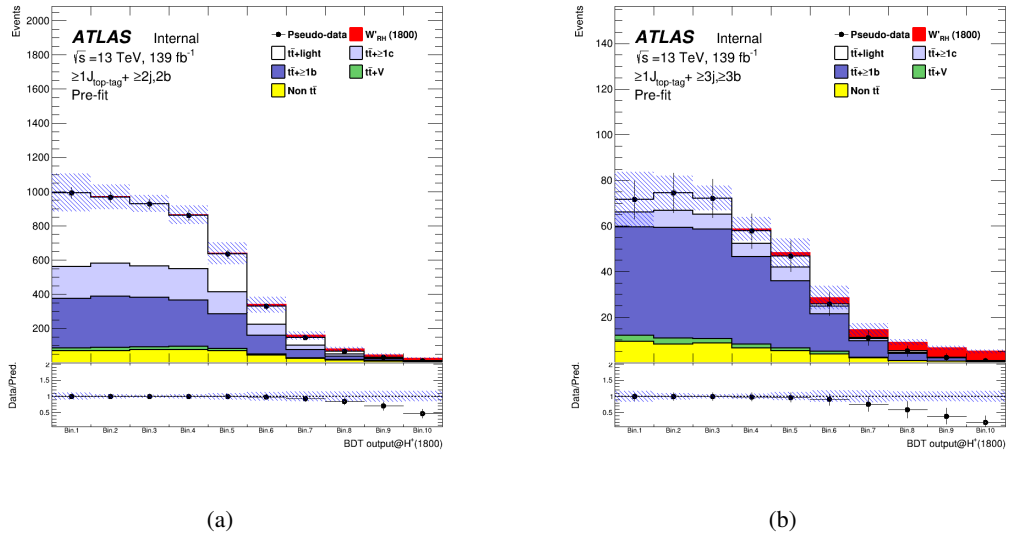


Figure 56: Pre-fit plots in the SR1 (left) and SR2 (right) for 1800 GeV mass hypothesis of W'_R signal.

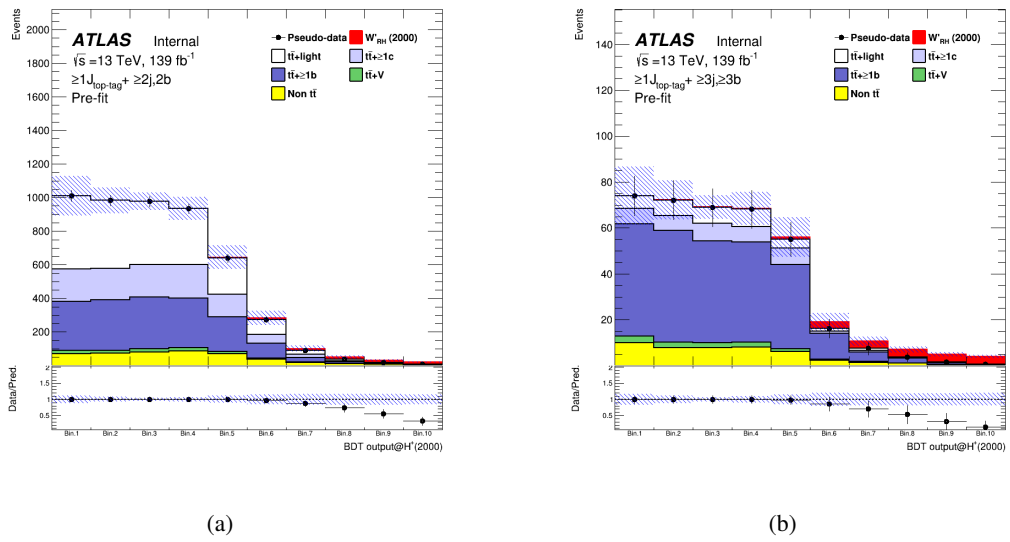


Figure 57: Pre-fit plots in the SR1 (left) and SR2 (right) for 2000 GeV mass hypothesis of W'_R signal.

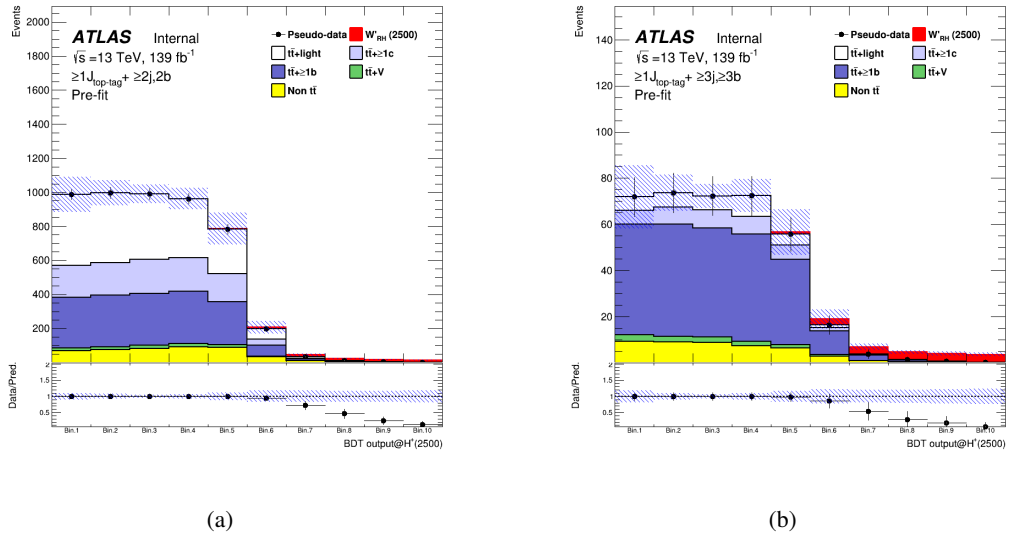


Figure 58: Pre-fit plots in the SR1 (left) and SR2 (right) for 2500 GeV mass hypothesis of W'_R signal.

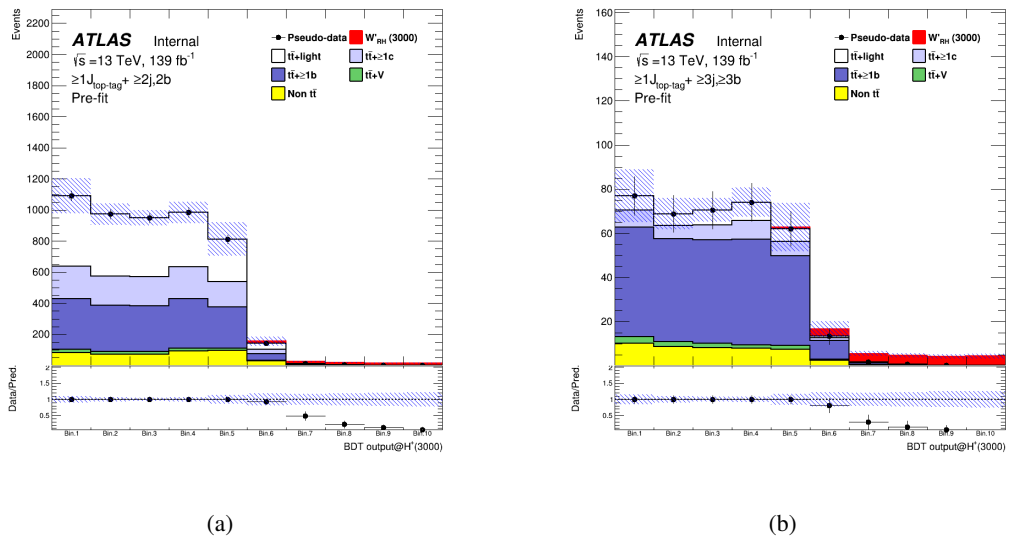


Figure 59: Pre-fit plots in the SR1 (left) and SR2 (right) for 3000 GeV mass hypothesis of W'_R signal.

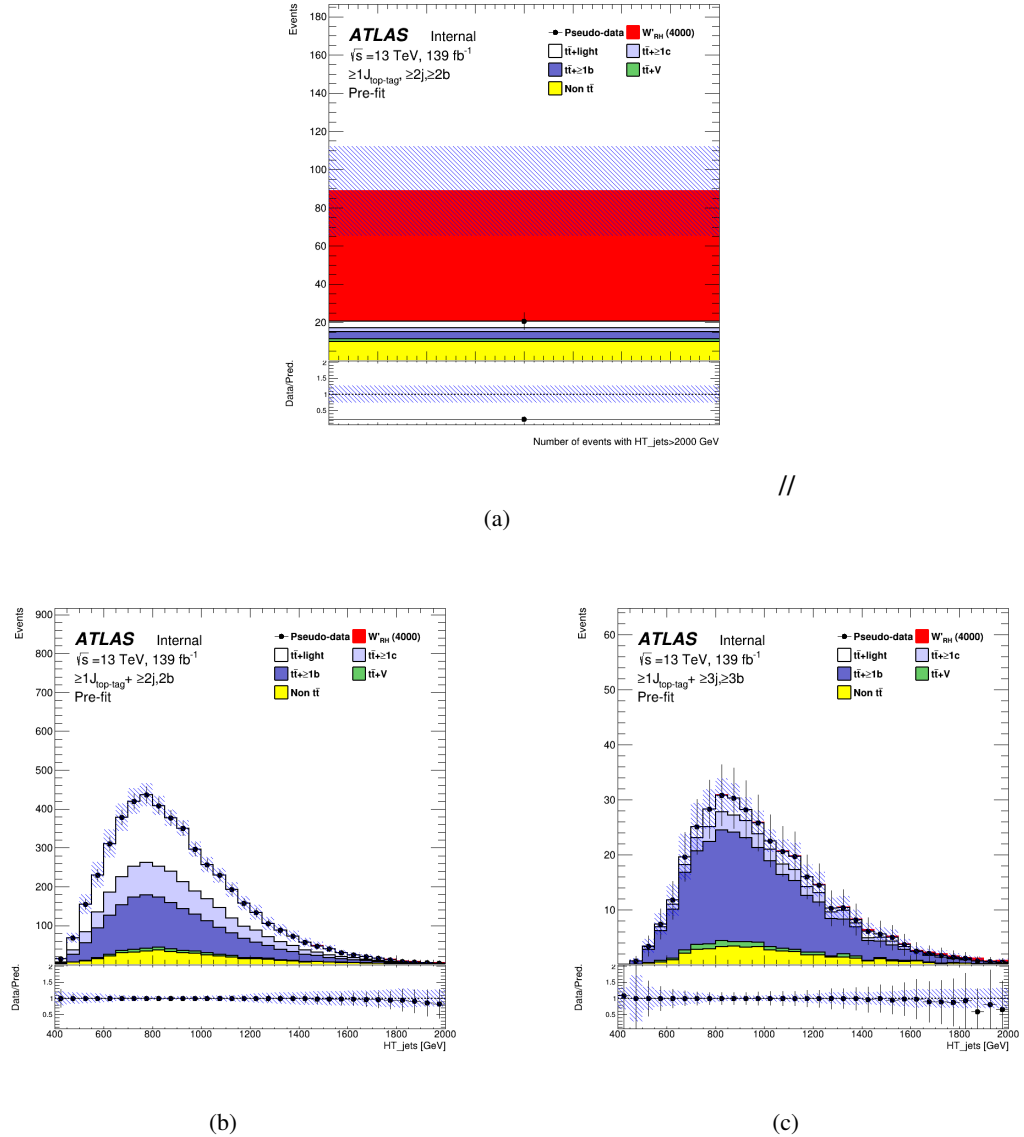


Figure 60: Pre-fit plots in the SR (top), CR1 (bottom-left), and CR2 (bottom-right) for 4000 GeV mass hypothesis of W'_R signal.

7.3.2 Asimov fit results

In the following, the results of the fitting to Asimov datasets are presented. Figures 61 to 80 show the nuisance parameters, normalization factors, correlation matrices, the effect of the different nuisance parameters before and after the fit and post-fit plots from the fits under each H^+ mass hypotheses. Similarly, Figure 81 to 98 and Figure 99 to 116 show the results from the fits under each W'_L and W'_R mass hypotheses, respectively.

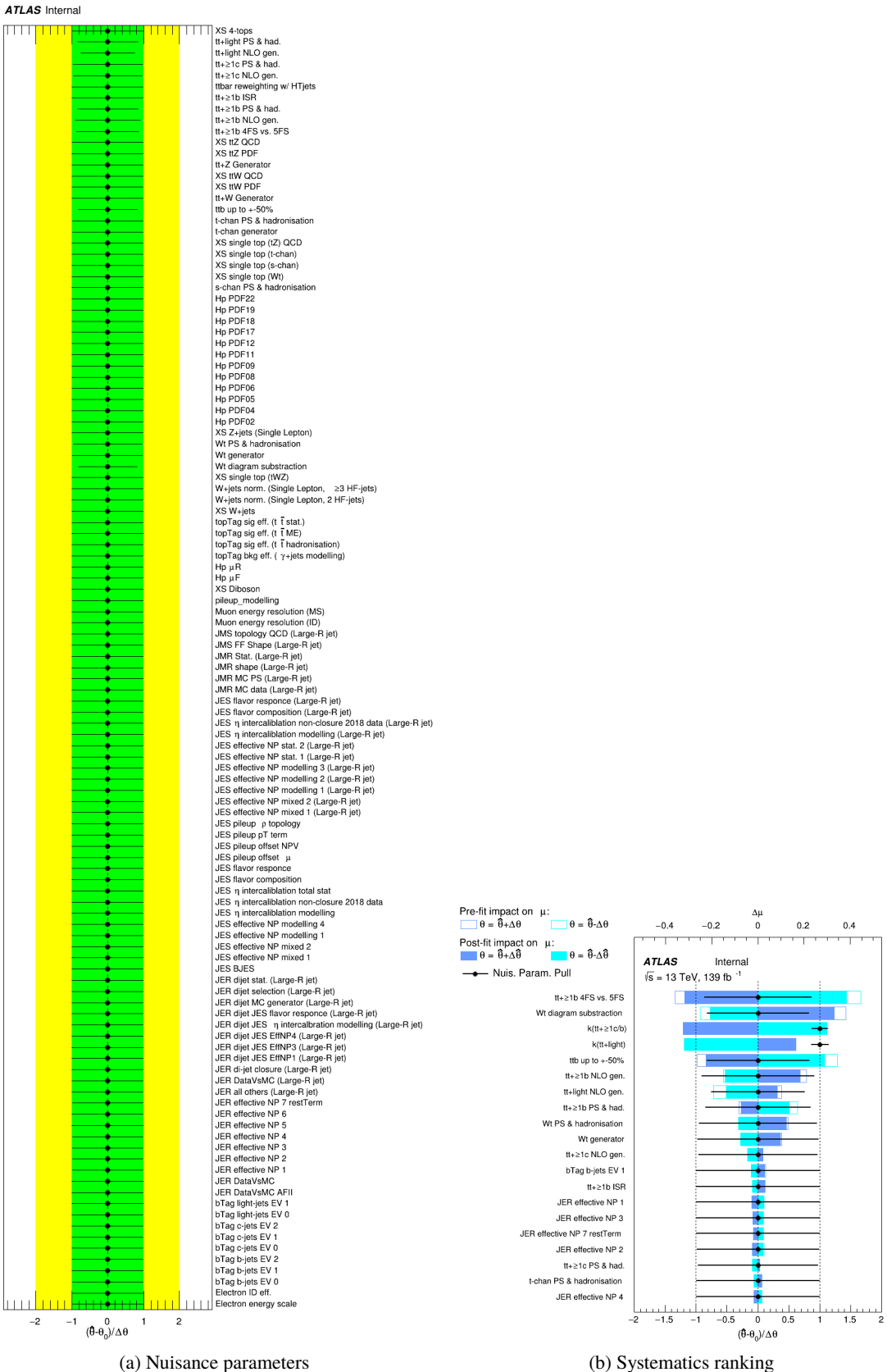
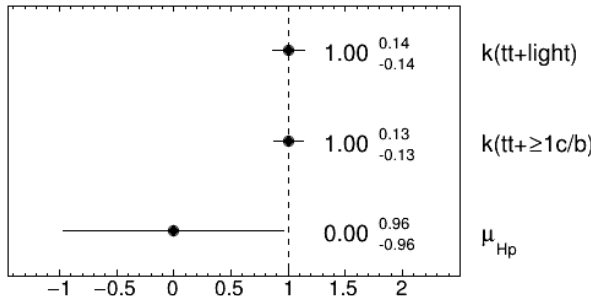
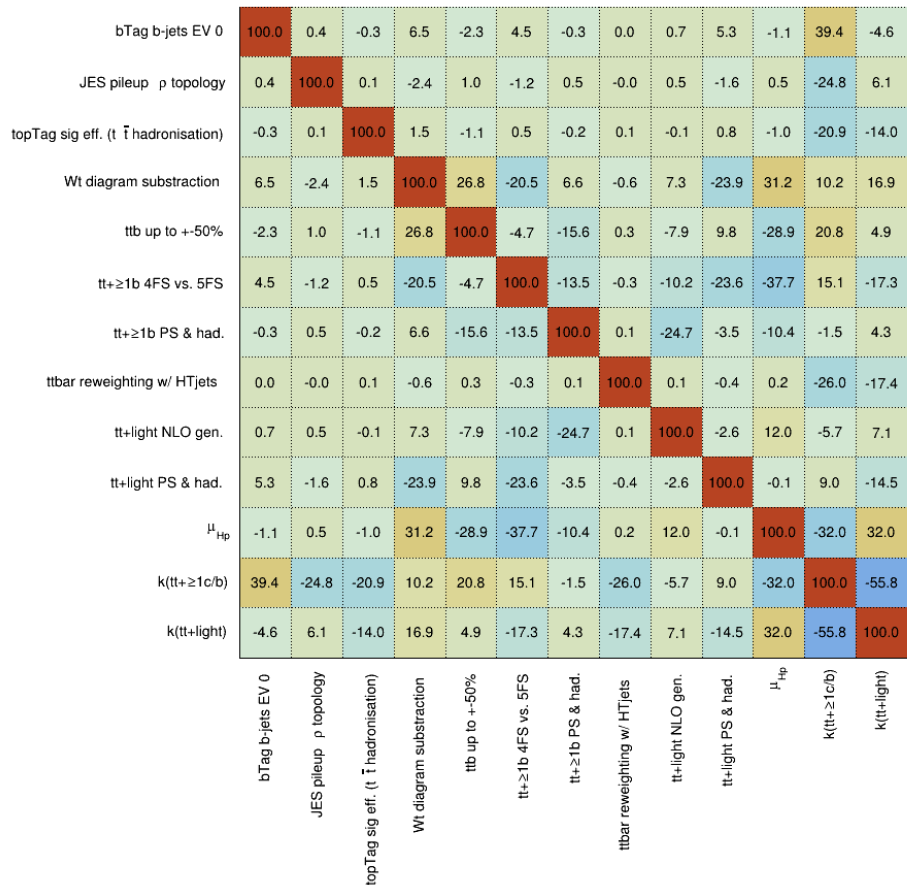


Figure 61: Nuisance parameters (left) and ranking plot (right) of the effect of various nuisance parameters before and after the fit for the 1000 GeV H^+ mass hypotheses.

ATLAS Internal

(a) Norm. factors

ATLAS Internal

(b) Correlation matrix

Figure 62: Signal strength and normalization factors (top) and correlation matrix (bottom) for the 1000 GeV H^+ mass hypotheses.

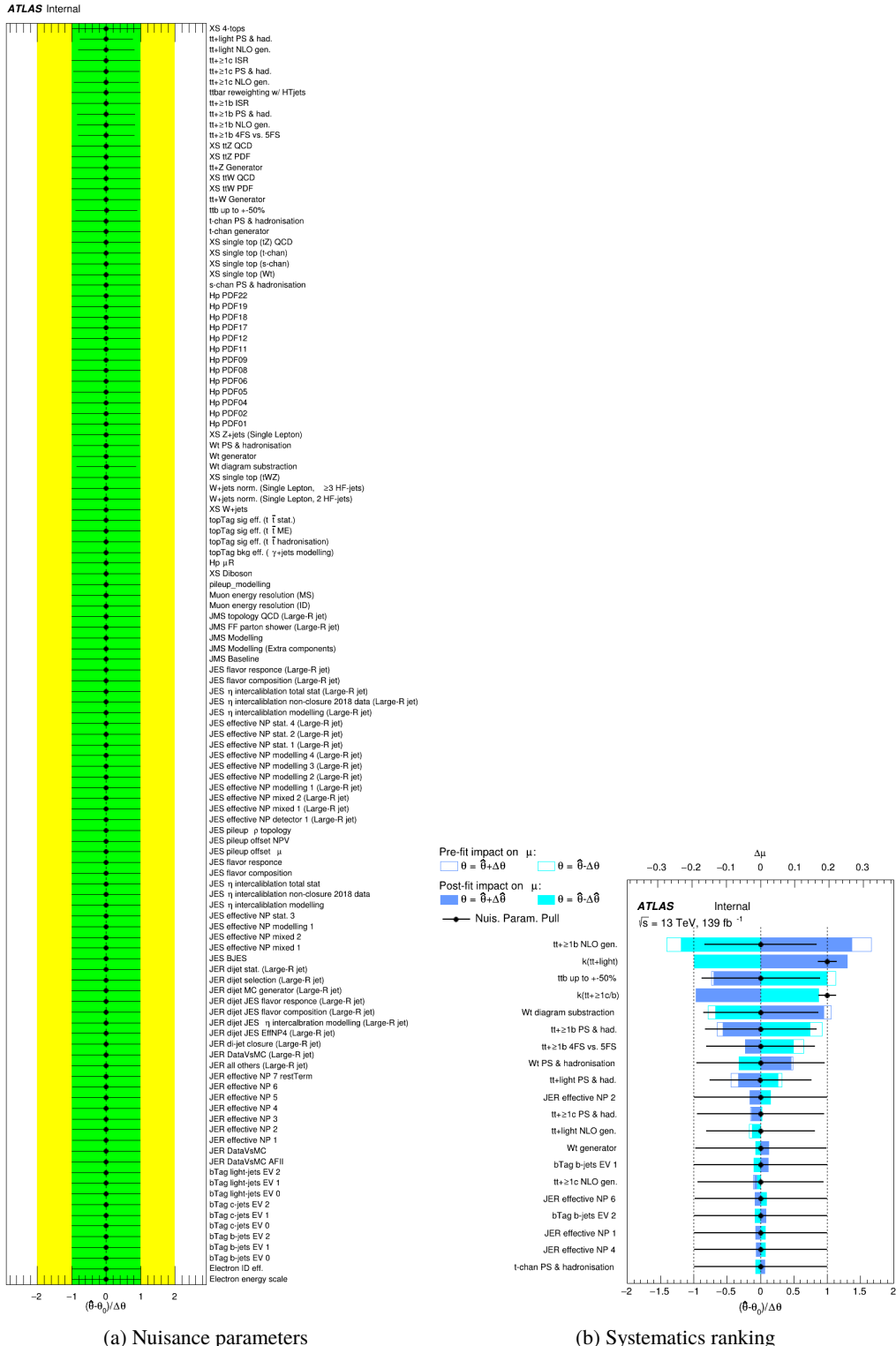
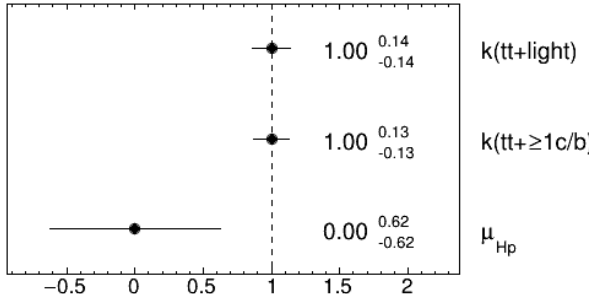


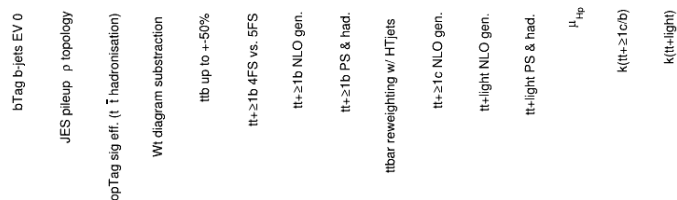
Figure 63: Nuisance parameters (left) and ranking plot (right) of the effect of various nuisance parameters before and after the fit for the 1200 GeV H^+ mass hypotheses.

ATLAS Internal

(a) Norm. factors

ATLAS Internal

bTag b-jets EV 0	100.0	0.6	0.3	2.9	-2.5	3.3	2.0	0.3	-0.1	2.0	1.1	3.9	1.1	39.4	-5.2
JES pileup p topology	0.6	100.0	-0.2	-2.8	2.7	-1.7	-1.5	0.4	0.1	-1.2	-0.4	-3.7	-0.5	-24.5	5.3
topTag sig eff. ($t\bar{t}$ hadronisation)	0.3	-0.2	100.0	-0.3	-1.0	-4.7	-1.2	-1.9	0.0	-2.7	-4.4	-3.2	-1.4	-20.1	-15.4
Wt diagram subtraction	2.9	-2.8	-0.3	100.0	25.8	-8.3	-5.9	4.7	-0.1	-4.4	-2.9	-19.9	27.7	7.2	22.7
ttb up to +50%	-2.5	2.7	-1.0	25.8	100.0	-4.8	4.9	-12.2	-0.2	0.7	-7.3	9.9	-28.8	20.7	7.0
tt+≥1b 4FS vs. 5FS	3.3	-1.7	-4.7	-8.3	-4.8	100.0	-20.6	-31.3	-0.4	-20.4	-24.4	-13.9	-11.4	9.3	-10.1
tt+≥1b NLO gen.	2.0	-1.5	-1.2	-5.9	4.9	-20.6	100.0	-28.8	2.6	-5.1	-2.2	-15.2	41.0	-8.5	2.4
tt+≥1b PS & had.	0.3	0.4	-1.9	4.7	-12.2	-31.3	-28.8	100.0	1.2	-6.8	-13.2	0.4	-20.5	2.2	-0.6
ttbar reweighting w/ HTjets	-0.1	0.1	0.0	-0.1	-0.2	-0.4	2.6	1.2	100.0	-0.4	-0.6	2.1	-1.2	-26.1	-17.2
tt+≥1c NLO gen.	2.0	-1.2	-2.7	-4.4	0.7	-20.4	-5.1	-6.8	-0.4	100.0	-16.0	-11.6	-1.1	5.3	-5.4
tt+light NLO gen.	1.1	-0.4	-4.4	-2.9	-7.3	-24.4	-2.2	-13.2	-0.6	-16.0	100.0	-21.6	1.7	1.5	-1.1
tt+light PS & had.	3.9	-3.7	-3.2	-19.9	9.9	-13.9	-15.2	0.4	2.1	-11.6	-21.6	100.0	-10.0	11.0	-14.5
μ_{H_p}	1.1	-0.5	-1.4	27.7	-28.8	-11.4	41.0	-20.5	-1.2	-1.1	1.7	-10.0	100.0	-28.9	30.4
$k(t\bar{t}+\geq 1c/b)$	39.4	-24.5	-20.1	7.2	20.7	9.3	-8.5	2.2	-26.1	5.3	1.5	11.0	-28.9	100.0	-55.0
$k(t\bar{t}+\text{light})$	-5.2	5.3	-15.4	22.7	7.0	-10.1	2.4	-0.6	-17.2	-5.4	-1.1	-14.5	30.4	-55.0	100.0



(b) Correlation matrix

Figure 64: Signal strength and normalization factors (top) and correlation matrix (bottom) for the 1200 GeV H^+ mass hypotheses.

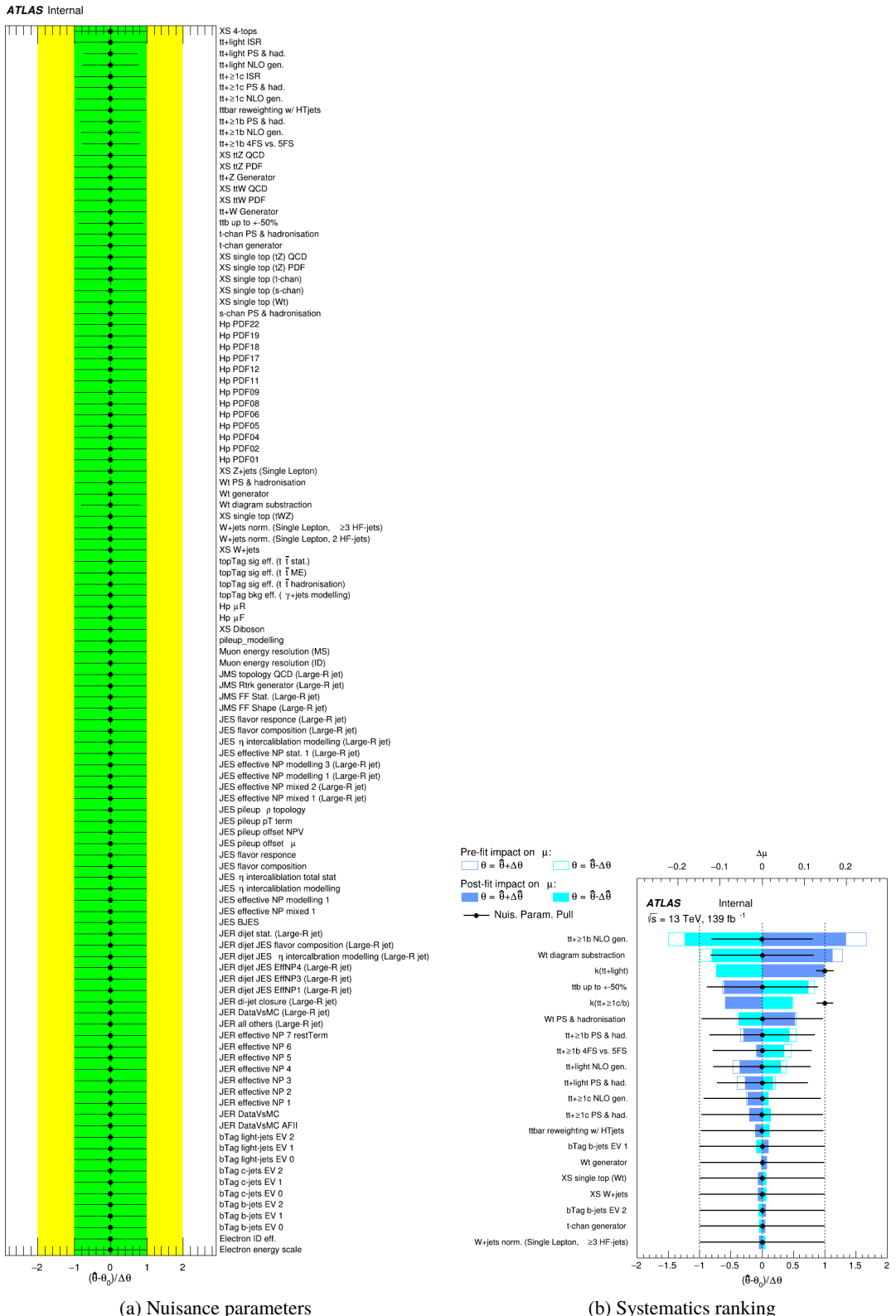
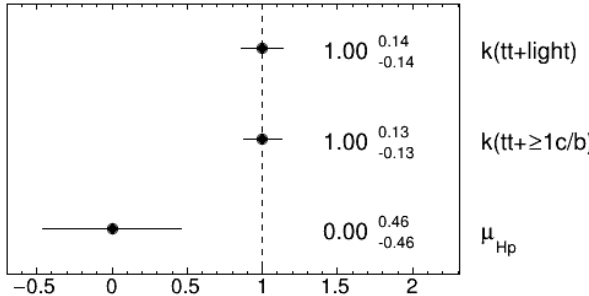


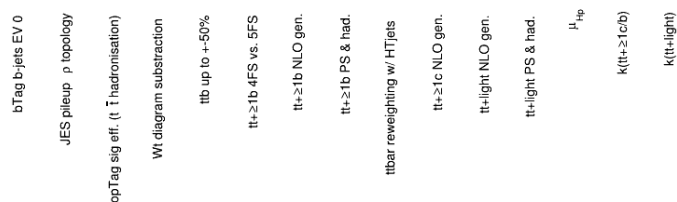
Figure 65: Nuisance parameters (left) and ranking plot (right) of the effect of various nuisance parameters before and after the fit for the 1400 GeV H^+ mass hypotheses.

ATLAS Internal

(a) Norm. factors

ATLAS Internal

bTag b-jets EV 0	100.0	0.2	0.3	2.1	-0.3	2.4	0.4	-0.3	0.0	1.1	1.7	-0.7	1.3	41.0	-6.8
JES pileup ρ topology	0.2	100.0	-0.2	-1.9	0.5	-1.5	0.9	1.2	-0.2	-1.0	-1.8	0.6	-0.9	-25.6	6.6
topTag sig eff. ($t\bar{t}$ hadronisation)	0.3	-0.2	100.0	-0.7	-0.8	-6.5	-3.7	-3.1	0.5	-2.8	-6.3	-2.4	-1.2	-20.4	-16.0
Wt diagram subtraction	2.1	-1.9	-0.7	100.0	21.0	-10.9	-8.2	8.1	4.3	-2.9	-9.0	-12.1	35.0	5.8	18.4
ttb up to +50%	-0.3	0.5	-0.8	21.0	100.0	-7.0	-0.1	-12.8	-3.8	-1.8	3.2	11.9	-24.0	22.6	2.8
tt+≥1b 4FS vs. 5FS	2.4	-1.5	-6.5	-10.9	-7.0	100.0	-31.1	-32.9	-0.5	-23.2	-28.5	12.8	-8.1	8.5	-10.7
tt+≥1b NLO gen.	0.4	0.9	-3.7	-8.2	-0.1	-31.1	100.0	-34.9	7.7	-3.8	-4.2	-11.9	42.2	-8.7	0.2
tt+≥1b PS & had.	-0.3	1.2	-3.1	8.1	-12.8	-32.9	-34.9	100.0	1.6	-7.1	-2.7	3.5	-12.1	-1.1	3.8
ttbar reweighting w/ HTjets	0.0	-0.2	0.5	4.3	-3.8	-0.5	7.7	1.6	100.0	-1.0	4.3	12.0	-3.5	-26.1	-15.7
tt+≥1c NLO gen.	1.1	-1.0	-2.8	-2.9	-1.8	-23.2	-3.8	-7.1	-1.0	100.0	-20.3	5.6	-5.9	5.1	-4.8
tt+light NLO gen.	1.7	-1.8	-6.3	-9.0	3.2	-28.5	-4.2	-2.7	4.3	-20.3	100.0	-43.5	-11.0	8.0	-10.3
tt+light PS & had.	-0.7	0.6	-2.4	-12.1	11.9	12.8	-11.9	3.5	12.0	5.6	-43.5	100.0	-7.5	-2.3	-5.1
μ_{H_p}	1.3	-0.9	-1.2	35.0	-24.0	-8.1	42.2	-12.1	-3.5	-5.9	-11.0	-7.5	100.0	-17.4	24.1
$k(t\bar{t}+\geq 1c/b)$	41.0	-25.6	-20.4	5.8	22.6	8.5	-8.7	-1.1	-26.1	5.1	8.0	-2.3	-17.4	100.0	-56.3
$k(t\bar{t}+\text{light})$	-6.8	6.6	-16.0	18.4	2.8	-10.7	0.2	3.8	-15.7	-4.8	-10.3	-5.1	24.1	-56.3	100.0



(b) Correlation matrix

Figure 66: Signal strength and normalization factors (top) and correlation matrix (bottom) for the 1400 GeV H^+ mass hypotheses.

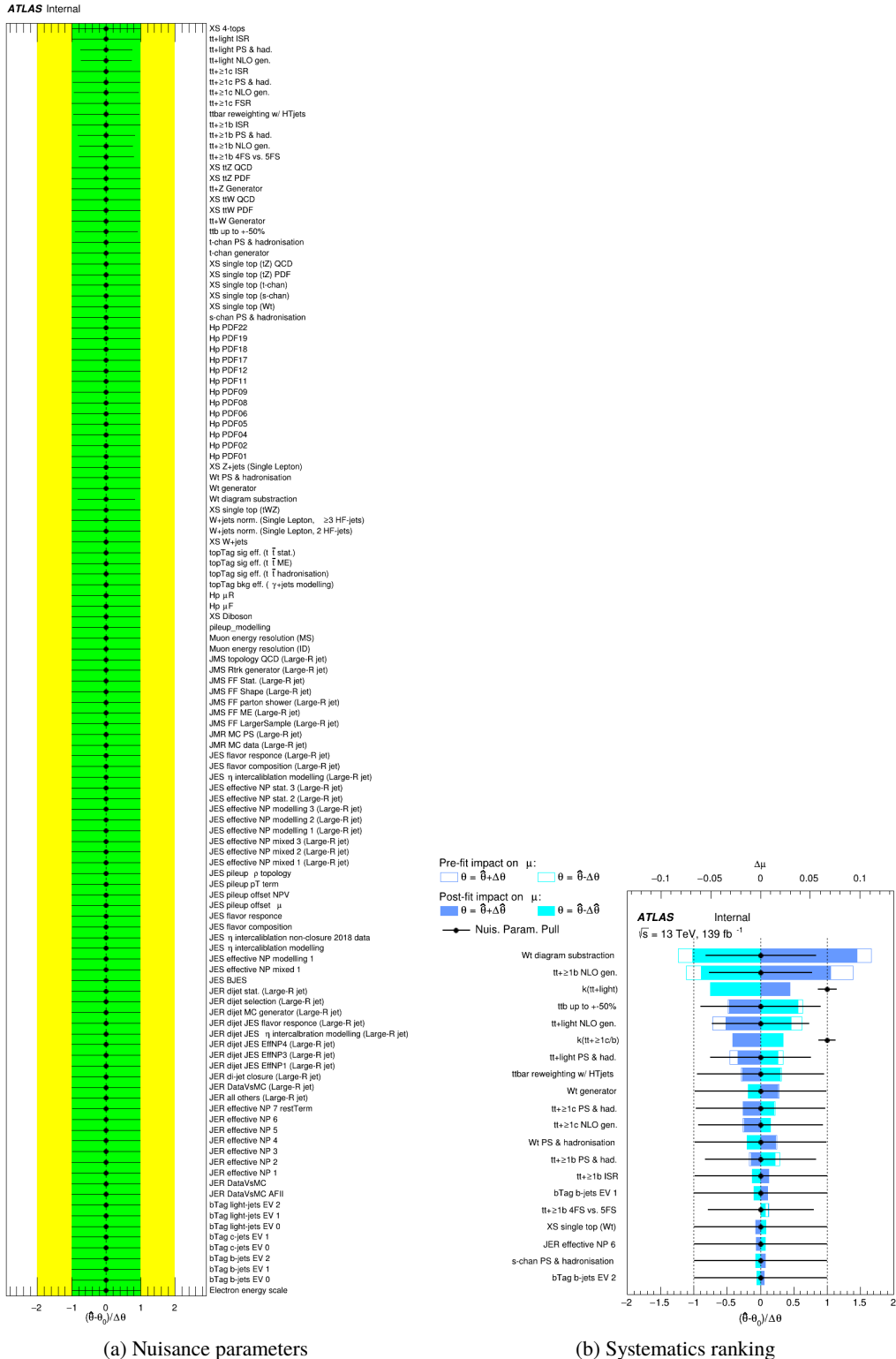
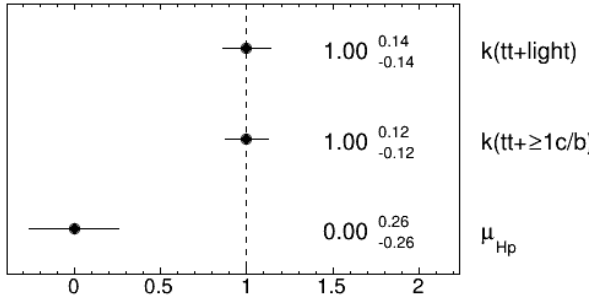


Figure 67: Nuisance parameters (left) and ranking plot (right) of the effect of various nuisance parameters before and after the fit for the 1600 GeV H^+ mass hypotheses.

ATLAS Internal

(a) Norm. factors

ATLAS Internal

bTag b-jets EV 0	100.0	0.1	0.3	0.6	3.2	2.4	2.3	-0.6	0.5	2.0	-0.2	1.0	42.0	-7.5
JES pileup p topology	0.1	100.0	-0.1	-1.4	-0.8	1.2	1.0	0.2	-0.5	-2.3	0.1	-0.6	-26.0	6.7
topTag sig eff. ($t\bar{t}$ hadronisation)	0.3	-0.1	100.0	-1.0	-6.0	-3.7	-3.2	0.9	-2.6	-7.0	-2.1	-0.7	-20.9	-16.0
Wt diagram subtraction	0.6	-1.4	-1.0	100.0	-10.8	-7.1	7.8	9.5	-1.2	-8.0	-14.2	35.4	3.9	20.8
$tt+\geq 1b$ 4FS vs. 5FS	3.2	-0.8	-6.0	-10.8	100.0	-28.1	-39.4	0.3	-12.0	-37.5	12.4	-0.4	6.6	-8.7
$tt+\geq 1b$ NLO gen.	2.4	1.2	-3.7	-7.1	-28.1	100.0	-34.0	15.7	0.8	4.5	-22.7	25.7	-8.7	-0.8
$tt+\geq 1b$ PS & had.	2.3	1.0	-3.2	7.8	-39.4	-34.0	100.0	-1.8	-2.9	-10.0	11.7	-4.9	1.2	2.9
ttbar reweighting w/ HTjets	-0.6	0.2	0.9	9.5	0.3	15.7	-1.8	100.0	-0.8	-2.6	16.3	-7.4	-26.3	-13.2
$tt+\geq 1c$ NLO gen.	0.5	-0.5	-2.6	-1.2	-12.0	0.8	-2.9	-0.8	100.0	-32.2	-11.1	-5.6	2.8	-2.2
$tt+\text{light}$ NLO gen.	2.0	-2.3	-7.0	-8.0	-37.5	4.5	-10.0	-2.6	-32.2	100.0	-18.3	-13.2	10.9	-10.7
$tt+\text{light}$ PS & had.	-0.2	0.1	-2.1	-14.2	12.4	-22.7	11.7	16.3	-11.1	-18.3	100.0	-8.1	-4.7	-5.9
μ_{H_p}	1.0	-0.6	-0.7	35.4	-0.4	25.7	-4.9	-7.4	-5.6	-13.2	-8.1	100.0	-9.7	20.9
$k(tt+\geq 1c/b)$	42.0	-26.0	-20.9	3.9	6.6	-8.7	1.2	-26.3	2.8	10.9	-4.7	-9.7	100.0	-56.3
$k(tt+\text{light})$	-7.5	6.7	-16.0	20.8	-8.7	-0.8	2.9	-13.2	-2.2	-10.7	-5.9	20.9	-56.3	100.0

(b) Correlation matrix

Figure 68: Signal strength and normalization factors (top) and correlation matrix (bottom) for the 1600 GeV H^+ mass hypotheses.

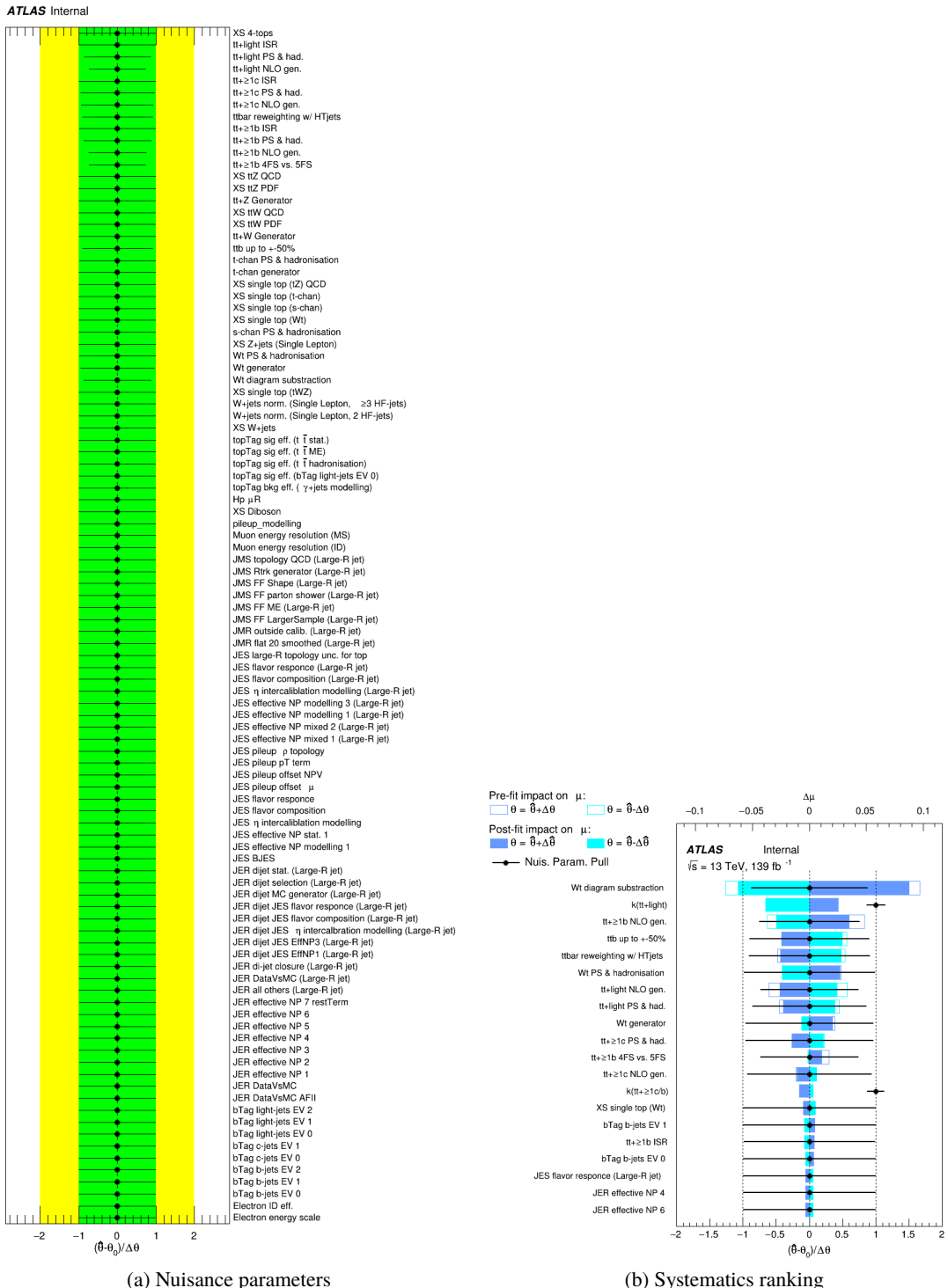
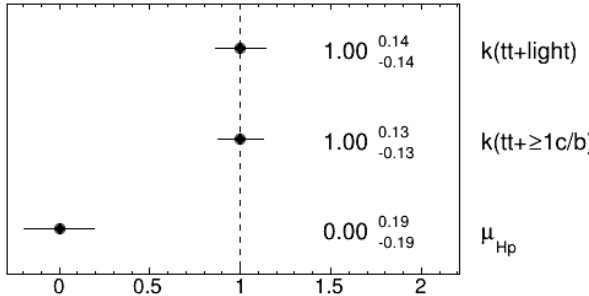


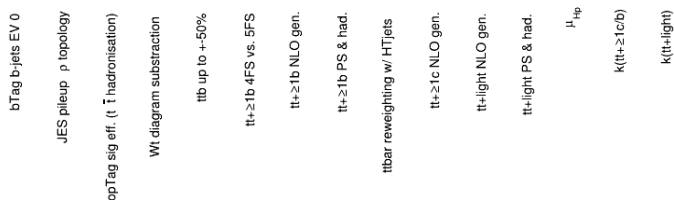
Figure 69: Nuisance parameters (left) and ranking plot (right) of the effect of various nuisance parameters before and after the fit for the 1800 GeV H^+ mass hypotheses.

ATLAS Internal

(a) Norm. factors

ATLAS Internal

bTag b-jets EV 0	100.0	0.1	0.3	-0.0	0.8	3.5	2.0	1.8	-0.5	0.9	1.3	0.0	1.9	42.1	-7.7
JES pileup p topology	0.1	100.0	-0.1	0.4	-0.4	-0.5	1.1	0.6	-0.4	-0.8	-1.5	0.1	-1.0	-26.2	7.6
topTag sig eff. ($t\bar{t}$ hadronisation)	0.3	-0.1	100.0	-0.4	-0.4	-7.1	-2.7	-2.6	0.3	-2.7	-6.3	-1.3	-0.8	-21.0	-15.4
Wt diagram subtraction	-0.0	0.4	-0.4	100.0	13.6	-1.9	-5.4	4.4	14.7	-4.8	-8.9	-12.7	40.8	0.3	23.5
ttb up to +50%	0.8	-0.4	-0.4	13.6	100.0	-6.8	-2.7	-8.0	-10.8	1.9	1.4	6.4	-15.3	23.7	1.3
tt+≥1b 4FS vs. 5FS	3.5	-0.5	-7.1	-1.9	-6.8	100.0	-27.0	-31.5	-2.9	-18.0	-35.9	7.3	3.5	5.4	-3.9
tt+≥1b NLO gen.	2.0	1.1	-2.7	-5.4	-2.7	-27.0	100.0	-38.7	17.0	2.5	-0.7	-14.3	16.8	-7.3	-1.7
tt+≥1b PS & had.	1.8	0.6	-2.6	4.4	-8.0	-31.5	-38.7	100.0	1.1	0.6	-2.6	-0.5	-0.5	-1.4	2.9
ttbar reweighting w/ HTjets	-0.5	-0.4	0.3	14.7	-10.8	-2.9	17.0	1.1	100.0	1.6	-3.6	10.5	-13.7	-25.2	-9.4
tt+≥1c NLO gen.	0.9	-0.8	-2.7	-4.8	1.9	-18.0	2.5	0.6	1.6	100.0	-30.2	-8.8	-5.0	4.2	-6.2
tt+light NLO gen.	1.3	-1.5	-6.3	-8.9	1.4	-35.9	-0.7	-2.6	-3.6	-30.2	100.0	-31.6	-13.6	9.0	-10.1
tt+light PS & had.	0.0	0.1	-1.3	-12.7	6.4	7.3	-14.3	-0.5	10.5	-8.8	-31.6	100.0	-12.2	-0.3	-8.3
μ_{H_p}	1.9	-1.0	-0.8	40.8	-15.3	3.5	16.8	-0.5	-13.7	-5.0	-13.6	-12.2	100.0	-3.7	22.0
$k_{(tt+≥1c/b)}$	42.1	-26.2	-21.0	0.3	23.7	5.4	-7.3	-1.4	-25.2	4.2	9.0	-0.3	-3.7	100.0	-58.2
$k_{(tt+light)}$	-7.7	7.6	-15.4	23.5	1.3	-3.9	-1.7	2.9	-9.4	-6.2	-10.1	-8.3	22.0	-58.2	100.0



(b) Correlation matrix

Figure 70: Signal strength and normalization factors (top) and correlation matrix (bottom) for the 1800 GeV H^+ mass hypotheses.

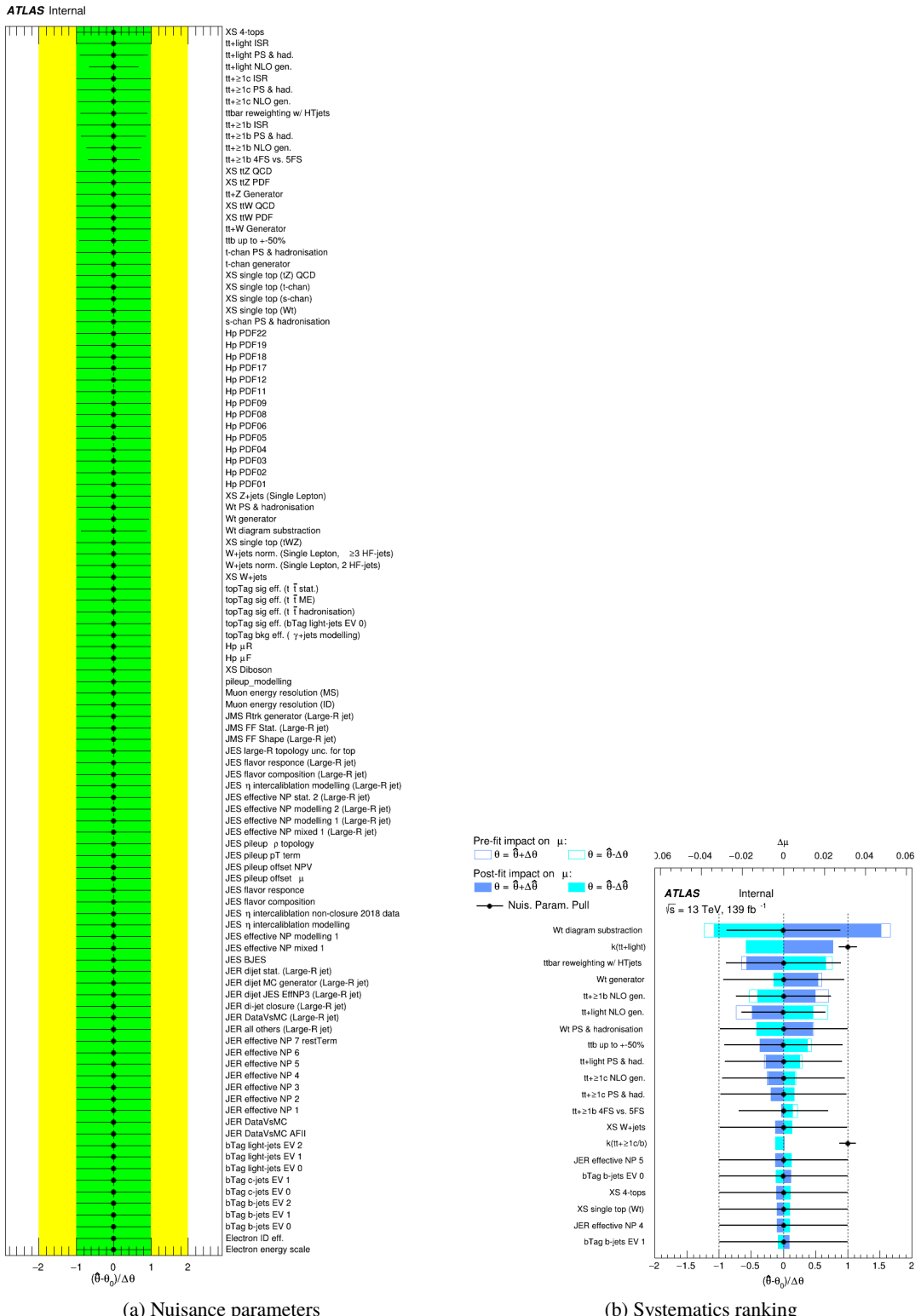
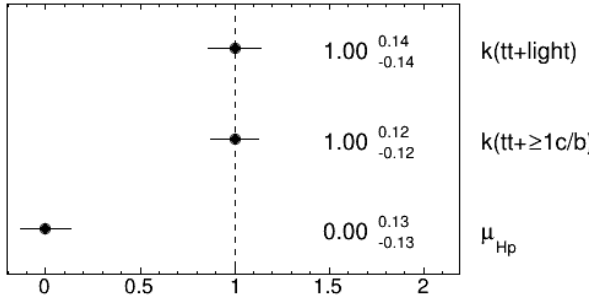


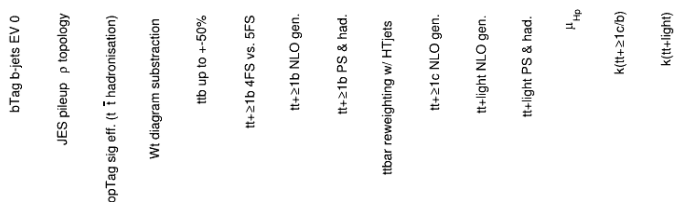
Figure 71: Nuisance parameters (left) and ranking plot (right) of the effect of various nuisance parameters before and after the fit for the 2000 GeV H^+ mass hypotheses.

ATLAS Internal

(a) Norm. factors

ATLAS Internal

bTag b-jets EV 0	100.0	-0.0	0.3	-0.2	0.7	3.0	2.0	1.5	0.2	0.6	2.1	0.2	2.7	42.4	-7.9
JES pileup ρ topology	-0.0	100.0	0.2	-0.0	-0.3	2.6	-0.1	0.9	0.5	-0.1	1.2	-0.3	-1.2	-27.2	7.8
topTag sig eff. ($t\bar{t}$ hadronisation)	0.3	0.2	100.0	-0.6	0.8	-7.8	-2.4	-2.8	0.1	-1.2	-6.5	-1.1	-1.0	-20.9	-15.6
Wt diagram subtraction	-0.2	-0.0	-0.6	100.0	6.4	-3.3	-4.5	4.9	18.7	-8.4	-11.1	-7.7	32.9	-0.8	22.0
ttb up to +50%	0.7	-0.3	0.8	6.4	100.0	2.0	-4.6	-6.0	-10.6	0.2	-0.3	4.6	-9.5	22.0	-1.5
$t\bar{t}+\geq 1\text{b}$ 4FS vs. 5FS	3.0	2.6	-7.8	-3.3	2.0	100.0	-27.9	-42.5	-6.9	-6.7	-37.9	5.0	-2.4	8.3	-4.7
$t\bar{t}+\geq 1\text{b}$ NLO gen.	2.0	-0.1	-2.4	-4.5	-4.6	-27.9	100.0	-38.1	21.0	-7.9	-0.7	-8.2	10.6	-7.4	-2.5
$t\bar{t}+\geq 1\text{b}$ PS & had.	1.5	0.9	-2.8	4.9	-6.0	-42.5	-38.1	100.0	-1.3	-2.3	-2.1	1.8	1.6	-0.5	3.8
ttbar reweighting w/ HTjets	0.2	0.5	0.1	18.7	-10.6	-6.9	21.0	-1.3	100.0	8.0	-3.6	11.5	-14.5	-23.8	-8.1
$t\bar{t}+\geq 1\text{c}$ NLO gen.	0.6	-0.1	-1.2	-8.4	0.2	-6.7	-7.9	-2.3	8.0	100.0	-20.9	-10.7	-5.3	-0.6	-5.8
$t\bar{t}+\text{light}$ NLO gen.	2.1	1.2	-6.5	-11.1	-0.3	-37.9	-0.7	-2.1	-3.6	-20.9	100.0	-29.0	-11.4	11.3	-13.9
$t\bar{t}+\text{light}$ PS & had.	0.2	-0.3	-1.1	-7.7	4.6	5.0	-8.2	1.8	11.5	-10.7	-29.0	100.0	-6.3	-1.2	-6.1
μ_{H_p}	2.7	-1.2	-1.0	32.9	-9.5	-2.4	10.6	1.6	-14.5	-5.3	-11.4	-6.3	100.0	2.1	15.6
$k(t\bar{t}+\geq 1\text{c}/b)$	42.4	-27.2	-20.9	-0.8	22.0	8.3	-7.4	-0.5	-23.8	-0.6	11.3	-1.2	2.1	100.0	-59.5
$k(t\bar{t}+\text{light})$	-7.9	7.8	-15.6	22.0	-1.5	-4.7	-2.5	3.8	-8.1	-5.8	-13.9	-6.1	15.6	-59.5	100.0



(b) Correlation matrix

Figure 72: Signal strength and normalization factors (top) and correlation matrix (bottom) for the 2000 GeV H^+ mass hypotheses.

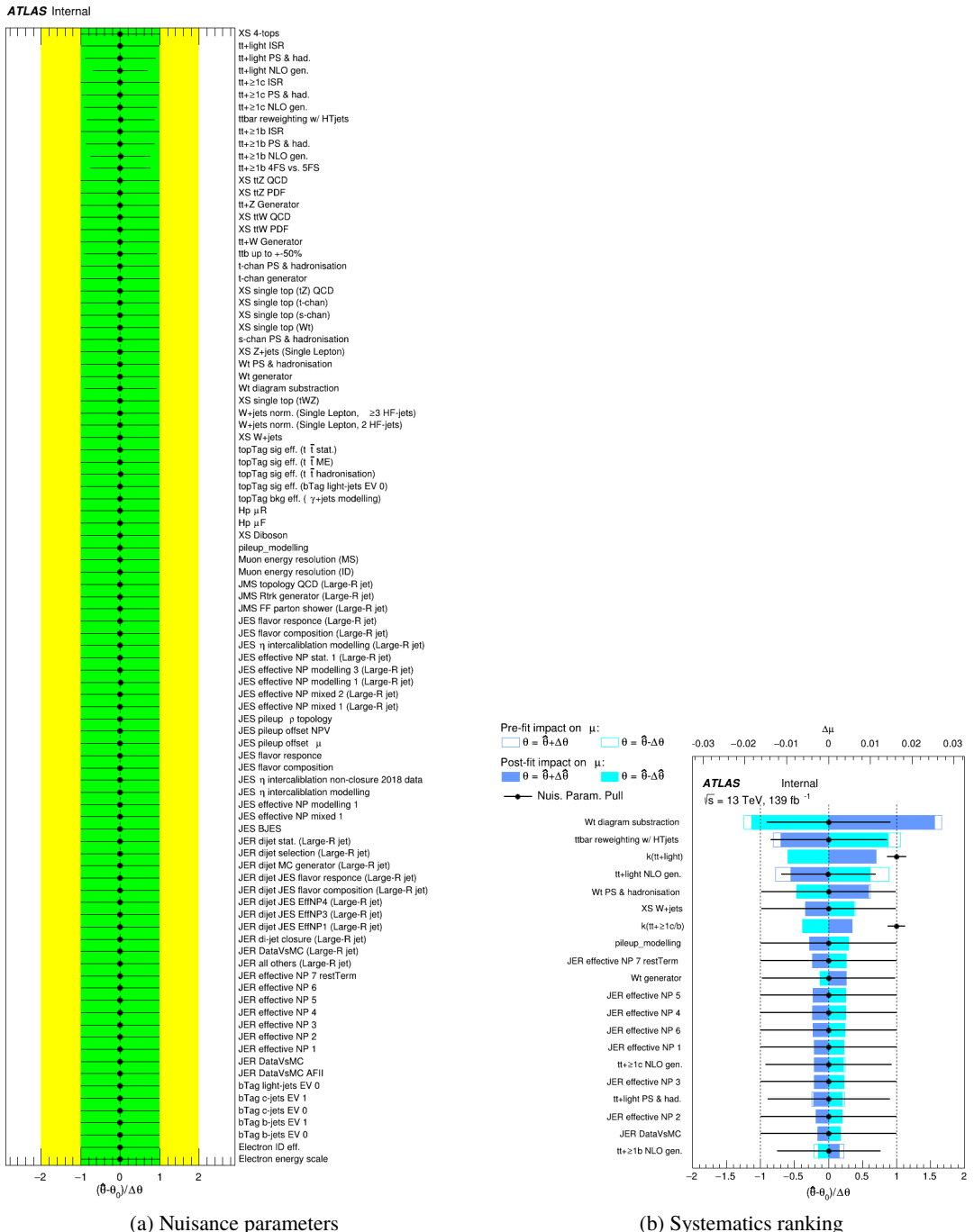
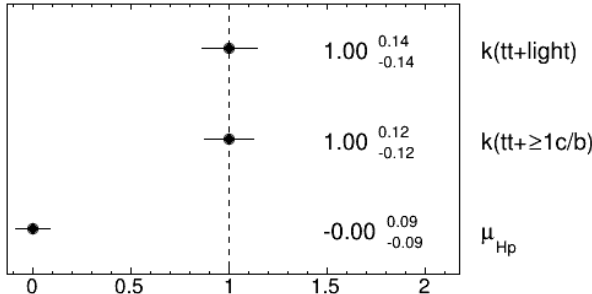


Figure 73: Nuisance parameters (left) and ranking plot (right) of the effect of various nuisance parameters before and after the fit for the 2500 GeV H^+ mass hypotheses.

ATLAS Internal

(a) Norm. factors

ATLAS Internal

bTag b-jets EV 0	100.0	-0.0	0.2	-0.3	0.8	2.6	1.4	1.5	0.9	0.6	2.0	2.2	42.2	-8.3
JES pileup ρ topology	-0.0	100.0	0.2	0.0	0.2	2.0	-0.2	0.6	0.8	-0.5	0.8	-1.0	-27.1	7.7
topTag sig eff. ($t\bar{t}$ hadronisation)	0.2	0.2	100.0	-0.9	-0.5	-6.8	-1.7	-2.5	-0.5	-1.1	-6.7	-1.0	-21.0	-15.3
Wt diagram subtraction	-0.3	0.0	-0.9	100.0	6.1	-6.4	-1.8	2.0	14.4	-6.2	-18.0	28.7	1.3	24.0
ttb up to $\pm 50\%$	0.8	0.2	-0.5	6.1	100.0	-6.5	1.5	-6.9	-14.0	0.2	2.7	0.9	22.6	0.2
$t\bar{t}+\geq 1\text{b}$ 4FS vs. 5FS	2.6	2.0	-6.8	-6.4	-6.5	100.0	-33.9	-38.5	-7.4	-6.0	-39.8	-2.4	4.2	-2.4
$t\bar{t}+\geq 1\text{b}$ NLO gen.	1.4	-0.2	-1.7	-1.8	1.5	-33.9	100.0	-37.5	24.8	-8.0	5.4	2.9	-6.8	-3.2
$t\bar{t}+\geq 1\text{b}$ PS & had.	1.5	0.6	-2.5	2.0	-6.9	-38.5	-37.5	100.0	-0.4	-1.8	0.3	0.1	-0.8	2.2
ttbar reweighting w/ HTjets	0.9	0.8	-0.5	14.4	-14.0	-7.4	24.8	-0.4	100.0	9.1	7.0	-14.7	-23.2	-7.8
$t\bar{t}+\geq 1\text{c}$ NLO gen.	0.6	-0.5	-1.1	-6.2	0.2	-6.0	-8.0	-1.8	9.1	100.0	-29.0	-4.3	0.2	-6.2
$t\bar{t}+\text{light}$ NLO gen.	2.0	0.8	-6.7	-18.0	2.7	-39.8	5.4	0.3	7.0	-29.0	100.0	-11.4	8.1	-16.7
μ_{H_p}	2.2	-1.0	-1.0	28.7	0.9	-2.4	2.9	0.1	-14.7	-4.3	-11.4	100.0	6.9	13.2
k($t\bar{t}+\geq 1\text{c}/b$)	42.2	-27.1	-21.0	1.3	22.6	4.2	-6.8	-0.8	-23.2	0.2	8.1	6.9	100.0	-59.2
k($t\bar{t}+\text{light}$)	-8.3	7.7	-15.3	24.0	0.2	-2.4	-3.2	2.2	-7.8	-6.2	-16.7	13.2	-59.2	100.0

(b) Correlation matrix

Figure 74: Signal strength and normalization factors (top) and correlation matrix (bottom) for the 2500 GeV H^+ mass hypotheses.

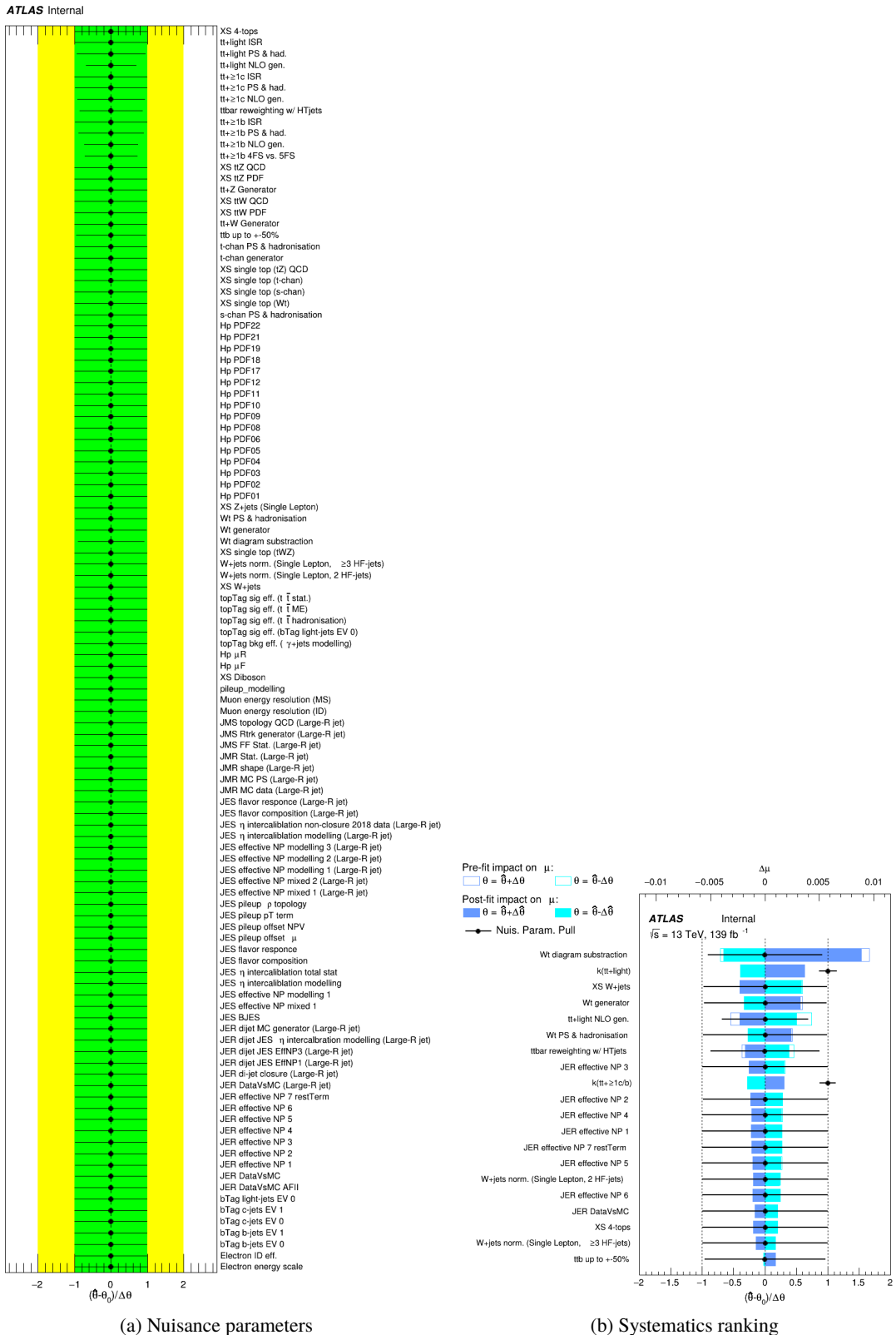
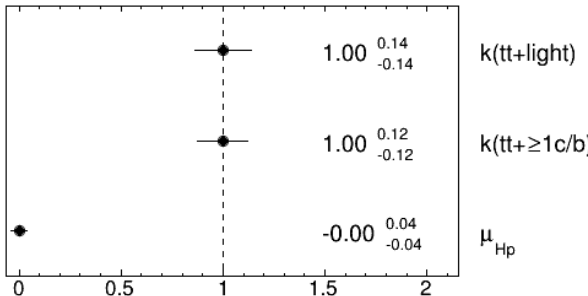


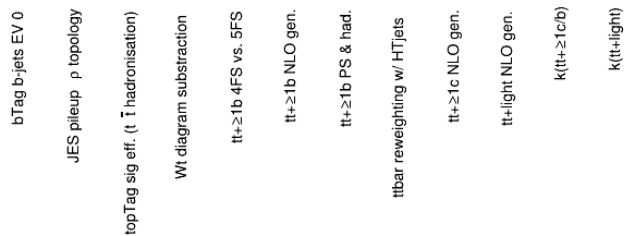
Figure 75: Nuisance parameters (left) and ranking plot (right) of the effect of various nuisance parameters before and after the fit for the 3000 GeV H^+ mass hypotheses.

ATLAS Internal

(a) Norm. factors

ATLAS Internal

bTag b-jets EV 0	100.0	0.0	0.2	-0.4	2.1	1.4	1.4	0.8	0.0	2.3	42.4	-8.3
JES pileup p topology	0.0	100.0	-0.0	-0.4	0.2	0.3	0.3	0.4	-0.5	-1.2	-27.1	7.5
topTag sig eff. ($t\bar{t}$ hadronisation)	0.2	-0.0	100.0	-0.3	-5.7	-2.4	-2.2	0.6	-1.5	-4.8	-21.5	-15.1
Wt diagram subtraction	-0.4	-0.4	-0.3	100.0	-3.1	-2.0	1.4	11.2	-6.7	-13.8	2.0	23.0
$tt+\geq 1b$ 4FS vs. 5FS	2.1	0.2	-5.7	-3.1	100.0	-34.4	-35.2	-4.4	-8.5	-37.7	5.0	-2.2
$tt+\geq 1b$ NLO gen.	1.4	0.3	-2.4	-2.0	-34.4	100.0	-33.4	24.6	-2.1	1.4	-8.3	-2.2
$tt+\geq 1b$ PS & had.	1.4	0.3	-2.2	1.4	-35.2	-33.4	100.0	-1.1	2.7	-5.6	0.9	1.1
ttbar reweighting w/ HTjets	0.8	0.4	0.6	11.2	-4.4	24.6	-1.1	100.0	15.8	11.4	-21.4	-10.4
$tt+\geq 1c$ NLO gen.	0.0	-0.5	-1.5	-6.7	-8.5	-2.1	2.7	15.8	100.0	-33.7	-2.0	-7.3
$tt+\text{light}$ NLO gen.	2.3	-1.2	-4.8	-13.8	-37.7	1.4	-5.6	11.4	-33.7	100.0	8.1	-17.4
$k(tt+\geq 1c/b)$	42.4	-27.1	-21.5	2.0	5.0	-8.3	0.9	-21.4	-2.0	8.1	100.0	-59.5
$k(tt+\text{light})$	-8.3	7.5	-15.1	23.0	-2.2	-2.2	1.1	-10.4	-7.3	-17.4	-59.5	100.0



(b) Correlation matrix

Figure 76: Signal strength and normalization factors (top) and correlation matrix (bottom) for the 3000 GeV H^+ mass hypotheses.

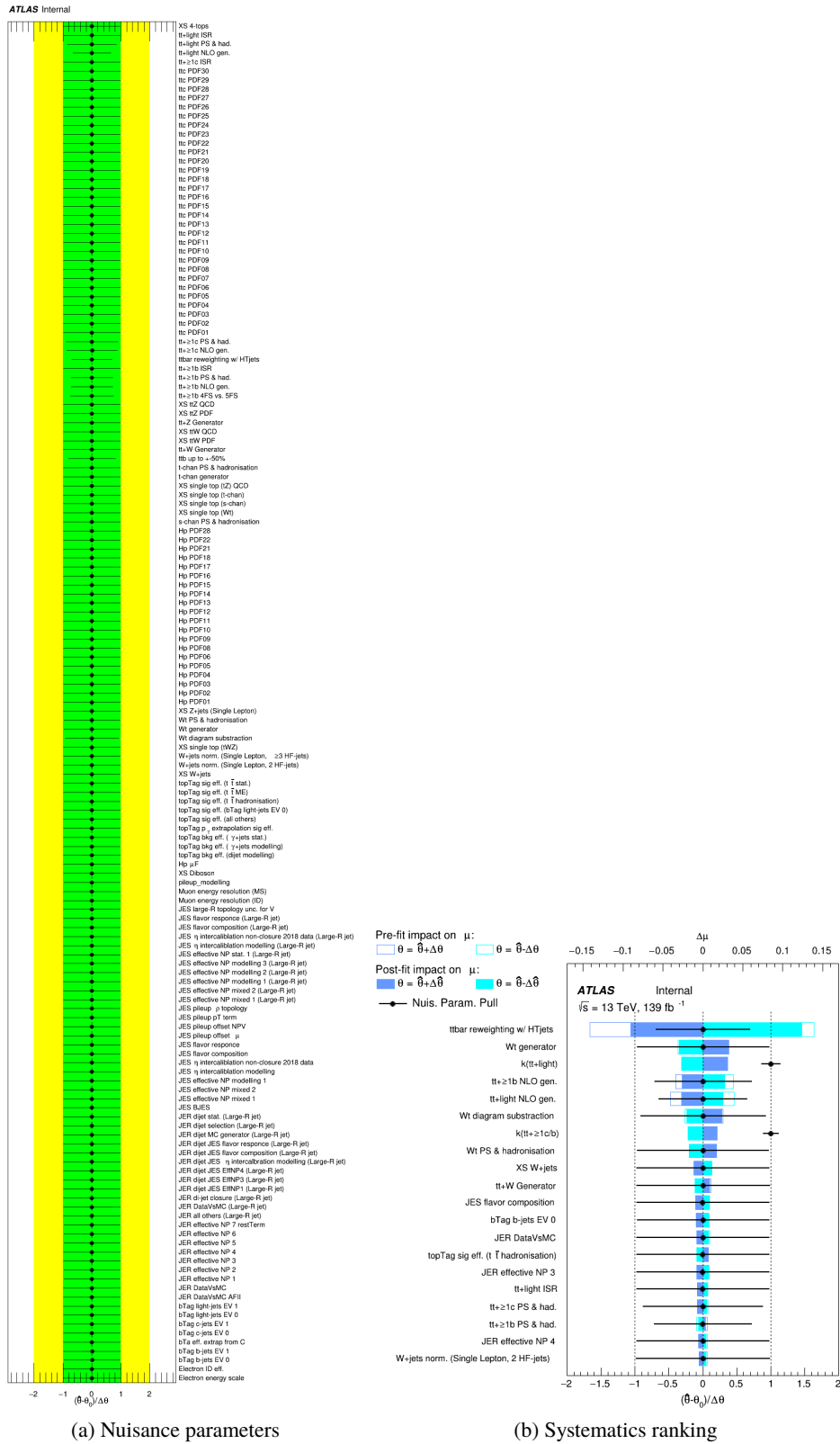
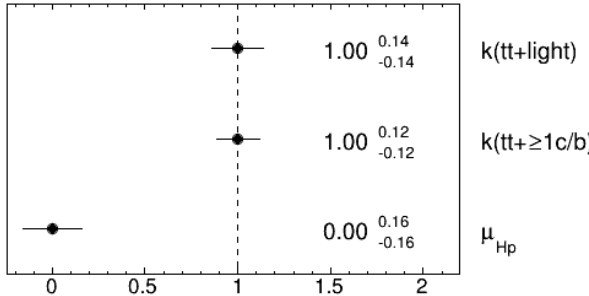


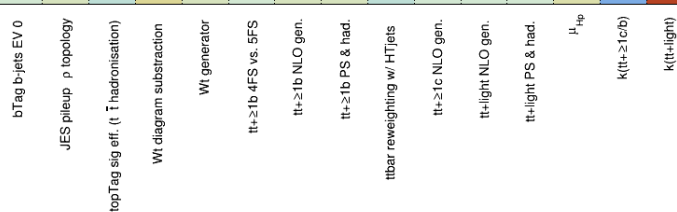
Figure 77: Nuisance parameters (left) and ranking plot (right) of the effect of various nuisance parameters before and after the fit for the 4000 GeV H^+ mass hypotheses.

ATLAS Internal

(a) Norm. factors

ATLAS Internal

bTag b-jets EV 0	100.0	0.1	1.3	0.7	0.3	6.9	-1.1	4.7	6.4	4.6	0.1	1.0	4.5	41.4	-6.7
JES pileup ρ topology	0.1	100.0	0.6	0.0	0.1	2.9	1.0	0.4	-0.4	0.7	-1.1	0.4	-2.2	-27.4	6.8
topTag sig eff. ($t\bar{t}$ hadronisation)	1.3	0.6	100.0	-1.1	-0.4	-8.7	-1.5	-3.6	-2.3	-4.6	-3.2	-3.3	4.3	-21.2	-15.5
Wt diagram subtraction	0.7	0.0	-1.1	100.0	-3.1	-3.5	-3.9	2.2	5.2	-9.0	-15.9	-6.3	15.3	4.6	27.3
Wt generator	0.3	0.1	-0.4	-3.1	100.0	-0.4	0.2	1.4	0.7	-2.6	-8.3	-2.1	21.1	-3.6	5.9
$t\bar{t}+\geq 1\text{b}$ 4FS vs. 5FS	6.9	2.9	-8.7	-3.5	-0.4	100.0	-23.2	-36.4	-2.2	-22.4	5.7	-12.1	1.9	8.0	-5.0
$t\bar{t}+\geq 1\text{b}$ NLO gen.	-1.1	1.0	-1.5	-3.9	0.2	-23.2	100.0	-45.0	18.1	-3.5	-13.6	-6.1	-16.9	-9.9	2.0
$t\bar{t}+\geq 1\text{b}$ PS & had.	4.7	0.4	-3.6	2.2	1.4	-36.4	-45.0	100.0	-3.6	-6.6	3.8	4.9	3.0	0.9	2.7
ttbar reweighting w/ HTjets	6.4	-0.4	-2.3	5.2	0.7	-2.2	18.1	-3.6	100.0	-2.9	11.2	-2.7	-75.9	-9.4	-13.5
$t\bar{t}+\geq 1\text{c}$ NLO gen.	4.6	0.7	-4.6	-9.0	-2.6	-22.4	-3.5	-6.6	-2.9	100.0	-21.0	-11.5	0.9	7.1	-5.9
$t\bar{t}+\text{light}$ NLO gen.	0.1	-1.1	-3.2	-15.9	-8.3	5.7	-13.6	3.8	11.2	-21.0	100.0	-53.8	-16.1	0.2	-9.1
$t\bar{t}+\text{light}$ PS & had.	1.0	0.4	-3.3	-6.3	-2.1	-12.1	-6.1	4.9	-2.7	-11.5	-53.8	100.0	-0.9	3.6	-4.5
μ_{H_p}	-4.5	-2.2	4.3	15.3	21.1	1.9	-16.9	3.0	-75.9	0.9	-16.1	-0.9	100.0	11.6	17.9
$k(t\bar{t}+\geq 1\text{c}/b)$	41.4	-27.4	-21.2	4.6	-3.6	8.0	-9.9	0.9	-9.4	7.1	0.2	3.6	11.6	100.0	-58.8
$k(t\bar{t}+\text{light})$	-6.7	6.8	-15.5	27.3	5.9	-5.0	2.0	2.7	-13.5	-5.9	-9.1	-4.5	17.9	-58.8	100.0



(b) Correlation matrix

Figure 78: Signal strength and normalization factors (top) and correlation matrix (bottom) for the 4000 GeV H^+ mass hypotheses.

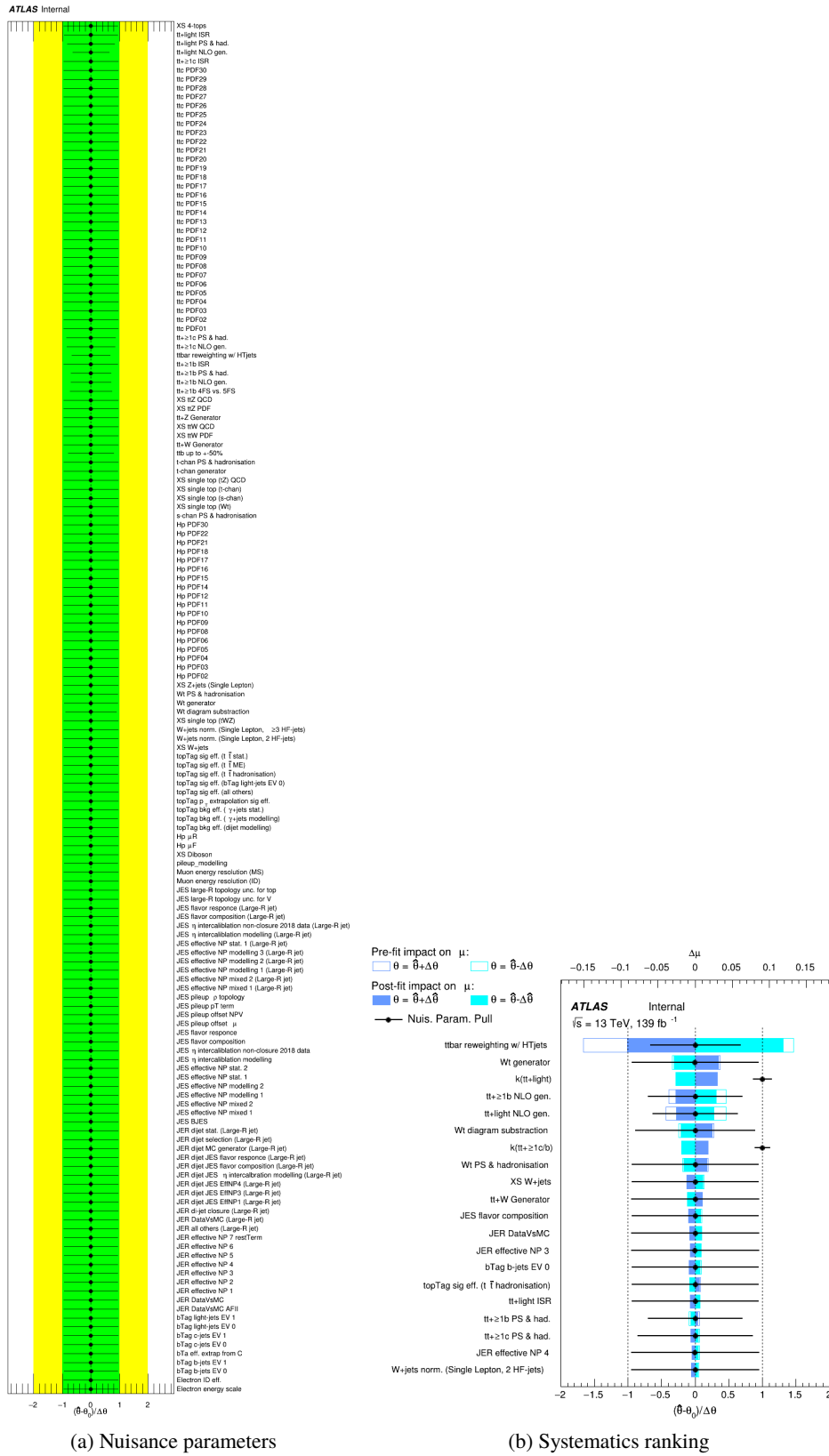
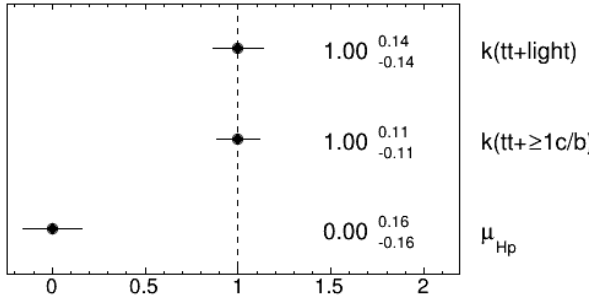


Figure 79: Nuisance parameters (left) and ranking plot (right) of the effect of various nuisance parameters before and after the fit for the 5000 GeV H^+ mass hypotheses.

ATLAS Internal

(a) Norm. factors

ATLAS Internal

	bTag b-jets EV 0	0.2	1.3	0.7	0.2	6.7	-0.8	4.6	6.2	4.4	0.1	1.0	-4.4	40.6	-6.3
JES pileup ρ topology	0.2	100.0	0.5	0.1	0.1	2.8	1.0	0.4	-0.4	0.7	-1.0	0.4	-2.1	-26.9	6.6
topTag sig eff. ($t\bar{t}$ hadronisation)	1.3	0.5	100.0	-1.0	-0.4	-8.5	-1.7	-3.6	-2.3	-4.5	-3.2	-3.2	4.2	-20.9	-15.3
Wt diagram subtraction	0.7	0.1	-1.0	100.0	-3.0	-3.5	-4.0	2.0	5.5	-8.8	-15.6	-6.3	15.0	4.7	26.6
Wt generator	0.2	0.1	-0.4	-3.0	100.0	-0.4	0.0	1.4	1.0	-2.6	-8.1	-2.1	20.7	-3.4	5.7
$tt+\geq 1b$ 4FS vs. 5FS	6.7	2.8	-8.5	-3.5	-0.4	100.0	-23.3	-36.1	-2.4	-22.0	4.9	-11.9	2.1	7.9	-4.9
$tt+\geq 1b$ NLO gen.	-0.8	1.0	-1.7	-4.0	0.0	-23.3	100.0	-44.3	18.2	-3.9	-13.5	-6.3	-17.2	-9.6	1.9
$tt+\geq 1b$ PS & had.	4.6	0.4	-3.6	2.0	1.4	-36.1	-44.3	100.0	-3.3	-6.7	3.7	4.5	2.7	0.9	2.5
ttbar reweighting w/ HTjets	6.2	-0.4	-2.3	5.5	1.0	-2.4	18.2	-3.3	100.0	-2.8	11.0	-2.5	-75.1	-9.7	-12.9
$tt+\geq 1c$ NLO gen.	4.4	0.7	-4.5	-8.8	-2.6	-22.0	-3.9	-6.7	-2.8	100.0	-20.9	-11.5	1.0	6.8	-5.7
tt+light NLO gen.	0.1	-1.0	-3.2	-15.6	-8.1	4.9	-13.5	3.7	11.0	-20.9	100.0	-52.8	-15.8	0.2	-8.8
tt+light PS & had.	1.0	0.4	-3.2	-6.3	-2.1	-11.9	-6.3	4.5	-2.5	-11.5	-52.8	100.0	-1.0	3.6	-4.5
μ_{H_p}	-4.4	-2.1	4.2	15.0	20.7	2.1	-17.2	2.7	-75.1	1.0	-15.8	-1.0	100.0	11.7	17.0
$k(tt+\geq 1c/b)$	40.6	-26.9	-20.9	4.7	-3.4	7.9	-9.6	0.9	-9.7	6.8	0.2	3.6	11.7	100.0	-59.9
$k(tt+\text{light})$	-6.3	6.6	-15.3	26.6	5.7	-4.9	1.9	2.5	-12.9	-5.7	-8.8	-4.5	17.0	-59.9	100.0

(b) Correlation matrix

Figure 80: Signal strength and normalization factors (top) and correlation matrix (bottom) for the 5000 GeV H^+ mass hypotheses.

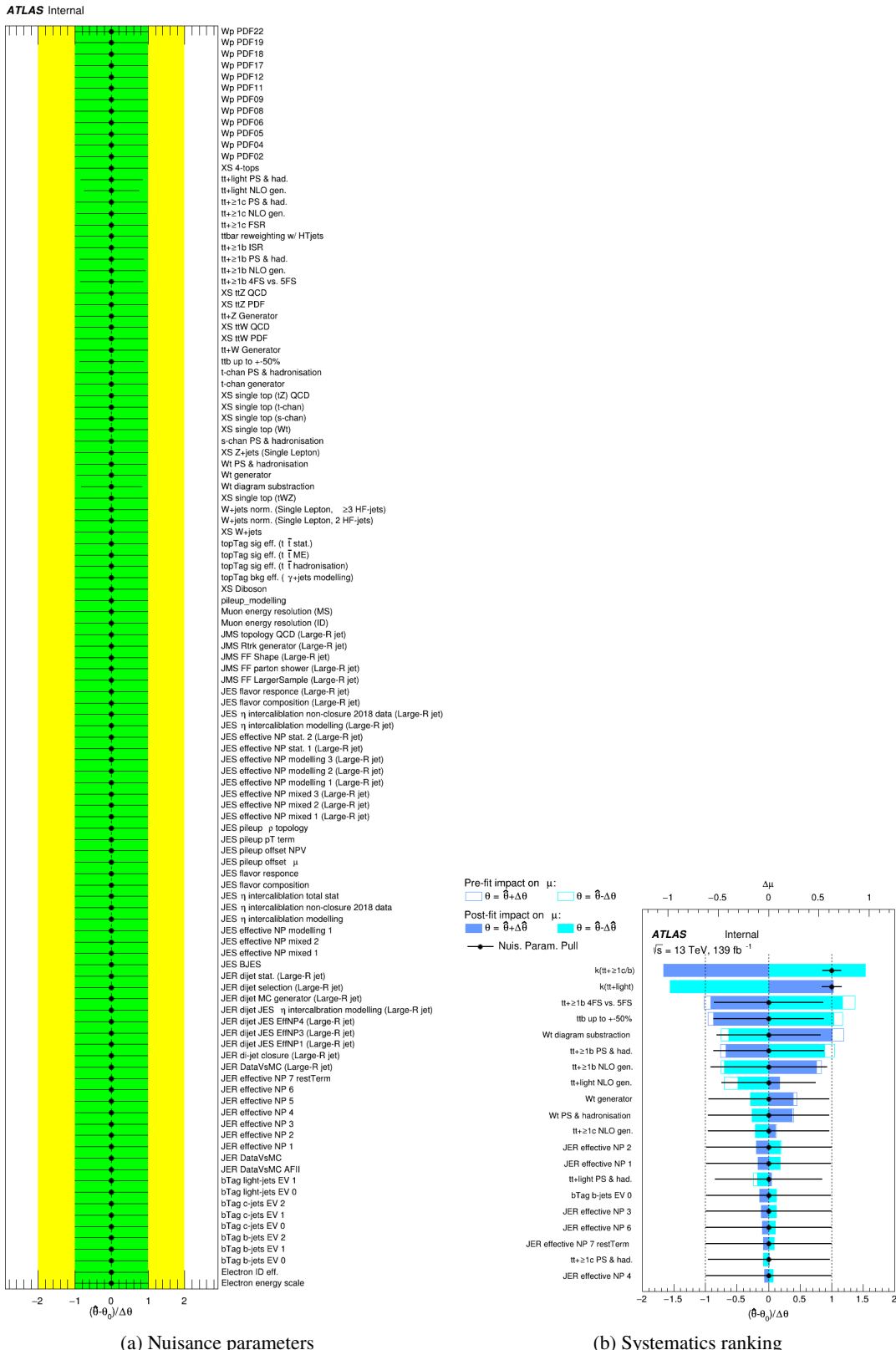
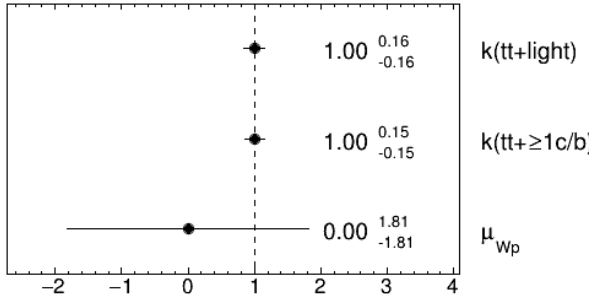
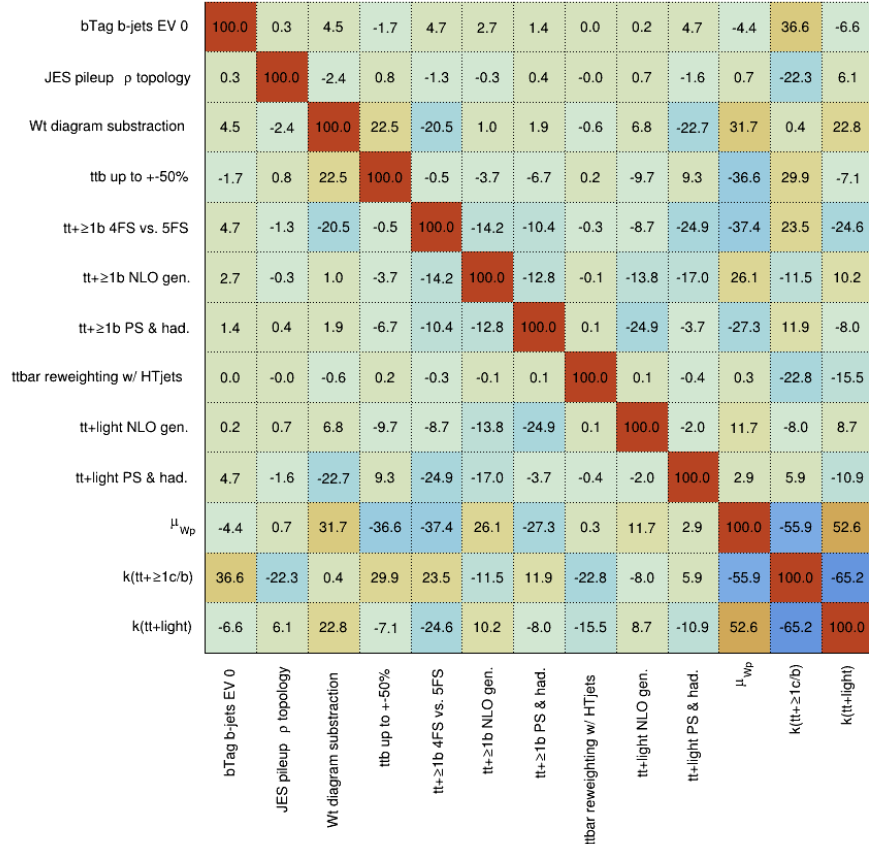


Figure 81: Nuisance parameters (left) and ranking plot (right) of the effect of various nuisance parameters before and after the fit for the 1000 GeV W'_L mass hypotheses.

ATLAS Internal

(a) Norm. factors

ATLAS Internal

(b) Correlation matrix

Figure 82: Signal strength and normalization factors (top) and correlation matrix (bottom) for the 1000 GeV W'_L mass hypotheses.

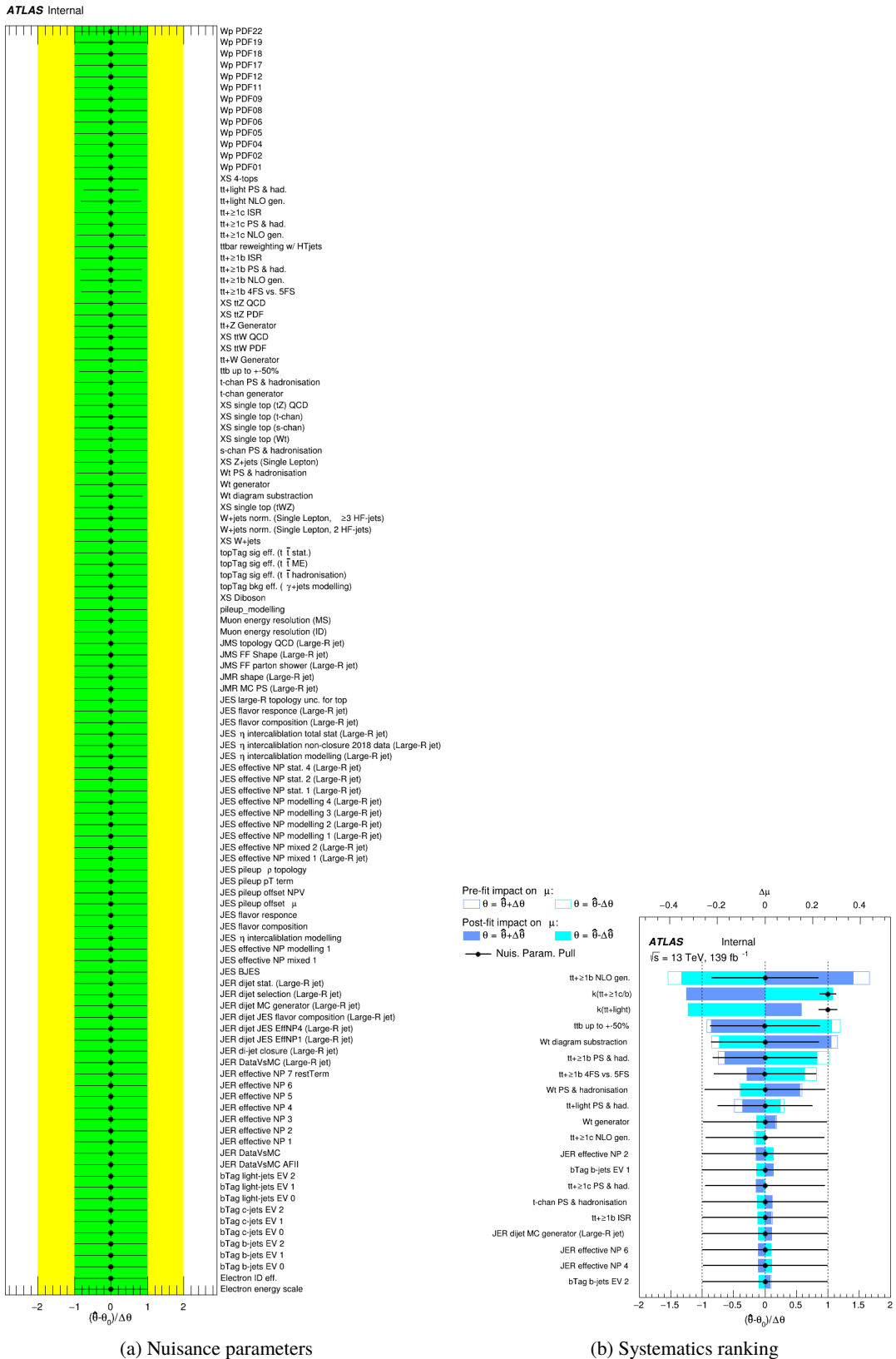
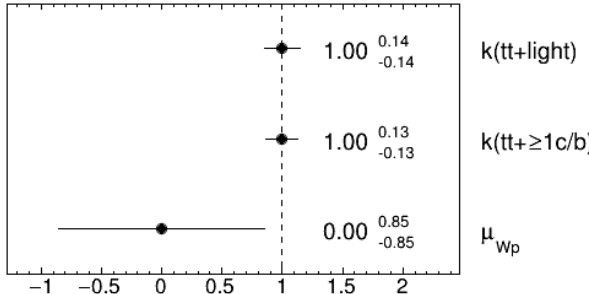
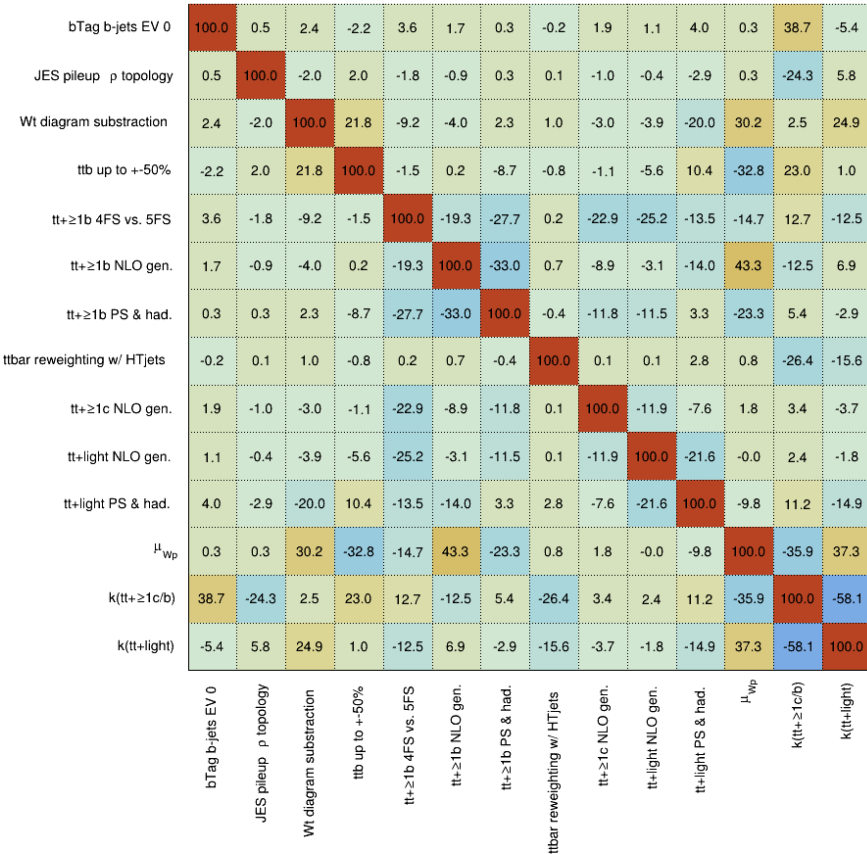


Figure 83: Nuisance parameters (left) and ranking plot (right) of the effect of various nuisance parameters before and after the fit for the 1200 GeV W'_L mass hypotheses.

ATLAS Internal

(a) Norm. factors

ATLAS Internal

(b) Correlation matrix

Figure 84: Signal strength and normalization factors (top) and correlation matrix (bottom) for the 1200 GeV W'_L mass hypotheses.

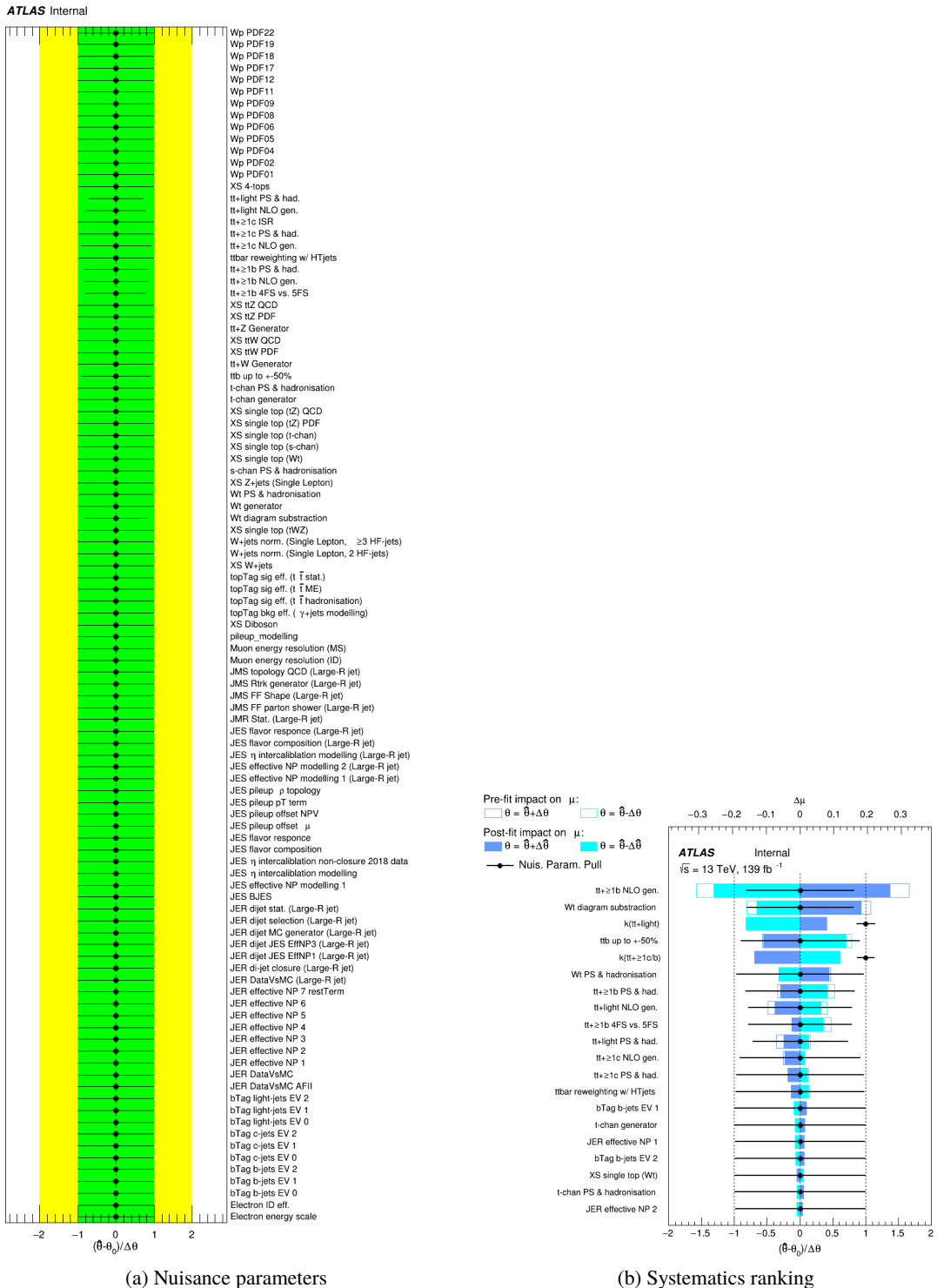
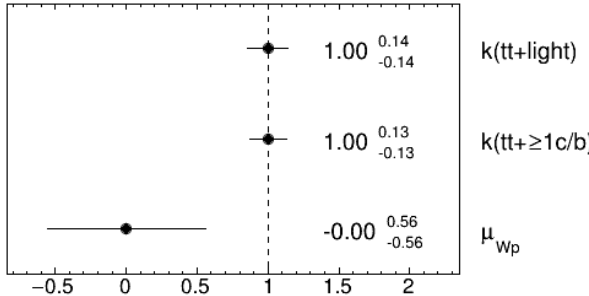
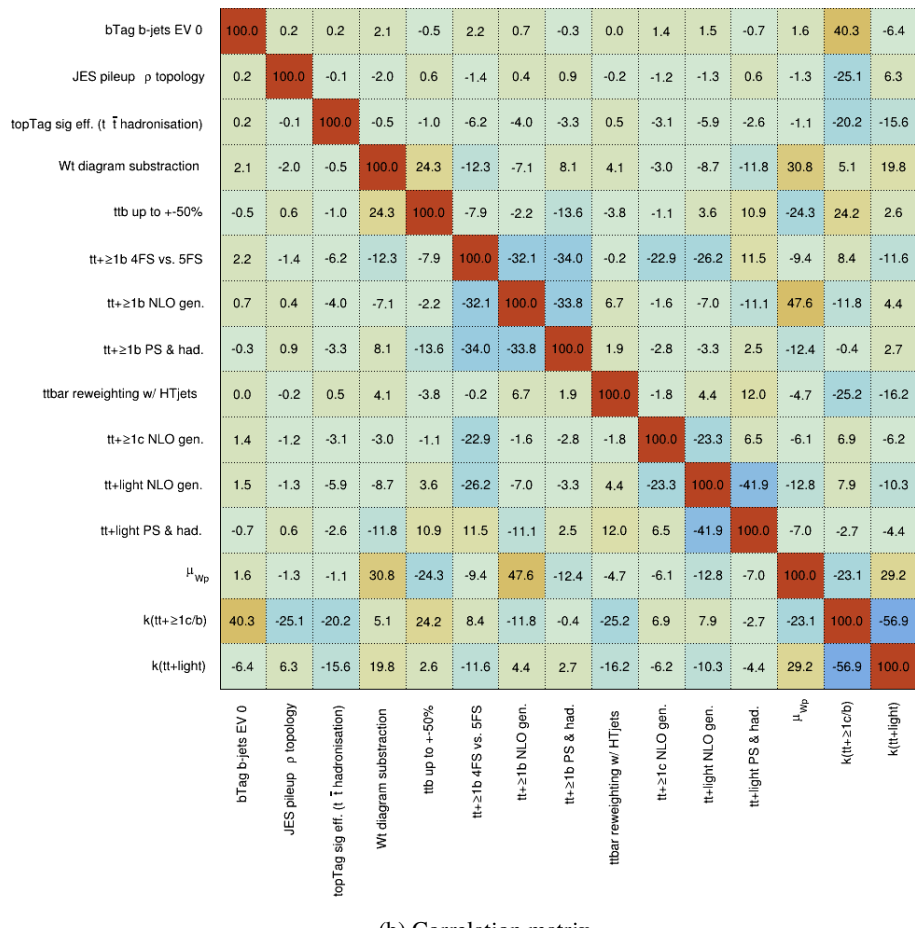
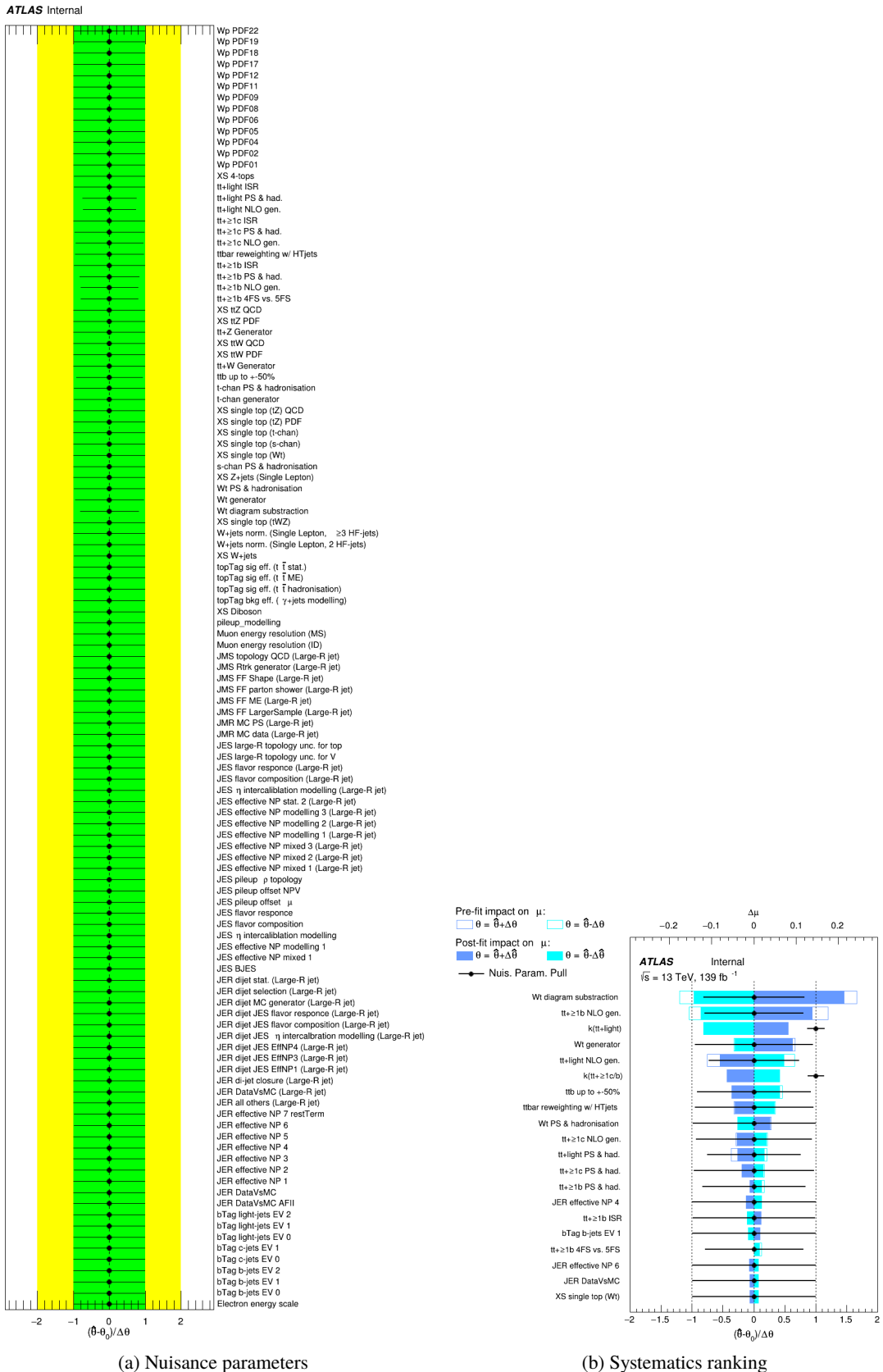


Figure 85: Nuisance parameters (left) and ranking plot (right) of the effect of various nuisance parameters before and after the fit for the 1400 GeV W'_L mass hypotheses.

ATLAS Internal**ATLAS Internal**

(b) Correlation matrix

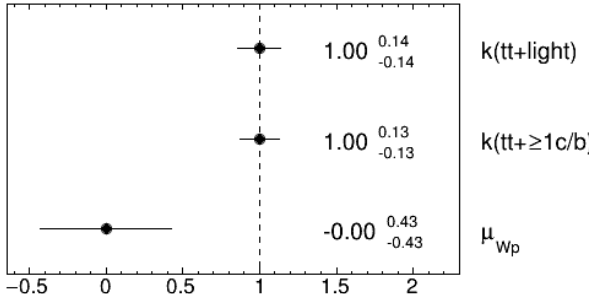
Figure 86: Signal strength and normalization factors (top) and correlation matrix (bottom) for the 1400 GeV W'_L mass hypotheses.



(a) Nuisance parameters

(b) Systematics ranking

Figure 87: Nuisance parameters (left) and ranking plot (right) of the effect of various nuisance parameters before and after the fit for the 1600 GeV W'_L mass hypotheses.

ATLAS Internal

(a) Norm. factors

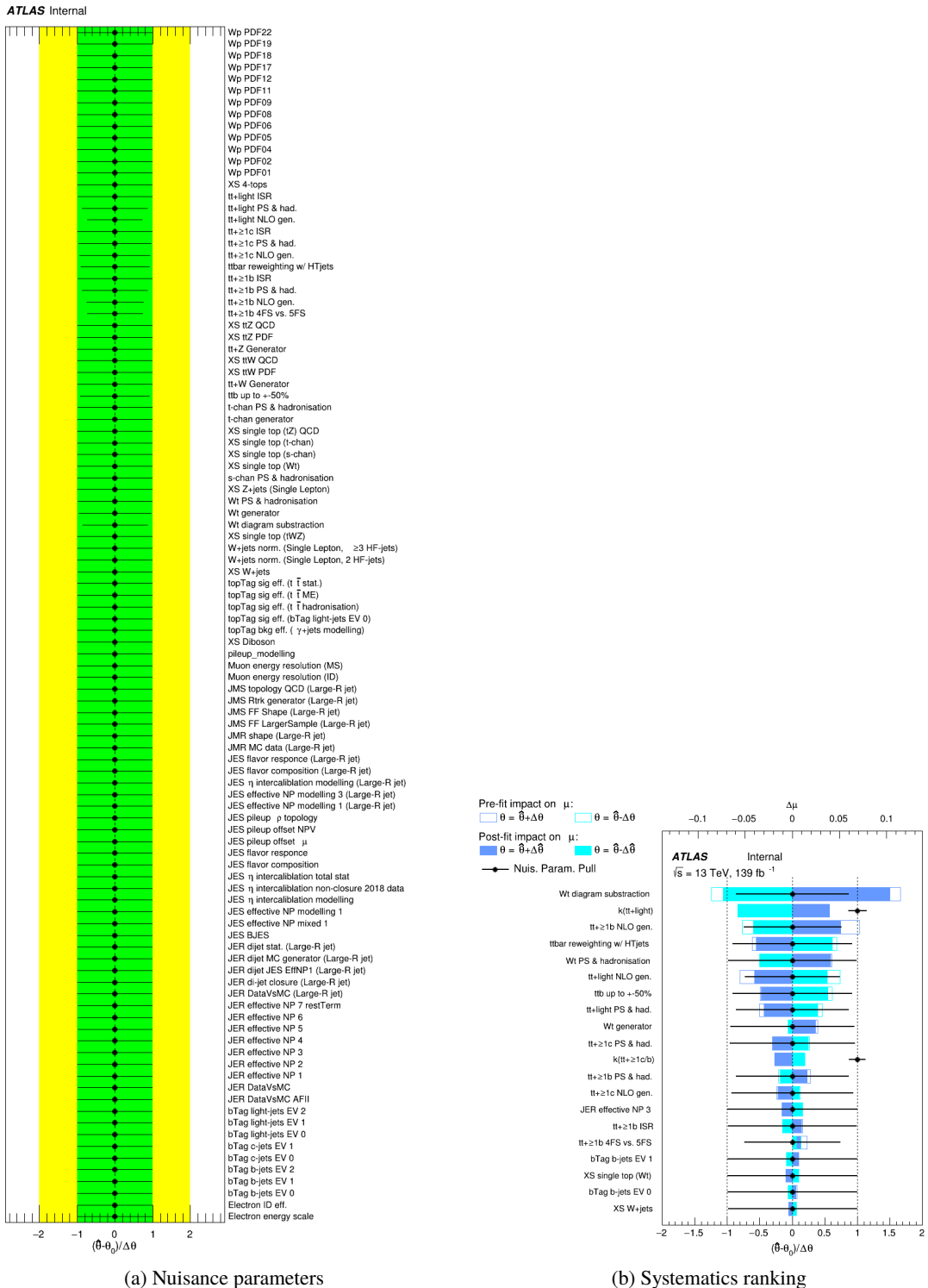
ATLAS Internal

	bTag b-jets EV 0	0.0	0.2	-0.0	0.1	2.3	2.1	2.2	-0.3	-0.2	0.3	-1.2	0.6	41.9	-7.8
JES pileup ρ topology	0.0	100.0	-0.1	-1.2	-0.5	-0.8	1.0	0.8	0.2	-0.5	-2.4	0.2	-1.1	-25.8	6.7
topTag sig eff. ($t\bar{t}$ hadronisation)	0.2	-0.1	100.0	-1.3	-0.3	-6.1	-3.7	-3.1	1.0	-2.6	-6.9	-2.2	-0.6	-20.8	-15.9
Wt diagram subtraction	-0.0	-1.2	-1.3	100.0	-20.2	-11.6	0.6	7.6	6.0	-1.1	-10.2	-12.5	47.2	0.7	23.5
Wt generator	0.1	-0.5	-0.3	-20.2	100.0	-4.0	1.4	3.5	1.9	1.0	-1.2	-1.5	15.7	-2.9	-0.8
$t\bar{t} + \geq 1b$ 4FS vs. 5FS	2.3	-0.8	-6.1	-11.6	-4.0	100.0	-27.6	-39.2	0.3	-11.3	-38.1	12.2	-1.6	6.3	-8.7
$t\bar{t} + \geq 1b$ NLO gen.	2.1	1.0	-3.7	0.6	1.4	-27.6	100.0	-34.2	13.4	-1.3	1.8	-24.0	31.4	-10.6	4.3
$t\bar{t} + \geq 1b$ PS & had.	2.2	0.8	-3.1	7.6	3.5	-39.2	-34.2	100.0	-1.1	-2.5	-9.6	12.2	-3.4	0.2	3.1
ttbar reweighting w/ HTjets	-0.3	0.2	1.0	6.0	1.9	0.3	13.4	-1.1	100.0	0.2	-2.1	17.4	-10.9	-25.2	-15.1
$t\bar{t} + \geq 1c$ NLO gen.	-0.2	-0.5	-2.6	-1.1	1.0	-11.3	-1.3	-2.5	0.2	100.0	-31.8	-12.8	-8.9	3.2	-2.8
$t\bar{t} + \text{light}$ NLO gen.	0.3	-2.4	-6.9	-10.2	-1.2	-38.1	1.8	-9.6	-2.1	-31.8	100.0	-16.2	-18.3	11.7	-12.5
$t\bar{t} + \text{light}$ PS & had.	-1.2	0.2	-2.2	-12.5	-1.5	12.2	-24.0	12.2	17.4	-12.8	-16.2	100.0	-7.7	-4.0	-6.0
μ_{W_p}	0.6	-1.1	-0.6	47.2	15.7	-1.6	31.4	-3.4	-10.9	-8.9	-18.3	-7.7	100.0	-14.4	29.5
$k(t\bar{t} + \geq 1c/b)$	41.9	-25.8	-20.8	0.7	-2.9	6.3	-10.6	0.2	-25.2	3.2	11.7	-4.0	-14.4	100.0	-57.3
$k(t\bar{t} + \text{light})$	-7.8	6.7	-15.9	23.5	-0.8	-8.7	4.3	3.1	-15.1	-2.8	-12.5	-6.0	29.5	-57.3	100.0



(b) Correlation matrix

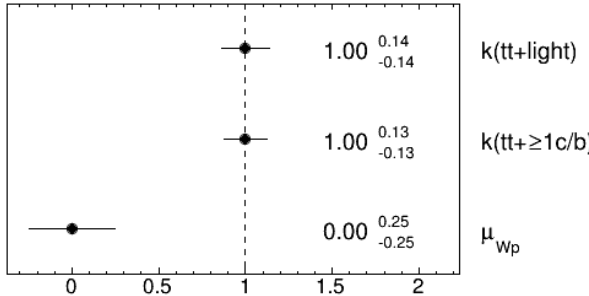
Figure 88: Signal strength and normalization factors (top) and correlation matrix (bottom) for the 1600 GeV W'_L mass hypotheses.



(a) Nuisance parameters

(b) Systematics ranking

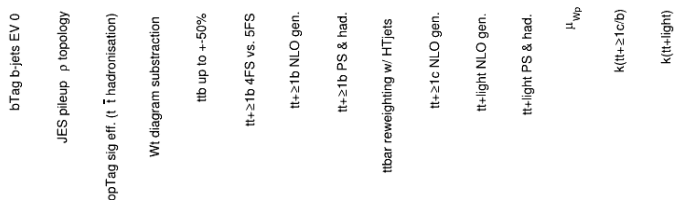
Figure 89: Nuisance parameters (left) and ranking plot (right) of the effect of various nuisance parameters before and after the fit for the 1800 GeV W'_L mass hypotheses.

ATLAS Internal

(a) Norm. factors

ATLAS Internal

bTag b-jets EV 0	100.0	0.1	0.3	0.3	0.6	3.4	2.1	1.6	-0.6	1.0	1.4	0.2	1.9	41.9	-7.3
JES pileup p topology	0.1	100.0	-0.1	-0.4	-0.0	-0.7	0.7	0.6	0.1	-0.8	-1.7	-0.3	-1.0	-26.3	7.2
topTag sig eff. ($t\bar{t}$ hadronisation)	0.3	-0.1	100.0	-0.5	-0.3	-7.1	-2.7	-2.7	0.5	-2.7	-6.4	-1.4	-0.6	-20.9	-15.5
Wt diagram subtraction	0.3	-0.4	-0.5	100.0	13.1	-4.2	-3.7	6.9	13.5	-3.3	-8.9	-13.3	39.1	-0.2	23.8
ttb up to +50%	0.6	-0.0	-0.3	13.1	100.0	-6.5	-5.1	-7.5	-9.7	1.9	1.2	7.0	-16.4	23.8	0.5
tt+≥1b 4FS vs. 5FS	3.4	-0.7	-7.1	-4.2	-6.5	100.0	-27.7	-31.3	-2.7	-17.9	-35.5	6.2	0.9	5.9	-5.1
tt+≥1b NLO gen.	2.1	0.7	-2.7	-3.7	-5.1	-27.7	100.0	-37.4	15.1	2.3	-1.6	-13.3	19.0	-7.7	-0.4
tt+≥1b PS & had.	1.6	0.6	-2.7	6.9	-7.5	-31.3	-37.4	100.0	0.8	-0.1	-4.2	-1.2	5.9	-2.4	5.0
ttbar reweighting w/ HTjets	-0.6	0.1	0.5	13.5	-9.7	-2.7	15.1	0.8	100.0	-0.1	-2.9	12.2	-16.3	-24.7	-10.7
tt+≥1c NLO gen.	1.0	-0.8	-2.7	-3.3	1.9	-17.9	2.3	-0.1	-0.1	100.0	-31.2	-8.1	-5.2	4.8	-5.3
tt+light NLO gen.	1.4	-1.7	-6.4	-8.9	1.2	-35.5	-1.6	-4.2	-2.9	-31.2	100.0	-30.5	-16.1	9.7	-11.1
tt+light PS & had.	0.2	-0.3	-1.4	-13.3	7.0	6.2	-13.3	-1.2	12.2	-8.1	-30.5	100.0	-12.0	0.2	-9.6
μ_{W_p}	1.9	-1.0	-0.6	39.1	-16.4	0.9	19.0	5.9	-16.3	-5.2	-16.1	-12.0	100.0	-6.8	25.6
k(tt+≥1c/b)	41.9	-26.3	-20.9	-0.2	23.8	5.9	-7.7	-2.4	-24.7	4.8	9.7	0.2	-6.8	100.0	-58.2
k(tt+light)	-7.3	7.2	-15.5	23.8	0.5	-5.1	-0.4	5.0	-10.7	-5.3	-11.1	-9.6	25.6	-58.2	100.0



(b) Correlation matrix

Figure 90: Signal strength and normalization factors (top) and correlation matrix (bottom) for the 1800 GeV W'_L mass hypotheses.

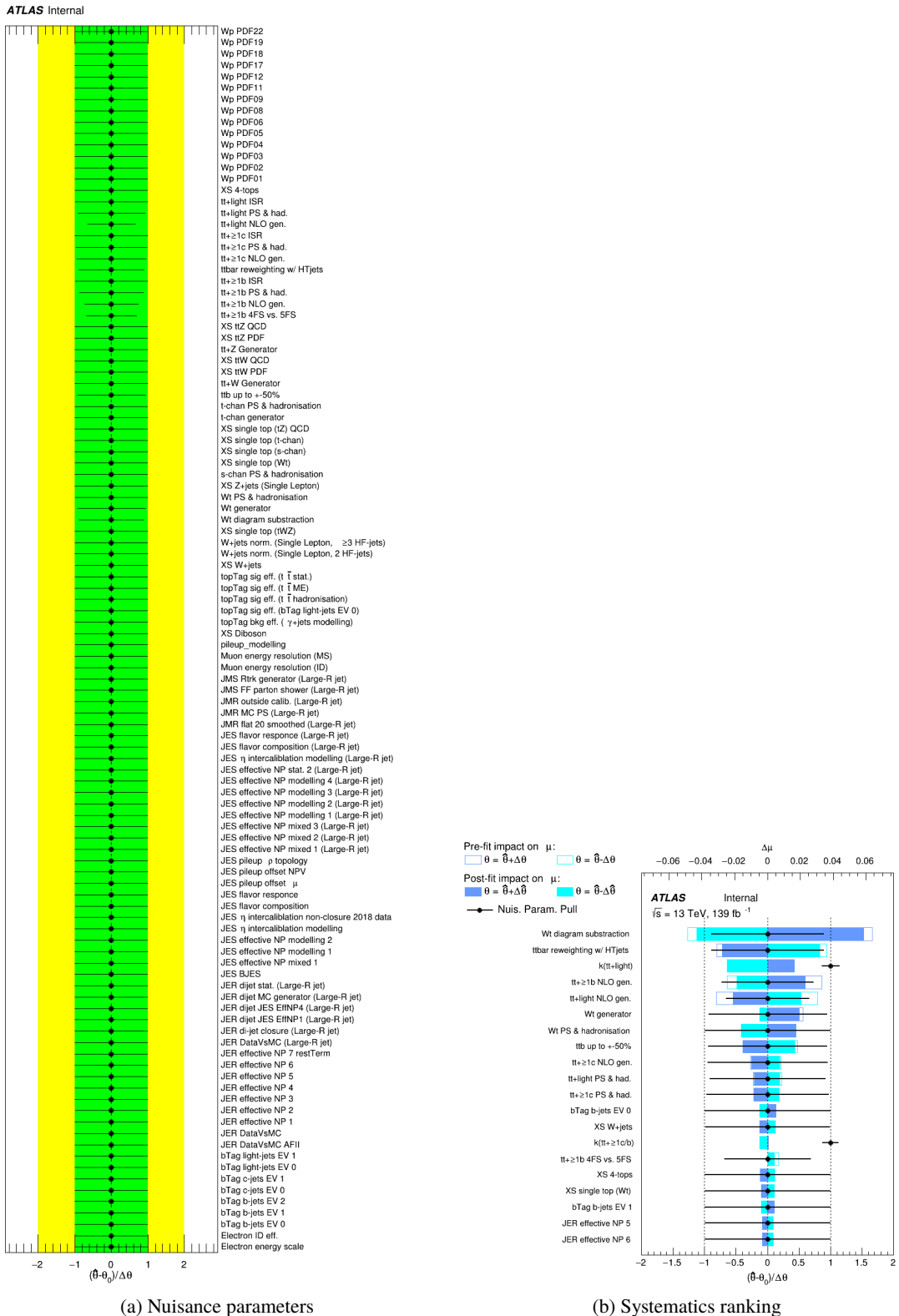
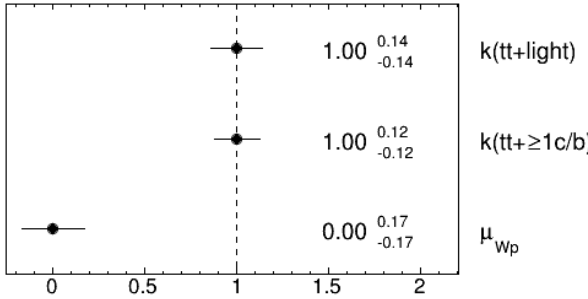


Figure 91: Nuisance parameters (left) and ranking plot (right) of the effect of various nuisance parameters before and after the fit for the 2000 GeV W'_L mass hypotheses.

ATLAS Internal

(a) Norm. factors

ATLAS Internal

bTag b-jets EV 0	100.0	0.0	0.2	-0.1	0.3	3.0	2.0	1.6	0.0	0.6	2.0	0.3	2.9	42.1	-7.8
JES pileup p topology	0.0	100.0	0.0	-0.8	0.4	0.5	0.4	0.8	0.7	-0.3	-0.6	-0.3	-1.3	-26.7	7.1
topTag sig eff. ($t\bar{t}$ hadronisation)	0.2	0.0	100.0	-0.5	0.8	-8.0	-2.2	-2.8	0.1	-1.3	-6.3	-1.0	-1.0	-20.8	-15.4
Wt diagram subtraction	-0.1	-0.8	-0.5	100.0	7.8	-2.9	-5.0	4.9	16.9	-7.5	-10.8	-9.0	32.9	0.2	22.9
ttb up to +50%	0.3	0.4	0.8	7.8	100.0	2.0	-4.6	-6.7	-9.9	1.1	-1.6	3.6	-10.5	21.7	0.9
tt+≥1b 4FS vs. 5FS	3.0	0.5	-8.0	-2.9	2.0	100.0	-27.2	-42.8	-7.6	-6.3	-36.7	5.5	-1.1	8.3	-4.1
tt+≥1b NLO gen.	2.0	0.4	-2.2	-5.0	-4.6	-27.2	100.0	-37.3	21.1	-7.9	-1.1	-8.3	12.5	-7.2	-3.1
tt+≥1b PS & had.	1.6	0.8	-2.8	4.9	-6.7	-42.8	-37.3	100.0	-1.5	-1.8	-3.2	1.9	0.8	-0.5	3.5
ttbar reweighting w/ HTjets	0.0	0.7	0.1	16.9	-9.9	-7.6	21.1	-1.5	100.0	8.0	-1.8	13.0	-17.5	-24.5	-8.8
tt+≥1c NLO gen.	0.6	-0.3	-1.3	-7.5	1.1	-6.3	-7.9	-1.8	8.0	100.0	-22.4	-11.1	-5.7	0.0	-5.8
tt+light NLO gen.	2.0	-0.6	-6.3	-10.8	-1.6	-36.7	-1.1	-3.2	-1.8	-22.4	100.0	-27.2	-12.7	10.4	-13.1
tt+light PS & had.	0.3	-0.3	-1.0	-9.0	3.6	5.5	-8.3	1.9	13.0	-11.1	-27.2	100.0	-4.9	-1.1	-6.9
μ_{W_p}	2.9	-1.3	-1.0	32.9	-10.5	-1.1	12.5	0.8	-17.5	-5.7	-12.7	-4.9	100.0	1.8	16.5
k($t\bar{t} + \geq 1 c/b$)	42.1	-26.7	-20.8	0.2	21.7	8.3	-7.2	-0.5	-24.5	0.0	10.4	-1.1	1.8	100.0	-58.5
k($t\bar{t}$ +light)	-7.8	7.1	-15.4	22.9	0.9	-4.1	-3.1	3.5	-8.8	-5.8	-13.1	-6.9	16.5	-58.5	100.0

(b) Correlation matrix

Figure 92: Signal strength and normalization factors (top) and correlation matrix (bottom) for the 2000 GeV W'_L mass hypotheses.

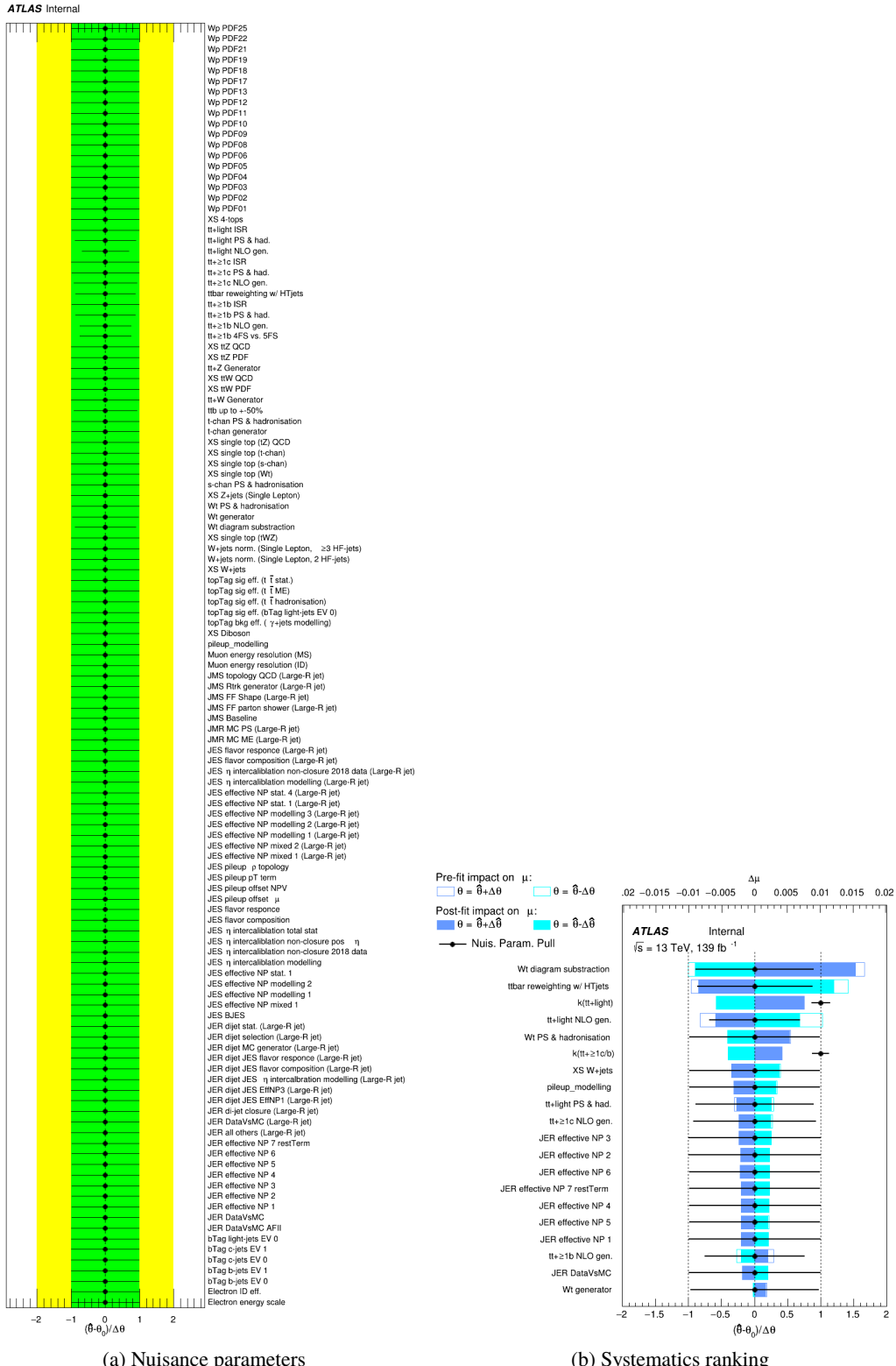
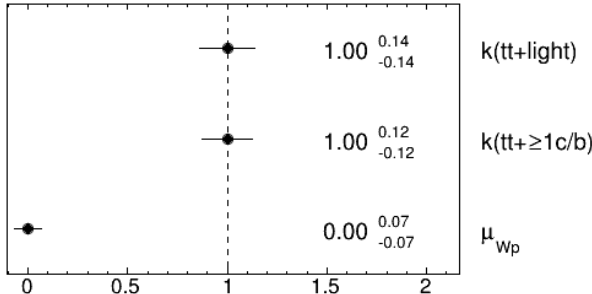


Figure 93: Nuisance parameters (left) and ranking plot (right) of the effect of various nuisance parameters before and after the fit for the 2500 GeV W'_L mass hypotheses.

ATLAS Internal

(a) Norm. factors

ATLAS Internal

bTag b-jets EV 0	100.0	-0.0	0.2	-0.3	0.8	2.5	1.4	1.5	0.7	0.8	2.2	0.4	42.3	-8.3
JES pileup ρ topology	-0.0	100.0	0.2	0.9	-0.2	2.2	0.3	0.6	-0.2	-0.1	1.3	-0.8	-26.9	8.3
topTag sig eff. ($t\bar{t}$ hadronisation)	0.2	0.2	100.0	-1.0	-0.4	-6.6	-1.7	-2.4	-0.2	-1.1	-6.9	0.4	-21.2	-15.4
Wt diagram subtraction	-0.3	0.9	-1.0	100.0	7.1	-7.4	-2.4	2.5	14.8	-3.9	-16.1	-2.5	1.0	22.5
ttb up to $\pm 50\%$	0.8	-0.2	-0.4	7.1	100.0	-7.0	1.4	-7.2	-13.1	-1.2	3.9	1.9	23.0	0.6
$t\bar{t}+\geq 1b$ 4FS vs. 5FS	2.5	2.2	-6.6	-7.4	-7.0	100.0	-33.7	-38.4	-6.0	-7.4	-39.4	10.9	3.8	-3.1
$t\bar{t}+\geq 1b$ NLO gen.	1.4	0.3	-1.7	-2.4	1.4	-33.7	100.0	-37.7	24.5	-7.5	5.6	-10.4	-7.4	-2.9
$t\bar{t}+\geq 1b$ PS & had.	1.5	0.6	-2.4	2.5	-7.2	-38.4	-37.7	100.0	-0.7	-3.5	0.7	4.0	-0.6	2.5
ttbar reweighting w/ HTjets	0.7	-0.2	-0.2	14.8	-13.1	-6.0	24.5	-0.7	100.0	4.0	5.3	10.9	-22.7	-8.8
$t\bar{t}+\geq 1c$ NLO gen.	0.8	-0.1	-1.1	-3.9	-1.2	-7.4	-7.5	-3.5	4.0	100.0	-27.7	-16.2	0.8	-3.9
$t\bar{t}+\text{light}$ NLO gen.	2.2	1.3	-6.9	-16.1	3.9	-39.4	5.6	0.7	5.3	-27.7	100.0	-21.1	8.0	-15.3
$t\bar{t}+\text{light}$ PS & had.	0.4	-0.8	0.4	-2.5	1.9	10.9	-10.4	4.0	10.9	-16.2	-21.1	100.0	-1.1	-4.5
$k(t\bar{t}+\geq 1c/b)$	42.3	-26.9	-21.2	1.0	23.0	3.8	-7.4	-0.6	-22.7	0.8	8.0	-1.1	100.0	-59.5
$k(t\bar{t}+\text{light})$	-8.3	8.3	-15.4	22.5	0.6	-3.1	-2.9	2.5	-8.8	-3.9	-15.3	-4.5	-59.5	100.0

(b) Correlation matrix

Figure 94: Signal strength and normalization factors (top) and correlation matrix (bottom) for the 2500 GeV W'_L mass hypotheses.

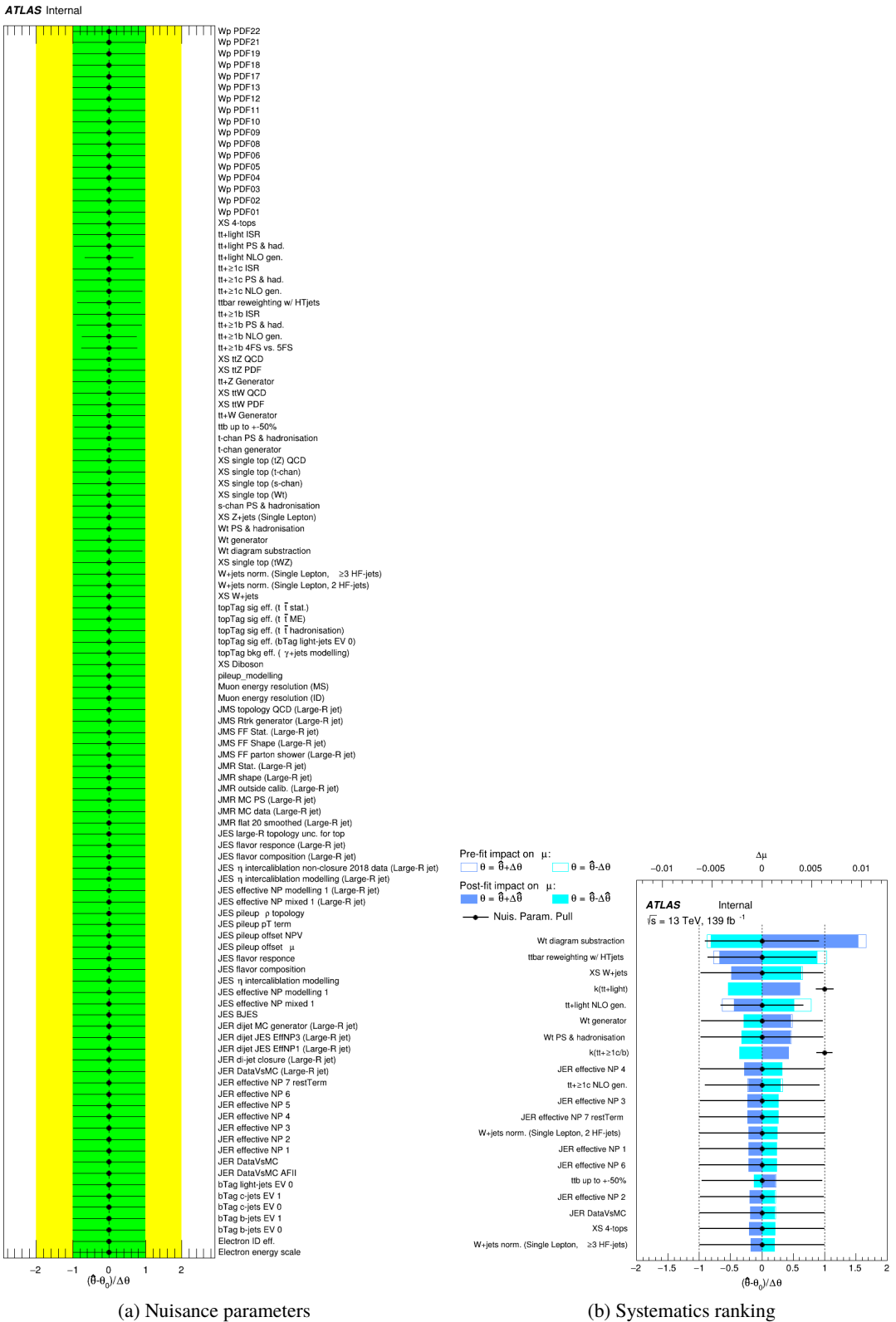
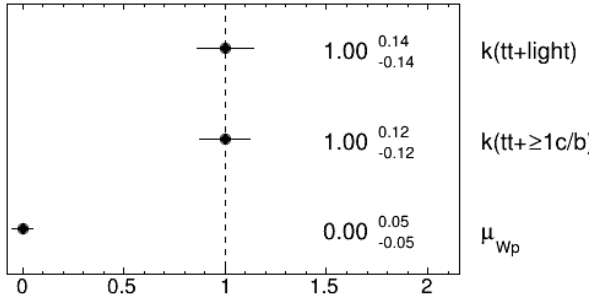


Figure 95: Nuisance parameters (left) and ranking plot (right) of the effect of various nuisance parameters before and after the fit for the 3000 GeV W'_L mass hypotheses.

ATLAS Internal

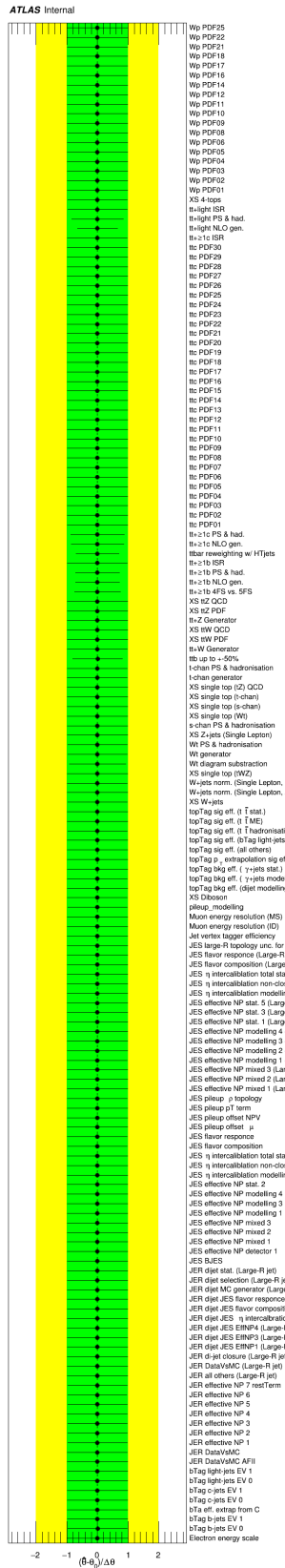
(a) Norm. factors

ATLAS Internal

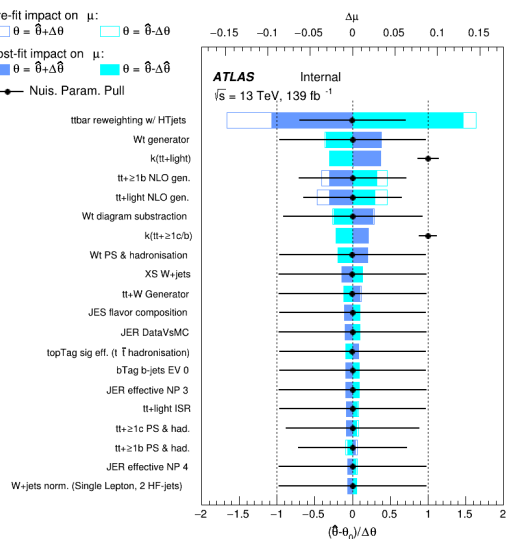
bTag b-jets EV 0	100.0	0.0	0.1	0.1	0.1	1.2	-0.0	0.5	0.9	0.7	3.5	42.1	-7.8
JES pileup ρ topology	0.0	100.0	0.0	-0.0	0.0	0.5	0.1	0.3	0.0	-0.1	0.3	-27.0	7.8
topTag sig eff. ($t\bar{t}$ hadronisation)	0.1	0.0	100.0	-0.3	-0.1	-4.7	-2.6	-2.0	0.4	-1.4	-5.3	-21.5	-15.2
Wt diagram subtraction	0.1	-0.0	-0.3	100.0	3.3	-1.9	-3.8	1.4	13.4	-7.4	-12.9	1.7	22.8
ttb up to +50%	0.1	0.0	-0.1	3.3	100.0	-2.8	-1.2	-4.6	-4.6	3.4	6.2	20.1	-1.6
tt+≥1b 4FS vs. 5FS	1.2	0.5	-4.7	-1.9	-2.8	100.0	-35.6	-32.6	-5.2	-3.4	-46.4	4.2	-1.0
tt+≥1b NLO gen.	-0.0	0.1	-2.6	-3.8	-1.2	-35.6	100.0	-35.6	24.9	-7.0	6.0	-6.7	-5.3
tt+≥1b PS & had.	0.5	0.3	-2.0	1.4	-4.6	-32.6	-35.6	100.0	0.4	3.4	-3.2	0.5	0.5
ttbar reweighting w/ HT jets	0.9	0.0	0.4	13.4	-4.6	-5.2	24.9	0.4	100.0	15.3	3.7	-21.4	-9.0
tt+≥1c NLO gen.	0.7	-0.1	-1.4	-7.4	3.4	-3.4	-7.0	3.4	15.3	100.0	-34.4	-1.8	-7.8
tt+light NLO gen.	3.5	0.3	-5.3	-12.9	6.2	-46.4	6.0	-3.2	3.7	-34.4	100.0	9.3	-14.2
$k(tt+\geq 1c/b)$	42.1	-27.0	-21.5	1.7	20.1	4.2	-6.7	0.5	-21.4	-1.8	9.3	100.0	-59.7
$k(tt+\text{light})$	-7.8	7.8	-15.2	22.8	-1.6	-1.0	-5.3	0.5	-9.0	-7.8	-14.2	-59.7	100.0

(b) Correlation matrix

Figure 96: Signal strength and normalization factors (top) and correlation matrix (bottom) for the 3000 GeV W'_L mass hypotheses.

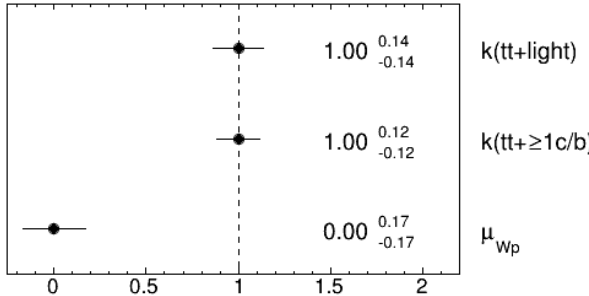


(a) Nuisance parameters



(b) Systematics ranking

Figure 97: Nuisance parameters (left) and ranking plot (right) of the effect of various nuisance parameters before and after the fit for the 4000 GeV W'_L mass hypotheses.

ATLAS Internal

(a) Norm. factors

ATLAS Internal

bTag b-jets EV 0	100.0	0.1	1.3	0.7	0.3	6.9	-1.1	4.7	6.4	4.6	0.1	1.0	4.5	41.3	-6.6
JES pileup ρ topology	0.1	100.0	0.6	0.0	0.1	2.9	1.0	0.4	-0.4	0.7	-1.1	0.4	-2.1	-27.3	6.8
topTag sig eff. ($t\bar{t}$ hadronisation)	1.3	0.6	100.0	-1.0	-0.4	-8.7	-1.5	-3.6	-2.4	-4.6	-3.2	-3.3	4.3	-21.2	-15.5
Wt diagram subtraction	0.7	0.0	-1.0	100.0	-3.0	-3.4	-3.9	2.2	4.8	-9.0	-15.9	-6.3	15.5	4.6	27.3
Wt generator	0.3	0.1	-0.4	-3.0	100.0	-0.4	0.2	1.4	0.4	-2.6	-8.2	-2.2	21.0	-3.5	6.0
$t\bar{t}+\geq 1b$ 4FS vs. 5FS	6.9	2.9	-8.7	-3.4	-0.4	100.0	-23.2	-36.4	-2.4	-22.3	5.6	-12.1	2.1	8.0	-5.0
$t\bar{t}+\geq 1b$ NLO gen.	-1.1	1.0	-1.5	-3.9	0.2	-23.2	100.0	-44.9	18.1	-3.6	-13.6	-6.2	-16.8	-9.8	2.0
$t\bar{t}+\geq 1b$ PS & had.	4.7	0.4	-3.6	2.2	1.4	-36.4	-44.9	100.0	-3.6	-6.6	3.8	4.9	3.0	0.9	2.7
ttbar reweighting w/ HTjets	6.4	-0.4	-2.4	4.8	0.4	-2.4	18.1	-3.6	100.0	-2.8	11.2	-2.6	-76.4	-9.5	-13.8
$t\bar{t}+\geq 1c$ NLO gen.	4.6	0.7	-4.6	-9.0	-2.6	-22.3	-3.6	-6.6	-2.8	100.0	-20.9	-11.4	0.9	7.0	-5.8
$t\bar{t}+\text{light}$ NLO gen.	0.1	-1.1	-3.2	-15.9	-8.2	5.6	-13.6	3.8	11.2	-20.9	100.0	-53.7	-15.9	0.2	-9.1
$t\bar{t}+\text{light}$ PS & had.	1.0	0.4	-3.3	-6.3	-2.2	-12.1	-6.2	4.9	-2.6	-11.4	-53.7	100.0	-1.0	3.6	-4.5
μ_{Wp}	-4.5	-2.1	4.3	15.5	21.0	2.1	-16.8	3.0	-76.4	0.9	-15.9	-1.0	100.0	11.6	18.1
$k(t\bar{t}+\geq 1c/b)$	41.3	-27.3	-21.2	4.6	-3.5	8.0	-9.8	0.9	-9.5	7.0	0.2	3.6	11.6	100.0	-58.7
$k(t\bar{t}+\text{light})$	-6.6	6.8	-15.5	27.3	6.0	-5.0	2.0	2.7	-13.8	-5.8	-9.1	-4.5	18.1	-58.7	100.0

(b) Correlation matrix

Figure 98: Signal strength and normalization factors (top) and correlation matrix (bottom) for the 4000 GeV W'_L mass hypotheses.

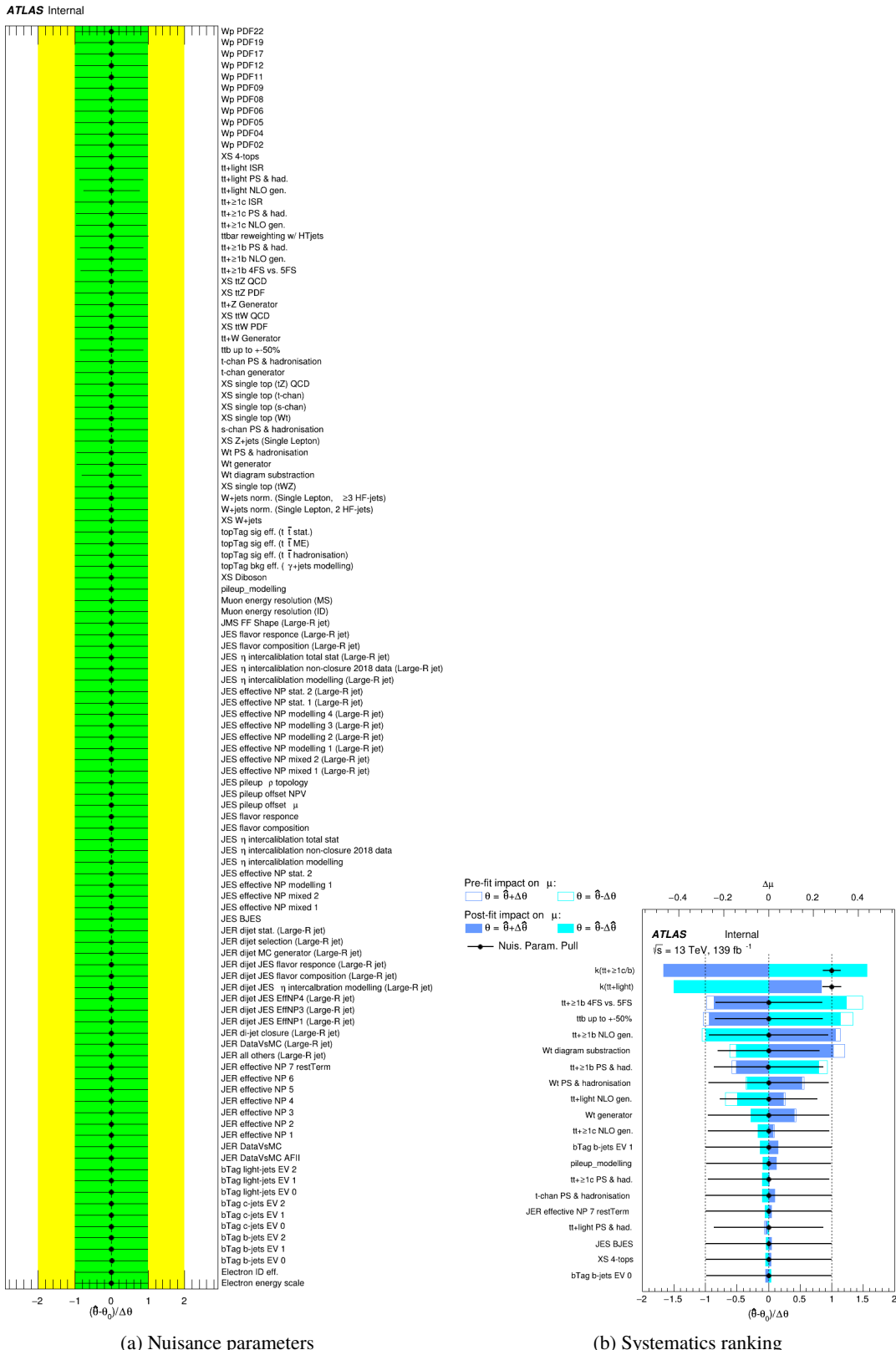
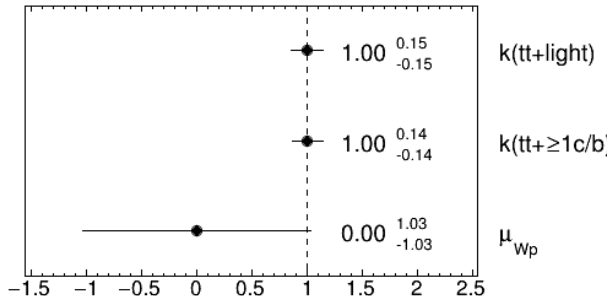
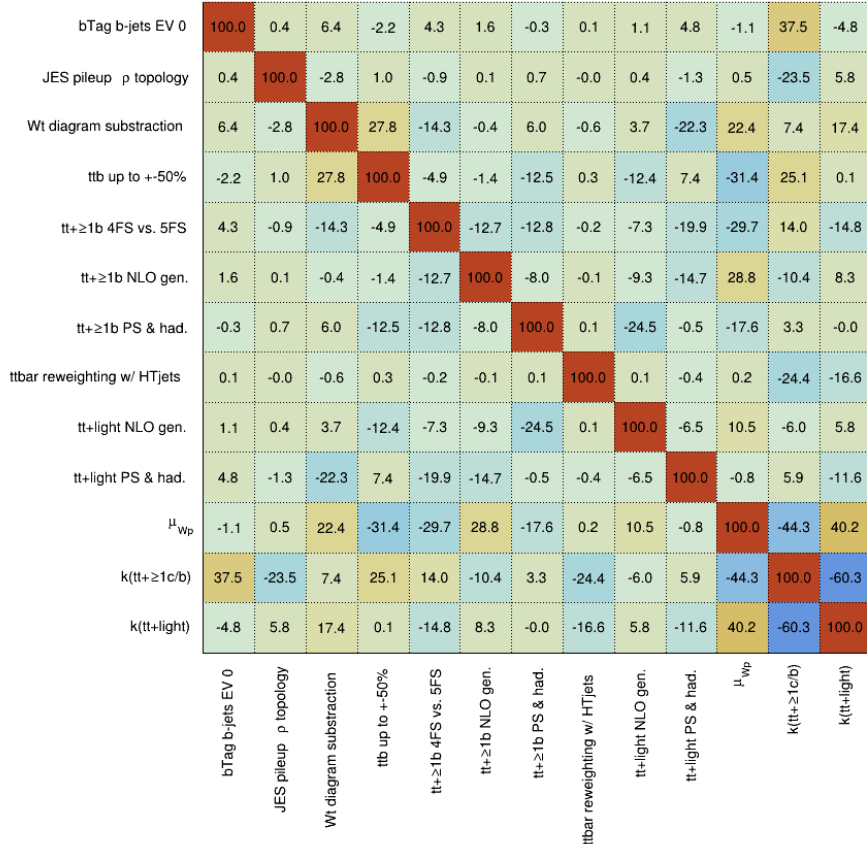


Figure 99: Nuisance parameters (left) and ranking plot (right) of the effect of various nuisance parameters before and after the fit for the 1000 GeV W'_R mass hypotheses.

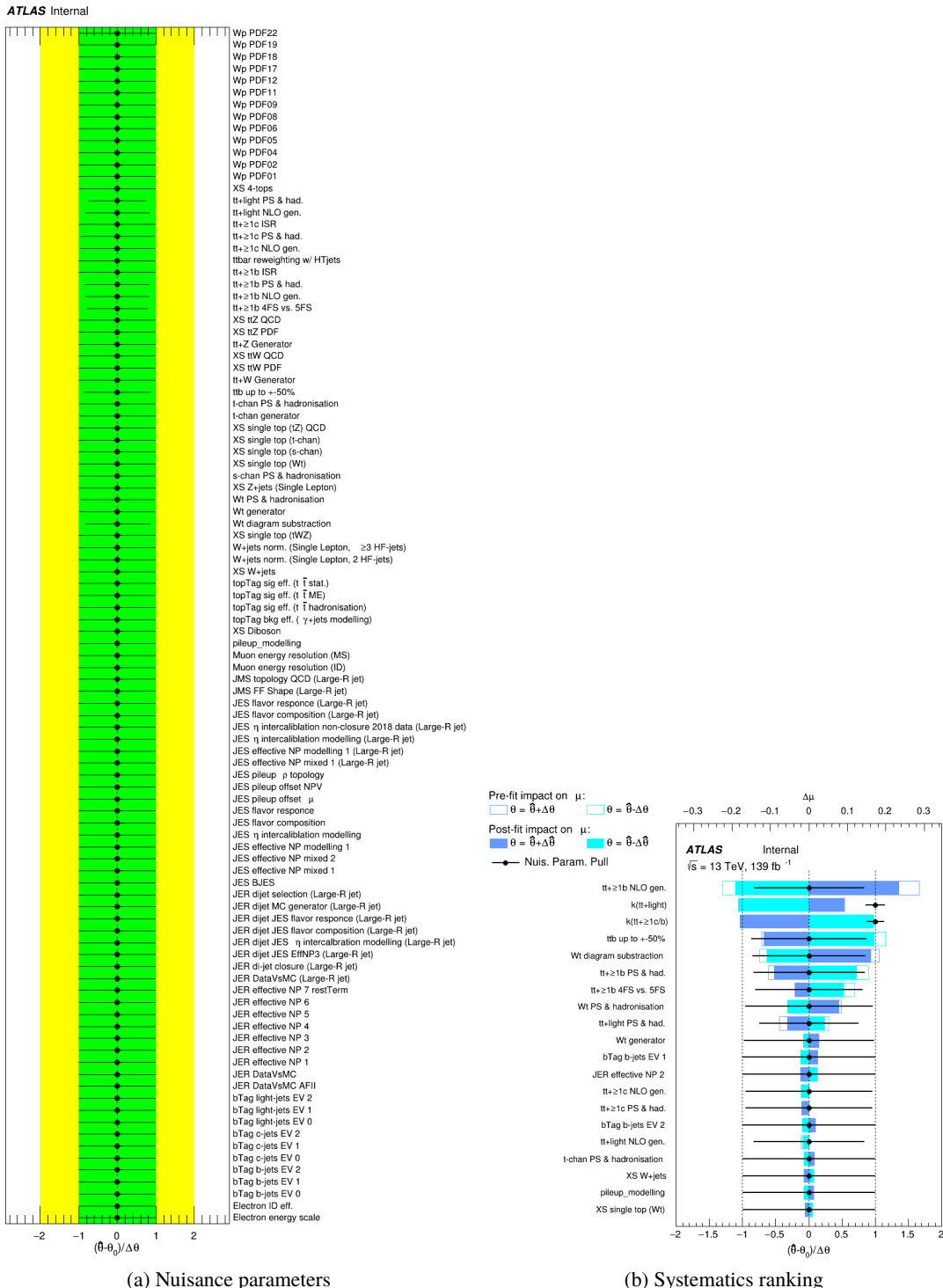
ATLAS Internal

(a) Norm. factors

ATLAS Internal

(b) Correlation matrix

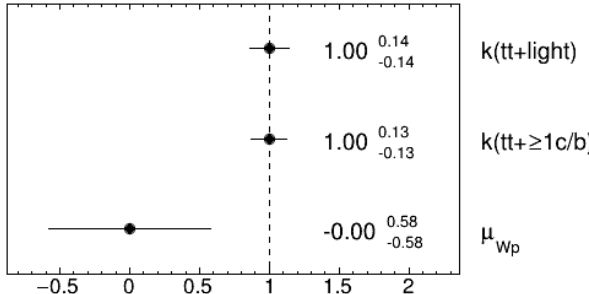
Figure 100: Signal strength and normalization factors (top) and correlation matrix (bottom) for the 1000 GeV W'_R mass hypotheses.



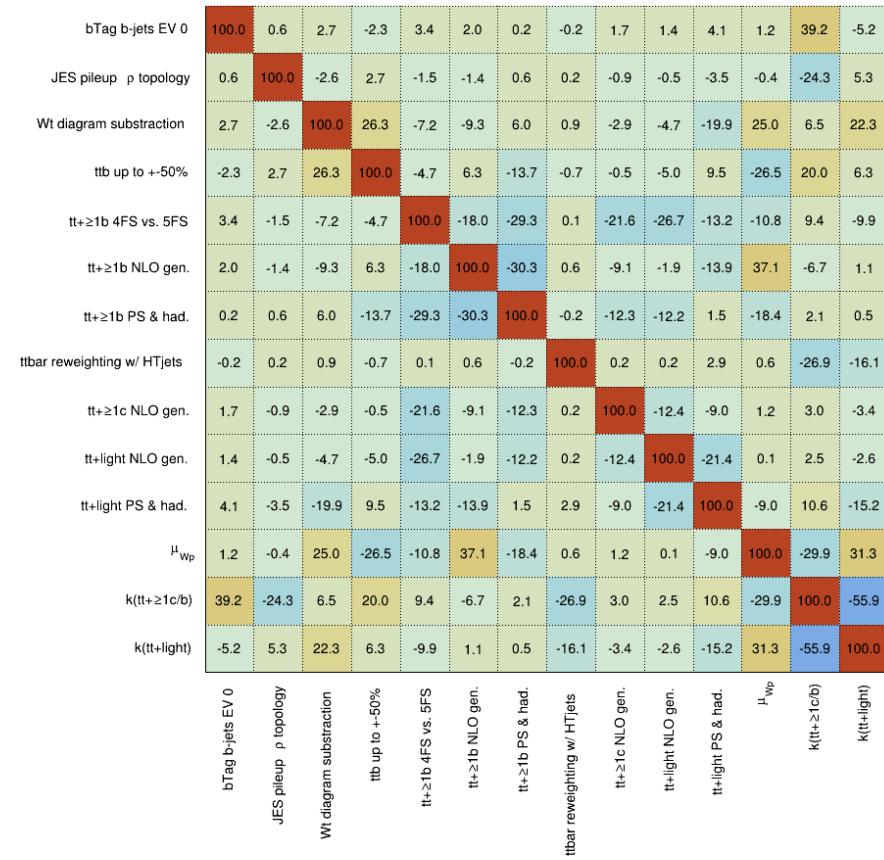
(a) Nuisance parameters

(b) Systematics ranking

Figure 101: Nuisance parameters (left) and ranking plot (right) of the effect of various nuisance parameters before and after the fit for the 1200 GeV W'_R mass hypotheses.

ATLAS Internal

(a) Norm. factors

ATLAS Internal

(b) Correlation matrix

Figure 102: Signal strength and normalization factors (top) and correlation matrix (bottom) for the 1200 GeV W'_R mass hypotheses.

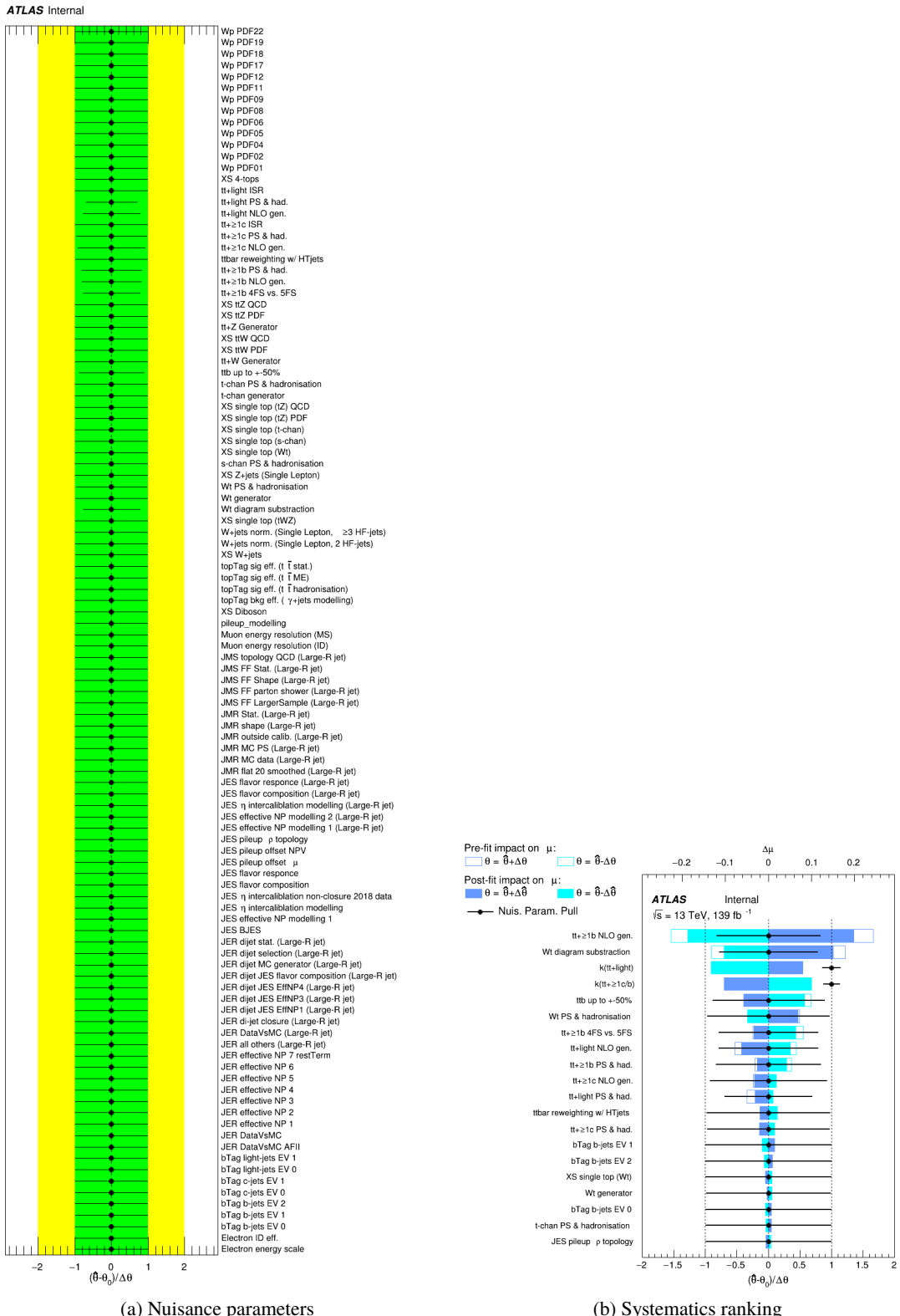
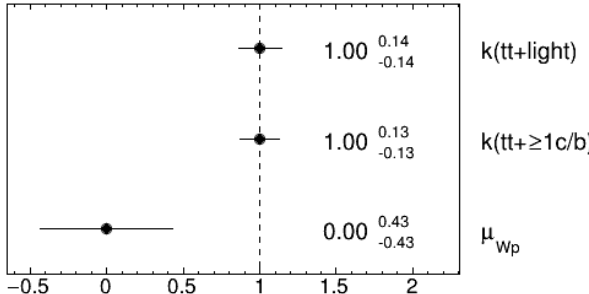


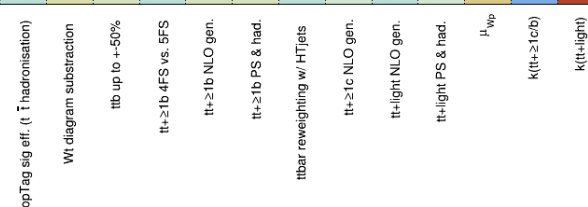
Figure 103: Nuisance parameters (left) and ranking plot (right) of the effect of various nuisance parameters before and after the fit for the 1400 GeV W'_R mass hypotheses.

ATLAS Internal

(a) Norm. factors

ATLAS Internal

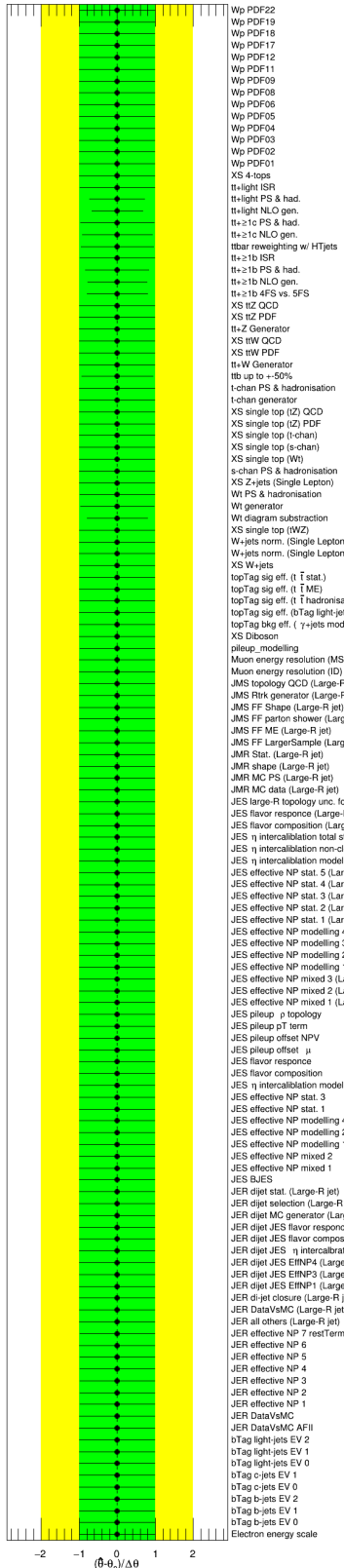
bTag b-jets EV 0	100.0	0.2	0.2	2.2	-0.4	2.2	0.6	-0.2	0.0	1.2	1.7	-0.8	1.7	40.3	-6.4
JES pileup p topology	0.2	100.0	-0.1	-2.0	0.5	-1.4	0.4	0.9	-0.2	-1.0	-1.4	0.7	-1.5	-25.1	6.3
topTag sig eff. ($t\bar{t}$ hadronisation)	0.2	-0.1	100.0	-0.4	-0.9	-6.3	-3.9	-3.3	0.5	-2.9	-6.2	-2.3	-1.0	-20.2	-15.5
Wt diagram subtraction	2.2	-2.0	-0.4	100.0	27.6	-13.5	-7.9	10.5	3.8	-4.3	-7.3	-10.7	33.7	4.8	18.8
ttb up to +50%	-0.4	0.5	-0.9	27.6	100.0	-8.3	2.5	-14.7	-4.4	-0.5	1.3	12.3	-18.0	22.7	3.3
tt+≥1b 4FS vs. 5FS	2.2	-1.4	-6.3	-13.5	-8.3	100.0	-32.1	-34.6	-0.3	-20.1	-28.4	13.6	-12.4	9.1	-12.2
tt+≥1b NLO gen.	0.6	0.4	-3.9	-7.9	2.5	-32.1	100.0	-34.6	6.8	-1.9	-6.8	-10.2	45.1	-12.1	5.3
tt+≥1b PS & had.	-0.2	0.9	-3.3	10.5	-14.7	-34.6	-34.6	100.0	1.7	-2.4	-3.3	4.0	-7.9	-1.2	3.7
ttbar reweighting w/ HTjets	0.0	-0.2	0.5	3.8	-4.4	-0.3	6.8	1.7	100.0	-0.6	4.2	13.0	-4.5	-25.3	-16.3
tt+≥1c NLO gen.	1.2	-1.0	-2.9	-4.3	-0.5	-20.1	-1.9	-2.4	-0.6	100.0	-24.3	3.9	-6.4	6.3	-6.4
tt+light NLO gen.	1.7	-1.4	-6.2	-7.3	1.3	-28.4	-6.8	-3.3	4.2	-24.3	100.0	-41.3	-13.3	9.0	-10.8
tt+light PS & had.	-0.8	0.7	-2.3	-10.7	12.3	13.6	-10.2	4.0	13.0	3.9	-41.3	100.0	-5.1	-3.0	-4.0
μ_{W_p}	1.7	-1.5	-1.0	33.7	-18.0	-12.4	45.1	-7.9	-4.5	-6.4	-13.3	-5.1	100.0	-23.4	31.1
k($t\bar{t}+\geq 1c/b$)	40.3	-25.1	-20.2	4.8	22.7	9.1	-12.1	-1.2	-25.3	6.3	9.0	-3.0	-23.4	100.0	-57.6
k($t\bar{t}+\text{light}$)	-6.4	6.3	-15.5	18.8	3.3	-12.2	5.3	3.7	-16.3	-6.4	-10.8	-4.0	31.1	-57.6	100.0



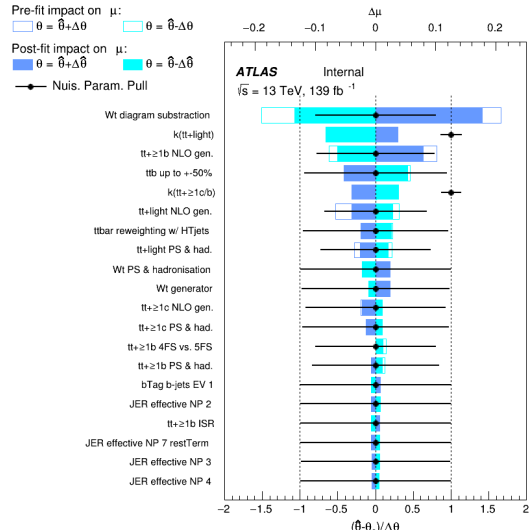
(b) Correlation matrix

Figure 104: Signal strength and normalization factors (top) and correlation matrix (bottom) for the 1400 GeV W'_R mass hypotheses.

ATLAS Internal

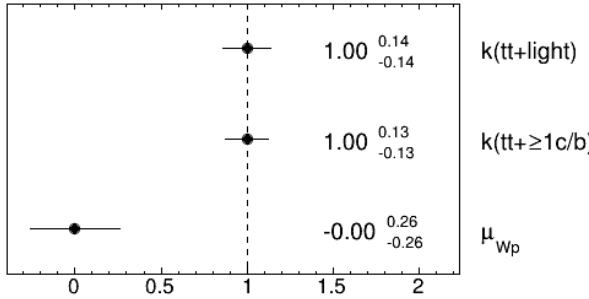
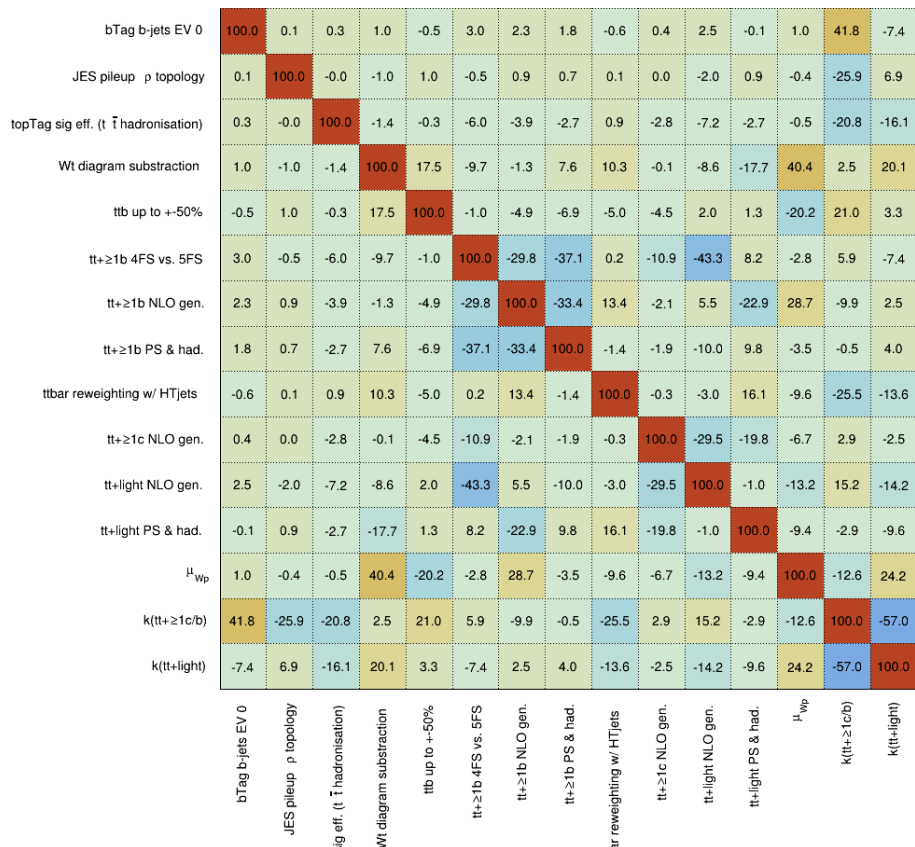


(a) Nuisance parameters



(b) Systematics ranking

Figure 105: Nuisance parameters (left) and ranking plot (right) of the effect of various nuisance parameters before and after the fit for the 1600 GeV W'_R mass hypotheses.

ATLAS Internal**ATLAS Internal**

(b) Correlation matrix

Figure 106: Signal strength and normalization factors (top) and correlation matrix (bottom) for the 1600 GeV W'_R mass hypotheses.

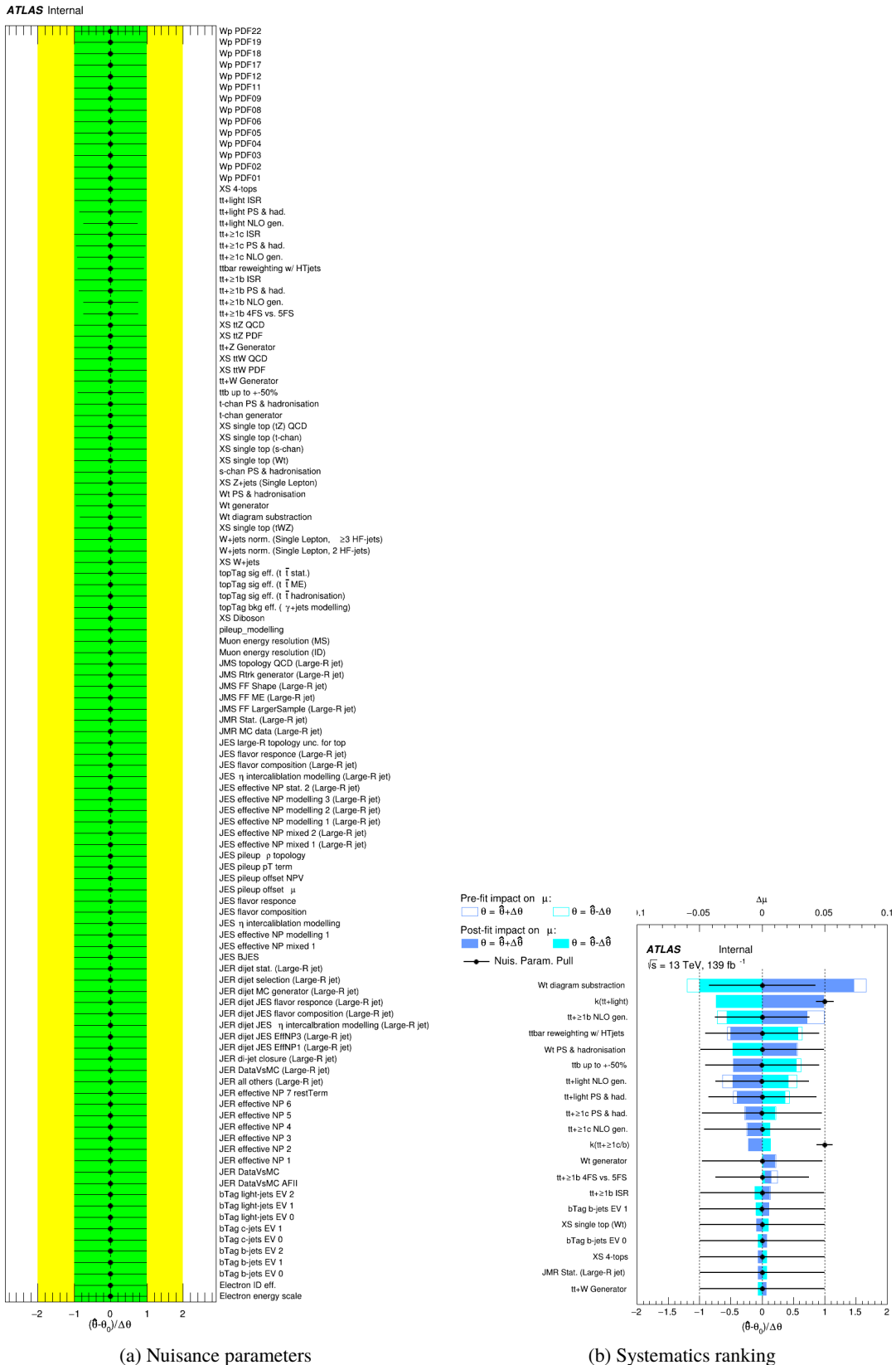
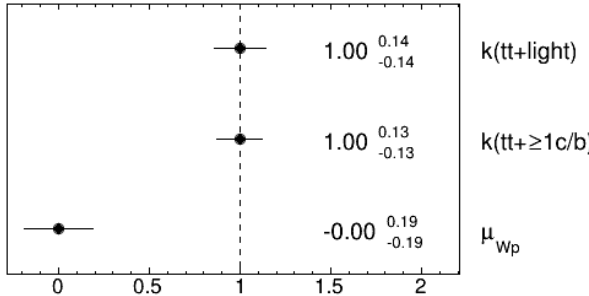


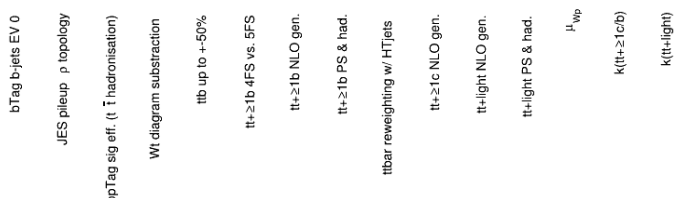
Figure 107: Nuisance parameters (left) and ranking plot (right) of the effect of various nuisance parameters before and after the fit for the 1800 GeV W'_R mass hypotheses.

ATLAS Internal

(a) Norm. factors

ATLAS Internal

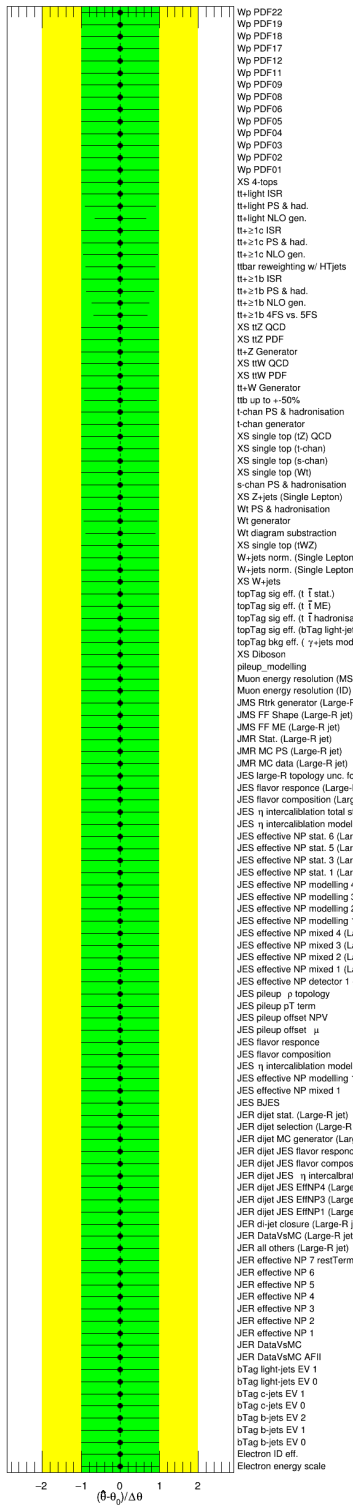
bTag b-jets EV 0	100.0	0.1	0.3	0.0	0.9	3.4	2.1	1.8	-0.2	0.9	1.4	-0.0	1.9	42.1	-7.7
JES pileup ρ topology	0.1	100.0	-0.1	0.2	-0.4	-0.8	0.6	0.1	-0.3	-0.7	-1.0	0.1	-1.5	-26.3	7.6
topTag sig eff. ($t\bar{t}$ hadronisation)	0.3	-0.1	100.0	-0.3	-0.5	-6.7	-3.0	-2.7	0.2	-2.6	-6.6	-1.4	-0.6	-20.9	-15.4
Wt diagram subtraction	0.0	0.2	-0.3	100.0	12.7	-3.5	-5.0	5.8	15.1	-2.7	-9.5	-11.2	35.7	-0.4	22.1
ttb up to +50%	0.9	-0.4	-0.5	12.7	100.0	-6.6	-2.6	-8.6	-10.2	-0.6	4.6	6.6	-15.2	24.0	-1.0
tt+ ≥ 1 b 4FS vs. 5FS	3.4	-0.8	-6.7	-3.5	-6.6	100.0	-28.5	-31.8	-4.6	-16.7	-37.6	6.3	1.5	5.7	-3.7
tt+ ≥ 1 b NLO gen.	2.1	0.6	-3.0	-5.0	-2.6	-28.5	100.0	-38.5	17.6	1.9	0.7	-13.0	17.1	-7.2	-1.6
tt+ ≥ 1 b PS & had.	1.8	0.1	-2.7	5.8	-8.6	-31.8	-38.5	100.0	0.8	-0.3	-2.0	-1.1	1.1	-1.1	3.3
ttbar reweighting w/ HTjets	-0.2	-0.3	0.2	15.1	-10.2	-4.6	17.6	0.8	100.0	-1.8	0.7	11.1	-14.4	-24.1	-10.4
tt+ ≥ 1 c NLO gen.	0.9	-0.7	-2.6	-2.7	-0.6	-16.7	1.9	-0.3	-1.8	100.0	-30.9	-9.2	-5.1	4.5	-4.4
tt+light NLO gen.	1.4	-1.0	-6.6	-9.5	4.6	-37.6	0.7	-2.0	0.7	-30.9	100.0	-27.1	-12.3	8.3	-11.1
tt+light PS & had.	-0.0	0.1	-1.4	-11.2	6.6	6.3	-13.0	-1.1	11.1	-9.2	-27.1	100.0	-10.6	-0.5	-7.7
μ_{W_p}	1.9	-1.5	-0.6	35.7	-15.2	1.5	17.1	1.1	-14.4	-5.1	-12.3	-10.6	100.0	-5.0	21.8
k(tt+ ≥ 1 c/b)	42.1	-26.3	-20.9	-0.4	24.0	5.7	-7.2	-1.1	-24.1	4.5	8.3	-0.5	-5.0	100.0	-59.0
k(tt+light)	-7.7	7.6	-15.4	22.1	-1.0	-3.7	-1.6	3.3	-10.4	-4.4	-11.1	-7.7	21.8	-59.0	100.0



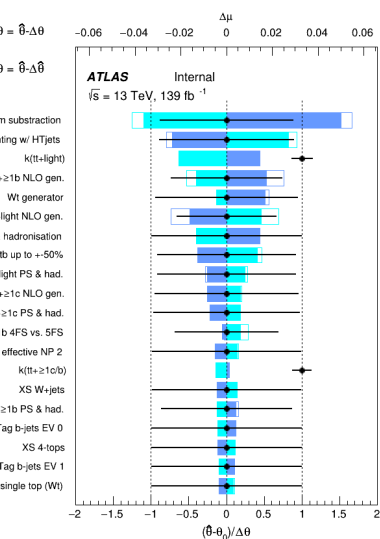
(b) Correlation matrix

Figure 108: Signal strength and normalization factors (top) and correlation matrix (bottom) for the 1800 GeV W'_R mass hypotheses.

ATLAS Internal

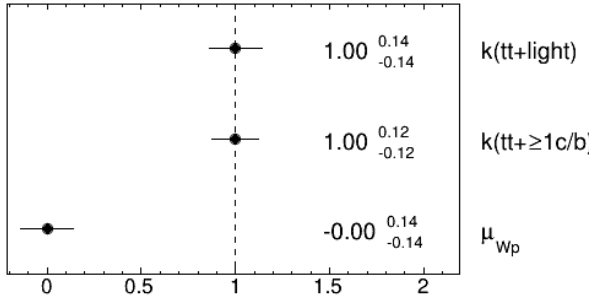


(a) Nuisance parameters



(b) Systematics ranking

Figure 109: Nuisance parameters (left) and ranking plot (right) of the effect of various nuisance parameters before and after the fit for the 2000 GeV W'_R mass hypotheses.

ATLAS Internal

(a) Norm. factors

ATLAS Internal

	bTag b-jets EV 0	0.1	0.2	-0.0	0.6	3.0	2.1	1.5	-0.0	0.6	2.0	0.2	2.9	42.3	-7.7
JES pileup ρ topology	0.1	100.0	-0.1	-0.2	0.2	-0.6	0.9	0.6	-0.1	-0.2	-2.4	-0.2	-1.5	-26.4	7.3
topTag sig eff. ($t\bar{t}$ hadronisation)	0.2	-0.1	100.0	-0.5	0.8	-8.1	-2.2	-2.8	0.1	-1.2	-6.6	-1.1	-0.8	-20.8	-15.6
Wt diagram subtraction	-0.0	-0.2	-0.5	100.0	8.1	-4.0	-3.7	5.5	17.3	-8.0	-11.3	-7.4	33.4	0.3	22.2
ttb up to +50%	0.6	0.2	0.8	8.1	100.0	2.3	-4.5	-5.8	-9.8	0.9	-1.1	3.4	-10.4	21.9	0.6
tt+ ≥ 1 b 4FS vs. 5FS	3.0	-0.6	-8.1	-4.0	2.3	100.0	-27.8	-42.1	-6.6	-6.8	-38.1	5.6	-3.2	9.2	-5.4
tt+ ≥ 1 b NLO gen.	2.1	0.9	-2.2	-3.7	-4.5	-27.8	100.0	-38.1	21.0	-8.5	0.2	-8.2	10.9	-8.0	-2.0
tt+ ≥ 1 b PS & had.	1.5	0.6	-2.8	5.5	-5.8	-42.1	-38.1	100.0	-2.3	-1.3	-3.4	1.5	3.0	-0.4	4.2
ttbar reweighting w/ HTjets	-0.0	-0.1	0.1	17.3	-9.8	-6.6	21.0	-2.3	100.0	8.3	-2.2	11.0	-17.8	-24.0	-8.7
tt+ ≥ 1 c NLO gen.	0.6	-0.2	-1.2	-8.0	0.9	-6.8	-8.5	-1.3	8.3	100.0	-21.7	-10.9	-5.5	-0.3	-6.0
tt+light NLO gen.	2.0	-2.4	-6.6	-11.3	-1.1	-38.1	0.2	-3.4	-2.2	-21.7	100.0	-28.0	-11.5	11.8	-14.5
tt+light PS & had.	0.2	-0.2	-1.1	-7.4	3.4	5.6	-8.2	1.5	11.0	-10.9	-28.0	100.0	-6.1	-1.1	-5.8
μ_{W_p}	2.9	-1.5	-0.8	33.4	-10.4	-3.2	10.9	3.0	-17.8	-5.5	-11.5	-6.1	100.0	2.3	16.6
k($t\bar{t} + \geq 1 c/b$)	42.3	-26.4	-20.8	0.3	21.9	9.2	-8.0	-0.4	-24.0	-0.3	11.8	-1.1	2.3	100.0	-58.6
k($t\bar{t}$ +light)	-7.7	7.3	-15.6	22.2	0.6	-5.4	-2.0	4.2	-8.7	-6.0	-14.5	-5.8	16.6	-58.6	100.0

(b) Correlation matrix

Figure 110: Signal strength and normalization factors (top) and correlation matrix (bottom) for the 2000 GeV W'_R mass hypotheses.

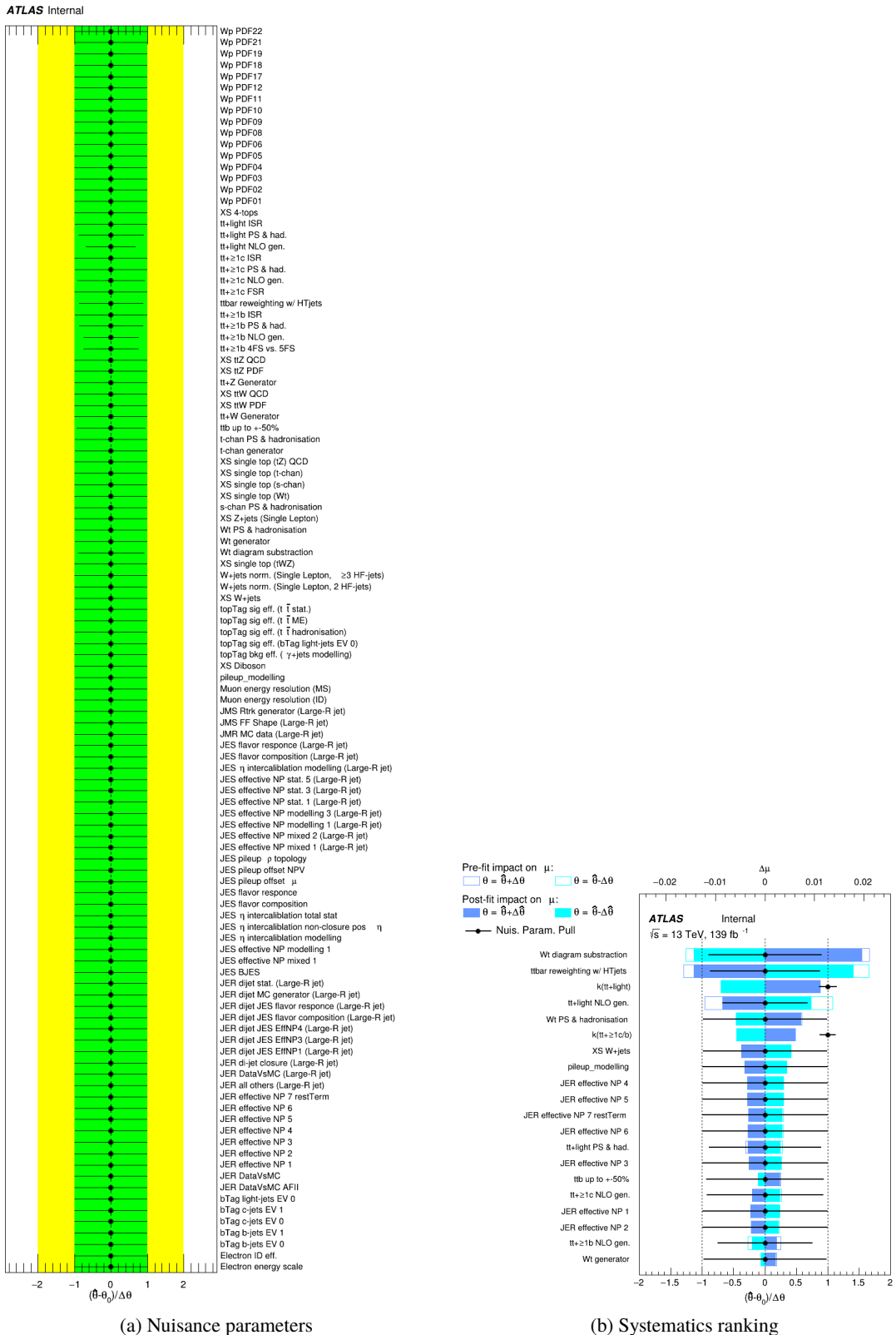
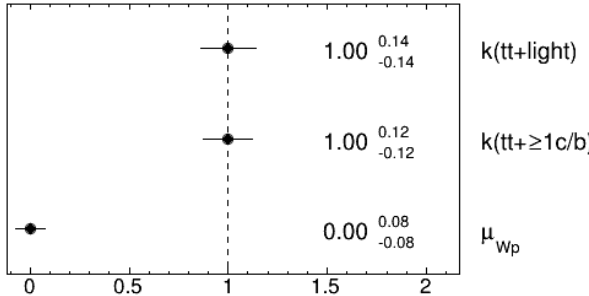


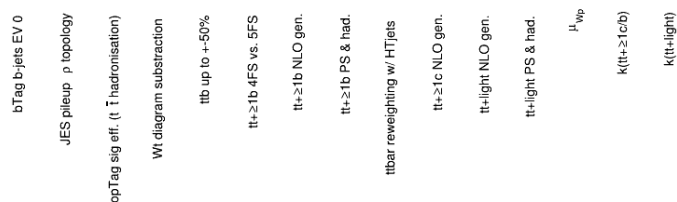
Figure 111: Nuisance parameters (left) and ranking plot (right) of the effect of various nuisance parameters before and after the fit for the 2500 GeV W'_R mass hypotheses.

ATLAS Internal

(a) Norm. factors

ATLAS Internal

bTag b-jets EV 0	100.0	0.1	0.2	-0.3	1.0	2.6	1.3	1.6	0.8	0.7	2.1	0.3	1.9	42.2	-8.2
JES pileup ρ topology	0.1	100.0	-0.1	-0.0	-0.3	-0.1	1.0	0.3	-0.5	-0.4	-1.9	-0.3	-1.4	-26.5	7.7
topTag sig eff. ($t\bar{t}$ hadronisation)	0.2	-0.1	100.0	-0.9	-0.5	-6.7	-1.5	-2.4	-0.5	-1.1	-7.0	0.5	-0.7	-21.0	-15.3
W_t diagram subtraction	-0.3	-0.0	-0.9	100.0	5.6	-6.7	-2.0	2.9	13.8	-5.8	-18.0	-3.1	25.1	1.3	23.4
ttb up to +50%	1.0	-0.3	-0.5	5.6	100.0	-7.5	2.6	-7.1	-14.5	-0.5	4.4	2.0	3.4	23.8	0.2
$t\bar{t}+\geq 1b$ 4FS vs. 5FS	2.6	-0.1	-6.7	-6.7	-7.5	100.0	-33.4	-38.9	-6.9	-6.3	-39.2	11.2	-2.2	4.2	-2.7
$t\bar{t}+\geq 1b$ NLO gen.	1.3	1.0	-1.5	-2.0	2.6	-33.4	100.0	-37.3	24.6	-8.9	5.2	-11.0	3.2	-7.3	-2.7
$t\bar{t}+\geq 1b$ PS & had.	1.6	0.3	-2.4	2.9	-7.1	-38.9	-37.3	100.0	-1.0	-2.9	1.2	4.0	0.1	-0.7	2.7
ttbar reweighting w/ HTjets	0.8	-0.5	-0.5	13.8	-14.5	-6.9	24.6	-1.0	100.0	6.6	7.2	11.6	-21.1	-23.0	-9.4
$t\bar{t}+\geq 1c$ NLO gen.	0.7	-0.4	-1.1	-5.8	-0.5	-6.3	-8.9	-2.9	6.6	100.0	-28.3	-16.3	-3.9	0.6	-5.5
$t\bar{t}+\text{light}$ NLO gen.	2.1	-1.9	-7.0	-18.0	4.4	-39.2	5.2	1.2	7.2	-28.3	100.0	-20.6	-12.1	9.1	-17.3
$t\bar{t}+\text{light}$ PS & had.	0.3	-0.3	0.5	-3.1	2.0	11.2	-11.0	4.0	11.6	-16.3	-20.6	100.0	-4.4	-0.9	-5.2
μ_{W_p}	1.9	-1.4	-0.7	25.1	3.4	-2.2	3.2	0.1	-21.1	-3.9	-12.1	-4.4	100.0	7.9	13.5
$k(t\bar{t}+\geq 1c/b)$	42.2	-26.5	-21.0	1.3	23.8	4.2	-7.3	-0.7	-23.0	0.6	9.1	-0.9	7.9	100.0	-58.8
$k(t\bar{t}+\text{light})$	-8.2	7.7	-15.3	23.4	0.2	-2.7	-2.7	2.7	-9.4	-5.5	-17.3	-5.2	13.5	-58.8	100.0



(b) Correlation matrix

Figure 112: Signal strength and normalization factors (top) and correlation matrix (bottom) for the 2500 GeV W'_R mass hypotheses.

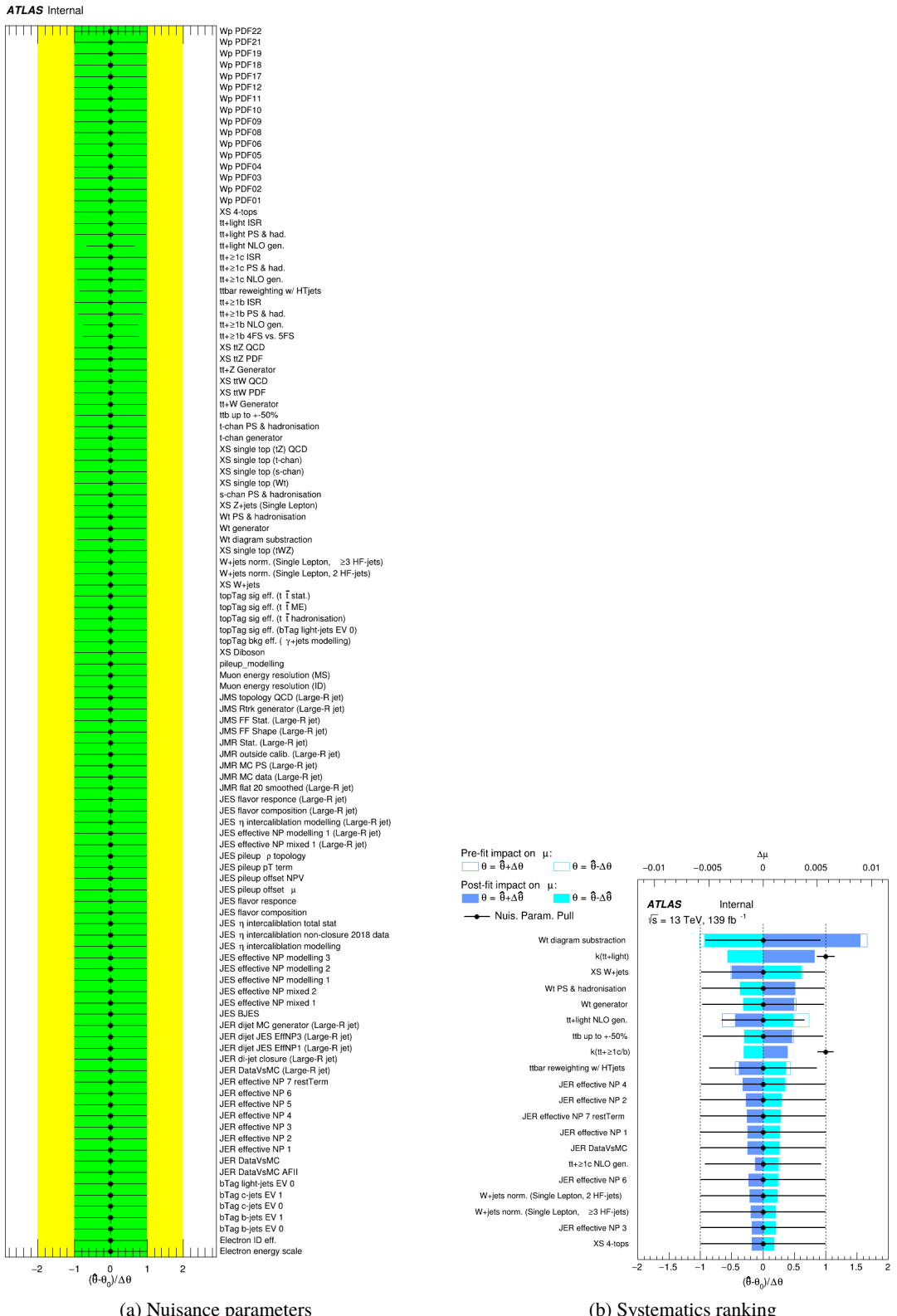
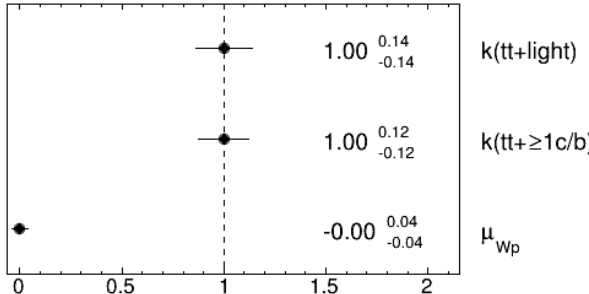


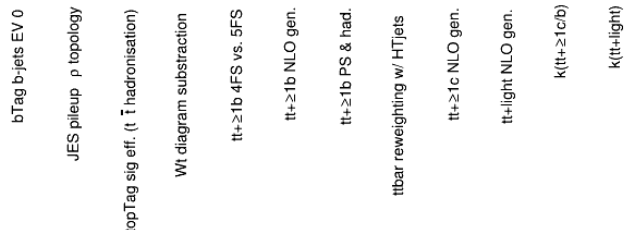
Figure 113: Nuisance parameters (left) and ranking plot (right) of the effect of various nuisance parameters before and after the fit for the 3000 GeV W'_R mass hypotheses.

ATLAS Internal

(a) Norm. factors

ATLAS Internal

bTag b-jets EV 0	100.0	0.0	0.1	0.0	1.1	0.0	0.4	0.5	0.8	3.4	42.1	-7.8
JES pileup p topology	0.0	100.0	0.0	0.2	0.6	-0.1	0.2	0.3	-0.0	0.4	-27.0	7.9
topTag sig eff. ($t\bar{t}$ hadronisation)	0.1	0.0	100.0	-0.3	-4.7	-2.6	-2.0	0.6	-1.4	-5.3	-21.5	-15.1
Wt diagram subtraction	0.0	0.2	-0.3	100.0	-0.9	-4.7	2.1	13.1	-8.0	-12.8	1.6	23.8
$tt+\geq 1b$ 4FS vs. 5FS	1.1	0.6	-4.7	-0.9	100.0	-36.1	-32.8	-5.0	-4.8	-47.3	3.9	-0.5
$tt+\geq 1b$ NLO gen.	0.0	-0.1	-2.6	-4.7	-36.1	100.0	-36.0	25.8	-5.8	7.1	-6.6	-5.8
$tt+\geq 1b$ PS & had.	0.4	0.2	-2.0	2.1	-32.8	-36.0	100.0	-1.0	3.0	-3.1	0.7	1.1
ttbar reweighting w/ HTjets	0.5	0.3	0.6	13.1	-5.0	25.8	-1.0	100.0	15.8	7.2	-22.0	-8.5
$tt+\geq 1c$ NLO gen.	0.8	-0.0	-1.4	-8.0	-4.8	-5.8	3.0	15.8	100.0	-34.0	-1.4	-8.0
$tt+\text{light}$ NLO gen.	3.4	0.4	-5.3	-12.8	-47.3	7.1	-3.1	7.2	-34.0	100.0	8.7	-14.3
$k(tt+\geq 1c/b)$	42.1	-27.0	-21.5	1.6	3.9	-6.6	0.7	-22.0	-1.4	8.7	100.0	-59.5
$k(tt+\text{light})$	-7.8	7.9	-15.1	23.8	-0.5	-5.8	1.1	-8.5	-8.0	-14.3	-59.5	100.0



(b) Correlation matrix

Figure 114: Signal strength and normalization factors (top) and correlation matrix (bottom) for the 3000 GeV W'_R mass hypotheses.

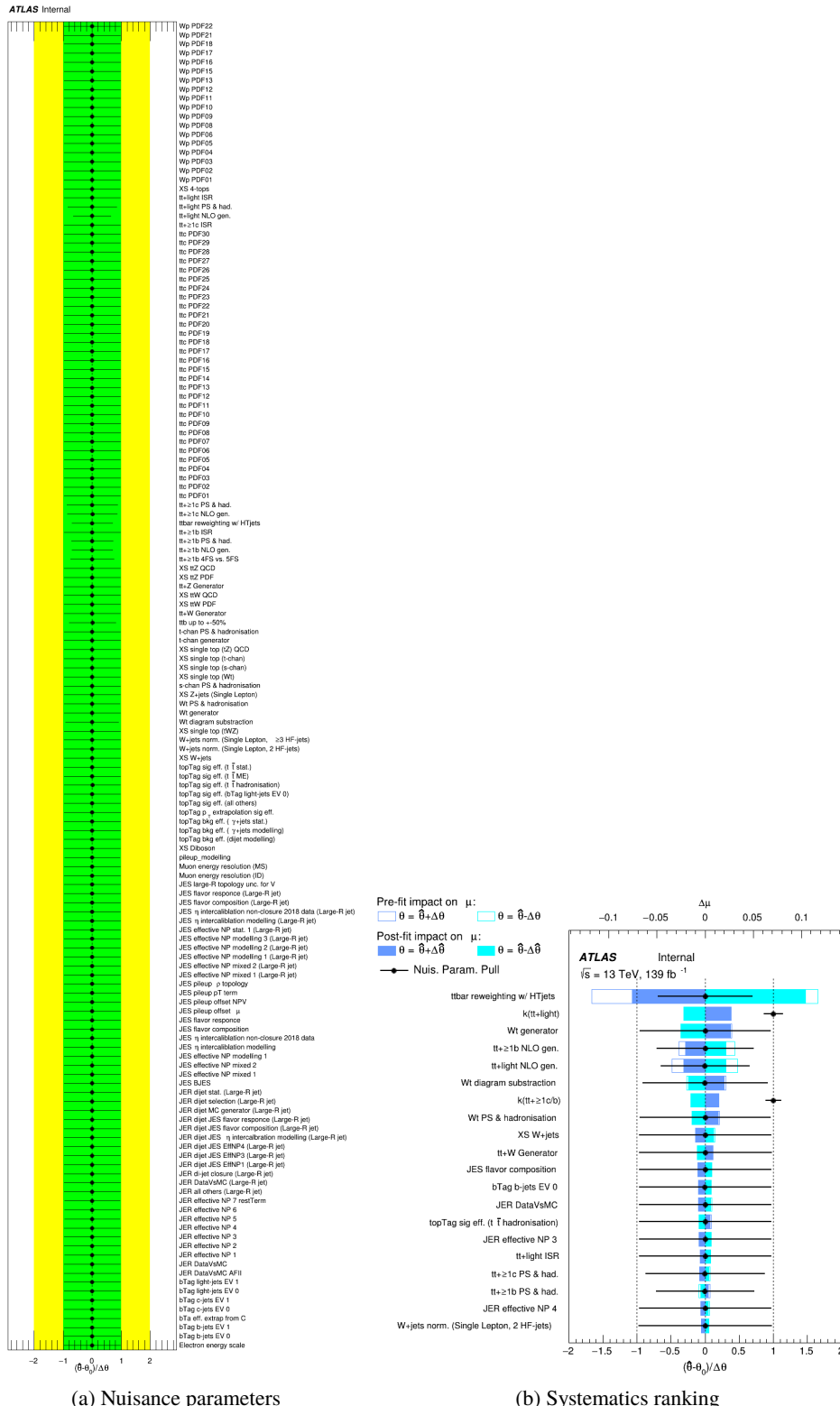
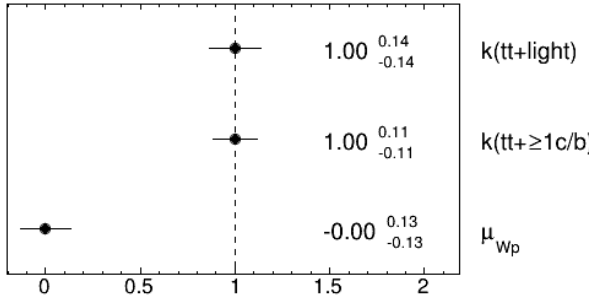


Figure 115: Nuisance parameters (left) and ranking plot (right) of the effect of various nuisance parameters before and after the fit for the 4000 GeV W'_R mass hypotheses.

ATLAS Internal

(a) Norm. factors

ATLAS Internal

bTag b-jets EV 0	100.0	0.1	1.4	0.7	0.3	6.8	-1.1	4.7	6.3	4.6	0.1	1.0	-4.4	41.2	-6.6
JES pileup ρ topology	0.1	100.0	0.6	0.0	0.1	2.9	1.0	0.4	-0.3	0.7	-1.0	0.4	-2.2	-27.3	6.8
topTag sig eff. ($t\bar{t}$ hadronisation)	1.4	0.6	100.0	-1.0	-0.4	-8.7	-1.5	-3.6	-2.4	-4.5	-3.2	-3.3	4.3	-21.1	-15.4
W_t diagram subtraction	0.7	0.0	-1.0	100.0	-3.0	-3.5	-3.8	2.2	4.8	-9.0	-15.8	-6.3	15.5	4.6	27.2
W_t generator	0.3	0.1	-0.4	-3.0	100.0	-0.4	0.4	1.4	0.4	-2.7	-8.3	-2.2	20.9	-3.6	6.0
$t\bar{t}+\geq 1b$ 4FS vs. 5FS	6.8	2.9	-8.7	-3.5	-0.4	100.0	-23.2	-36.4	-2.2	-22.2	5.5	-12.1	1.8	8.0	-5.0
$t\bar{t}+\geq 1b$ NLO gen.	-1.1	1.0	-1.5	-3.8	0.4	-23.2	100.0	-44.9	17.4	-3.6	-13.8	-6.2	-15.9	-9.6	2.1
$t\bar{t}+\geq 1b$ PS & had.	4.7	0.4	-3.6	2.2	1.4	-36.4	-44.9	100.0	-3.6	-6.6	3.8	4.8	3.0	0.9	2.6
ttbar reweighting w/ HTjets	6.3	-0.3	-2.4	4.8	0.4	-2.2	17.4	-3.6	100.0	-2.7	11.3	-2.4	-76.4	-9.3	-14.1
$t\bar{t}+\geq 1c$ NLO gen.	4.6	0.7	-4.5	-9.0	-2.7	-22.2	-3.6	-6.6	-2.7	100.0	-20.9	-11.4	0.8	6.9	-5.8
$t\bar{t}+\text{light}$ NLO gen.	0.1	-1.0	-3.2	-15.8	-8.3	5.5	-13.8	3.8	11.3	-20.9	100.0	-53.5	-16.1	0.2	-9.1
$t\bar{t}+\text{light}$ PS & had.	1.0	0.4	-3.3	-6.3	-2.2	-12.1	-6.2	4.8	-2.4	-11.4	-53.5	100.0	-1.2	3.6	-4.5
μ_{W_p}	-4.4	-2.2	4.3	15.5	20.9	1.8	-15.9	3.0	-76.4	0.8	-16.1	-1.2	100.0	11.3	18.4
$k(t\bar{t}+\geq 1c/b)$	41.2	-27.3	-21.1	4.6	-3.6	8.0	-9.6	0.9	-9.3	6.9	0.2	3.6	11.3	100.0	-58.9
$k(t\bar{t}+\text{light})$	-6.6	6.8	-15.4	27.2	6.0	-5.0	2.1	2.6	-14.1	-5.8	-9.1	-4.5	18.4	-58.9	100.0

(b) Correlation matrix

Figure 116: Signal strength and normalization factors (top) and correlation matrix (bottom) for the 4000 GeV W'_R mass hypotheses.

802 **7.3.3 Post-fit plots**

803 Figure 124 to 126 show the post-fit plots for each H^+ mass hypotheses. Similarly, Figure 127 to 135 and
 804 Figure 136 to 144 show the post-fit plots for each W'_L and W'_R mass hypotheses, respectively.

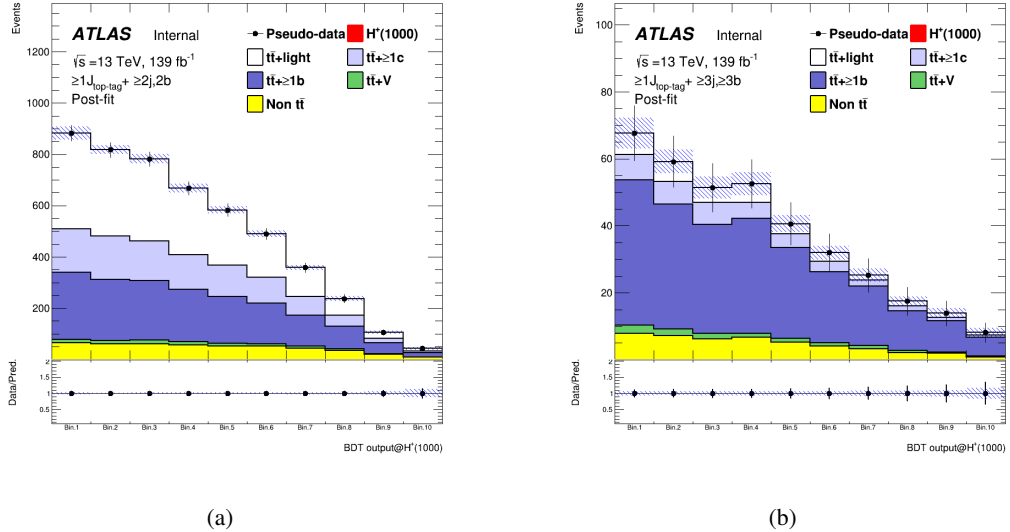


Figure 117: Post-fit plots in the SR1 (left) and SR2 (right) for 1000 GeV mass hypothesis of H^+ signal.

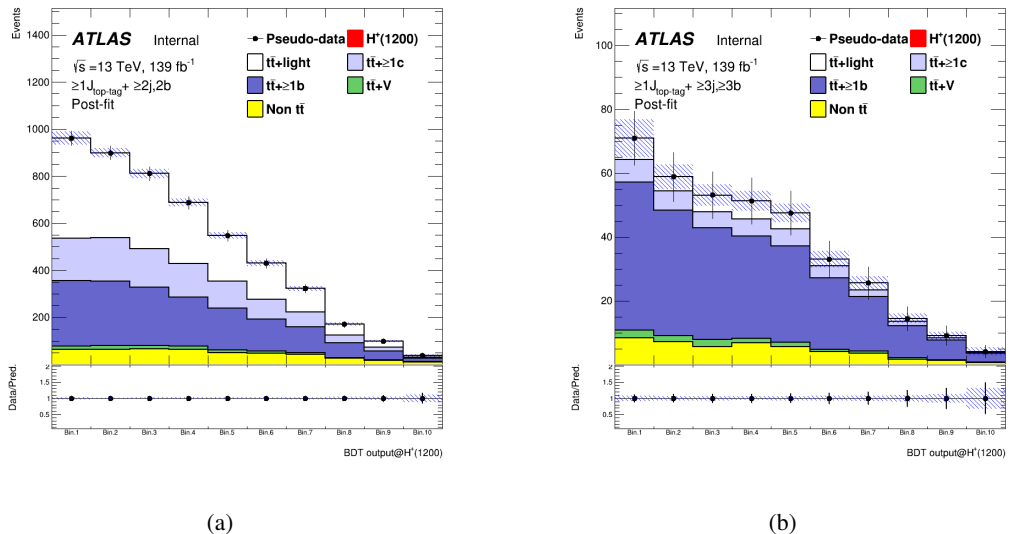


Figure 118: Post-fit plots in the SR1 (left) and SR2 (right) for 1200 GeV mass hypothesis of H^+ signal.

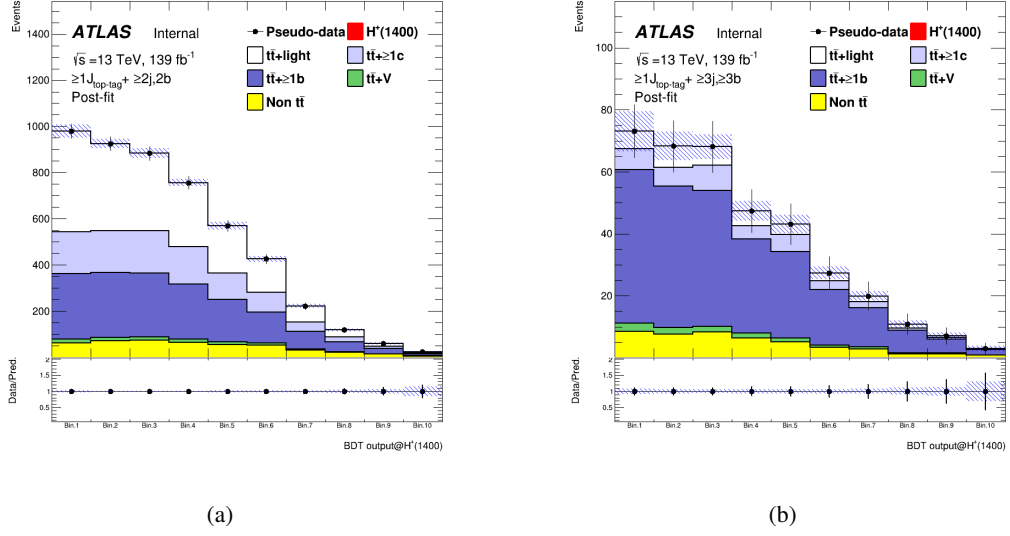


Figure 119: Post-fit plots in the SR1 (left) and SR2 (right) for 1400 GeV mass hypothesis of H^+ signal.

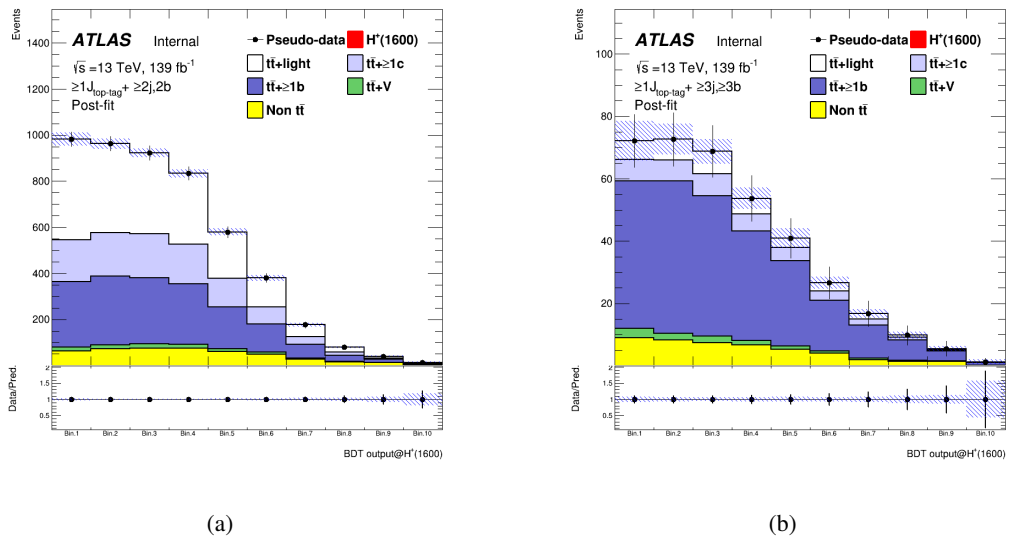


Figure 120: Post-fit plots in the SR1 (left) and SR2 (right) for 1600 GeV mass hypothesis of H^+ signal.

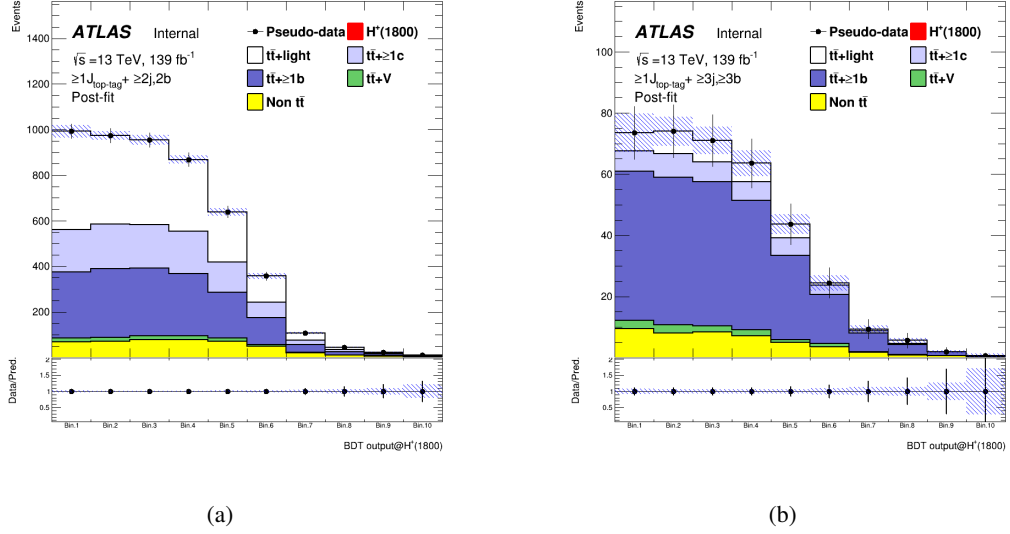


Figure 121: Post-fit plots in the SR1 (left) and SR2 (right) for 1800 GeV mass hypothesis of H^+ signal.

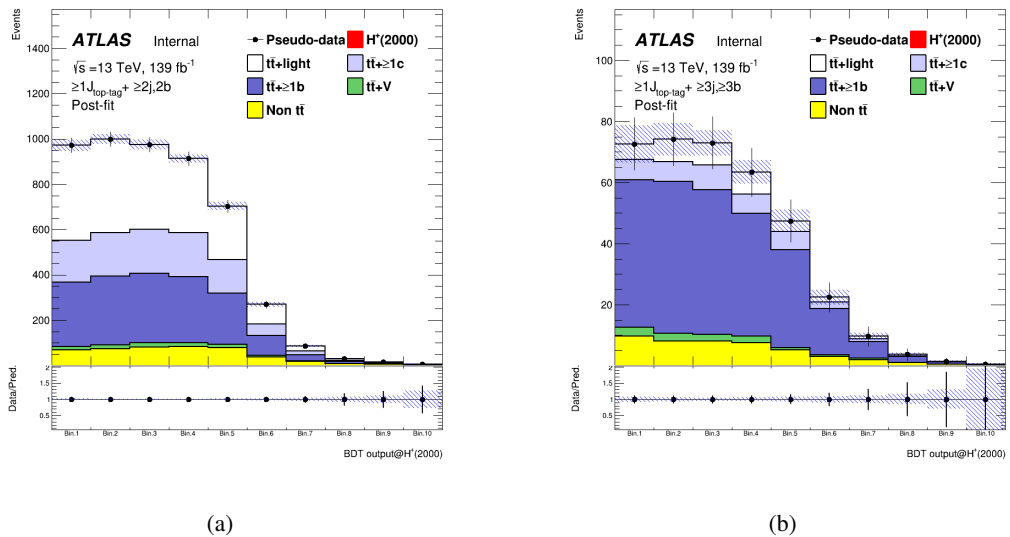


Figure 122: Post-fit plots in the SR1 (left) and SR2 (right) for 2000 GeV mass hypothesis of H^+ signal.

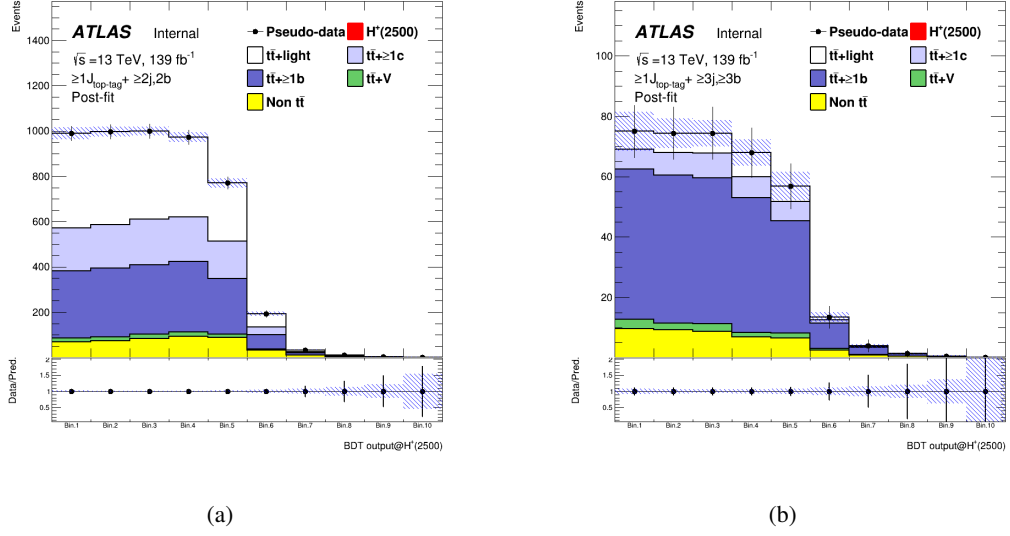


Figure 123: Post-fit plots in the SR1 (left) and SR2 (right) for 2500 GeV mass hypothesis of H^+ signal.

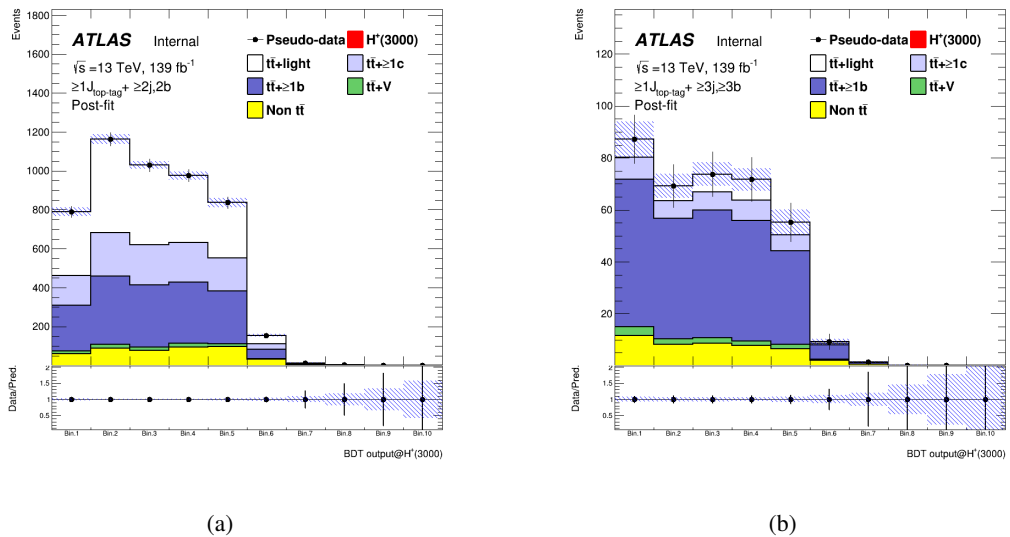
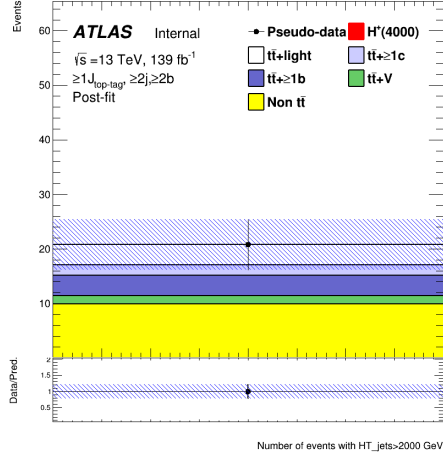
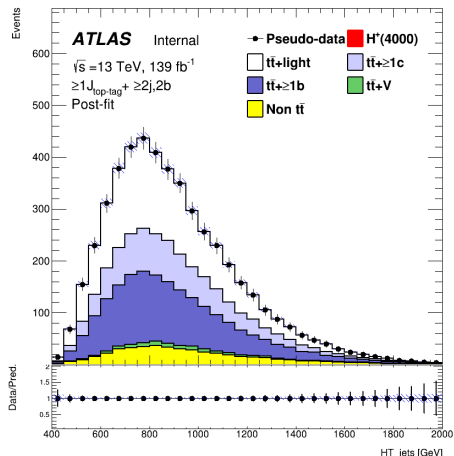


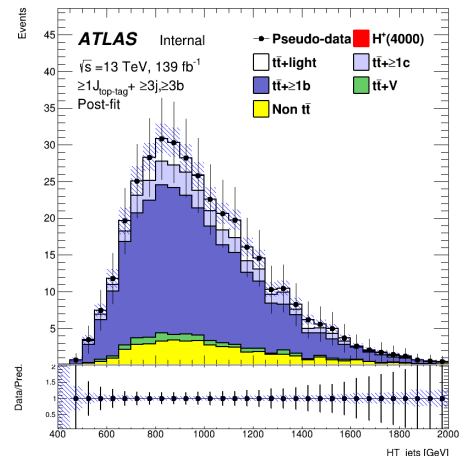
Figure 124: Post-fit plots in the SR1 (left) and SR2 (right) for 3000 GeV mass hypothesis of H^+ signal.



(a)

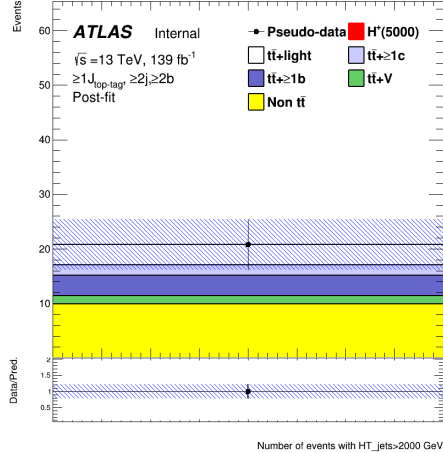


(b)

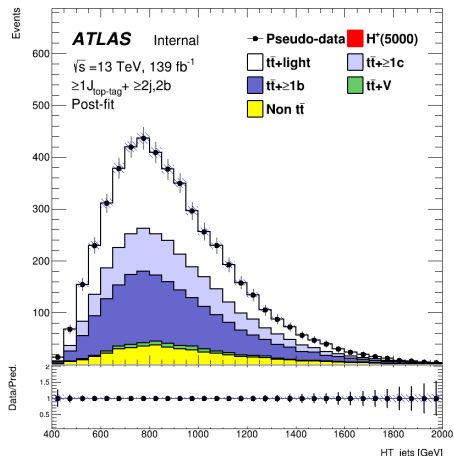


(c)

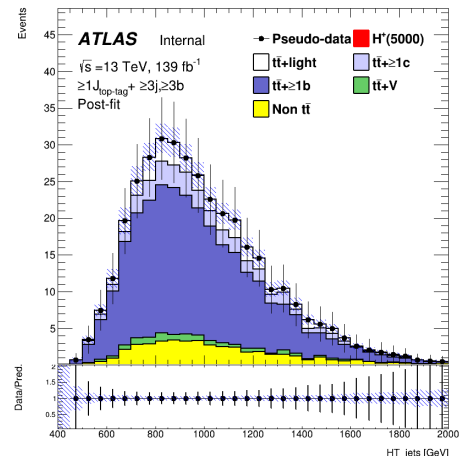
Figure 125: Post-fit plots in the SR (top), CR1 (bottom-left), and CR2 (bottom-right) for 4000 GeV mass hypothesis of H^+ signal.



(a)



(b)



(c)

Figure 126: Post-fit plots in the SR (top), CR1 (bottom-left), and CR2 (bottom-right) for 5000 GeV mass hypothesis of H^+ signal.

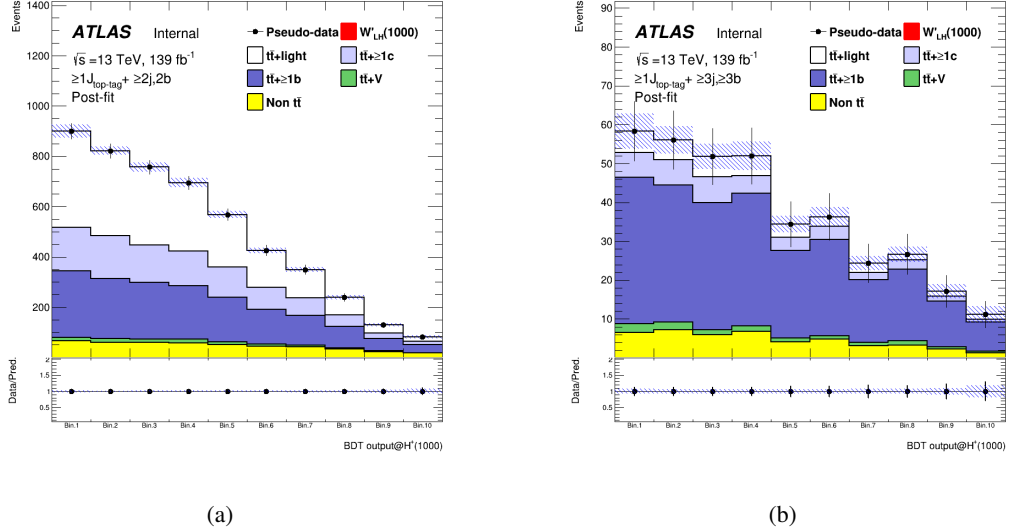


Figure 127: Post-fit plots in the SR1 (left) and SR2 (right) for 1000 GeV mass hypothesis of W'_{L} signal.

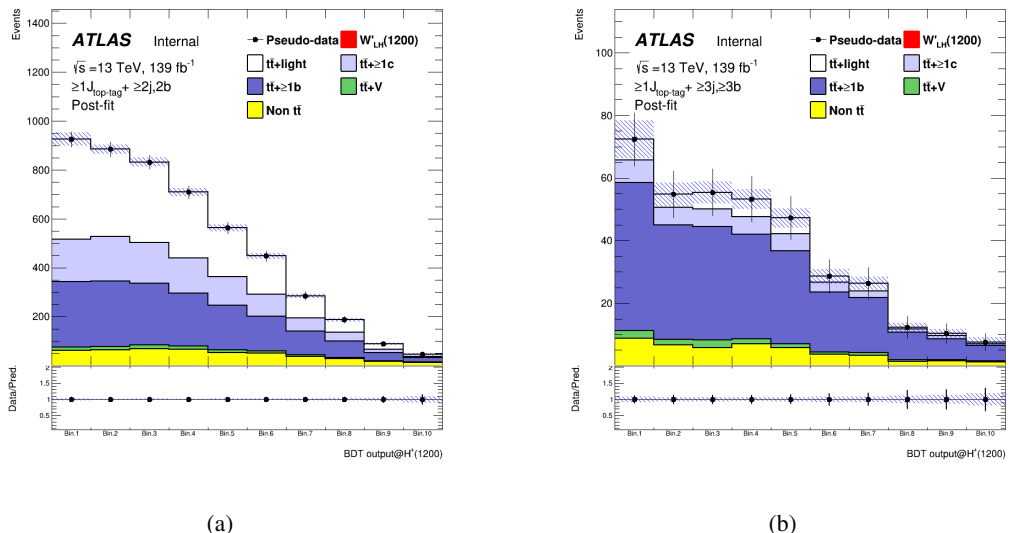


Figure 128: Post-fit plots in the SR1 (left) and SR2 (right) for 1200 GeV mass hypothesis of W'_{L} signal.

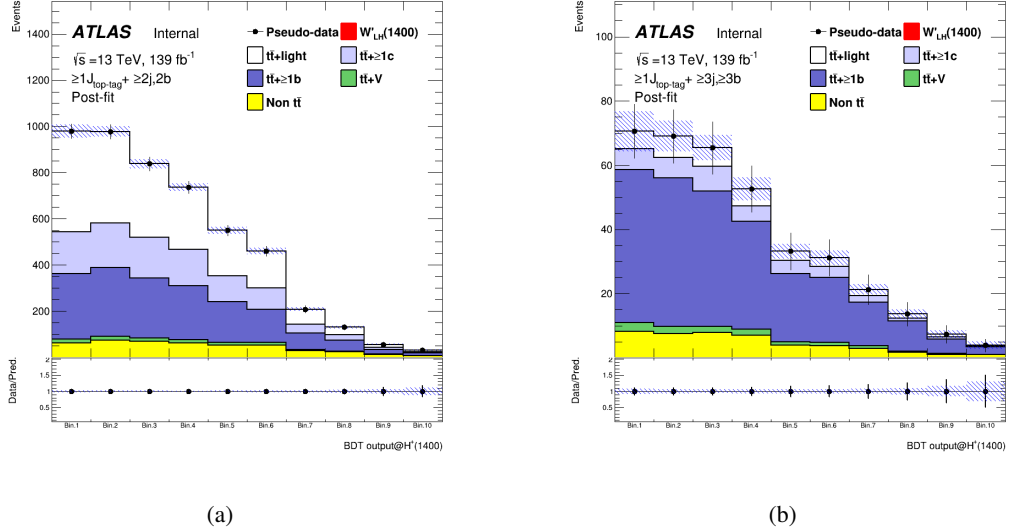


Figure 129: Post-fit plots in the SR1 (left) and SR2 (right) for 1400 GeV mass hypothesis of W'_L signal.

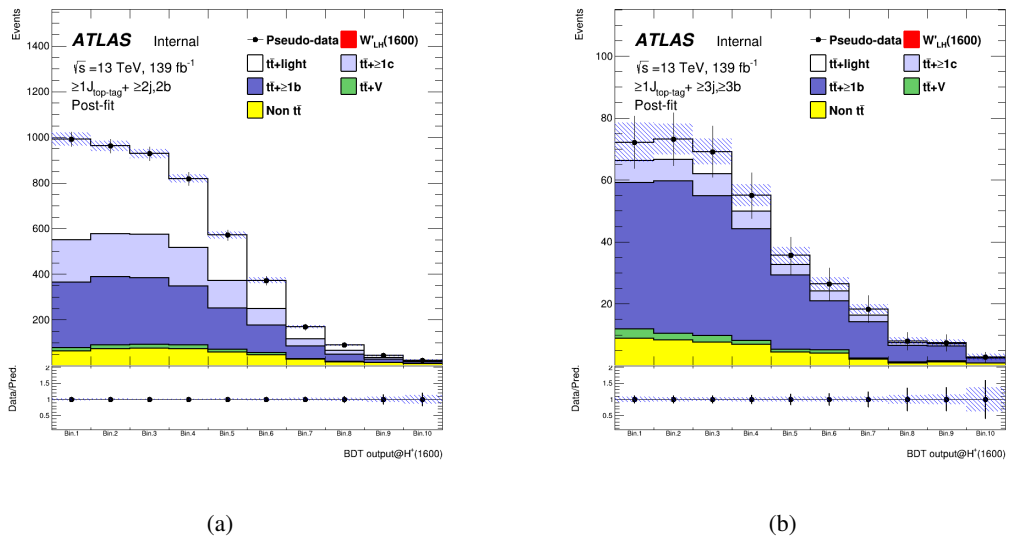


Figure 130: Post-fit plots in the SR1 (left) and SR2 (right) for 1600 GeV mass hypothesis of W'_L signal.

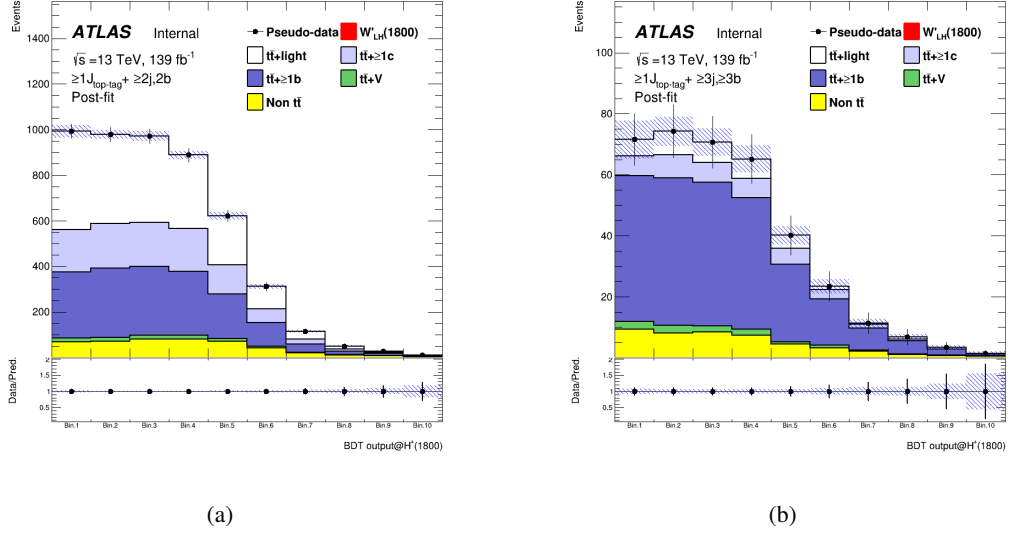


Figure 131: Post-fit plots in the SR1 (left) and SR2 (right) for 1800 GeV mass hypothesis of W'_L signal.

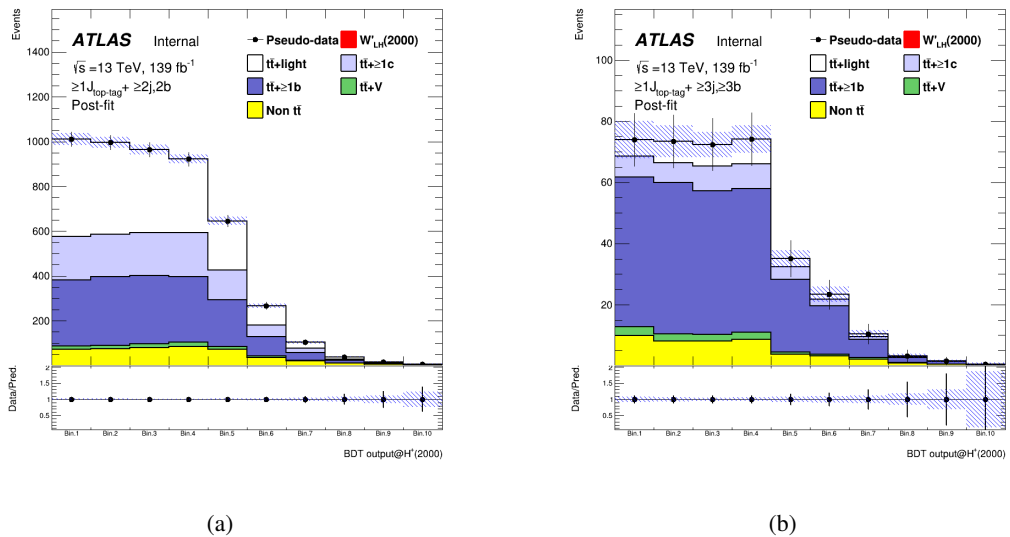


Figure 132: Post-fit plots in the SR1 (left) and SR2 (right) for 2000 GeV mass hypothesis of W'_L signal.

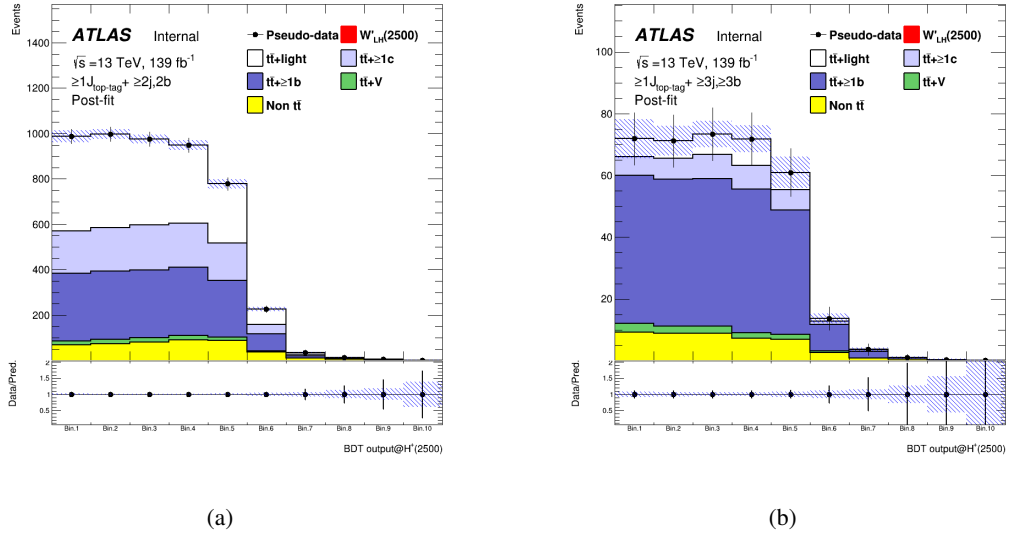


Figure 133: Post-fit plots in the SR1 (left) and SR2 (right) for 2500 GeV mass hypothesis of W'_L signal.

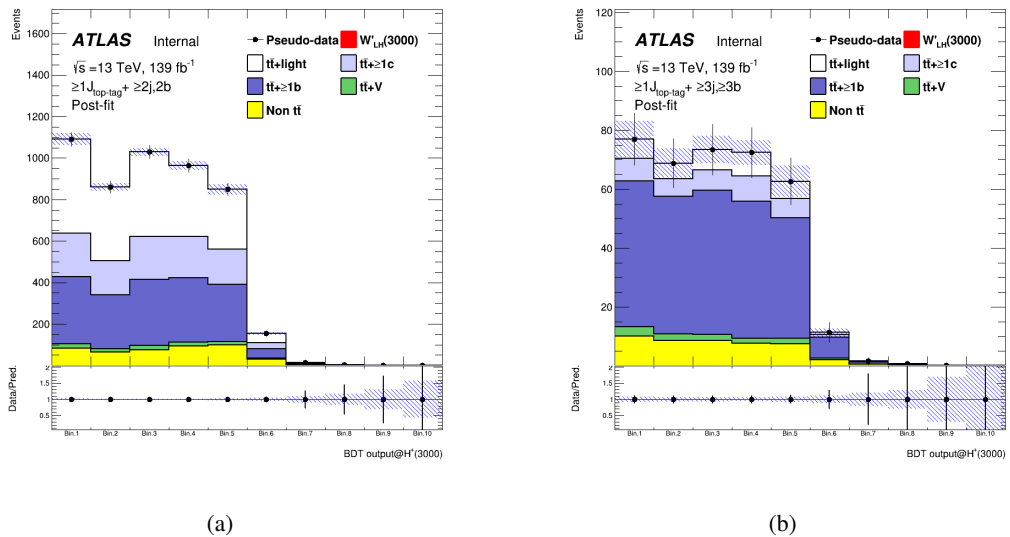
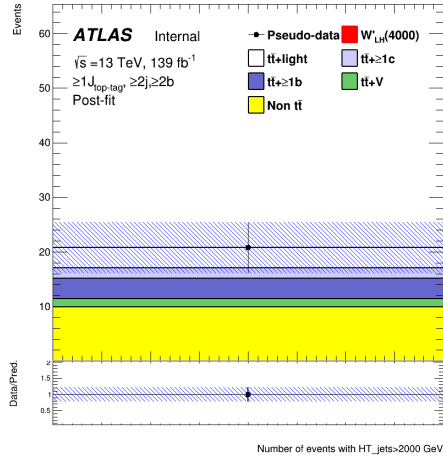
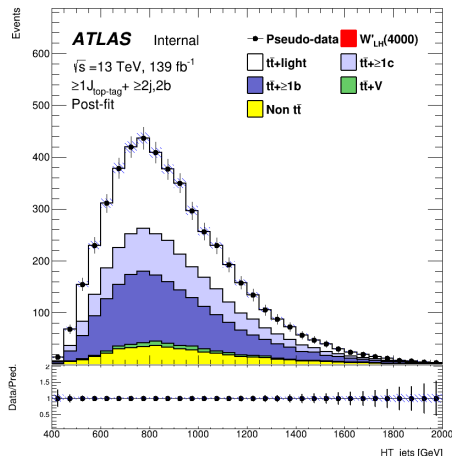


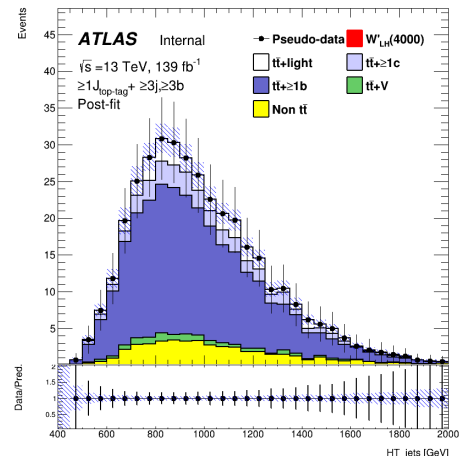
Figure 134: Post-fit plots in the SR1 (left) and SR2 (right) for 3000 GeV mass hypothesis of W'_L signal.



(a)



(b)



(c)

Figure 135: Post-fit plots in the SR (top), CR1 (bottom-left), and CR2 (bottom-right) for 4000 GeV mass hypothesis of W'_L signal.

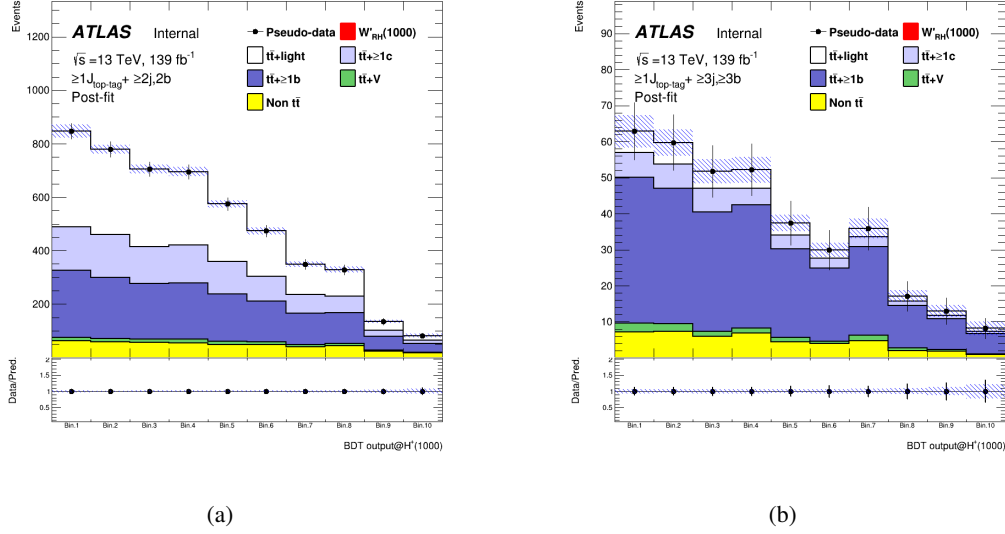


Figure 136: Post-fit plots in the SR1 (left) and SR2 (right) for 1000 GeV mass hypothesis of W'_R signal.

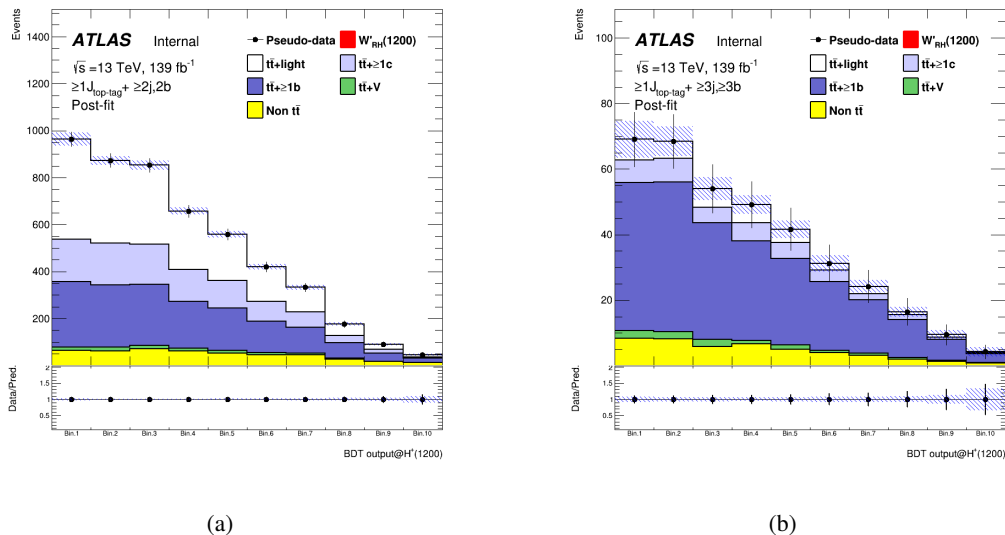


Figure 137: Post-fit plots in the SR1 (left) and SR2 (right) for 1200 GeV mass hypothesis of W'_R signal.

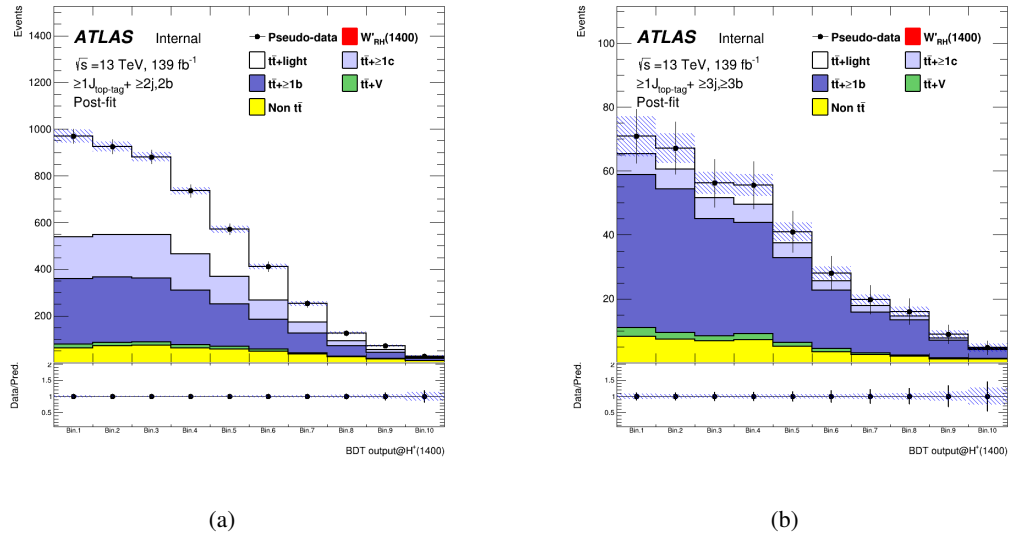


Figure 138: Post-fit plots in the SR1 (left) and SR2 (right) for 1400 GeV mass hypothesis of W'_R signal.

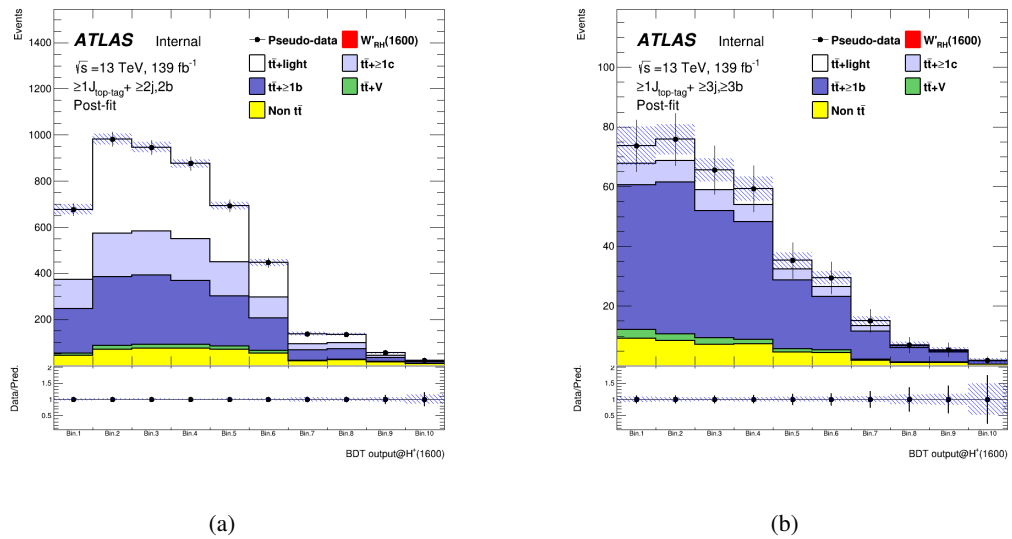


Figure 139: Post-fit plots in the SR1 (left) and SR2 (right) for 1600 GeV mass hypothesis of W'_R signal.

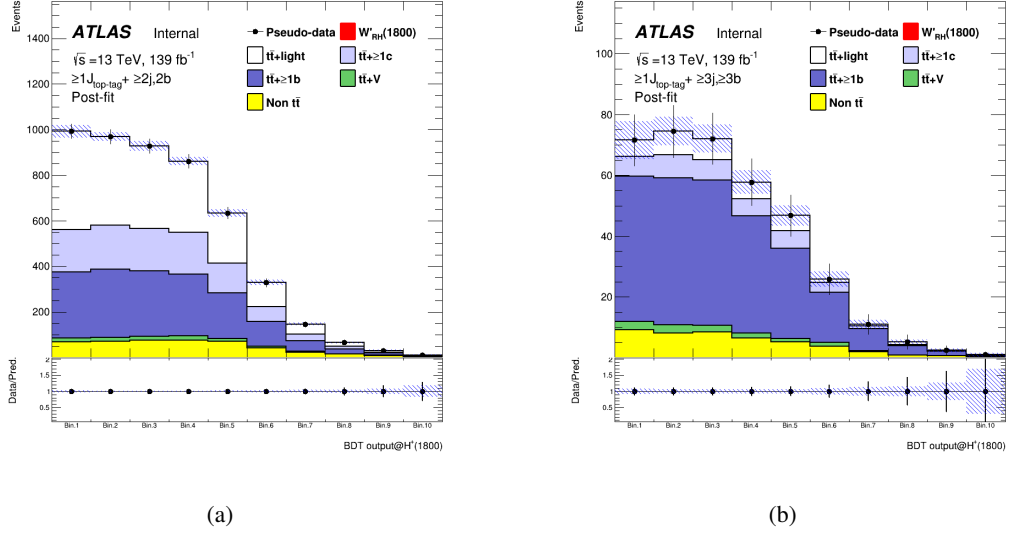


Figure 140: Post-fit plots in the SR1 (left) and SR2 (right) for 1800 GeV mass hypothesis of W'_R signal.

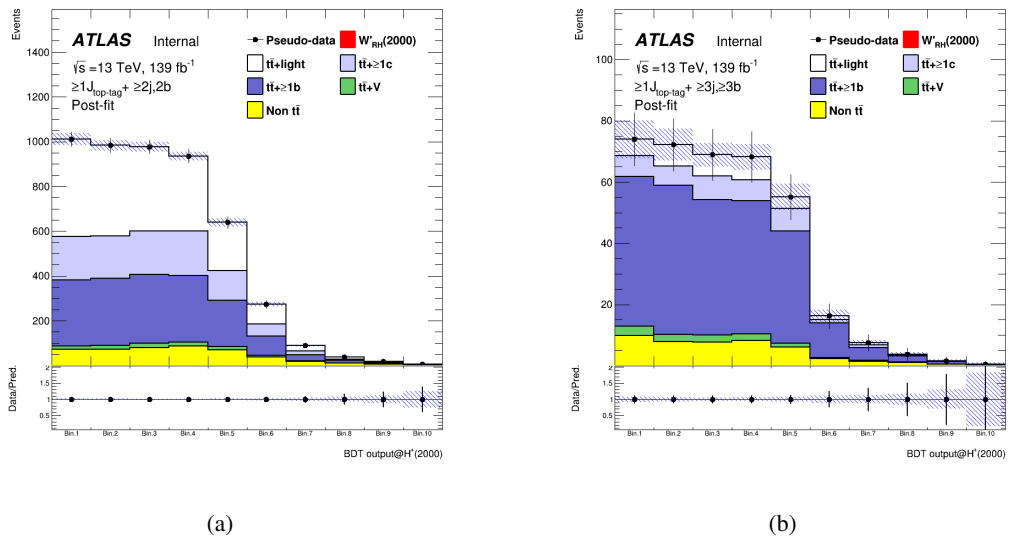


Figure 141: Post-fit plots in the SR1 (left) and SR2 (right) for 2000 GeV mass hypothesis of W'_R signal.

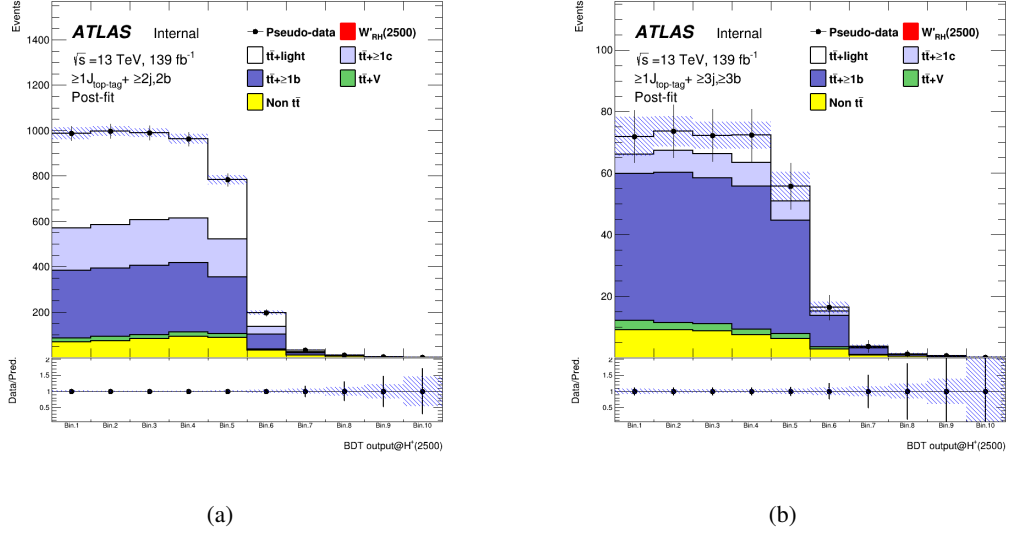


Figure 142: Post-fit plots in the SR1 (left) and SR2 (right) for 2500 GeV mass hypothesis of W'_R signal.

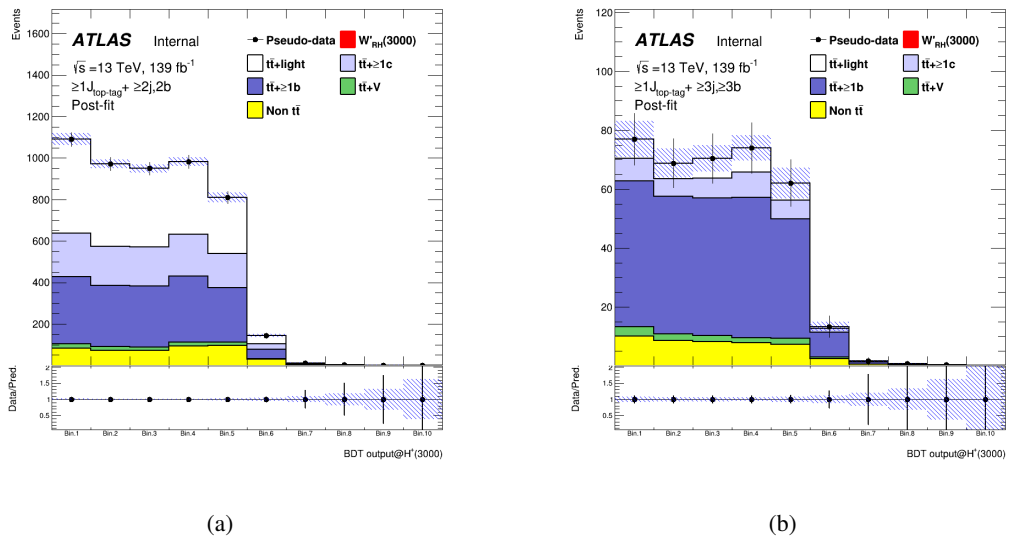


Figure 143: Post-fit plots in the SR1 (left) and SR2 (right) for 3000 GeV mass hypothesis of W'_R signal.

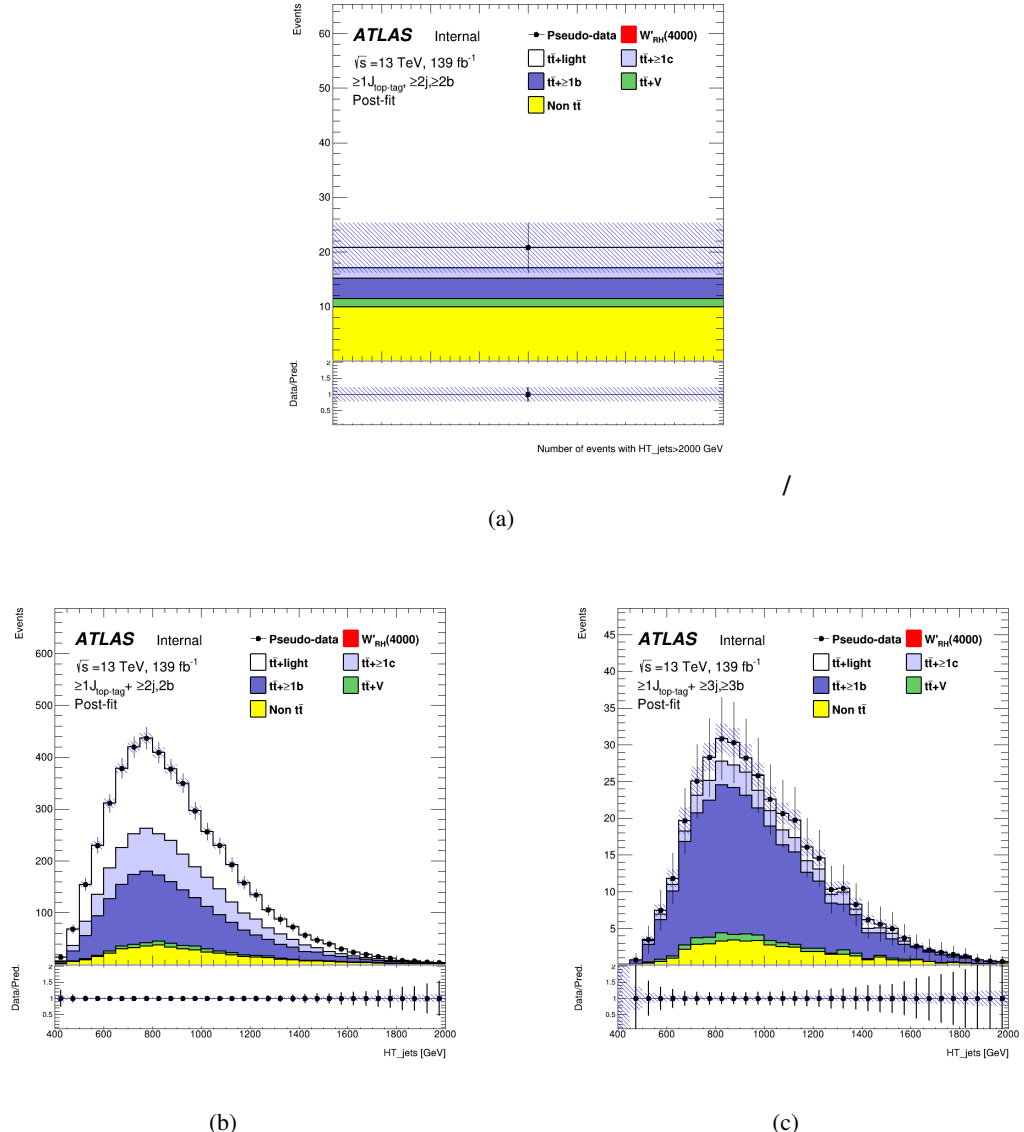


Figure 144: Post-fit plots in the SR (top), CR1 (bottom-left), and CR2 (bottom-right) for 4000 GeV mass hypothesis of W'_R signal.

805 7.3.4 Asimov fit results summary

806 Figure 145 to Figure 147 shows the fitted signal strength and $t\bar{t}$ + light and $t\bar{t}$ + $\geq 1c/b$ normalization factors
807 as a function of the signal mass hypothesis of the Asimov fit.

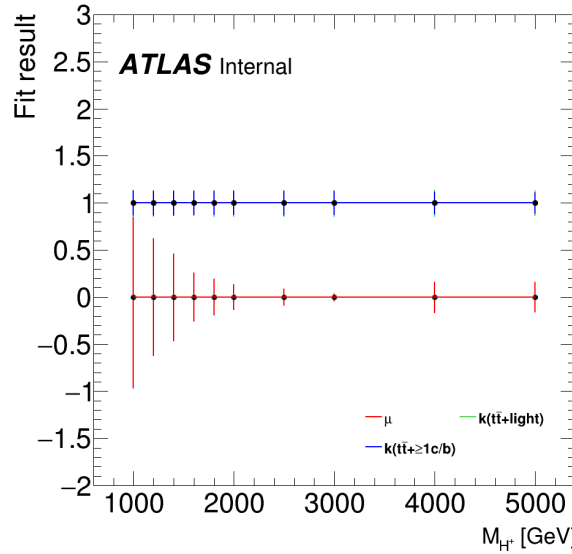


Figure 145: Fitted signal strength and $t\bar{t} + \text{light}$ and $t\bar{t} + \geq 1 c/b$ normalisation factors as a function of the H^+ mass hypothesis of the Asimov fit

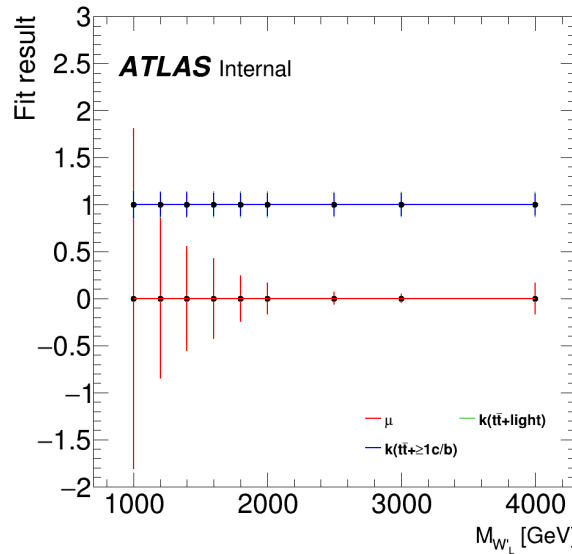


Figure 146: Fitted signal strength and $t\bar{t} + \text{light}$ and $t\bar{t} + \geq 1 c/b$ normalisation factors as a function of the W'_L mass hypothesis of the Asimov fit

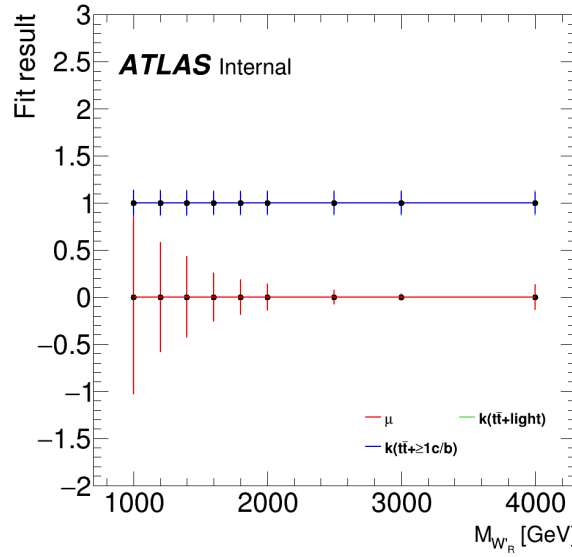


Figure 147: Fitted signal strength and $t\bar{t} + \text{light}$ and $t\bar{t} + \geq 1 c/b$ normalisation factors as a function of the W'_R mass hypothesis of the Asimov fit

808 7.4 Upper cross-section limits as a function of signal mass

809 The 95% confidence level (CL) upper limit for each production of $H^+ \rightarrow tb$ and $W'_{L/R} \rightarrow tb$ in association
 810 with a top quark and a bottom quark using the CL_S method is shown in Figure 148 to 150. The expected
 811 upper limits for H^+ signals are set between 0.0889 to 0.0067 pb in the mass range of $1000 \leq M_{H^+} \leq 5000$
 812 GeV. The ones for W'_L (W'_R) are set between 0.1568 (0.0948) to 0.0076 (0.0058) pb in the mass range of
 813 $1000 \leq M_{W'} \leq 4000$ GeV.

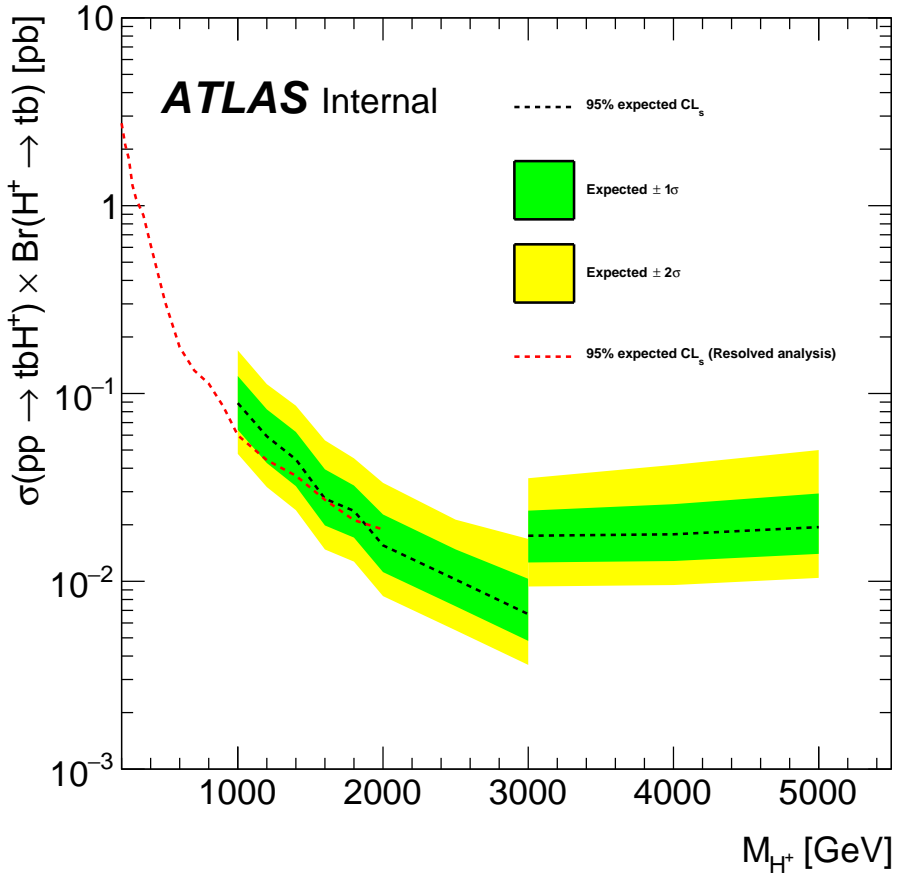


Figure 148: Expected limit for the production of $H^+ \rightarrow tb$ in association with a top quark and a bottom quark. The bands surrounding the expected limit show the 68% and 95% confidence intervals. The expected limit from ATLAS search using Run2 full data with the resolved channel is also shown[24].

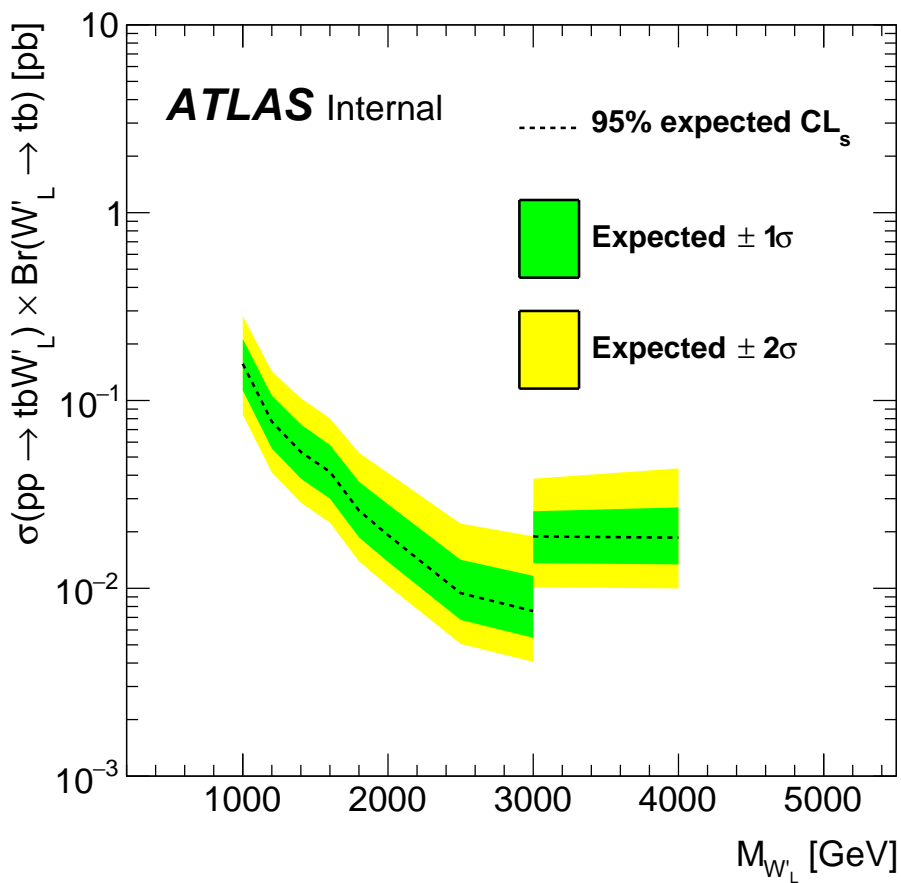


Figure 149: Expected limit for the production of $W'_L \rightarrow tb$ in association with a top quark and a bottom quark. The bands surrounding the expected limit show the 68% and 95% confidence intervals.

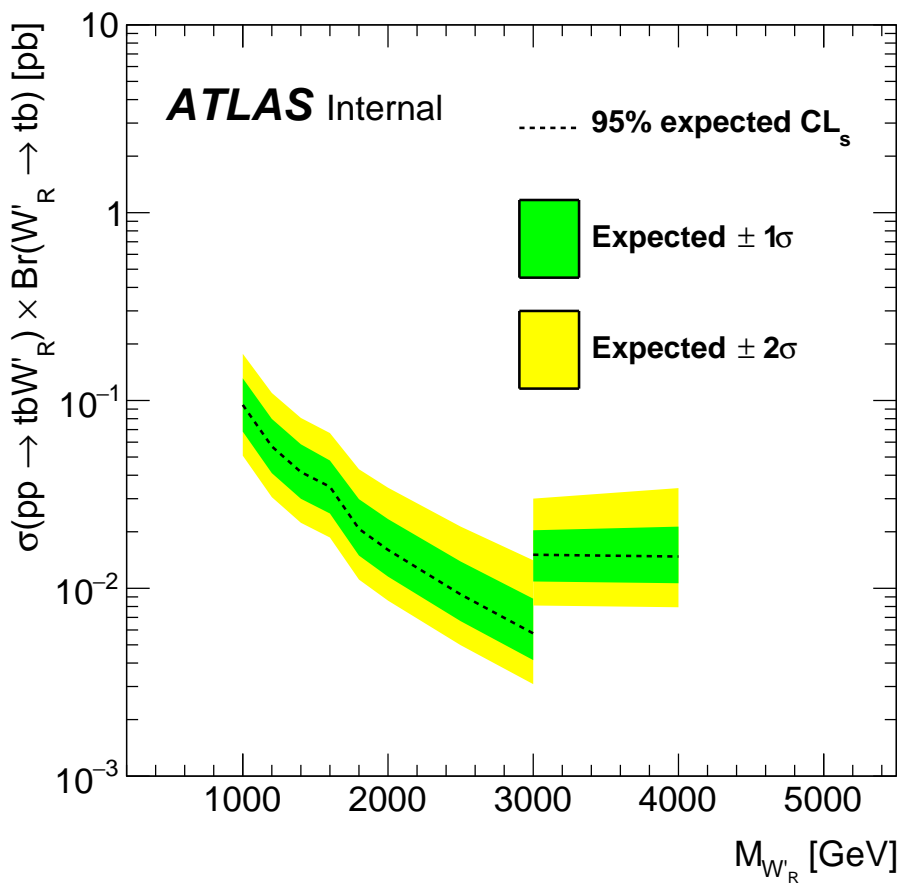


Figure 150: Expected limit for the production of $W'_R \rightarrow tb$ in association with a top quark and a bottom quark. The bands surrounding the expected limit show the 68% and 95% confidence intervals.

8 Summary and Conclusions

We have performed a search for charged Higgs boson H^+ as well as W' bosons produced in association with a top quark and a bottom quark, and decaying into a top quark and a bottom quark, in the lepton-plus-jets final state, in the regime where the top quark from the parent boson is highly boosted to be reconstructed as a top-tagged large- R jet. The H^+ signals are investigated in the mass ranges of $1000 \leq m_{H^+} \leq 5000$ GeV, while the W' signals are done in the mass range of $1000 \leq m_{W'_{LR}} \leq 4000$ GeV. The expected upper limits for H^+ signals are set between 0.0889 to 0.0067 pb. The ones for W'_L (W'_R) are set between 0.1568 (0.0948) to 0.0076 (0.0058) pb.

822 References

- 823 [1] ATLAS Collaboration, *Observation of a new particle in the search for the Standard Model Higgs*
 824 *boson with the ATLAS detector at the LHC*, *Phys. Lett. B* **716** (2012) 1, arXiv: [1207.7214](#)
 825 [[hep-ex](#)] (cit. on p. 5).
- 826 [2] CMS Collaboration, *Observation of a new boson at a mass of 125 GeV with the CMS experiment*
 827 *at the LHC*, *Phys. Lett. B* **716** (2012) 30, arXiv: [1207.7235](#) [[hep-ex](#)] (cit. on p. 5).
- 828 [3] ATLAS and CMS Collaborations, *Combined Measurement of the Higgs Boson Mass in pp*
 829 *Collisions at $\sqrt{s} = 7$ and 8 TeV with the ATLAS and CMS Experiments*, *Phys. Rev. Lett.* **114**
 830 (2015) 191803, arXiv: [1503.07589](#) [[hep-ex](#)] (cit. on p. 5).
- 831 [4] T. D. Lee, *A Theory of Spontaneous T Violation*, *Phys. Rev. D* **8** (1973) (cit. on p. 5).
- 832 [5] G. Branco, P. Ferreira, L. Lavoura, M. Rebelo and M. Sher et al., *Theory and phenomenology of*
 833 *two-Higgs-doublet models*, *Phys. Rept.* **516** (2012), arXiv: [1106.0034](#) [[hep-ph](#)] (cit. on p. 5).
- 834 [6] K. Inoue, A. Kakuto, H. Komatsu and S. Takeshita, *Aspects of Grand Unified Models with Softly*
 835 *Broken Supersymmetry*, *Prog.Theor.Phys.* **68** (1982) (cit. on p. 5).
- 836 [7] T. Cheng and L.-F. Li, *Neutrino Masses, Mixings and Oscillations in $SU(2) \times U(1)$ Models of*
 837 *Electroweak Interactions*, *Phys. Rev. D* **22** (1980) (cit. on p. 5).
- 838 [8] J. Schechter and J. Valle, *Neutrino Masses in $SU(2) \times U(1)$ Theories*, *Phys. Rev. D* **22** (1980) (cit. on
 839 p. 5).
- 840 [9] G. Lazarides, Q. Shafi and C. Wetterich, *Proton Lifetime and Fermion Masses in an $SO(10)$ Model*,
 841 *Nucl. Phys. B* **181** (1981) (cit. on p. 5).
- 842 [10] R. Mohapatra and G. Senjanovic, *Neutrino Masses and Mixings in Gauge Models with Spontaneous*
 843 *Parity Violation*, *Phys. Rev. D* **23** (1981) (cit. on p. 5).
- 844 [11] M. Magg and C. Wetterich, *Neutrino Mass Problem and Gauge Hierarchy*, *Phys. Lett. B* **94** (1980)
 845 (cit. on p. 5).
- 846 [12] ATLAS Collaboration, *Search for charged Higgs bosons decaying via $H^\pm \rightarrow \tau\nu$ in $t\bar{t}$ events using*
 847 *pp collision data at $\sqrt{s} = 7$ TeV with the ATLAS detector*, *JHEP* **06** (2012) 039, arXiv: [1204.2760](#)
 848 [[hep-ex](#)] (cit. on p. 5).
- 849 [13] ATLAS Collaboration, *Search for charged Higgs bosons through the violation of lepton universality*
 850 *in $t\bar{t}$ events using pp collision data at $\sqrt{s} = 7$ TeV with the ATLAS experiment*, *JHEP* **03** (2013) 076,
 851 arXiv: [1212.3572](#) [[hep-ex](#)] (cit. on p. 5).
- 852 [14] ATLAS Collaboration, *Search for charged Higgs bosons decaying via $H^\pm \rightarrow \tau^\pm\nu$ in fully hadronic*
 853 *final states using pp collision data at $\sqrt{s} = 8$ TeV with the ATLAS detector*, *JHEP* **03** (2015) 088,
 854 arXiv: [1412.6663](#) [[hep-ex](#)] (cit. on p. 5).
- 855 [15] CMS Collaboration, *Search for a light charged Higgs boson in top quark decays in pp collisions at*
 856 *$\sqrt{s} = 7$ TeV*, *JHEP* **07** (2012) 143, arXiv: [1205.5736](#) [[hep-ex](#)] (cit. on p. 5).
- 857 [16] CMS Collaboration, *Search for a charged Higgs boson in pp collisions at $\sqrt{s} = 8$ TeV*, *JHEP* **11**
 858 (2015) 018, arXiv: [1508.07774](#) [[hep-ex](#)] (cit. on p. 5).
- 859 [17] ATLAS Collaboration, *Search for charged Higgs bosons decaying via $H^\pm \rightarrow \tau^\pm\nu_\tau$ in the $\tau+jets$*
 860 *and $\tau+lepton$ final states with 36fb^{-1} of pp collision data recorded at $\sqrt{s} = 13$ TeV with the ATLAS*
 861 *experiment*, *JHEP* **09** (2018) 139, arXiv: [1807.07915](#) [[hep-ex](#)] (cit. on p. 5).

- [18] ATLAS Collaboration, *Search for a light charged Higgs boson in the decay channel $H^+ \rightarrow c\bar{s}$ in $t\bar{t}$ events using pp collisions at $\sqrt{s} = 7\text{ TeV}$ with the ATLAS detector*, *Eur. Phys. J. C* **73** (2013) 2465, arXiv: [1302.3694 \[hep-ex\]](#) (cit. on p. 5).
- [19] CMS Collaboration, *Search for a light charged Higgs boson decaying to $c\bar{s}$ in pp collisions at $\sqrt{s} = 8\text{ TeV}$* , *JHEP* **12** (2015) 178, arXiv: [1510.04252 \[hep-ex\]](#) (cit. on p. 5).
- [20] CMS Collaboration, *Search for a charged Higgs boson decaying to charm and bottom quarks in proton–proton collisions at $\sqrt{s} = 8\text{ TeV}$* , *JHEP* **11** (2018) 115, arXiv: [1808.06575 \[hep-ex\]](#) (cit. on p. 5).
- [21] ATLAS Collaboration, *Search for charged Higgs bosons in the $H^\pm \rightarrow tb$ decay channel in pp collisions at $\sqrt{s} = 8\text{ TeV}$ using the ATLAS detector*, *JHEP* **03** (2016) 127, arXiv: [1512.03704 \[hep-ex\]](#) (cit. on p. 5).
- [22] ATLAS Collaboration, *Search for charged Higgs bosons produced in association with a top quark and decaying via $H^\pm \rightarrow \tau\nu$ using pp collision data recorded at $\sqrt{s} = 13\text{ TeV}$ by the ATLAS detector*, *Phys. Lett. B* **759** (2016) 555, arXiv: [1603.09203 \[hep-ex\]](#) (cit. on p. 5).
- [23] ATLAS Collaboration, *Search for charged Higgs bosons decaying into top and bottom quarks at $\sqrt{s} = 13\text{ TeV}$ with the ATLAS detector*, *JHEP* **11** (2018) 085, arXiv: [1808.03599 \[hep-ex\]](#) (cit. on pp. 5, 55).
- [24] ATLAS Collaboration, *Search for a charged Higgs bosons decaying into a top-quark and a bottom-quark at $\sqrt{s} = 13\text{ TeV}$ with the ATLAS detector*, *JHEP* **16** (2021) 145, arXiv: [2102.10076 \[hep-ex\]](#) (cit. on pp. 5, 34, 55, 151).
- [25] CMS Collaboration, *Search for a charged Higgs boson decaying into top and bottom quarks in events with electrons or muons in proton–proton collisions at $\sqrt{s} = 13\text{ TeV}$* , *JHEP* **01** (2020) 096, arXiv: [1908.09206 \[hep-ex\]](#) (cit. on p. 5).
- [26] CMS Collaboration, *Search for charged Higgs bosons decaying into a top and a bottom quark in the all-jet final state of pp collisions at $\sqrt{s} = 13\text{ TeV}$* , (2020), arXiv: [2001.07763 \[hep-ex\]](#) (cit. on p. 5).
- [27] ATLAS Collaboration, *Search for dijet resonances in events with an isolated charged lepton using $\sqrt{s} = 13\text{ TeV}$ proton–proton collision data collected by the ATLAS detector*, *JHEP* **06** (2020) 151, arXiv: [2002.11325 \[hep-ex\]](#) (cit. on p. 5).
- [28] ATLAS Collaboration, *Search for a Charged Higgs Boson Produced in the Vector-Boson Fusion Mode with Decay $H^\pm \rightarrow W^\pm Z$ using pp Collisions at $\sqrt{s} = 8\text{ TeV}$ with the ATLAS Experiment*, *Phys. Rev. Lett.* **114** (2015) 231801, arXiv: [1503.04233 \[hep-ex\]](#) (cit. on p. 5).
- [29] CMS Collaboration, *Search for charged Higgs bosons produced via vector boson fusion and decaying into a pair of W and Z bosons using pp collisions at $\sqrt{s} = 13\text{ TeV}$* , *Phys. Rev. Lett.* **119** (2017) 141802, arXiv: [1705.02942 \[hep-ex\]](#) (cit. on p. 5).
- [30] ATLAS Collaboration, *Luminosity determination in pp collisions at $\sqrt{s} = 13\text{ TeV}$ using the ATLAS detector at the LHC*, ATLAS-CONF-2019-021, 2019, URL: <https://cds.cern.ch/record/2677054> (cit. on pp. 7, 51).
- [31] *LuminosityForPhysics twiki page*, URL: <https://twiki.cern.ch/twiki/bin/viewauth/Atlas/LuminosityForPhysics> (cit. on p. 7).
- [32] *Web directory for GoodRunsLists in atlas-groupdata area*, URL: <https://atlas-groupdata.web.cern.ch/atlas-groupdata/GoodRunsLists> (cit. on p. 7).

- [33] C. Degrande, M. Ubiali, M. Wiesemann and M. Zaro, *Heavy charged Higgs boson production at the LHC*, JHEP **10** (2015) 145, arXiv: [1507.02549 \[hep-ph\]](#) (cit. on p. 8).
- [34] J. Alwall et al., *The automated computation of tree-level and next-to-leading order differential cross sections, and their matching to parton shower simulations*, JHEP **07** (2014) 079, arXiv: [1405.0301 \[hep-ph\]](#) (cit. on pp. 8, 58).
- [35] R. D. Ball et al., *Parton distributions with LHC data*, Nucl. Phys. B **867** (2013) 244, arXiv: [1207.1303 \[hep-ph\]](#) (cit. on p. 8).
- [36] R. D. Ball et al., *Parton distributions for the LHC run II*, JHEP **04** (2015) 040, arXiv: [1410.8849 \[hep-ph\]](#) (cit. on pp. 8, 10).
- [37] T. Sjöstrand, S. Mrenna and P. Skands, *A brief introduction to PYTHIA 8.1*, Comput. Phys. Commun. **178** (2008) 852, arXiv: [0710.3820 \[hep-ph\]](#) (cit. on p. 8).
- [38] ATLAS Collaboration, *ATLAS Pythia 8 tunes to 7 TeV data*, ATL-PHYS-PUB-2014-021, 2014, URL: <https://cds.cern.ch/record/1966419> (cit. on pp. 8, 56).
- [39] M. Flechl, M. Klees, M. Krämer, M. Spira and M. Ubiali, *Improved cross-section predictions for heavy charged Higgs boson production at the LHC*, Physical Review D **91** (2015), URL: <http://dx.doi.org/10.1103/PhysRevD.91.075015>, ISSN:1550-2368 (cit. on p. 8).
- [40] S. Dittmaier, M. Krämer, M. Spira and M. Walser, *Charged-Higgs-boson production at the LHC: Next-to-leading-order supersymmetric QCD corrections*, Physical Review D **83** (2011), URL: <http://dx.doi.org/10.1103/PhysRevD.83.055005>, ISSN:1550-2368 (cit. on p. 8).
- [41] E. Berger, T. Han, J. Jiang and T. Plehn, *Associated production of a top quark and a charged Higgs boson*, Physical Review D **71** (2005), URL: <http://dx.doi.org/10.1103/PhysRevD.71.115012>, ISSN:1550-2368 (cit. on p. 8).
- [42] P. Nason, *A new method for combining NLO QCD with shower Monte Carlo algorithms*, JHEP **11** (2004) 040, arXiv: [hep-ph/0409146](#) (cit. on p. 10).
- [43] S. Frixione, P. Nason and C. Oleari, *Matching NLO QCD computations with parton shower simulations: the POWHEG method*, JHEP **11** (2007) 070, arXiv: [0709.2092 \[hep-ph\]](#) (cit. on p. 10).
- [44] S. Alioli, P. Nason, C. Oleari and E. Re, *A general framework for implementing NLO calculations in shower Monte Carlo programs: the POWHEG BOX*, JHEP **06** (2010) 043, arXiv: [1002.2581 \[hep-ph\]](#) (cit. on p. 10).
- [45] J. Campbell, R. Ellis, P. Nason and E. Re, *Top-pair production and decay at NLO matched with parton showers*, JHEP **04** (2015), arXiv: [1412.1828 \[hep-ph\]](#) (cit. on p. 10).
- [46] ATLAS Collaboration, *Studies on top-quark Monte Carlo modelling for Top2016*, ATL-PHYS-PUB-2016-020, 2016, URL: <https://cds.cern.ch/record/2216168> (cit. on pp. 10, 12).
- [47] T. Sjöstrand et al., *An introduction to PYTHIA 8.2*, Comput. Phys. Commun. **191** (2015) 159, arXiv: [1410.3012 \[hep-ph\]](#) (cit. on p. 10).
- [48] M. Bahr et al., *Herwig++ physics and manual*, Eur. Phys. J. C **58** (2008) 639, arXiv: [0803.0883 \[hep-ph\]](#) (cit. on p. 10).
- [49] J. Bellm et al., *Herwig 7.0/Herwig++ 3.0 release note*, Eur. Phys. J. C **76** (2016) 196, arXiv: [1512.01178 \[hep-ph\]](#) (cit. on p. 10).

- [50] ATLAS Collaboration, *Studies on top-quark Monte Carlo modelling with Sherpa and MG5_aMC@NLO*, ATL-PHYS-PUB-2017-007, 2017, URL: <https://cds.cern.ch/record/2261938> (cit. on p. 10).
- [51] H. B. Hartanto, B. Jäger, L. Reina and D. Wackerlo, *Higgs boson production in association with top quarks in the POWHEG BOX*, Phys. Rev. D **91** (2015) 094003, arXiv: [1501.04498 \[hep-ph\]](https://arxiv.org/abs/1501.04498) (cit. on p. 11).
- [52] E. Bothmann et al., *Event Generation with Sherpa 2.2*, SciPost Phys. **7** (2019) 034, arXiv: [1905.09127 \[hep-ph\]](https://arxiv.org/abs/1905.09127) (cit. on p. 11).
- [53] S. Catani, F. Krauss, R. Kuhn and B. R. Webber, *QCD Matrix Elements + Parton Showers*, JHEP **11** (2001) 063, arXiv: [hep-ph/0109231](https://arxiv.org/abs/hep-ph/0109231) (cit. on pp. 11, 13).
- [54] S. Höche, F. Krauss, S. Schumann and F. Siegert, *QCD matrix elements and truncated showers*, JHEP **05** (2009) 053, arXiv: [0903.1219 \[hep-ph\]](https://arxiv.org/abs/0903.1219) (cit. on pp. 11, 13).
- [55] R. Frederix, E. Re and P. Torrielli, *Single-top t-channel hadroproduction in the four-flavour scheme with POWHEG and aMC@NLO*, JHEP **09** (2012) 130, arXiv: [1207.5391 \[hep-ph\]](https://arxiv.org/abs/1207.5391) (cit. on pp. 11, 13).
- [56] S. Frixione, E. Laenen, P. Motylinski and B. R. Webber, *Angular correlations of lepton pairs from vector boson and top quark decays in Monte Carlo simulations*, JHEP **04** (2007) 081, arXiv: [hep-ph/0702198](https://arxiv.org/abs/hep-ph/0702198) (cit. on p. 12).
- [57] P. Artoisenet, R. Frederix, O. Mattelaer and R. Rietkerk, *Automatic spin-entangled decays of heavy resonances in Monte Carlo simulations*, JHEP **03** (2013) 015, arXiv: [1212.3460 \[hep-ph\]](https://arxiv.org/abs/1212.3460) (cit. on p. 12).
- [58] S. Frixione, E. Laenen, P. Motylinski, C. D. White and B. R. Webber, *Single-top hadroproduction in association with a W boson*, JHEP **07** (2008) 029, arXiv: [0805.3067 \[hep-ph\]](https://arxiv.org/abs/0805.3067) (cit. on pp. 12, 13, 57).
- [59] ATLAS Collaboration, *Measurement of the production cross-section of a single top quark in association with a Z boson in proton–proton collisions at 13 TeV with the ATLAS detector*, Phys. Lett. B **780** (2018) 557, arXiv: [1710.03659 \[hep-ex\]](https://arxiv.org/abs/1710.03659) (cit. on p. 13).
- [60] J. Pumplin et al., *New Generation of Parton Distributions with Uncertainties from Global QCD Analysis*, JHEP **07** (2002) 012, arXiv: [hep-ph/0201195](https://arxiv.org/abs/hep-ph/0201195) (cit. on p. 13).
- [61] R. Frederix, D. Pagani and M. Zaro, *Large NLO corrections in $t\bar{t}W^\pm$ and $t\bar{t}t\bar{t}$ hadroproduction from supposedly subleading EW contributions*, JHEP **02** (2018) 031, arXiv: [1711.02116 \[hep-ph\]](https://arxiv.org/abs/1711.02116) (cit. on p. 13).
- [62] T. Gleisberg and S. Höche, *Comix, a new matrix element generator*, JHEP **12** (2008) 039, arXiv: [0808.3674 \[hep-ph\]](https://arxiv.org/abs/0808.3674) (cit. on p. 13).
- [63] F. Cascioli, P. Maierhöfer and S. Pozzorini, *Scattering Amplitudes with Open Loops*, Phys. Rev. Lett. **108** (2012) 111601, arXiv: [1111.5206 \[hep-ph\]](https://arxiv.org/abs/1111.5206) (cit. on p. 13).
- [64] A. Denner, S. Dittmaier and L. Hofer, *Collier: A fortran-based complex one-loop library in extended regularizations*, Comput. Phys. Commun. **212** (2017) 220, arXiv: [1604.06792 \[hep-ph\]](https://arxiv.org/abs/1604.06792) (cit. on p. 13).
- [65] S. Schumann and F. Krauss, *A parton shower algorithm based on Catani–Seymour dipole factorisation*, JHEP **03** (2008) 038, arXiv: [0709.1027 \[hep-ph\]](https://arxiv.org/abs/0709.1027) (cit. on p. 13).

- 985 [66] J.-C. Winter, F. Krauss and G. Soff, *A modified cluster-hadronization model*, *Eur. Phys. J. C* **36**
 986 (2004) 381, arXiv: [hep-ph/0311085](#) (cit. on p. 13).
- 987 [67] S. Höche, F. Krauss, M. Schönherr and F. Siegert, *A critical appraisal of NLO+PS matching*
 988 *methods*, *JHEP* **09** (2012) 049, arXiv: [1111.1220 \[hep-ph\]](#) (cit. on p. 13).
- 989 [68] S. Höche, F. Krauss, M. Schönherr and F. Siegert, *QCD matrix elements + parton showers. The*
 990 *NLO case*, *JHEP* **04** (2013) 027, arXiv: [1207.5030 \[hep-ph\]](#) (cit. on p. 13).
- 991 [69] E. Bothmann, M. Schönherr and S. Schumann, *Reweighting QCD matrix-element and parton-*
 992 *shower calculations*, *Eur. Phys. J. C* **76** (2016) 590, arXiv: [1606.08753 \[hep-ph\]](#) (cit. on
 993 p. 13).
- 994 [70] ATLAS Collaboration, *Electron reconstruction and identification efficiency measurements with the*
 995 *ATLAS detector using the 2011 LHC proton–proton collision data*, *Eur. Phys. J. C* **74** (2014) 2941,
 996 arXiv: [1404.2240 \[hep-ex\]](#) (cit. on p. 15).
- 997 [71] ATLAS Collaboration, *Electron efficiency measurements with the ATLAS detector using the 2015*
 998 *LHC proton–proton collision data*, ATLAS-CONF-2016-024, 2016, URL: <https://cds.cern.ch/record/2157687> (cit. on p. 15).
- 1000 [72] *Lepton isolation recommendations*, URL: <https://twiki.cern.ch/twiki/bin/viewauth/AtlasProtected/IsolationSelectionTool> (cit. on p. 15).
- 1001 [73] ATLAS Collaboration, *Muon reconstruction performance of the ATLAS detector in proton–proton*
 1002 *collision data at $\sqrt{s} = 13 \text{ TeV}$* , *Eur. Phys. J. C* **76** (2016) 292, arXiv: [1603.05598 \[hep-ex\]](#)
 1003 (cit. on pp. 15, 52).
- 1004 [74] ATLAS Collaboration, *Reconstruction, Energy Calibration, and Identification of Hadronically*
 1005 *Decaying Tau Leptons in the ATLAS Experiment for Run-2 of the LHC*, ATL-PHYS-PUB-2015-045,
 1006 2015, URL: <https://cds.cern.ch/record/2064383> (cit. on p. 15).
- 1007 [75] M. Cacciari, G. P. Salam and G. Soyez, *The anti- k_t jet clustering algorithm*, *JHEP* **04** (2008) 063,
 1008 arXiv: [0802.1189 \[hep-ph\]](#) (cit. on p. 15).
- 1009 [76] ATLAS Collaboration, *Jet reconstruction and performance using particle flow with the ATLAS*
 1010 *Detector*, *Eur. Phys. J. C* **77** (2017) 466, arXiv: [1703.10485 \[hep-ex\]](#) (cit. on p. 15).
- 1011 [77] ATLAS Collaboration, *Jet energy scale and resolution measured in proton–proton collisions at*
 1012 *$\sqrt{s} = 13 \text{ TeV}$ with the ATLAS detector*, (2020), arXiv: [2007.02645 \[hep-ex\]](#) (cit. on p. 15).
- 1013 [78] ATLAS Collaboration, *Performance of pile-up mitigation techniques for jets in pp collisions*
 1014 *at $\sqrt{s} = 8 \text{ TeV}$ using the ATLAS detector*, *Eur. Phys. J. C* **76** (2016) 581, arXiv: [1510.03823](#)
 1015 *[hep-ex]* (cit. on pp. 15, 52).
- 1016 [79] ATLAS Collaboration, *ATLAS b-jet identification performance and efficiency measurement with*
 1017 *$t\bar{t}$ events in pp collisions at $\sqrt{s} = 13 \text{ TeV}$* , *Eur. Phys. J. C* **79** (2019) 970, arXiv: [1907.05120](#)
 1018 *[hep-ex]* (cit. on pp. 15, 54).
- 1019 [80] ATLAS Collaboration, *Topological cell clustering in the ATLAS calorimeters and its performance*
 1020 *in LHC Run 1*, *Eur. Phys. J. C* **77** (2017) 490, arXiv: [1603.02934 \[hep-ex\]](#) (cit. on p. 16).
- 1021 [81] D. Krohn, J. Thaler and L.-T. Wang, *Jet trimming*, *Journal of High Energy Physics* **2010** (2010) 84,
 1022 URL: [https://link.springer.com/article/10.1007/JHEP02\(2010\)084](https://link.springer.com/article/10.1007/JHEP02(2010)084), ISSN:1029-
 1023 8479 (cit. on p. 16).

- [82] S. Catani, Y. Dokshitzer, M. Seymour and B. Webber, *Longitudinally invariant K(t) clustering algorithms for hadron-hadron collisions*, Nuclear Physics B **406** (1993) 187, URL: <https://www.sciencedirect.com/science/article/pii/055032139390166M>, ISSN:0550-3213 (cit. on p. 16).
- [83] ATLAS Collaboration, *Identification of boosted, hadronically decaying W bosons and comparisons with ATLAS data taken at $\sqrt{s} = 8$ TeV*, Eur. Phys. J. C **76** (2016) 154, arXiv: [1510.05821 \[hep-ex\]](https://arxiv.org/abs/1510.05821) (cit. on p. 16).
- [84] ATLAS Collaboration, *Jet mass reconstruction with the ATLAS Detector in early Run 2 data*, ATLAS-CONF-2016-035, 2016, URL: <https://cds.cern.ch/record/2200211> (cit. on p. 16).
- [85] ATLAS Collaboration, *Boosted hadronic vector boson and top quark tagging with ATLAS using Run 2 data*, ATL-PHYS-PUB-2020-017, 2020, URL: <https://cds.cern.ch/record/2724149> (cit. on pp. 16, 54).
- [86] J. Thaler and K. Van Tilburg, *Identifying Boosted Objects with N-subjettiness*, JHEP **03** (2011) 015, arXiv: [1011.2268 \[hep-ph\]](https://arxiv.org/abs/1011.2268) (cit. on p. 16).
- [87] J. Thaler and L.-T. Wang, *Strategies to Identify Boosted Tops*, JHEP **07** (2008) 092, arXiv: [0806.0023 \[hep-ph\]](https://arxiv.org/abs/0806.0023) (cit. on p. 16).
- [88] A. Larkoski, G. Salam and J. Thaler, *Energy Correlation Functions for Jet Substructure*, JHEP **06** (2013) 108, arXiv: [1305.0007 \[hep-ph\]](https://arxiv.org/abs/1305.0007) (cit. on p. 16).
- [89] D. Adams and et al., *Recommendations of the Physics Objects and Analysis Harmonisation Study Groups 2014*, ATL-PHYS-INT-2014-018, 2014, URL: <https://cds.cern.ch/record/1743654> (cit. on p. 16).
- [90] *Documentation of the ATLAS AssociationUtils package*, URL: <https://gitlab.cern.ch/atlas/athena/blob/release/21.2.86/PhysicsAnalysis/AnalysisCommon/AssociationUtils/README.rst> (cit. on p. 16).
- [91] J. Gallicchio and Y.-T. Chien, *Quit Using Pseudorapidity, Transverse Energy, and Massless Constituents*, 2018, arXiv: [1802.05356 \[hep-ph\]](https://arxiv.org/abs/1802.05356) (cit. on p. 16).
- [92] A. Hoecker et al., *TMVA - Toolkit for Multivariate Data Analysis*, 2007, arXiv: [physics/0703039 \[physics.data-an\]](https://arxiv.org/abs/physics/0703039) (cit. on p. 21).
- [93] *Automatic binning implematation in TTHFitter*. URL: https://indico.cern.ch/event/455289/contributions/1953694/attachments/1209081/1762963/Calvet_binning_Htop_160108.pdf (cit. on pp. 37, 59).
- [94] G. Avoni and et al., *The new LUCID-2 detector for luminosity measurement and monitoring in ATLAS*, JINST **13** (2018) P07017 (cit. on p. 51).
- [95] ATLAS Collaboration, *Measurement of the Inelastic Proton–Proton Cross Section at $\sqrt{s} = 13$ TeV with the ATLAS Detector at the LHC*, Phys. Rev. Lett. **117** (2016) 182002, arXiv: [1606.02625 \[hep-ex\]](https://arxiv.org/abs/1606.02625) (cit. on p. 51).
- [96] ATLAS Collaboration, *Electron reconstruction and identification in the ATLAS experiment using the 2015 and 2016 LHC proton–proton collision data at $\sqrt{s} = 13$ TeV*, Eur. Phys. J. C **79** (2019) 639, arXiv: [1902.04655 \[hep-ex\]](https://arxiv.org/abs/1902.04655) (cit. on p. 52).
- [97] ATLAS Collaboration, *Electron and photon performance measurements with the ATLAS detector using the 2015–2017 LHC proton–proton collision data*, JINST **14** (2019) P12006, arXiv: [1908.00005 \[hep-ex\]](https://arxiv.org/abs/1908.00005) (cit. on p. 52).

- [98] ATLAS Collaboration, *Jet energy scale measurements and their systematic uncertainties in proton–proton collisions at $\sqrt{s} = 13\text{ TeV}$ with the ATLAS detector*, *Phys. Rev. D* **96** (2017) 072002, arXiv: [1703.09665 \[hep-ex\]](#) (cit. on p. 52).
- [99] ATLAS Collaboration, *Determination of jet calibration and energy resolution in proton–proton collisions at $\sqrt{s} = 8\text{ TeV}$ using the ATLAS detector*, (2019), arXiv: [1910.04482 \[hep-ex\]](#) (cit. on p. 52).
- [100] ATLAS Collaboration, *In situ calibration of large-radius jet energy and mass in 13 TeV proton–proton collisions with the ATLAS detector*, *Eur. Phys. J. C* **79** (2019) 135, arXiv: [1807.09477 \[hep-ex\]](#) (cit. on p. 53).
- [101] ATLAS Collaboration, *Measurement of the ATLAS Detector Jet Mass Response using Forward Folding with 80fb^{-1} of $\sqrt{s} = 13\text{ TeV}$ pp data*, ATLAS-CONF-2020-022, 2020, URL: <https://cds.cern.ch/record/2724442> (cit. on p. 53).
- [102] ATLAS Collaboration, *Measurement of b-tagging efficiency of c-jets in $t\bar{t}$ events using a likelihood approach with the ATLAS detector*, ATLAS-CONF-2018-001, 2018, URL: <https://cds.cern.ch/record/2306649> (cit. on p. 54).
- [103] ATLAS Collaboration, *Calibration of light-flavour b-jet mistagging rates using ATLAS proton–proton collision data at $\sqrt{s} = 13\text{ TeV}$* , ATLAS-CONF-2018-006, 2018, URL: <https://cds.cern.ch/record/2314418> (cit. on p. 54).
- [104] ATLAS Collaboration, *Performance of top-quark and W-boson tagging with ATLAS in Run 2 of the LHC*, *Eur. Phys. J. C* **79** (2019) 375, arXiv: [1808.07858 \[hep-ex\]](#) (cit. on p. 54).
- [105] J. Butterworth et al., *PDF4LHC recommendations for LHC Run II*, *J. Phys. G* **43** (2016) 023001, arXiv: [1510.03865 \[hep-ph\]](#) (cit. on p. 54).
- [106] D. de Florian et al., *Handbook of LHC Higgs Cross Sections: 4. Deciphering the Nature of the Higgs Sector*, (2016), arXiv: [1610.07922 \[hep-ph\]](#) (cit. on p. 57).
- [107] R. Raitio and W. W. Wada, *Higgs Boson Production at Large Transverse Momentum in QCD*, *Phys. Rev. D* **19** (1979) (cit. on p. 57).
- [108] W. Beenakker and et al., *NLO QCD corrections to t anti-t H production in hadron collisions*, *Nucl. Phys. B* **653** (2003), arXiv: [hep-ph/0211352 \[hep-ph\]](#) (cit. on p. 57).
- [109] S. Dawson, C. Jackson, L. H. Orr, L. Reina and D. Wackerlo, *Associated Higgs production with top quarks at the large hadron collider: NLO QCD corrections*, *Phys. Rev. D* **68** (2003), arXiv: [hep-ph/0305087 \[hep-ph\]](#) (cit. on p. 57).
- [110] Y. Zhang, W.-G. Ma, R.-Y. Zhang, C. Chen and L. Guo, *QCD NLO and EW NLO corrections to $t\bar{t}H$ production with top quark decays at hadron collider*, *Phys. Lett. B* **738** (2014), arXiv: [1407.1110 \[hep-ph\]](#) (cit. on p. 57).
- [111] S. Frixione, V. Hirschi, D. Pagani, H.-S. Shao and M. Zaro, *Electroweak and QCD corrections to top-pair hadroproduction in association with heavy bosons*, *JHEP* **06** (2015), arXiv: [1504.03446 \[hep-ph\]](#) (cit. on p. 57).
- [112] LHCTopWG, *NLO single-top channel cross sections*, 2017, URL: <https://twiki.cern.ch/twiki/bin/view/LHCPhysics/SingleTopRefXsec> (cit. on p. 57).
- [113] A. D. Martin, W. J. Stirling, R. S. Thorne and G. Watt, *Parton distributions for the LHC*, *Eur. Phys. J. C* **63** (2009) 189, arXiv: [0901.0002 \[hep-ph\]](#) (cit. on p. 57).

- 1108 [114] A. D. Martin, W. Stirling, R. Thorne and G. Watt, *Uncertainties on α_S in global PDF analyses*
1109 *and implications for predicted hadronic cross sections*, *Eur. Phys. J. C* **64** (2009) 653, arXiv:
1110 [0905.3531 \[hep-ph\]](https://arxiv.org/abs/0905.3531) (cit. on p. 57).
- 1111 [115] M. Aliev et al., *HATHOR – HAdronic Top and Heavy quarks crOss section calculatoR*, *Comput.*
1112 *Phys. Commun.* **182** (2011) 1034, arXiv: [1007.1327 \[hep-ph\]](https://arxiv.org/abs/1007.1327) (cit. on p. 57).
- 1113 [116] P. Kant et al., *HaTHor for single top-quark production: Updated predictions and uncertainty*
1114 *estimates for single top-quark production in hadronic collisions*, *Comput. Phys. Commun.* **191**
1115 (2015) 74, arXiv: [1406.4403 \[hep-ph\]](https://arxiv.org/abs/1406.4403) (cit. on p. 57).
- 1116 [117] LHCHXSWG1, *Recommended predictions for $t\bar{t}V$ cross sections*, URL: https://twiki.cern.ch/twiki/bin/view/LHCPhysics/LHCHXSWGTT#Plans_for_YR4 (cit. on p. 57).
- 1117 [118] J. M. Campbell and R. K. Ellis, *$t\bar{t}W^{+-}$ production and decay at NLO*, *JHEP* **07** (2012), arXiv:
1118 [1204.5678 \[hep-ph\]](https://arxiv.org/abs/1204.5678) (cit. on p. 57).
- 1119 [119] *ATLAS PMG Top processes twiki page*, URL: <https://twiki.cern.ch/twiki/bin/view/AtlasProtected/PmgTopProcesses> (cit. on p. 58).
- 1120 [120] ATLAS Collaboration, *Multi-boson simulation for 13 TeV ATLAS analyses*, ATL-PHYS-PUB-
1121 2016-002, 2016, URL: <https://cds.cern.ch/record/2119986> (cit. on p. 58).

1124 **Appendices**

1125 **A TOPQ1 DAOD list**

1126 **A.1 Data**

1127 Table 19 is the TOPQ1 DAOD list for data sample in this analysis.

data15_13TeV.AllYear.physics_Main.PhysCont.DAOD_TOPQ1.grp15_v01_p4513
data16_13TeV.AllYear.physics_Main.PhysCont.DAOD_TOPQ1.grp16_v01_p4513
data17_13TeV.AllYear.physics_Main.PhysCont.DAOD_TOPQ1.grp17_v01_p4513
data18_13TeV.AllYear.physics_Main.PhysCont.DAOD_TOPQ1.grp18_v01_p4513

1128 Table 19: TOPQ1 DAOD list for data sample in this analysis.

1128 **A.2 $\bar{t}bH^+$**

1129 Table 20 is the TOPQ1 DAOD list for H^+ sample in this analysis.

Nominal
mc16_13TeV.450004.aMcAtNloPythia8EvtGen_A14NNPDF23LO_Hplus4FS_H1000_tb.deriv.DAOD_TOPQ1.e7137_s3126_r9364_p4514
mc16_13TeV.450598.aMcAtNloPythia8EvtGen_A14NNPDF23LO_Hplus4FS_H1200_tb.deriv.DAOD_TOPQ1.e7429_s3126_r9364_p4514
mc16_13TeV.450599.aMcAtNloPythia8EvtGen_A14NNPDF23LO_Hplus4FS_H1400_tb.deriv.DAOD_TOPQ1.e7429_s3126_r9364_p4514
mc16_13TeV.450600.aMcAtNloPythia8EvtGen_A14NNPDF23LO_Hplus4FS_H1600_tb.deriv.DAOD_TOPQ1.e7429_s3126_r9364_p4514
mc16_13TeV.450601.aMcAtNloPythia8EvtGen_A14NNPDF23LO_Hplus4FS_H1800_tb.deriv.DAOD_TOPQ1.e7429_s3126_r9364_p4514
mc16_13TeV.450602.aMcAtNloPythia8EvtGen_A14NNPDF23LO_Hplus4FS_H2000_tb.deriv.DAOD_TOPQ1.e7429_s3126_r9364_p4514
mc16_13TeV.451490.aMcAtNloPythia8EvtGen_A14NNPDF23LO_Hplus4FS_H2500_tb.deriv.DAOD_TOPQ1.e7970_s3126_r9364_p4514
mc16_13TeV.451491.aMcAtNloPythia8EvtGen_A14NNPDF23LO_Hplus4FS_H3000_tb.deriv.DAOD_TOPQ1.e7970_s3126_r9364_p4514
mc16_13TeV.508710.MGPy8EG_A14NNPDF30_Hplus4FS_H4000_tb.deriv.DAOD_TOPQ1.e8276_s3126_r9364_p4514
mc16_13TeV.508711.MGPy8EG_A14NNPDF30_Hplus4FS_H5000_tb.deriv.DAOD_TOPQ1.e8276_s3126_r9364_p4514

1128 Table 20: TOPQ1 DAOD list for H^+ sample in this analysis.

1130 **A.3 $\bar{t}bW'$**

1131 Table 21 is the TOPQ1 DAOD list for the W' sample in this analysis.

Nominal
mc16_13TeV.510889.MGPy8EG_WprimeTbTb_lep_LH_1000_10.deriv.DAOD_TOPQ1.e8470_s3126_r9364_p4514
mc16_13TeV.510890.MGPy8EG_WprimeTbTb_lep_LH_1200_10.deriv.DAOD_TOPQ1.e8470_s3126_r9364_p4514
mc16_13TeV.510891.MGPy8EG_WprimeTbTb_lep_LH_1400_10.deriv.DAOD_TOPQ1.e8470_s3126_r9364_p4514
mc16_13TeV.510892.MGPy8EG_WprimeTbTb_lep_LH_1600_10.deriv.DAOD_TOPQ1.e8470_s3126_r9364_p4514
mc16_13TeV.510893.MGPy8EG_WprimeTbTb_lep_LH_1800_10.deriv.DAOD_TOPQ1.e8470_s3126_r9364_p4514
mc16_13TeV.510894.MGPy8EG_WprimeTbTb_lep_LH_2000_10.deriv.DAOD_TOPQ1.e8470_s3126_r9364_p4514
mc16_13TeV.510895.MGPy8EG_WprimeTbTb_lep_LH_2500_10.deriv.DAOD_TOPQ1.e8470_s3126_r9364_p4514
mc16_13TeV.510896.MGPy8EG_WprimeTbTb_lep_LH_3000_10.deriv.DAOD_TOPQ1.e8470_s3126_r9364_p4514
mc16_13TeV.510897.MGPy8EG_WprimeTbTb_lep_LH_4000_10.deriv.DAOD_TOPQ1.e8470_s3126_r9364_p4514
mc16_13TeV.510898.MGPy8EG_WprimeTbTb_lep_RH_1000_10.deriv.DAOD_TOPQ1.e8470_s3126_r9364_p4514
mc16_13TeV.510899.MGPy8EG_WprimeTbTb_lep_RH_1200_10.deriv.DAOD_TOPQ1.e8470_s3126_r9364_p4514
mc16_13TeV.510900.MGPy8EG_WprimeTbTb_lep_RH_1400_10.deriv.DAOD_TOPQ1.e8470_s3126_r9364_p4514
mc16_13TeV.510901.MGPy8EG_WprimeTbTb_lep_RH_1600_10.deriv.DAOD_TOPQ1.e8470_s3126_r9364_p4514
mc16_13TeV.510902.MGPy8EG_WprimeTbTb_lep_RH_1800_10.deriv.DAOD_TOPQ1.e8470_s3126_r9364_p4514
mc16_13TeV.510903.MGPy8EG_WprimeTbTb_lep_RH_2000_10.deriv.DAOD_TOPQ1.e8470_s3126_r9364_p4514
mc16_13TeV.510904.MGPy8EG_WprimeTbTb_lep_RH_2500_10.deriv.DAOD_TOPQ1.e8470_s3126_r9364_p4514
mc16_13TeV.510905.MGPy8EG_WprimeTbTb_lep_RH_3000_10.deriv.DAOD_TOPQ1.e8470_s3126_r9364_p4514
mc16_13TeV.510906.MGPy8EG_WprimeTbTb_lep_RH_4000_10.deriv.DAOD_TOPQ1.e8470_s3126_r9364_p4514

Table 21: TOPQ1 DAOD list for W' sample in this analysis.

¹¹³² **A.4 $t\bar{t} + \text{jets}$**

¹¹³³ Table 22 is the TOPQ1 DAOD list for $t\bar{t} + \text{jets}$ sample in this analysis.

Nominal
mc16_13TeV.410470.PhPy8EG_A14_ttbar_hdamp258p75_nonallhad.deriv.DAOD_TOPQ1.e6337_s3126_r9364_p4514
mc16_13TeV.410471.PhPy8EG_A14_ttbar_hdamp258p75_allhad.deriv.DAOD_TOPQ1.e6337_s3126_r9364_p4514
mc16_13TeV.411073.PhPy8EG_A14_ttbar_hdamp258p75_ljets_BBFilt.deriv.DAOD_TOPQ1.e6798_s3126_r9364_p4514
mc16_13TeV.411074.PhPy8EG_A14_ttbar_hdamp258p75_ljets_BFiltBBVeto.deriv.DAOD_TOPQ1.e6798_s3126_r9364_p4514
mc16_13TeV.411075.PhPy8EG_A14_ttbar_hdamp258p75_ljets_CFiltBVeto.deriv.DAOD_TOPQ1.e6798_s3126_r9364_p4514
mc16_13TeV.411076.PhPy8EG_A14_ttbar_hdamp258p75_dil_BBFilt.deriv.DAOD_TOPQ1.e6798_s3126_r9364_p4514
mc16_13TeV.411077.PhPy8EG_A14_ttbar_hdamp258p75_dil_BFiltBBVeto.deriv.DAOD_TOPQ1.e6798_s3126_r9364_p4514
mc16_13TeV.411078.PhPy8EG_A14_ttbar_hdamp258p75_dil_CFiltBVeto.deriv.DAOD_TOPQ1.e6798_s3126_r9364_p4514
Reference
mc16_13TeV.410470.PhPy8EG_A14_ttbar_hdamp258p75_nonallhad.deriv.DAOD_TOPQ1.e6337_a875_r9364_p4514
mc16_13TeV.410471.PhPy8EG_A14_ttbar_hdamp258p75_allhad.deriv.DAOD_TOPQ1.e6337_a875_r9364_p4514
mc16_13TeV.411073.PhPy8EG_A14_ttbar_hdamp258p75_ljets_BBFilt.deriv.DAOD_TOPQ1.e6798_a875_r9364_p4514
mc16_13TeV.411074.PhPy8EG_A14_ttbar_hdamp258p75_ljets_BFiltBBVeto.deriv.DAOD_TOPQ1.e6798_a875_r9364_p4514
mc16_13TeV.411075.PhPy8EG_A14_ttbar_hdamp258p75_ljets_CFiltBVeto.deriv.DAOD_TOPQ1.e6798_a875_r9364_p4514
mc16_13TeV.411076.PhPy8EG_A14_ttbar_hdamp258p75_dil_BBFilt.deriv.DAOD_TOPQ1.e6798_a875_r9364_p4514
mc16_13TeV.411077.PhPy8EG_A14_ttbar_hdamp258p75_dil_BFiltBBVeto.deriv.DAOD_TOPQ1.e6798_a875_r9364_p4514
mc16_13TeV.411078.PhPy8EG_A14_ttbar_hdamp258p75_dil_CFiltBVeto.deriv.DAOD_TOPQ1.e6798_a875_r9364_p4514
Alternative
mc16_13TeV.410557.PowhegHerwig7EvtGen_H7UE_tt_hdamp258p75_704_SingleLep.deriv.DAOD_TOPQ1.e6366_a875_r9364_p4514
mc16_13TeV.410558.PowhegHerwig7EvtGen_H7UE_tt_hdamp258p75_704_dil.deriv.DAOD_TOPQ1.e6366_a875_r9364_p4514
mc16_13TeV.411082.PhHerwig7EG_H7UE_ttbar_hdamp258p75_ljets_BBFilt.deriv.DAOD_TOPQ1.e6799_a875_r9364_p4514
mc16_13TeV.411083.PhHerwig7EG_H7UE_ttbar_hdamp258p75_ljets_BFiltBBVeto.deriv.DAOD_TOPQ1.e6799_a875_r9364_p4514
mc16_13TeV.411084.PhHerwig7EG_H7UE_ttbar_hdamp258p75_ljets_CFiltBVeto.deriv.DAOD_TOPQ1.e6799_a875_r9364_p4514
mc16_13TeV.411085.PhHerwig7EG_H7UE_ttbar_hdamp258p75_dil_BBFilt.deriv.DAOD_TOPQ1.e6799_a875_r9364_p4514
mc16_13TeV.411086.PhHerwig7EG_H7UE_ttbar_hdamp258p75_dil_BFiltBBVeto.deriv.DAOD_TOPQ1.e6799_a875_r9364_p4514
mc16_13TeV.411087.PhHerwig7EG_H7UE_ttbar_hdamp258p75_dil_CFiltBVeto.deriv.DAOD_TOPQ1.e6799_a875_r9364_p4514
mc16_13TeV.411088.PhHerwig7EG_H7UE_ttbar_hdamp258p75_allhad_BBFilt.deriv.DAOD_TOPQ1.e6799_a875_r9364_p4514
mc16_13TeV.411089.PhHerwig7EG_H7UE_ttbar_hdamp258p75_allhad_BFiltBBVeto.deriv.DAOD_TOPQ1.e6799_a875_r9364_p4514
mc16_13TeV.411090.PhHerwig7EG_H7UE_ttbar_hdamp258p75_allhad_CFiltBVeto.deriv.DAOD_TOPQ1.e6799_a875_r9364_p4514
mc16_13TeV.410464.aMcAtNloPy8EvtGen_MEN30NLO_A14N23LO_ttbar_noShWe_SingleLep.deriv.DAOD_TOPQ1.e6762_a875_r9364_p4514
mc16_13TeV.410465.aMcAtNloPy8EvtGen_MEN30NLO_A14N23LO_ttbar_noShWe_dil.deriv.DAOD_TOPQ1.e6762_a875_r9364_p4514
mc16_13TeV.410466.aMcAtNloPy8EvtGen_MEN30NLO_A14N23LO_ttbar_noShWe_AllHadronic.deriv.DAOD_TOPQ1.e6762_a875_r9364_p4514
mc16_13TeV.412066.aMcAtNloPy8EG_A14_ttbar_hdamp258p75_ljets_BBFilt.deriv.DAOD_TOPQ1.e7129_a875_r9364_p4514
mc16_13TeV.412067.aMcAtNloPy8EG_A14_ttbar_hdamp258p75_ljets_BFiltBBVeto.deriv.DAOD_TOPQ1.e7129_a875_r9364_p4514
mc16_13TeV.412068.aMcAtNloPy8EG_A14_ttbar_hdamp258p75_ljets_CFiltBVeto.deriv.DAOD_TOPQ1.e7129_a875_r9364_p4514
mc16_13TeV.412069.aMcAtNloPy8EG_A14_ttbar_hdamp258p75_dil_BBFilt.deriv.DAOD_TOPQ1.e7129_a875_r9364_p4514
mc16_13TeV.412070.aMcAtNloPy8EG_A14_ttbar_hdamp258p75_dil_BFiltBBVeto.deriv.DAOD_TOPQ1.e7129_a875_r9364_p4514
mc16_13TeV.412071.aMcAtNloPy8EG_A14_ttbar_hdamp258p75_dil_CFiltBVeto.deriv.DAOD_TOPQ1.e7129_a875_r9364_p4514

Table 22: TOPQ1 DAOD list for $t\bar{t}$ + jets sample in this analysis.

1134 A.5 $t\bar{t}H$

1135 Table 23 is the TOPQ1 DAOD list for $t\bar{t}H$ sample in this analysis.

Nominal	
mc16_13TeV.346343.PhPy8EG_A14NNPDF23_NNPDF30ME_ttH125_allhad.deriv.DAOD_TOPQ1.e7148_s3126_r9364_p4514	
mc16_13TeV.346344.PhPy8EG_A14NNPDF23_NNPDF30ME_ttH125_semilep.deriv.DAOD_TOPQ1.e7148_s3126_r9364_p4514	
mc16_13TeV.346345.PhPy8EG_A14NNPDF23_NNPDF30ME_ttH125_dilep.deriv.DAOD_TOPQ1.e7148_s3126_r9364_p4514	
Reference	
mc16_13TeV.346343.PhPy8EG_A14NNPDF23_NNPDF30ME_ttH125_allhad.deriv.DAOD_TOPQ1.e7148_a875_r9364_p4514	
mc16_13TeV.346344.PhPy8EG_A14NNPDF23_NNPDF30ME_ttH125_semilep.deriv.DAOD_TOPQ1.e7148_a875_r9364_p4514	
mc16_13TeV.346345.PhPy8EG_A14NNPDF23_NNPDF30ME_ttH125_dilep.deriv.DAOD_TOPQ1.e7148_a875_r9364_p4514	
Alternative	
mc16_13TeV.346443.aMcAtNloPythia8EvtGen_ttH_noShWe_dilep.deriv.DAOD_TOPQ1.e7310_a875_r9364_p4514	
mc16_13TeV.346444.aMcAtNloPythia8EvtGen_ttH_noShWe_semilep.deriv.DAOD_TOPQ1.e7310_a875_r9364_p4514	
mc16_13TeV.346445.aMcAtNloPythia8EvtGen_ttH_noShWe_allhad.deriv.DAOD_TOPQ1.e7310_a875_r9364_p4514	
mc16_13TeV.346346.PhH7EG_H7UE_NNPDF30ME_ttH125_allhad.deriv.DAOD_TOPQ1.e7148_a875_r9364_p4514	
mc16_13TeV.346347.PhH7EG_H7UE_NNPDF30ME_ttH125_semilep.deriv.DAOD_TOPQ1.e7148_a875_r9364_p4514	
mc16_13TeV.346348.PhH7EG_H7UE_NNPDF30ME_ttH125_dilep.deriv.DAOD_TOPQ1.e7148_a875_r9364_p4514	

Table 23: TOPQ1 DAOD list for $t\bar{t}H$ sample in this analysis.

¹¹³⁶ **A.6 $t\bar{t}V$**

¹¹³⁷ Table 24 is the TOPQ1 DAOD list for $t\bar{t}V$ sample in this analysis.

Nominal	
mc16_13TeV.410155.aMcAtNloPythia8EvtGen_MEN30NLO_A14N23LO_ttW.deriv.DAOD_TOPQ1.e5070_s3126_r9364_p4514	
mc16_13TeV.410156.aMcAtNloPythia8EvtGen_MEN30NLO_A14N23LO_ttZnunu.deriv.DAOD_TOPQ1.e5070_s3126_r9364_p4514	
mc16_13TeV.410157.aMcAtNloPythia8EvtGen_MEN30NLO_A14N23LO_ttZqq.deriv.DAOD_TOPQ1.e5070_s3126_r9364_p4514	
mc16_13TeV.410218.aMcAtNloPythia8EvtGen_MEN30NLO_A14N23LO_ttee.deriv.DAOD_TOPQ1.e5070_s3126_r9364_p4514	
mc16_13TeV.410219.aMcAtNloPythia8EvtGen_MEN30NLO_A14N23LO_ttmumu.deriv.DAOD_TOPQ1.e5070_s3126_r9364_p4514	
mc16_13TeV.410220.aMcAtNloPythia8EvtGen_MEN30NLO_A14N23LO_ttautau.deriv.DAOD_TOPQ1.e5070_s3126_r9364_p4514	
mc16_13TeV.410276.aMcAtNloPythia8EvtGen_MEN30NLO_A14N23LO_tee_mll_1_5.deriv.DAOD_TOPQ1.e6087_s3126_r9364_p4514	
mc16_13TeV.410277.aMcAtNloPythia8EvtGen_MEN30NLO_A14N23LO_ttmumu_mll_1_5.deriv.DAOD_TOPQ1.e6087_s3126_r9364_p4514	
mc16_13TeV.410278.aMcAtNloPythia8EvtGen_MEN30NLO_A14N23LO_ttautau_mll_1_5.deriv.DAOD_TOPQ1.e6087_s3126_r9364_p4514	
Alternative	
mc16_13TeV.410142.Sherpa_NNPDF30NNLO_ttll_mll5.deriv.DAOD_TOPQ1.e4686_s3126_r9364_p4514	
mc16_13TeV.410143.Sherpa_NNPDF30NNLO_ttZnnqq.deriv.DAOD_TOPQ1.e4686_s3126_r9364_p4514	
mc16_13TeV.410144.Sherpa_NNPDF30NNLO_ttW.deriv.DAOD_TOPQ1.e4686_s3126_r9364_p4514	

Table 24: TOPQ1 DAOD list for $t\bar{t}V$ sample in this analysis.

¹¹³⁸ **A.7 Single top**

¹¹³⁹ Table 25 is the TOPQ1 DAOD list for single top sample in this analysis.

Nominal
mc16_13TeV.410644.PowhegPythia8EvtGen_A14_singletop_schan_lept_top.deriv.DAOD_TOPQ1.e6527_s3126_r9364_p4514
mc16_13TeV.410645.PowhegPythia8EvtGen_A14_singletop_schan_lept_antitop.deriv.DAOD_TOPQ1.e6527_s3126_r9364_p4514
mc16_13TeV.410646.PowhegPythia8EvtGen_A14_Wt_DR_inclusive_top.deriv.DAOD_TOPQ1.e6552_s3126_r9364_p4514
mc16_13TeV.410647.PowhegPythia8EvtGen_A14_Wt_DR_inclusive_antitop.deriv.DAOD_TOPQ1.e6552_s3126_r9364_p4514
mc16_13TeV.410658.PhPy8EG_A14_tchan_BW50_lept_top.deriv.DAOD_TOPQ1.e6671_s3126_r9364_p4514
mc16_13TeV.410659.PhPy8EG_A14_tchan_BW50_lept_antitop.deriv.DAOD_TOPQ1.e6671_s3126_r9364_p4514
Reference
mc16_13TeV.410644.PowhegPythia8EvtGen_A14_singletop_schan_lept_top.deriv.DAOD_TOPQ1.e6527_a875_r9364_p4514
mc16_13TeV.410645.PowhegPythia8EvtGen_A14_singletop_schan_lept_antitop.deriv.DAOD_TOPQ1.e6527_a875_r9364_p4514
mc16_13TeV.410646.PowhegPythia8EvtGen_A14_Wt_DR_inclusive_top.deriv.DAOD_TOPQ1.e6552_a875_r9364_p4514
mc16_13TeV.410647.PowhegPythia8EvtGen_A14_Wt_DR_inclusive_antitop.deriv.DAOD_TOPQ1.e6552_a875_r9364_p4514
mc16_13TeV.410658.PhPy8EG_A14_tchan_BW50_lept_top.deriv.DAOD_TOPQ1.e6671_a875_r9364_p4514
mc16_13TeV.410659.PhPy8EG_A14_tchan_BW50_lept_antitop.deriv.DAOD_TOPQ1.e6671_a875_r9364_p4514
Alternative
mc16_13TeV.410654.PowhegPythia8EvtGen_A14_Wt_DS_inclusive_top.deriv.DAOD_TOPQ1.e6552_s3126_r9364_p4514
mc16_13TeV.410655.PowhegPythia8EvtGen_A14_Wt_DS_inclusive_antitop.deriv.DAOD_TOPQ1.e6552_s3126_r9364_p4514
mc16_13TeV.411032.PowhegHerwig7EvtGen_H7UE_704_tchan_lept_antitop.deriv.DAOD_TOPQ1.e6719_a875_r9364_p4514
mc16_13TeV.411033.PowhegHerwig7EvtGen_H7UE_704_tchan_lept_top.deriv.DAOD_TOPQ1.e6719_a875_r9364_p4514
mc16_13TeV.411034.PhHerwig7EG_H7UE_singletop_schan_lept_top.deriv.DAOD_TOPQ1.e6734_a875_r9364_p4514
mc16_13TeV.411035.PhHerwig7EG_H7UE_singletop_schan_lept_antitop.deriv.DAOD_TOPQ1.e6734_a875_r9364_p4514
mc16_13TeV.411036.PowhegHerwig7EvtGen_H7UE_Wt_DR_inclusive_top.deriv.DAOD_TOPQ1.e6702_a875_r9364_p4514
mc16_13TeV.411037.PowhegHerwig7EvtGen_H7UE_Wt_DR_inclusive_antitop.deriv.DAOD_TOPQ1.e6702_a875_r9364_p4514
mc16_13TeV.412002.aMcAtNloPythia8EvtGen_HThalfscale_tW_inclusive.deriv.DAOD_TOPQ1.e6817_a875_r9364_p4514
mc16_13TeV.412004.aMcAtNloPy8EG_tchan_NLO.deriv.DAOD_TOPQ1.e6888_a875_r9364_p4514

Table 25: TOPQ1 DAOD list for single top sample in this analysis.

1140 A.8 tH

1141 Table 26 is the TOPQ1 DAOD list for tH sample in this analysis.

Nominal
mc16_13TeV.346676.aMcAtNloPythia8EvtGen_tHjb125_4fl_CPalpha_0.deriv.DAOD_TOPQ1.e7815_a875_r9364_p4514
mc16_13TeV.346678.aMcAtNloPythia8EvtGen_tWH125_4fl_CPalpha_0.deriv.DAOD_TOPQ1.e7816_a875_r9364_p4514

Table 26: TOPQ1 DAOD list for tH sample in this analysis.

1142 A.9 Rare t processes

1143 Table 27 is the TOPQ1 DAOD list for rare t processes' sample in this analysis.

Nominal
mc16_13TeV.410560.MadGraphPythia8EvtGen_A14_tZ_4fl_tchan_noAllHad.deriv.DAOD_TOPQ1.e5803_s3126_r9364_p4514
mc16_13TeV.410408.aMcAtNloPythia8EvtGen_tWZ_Ztoll_minDR1.deriv.DAOD_TOPQ1.e6423_s3126_r9364_p4514
mc16_13TeV.412043.aMcAtNloPythia8EvtGen_A14NNPDF31_SM4topsNLO.deriv.DAOD_TOPQ1.e7101_a875_r9364_p4514

Table 27: TOPQ1 DAOD list for rare processes' sample in this analysis.

1144 A.10 Vector bosons plus jets

1145 A.10.1 $W +$ jets

1146 Table 28 is the TOPQ1 DAOD list for $W +$ jets sample in this analysis.

Nominal
mc16_13TeV.364170.Sherpa_221_NNPDF30NNLO_Wenu_MAXHTPTV0_70_CVetoBVeto.deriv.DAOD_TOPQ1.e5340_s3126_r9364_p4512
mc16_13TeV.364171.Sherpa_221_NNPDF30NNLO_Wenu_MAXHTPTV0_70_CFilterBVeto.deriv.DAOD_TOPQ1.e5340_s3126_r9364_p4512
mc16_13TeV.364172.Sherpa_221_NNPDF30NNLO_Wenu_MAXHTPTV0_70_BFilter.deriv.DAOD_TOPQ1.e5340_s3126_r9364_p4512
mc16_13TeV.364173.Sherpa_221_NNPDF30NNLO_Wenu_MAXHTPTV70_140_CVetoBVeto.deriv.DAOD_TOPQ1.e5340_s3126_r9364_p4512
mc16_13TeV.364174.Sherpa_221_NNPDF30NNLO_Wenu_MAXHTPTV70_140_CFilterBVeto.deriv.DAOD_TOPQ1.e5340_s3126_r9364_p4512
mc16_13TeV.364175.Sherpa_221_NNPDF30NNLO_Wenu_MAXHTPTV70_140_BFilter.deriv.DAOD_TOPQ1.e5340_s3126_r9364_p4512
mc16_13TeV.364176.Sherpa_221_NNPDF30NNLO_Wenu_MAXHTPTV140_280_CVetoBVeto.deriv.DAOD_TOPQ1.e5340_s3126_r9364_p4512
mc16_13TeV.364177.Sherpa_221_NNPDF30NNLO_Wenu_MAXHTPTV140_280_CFilterBVeto.deriv.DAOD_TOPQ1.e5340_s3126_r9364_p4512
mc16_13TeV.364178.Sherpa_221_NNPDF30NNLO_Wenu_MAXHTPTV140_280_BFilter.deriv.DAOD_TOPQ1.e5340_s3126_r9364_p4512
mc16_13TeV.364179.Sherpa_221_NNPDF30NNLO_Wenu_MAXHTPTV280_500_CVetoBVeto.deriv.DAOD_TOPQ1.e5340_s3126_r9364_p4512
mc16_13TeV.364180.Sherpa_221_NNPDF30NNLO_Wenu_MAXHTPTV280_500_CFilterBVeto.deriv.DAOD_TOPQ1.e5340_s3126_r9364_p4512
mc16_13TeV.364181.Sherpa_221_NNPDF30NNLO_Wenu_MAXHTPTV280_500_BFilter.deriv.DAOD_TOPQ1.e5340_s3126_r9364_p4512
mc16_13TeV.364182.Sherpa_221_NNPDF30NNLO_Wenu_MAXHTPTV500_1000.deriv.DAOD_TOPQ1.e5340_s3126_r9364_p4512
mc16_13TeV.364183.Sherpa_221_NNPDF30NNLO_Wenu_MAXHTPTV1000_E_CMS.deriv.DAOD_TOPQ1.e5340_s3126_r9364_p4512
mc16_13TeV.364156.Sherpa_221_NNPDF30NNLO_Wmumu_MAXHTPTV0_70_CVetoBVeto.deriv.DAOD_TOPQ1.e5340_s3126_r9364_p4512
mc16_13TeV.364157.Sherpa_221_NNPDF30NNLO_Wmumu_MAXHTPTV0_70_CFilterBVeto.deriv.DAOD_TOPQ1.e5340_s3126_r9364_p4512
mc16_13TeV.364158.Sherpa_221_NNPDF30NNLO_Wmumu_MAXHTPTV0_70_BFilter.deriv.DAOD_TOPQ1.e5340_s3126_r9364_p4512
mc16_13TeV.364159.Sherpa_221_NNPDF30NNLO_Wmumu_MAXHTPTV70_140_CVetoBVeto.deriv.DAOD_TOPQ1.e5340_s3126_r9364_p4512
mc16_13TeV.364160.Sherpa_221_NNPDF30NNLO_Wmumu_MAXHTPTV70_140_CFilterBVeto.deriv.DAOD_TOPQ1.e5340_s3126_r9364_p4512
mc16_13TeV.364161.Sherpa_221_NNPDF30NNLO_Wmumu_MAXHTPTV70_140_BFilter.deriv.DAOD_TOPQ1.e5340_s3126_r9364_p4512
mc16_13TeV.364162.Sherpa_221_NNPDF30NNLO_Wmumu_MAXHTPTV140_280_CVetoBVeto.deriv.DAOD_TOPQ1.e5340_s3126_r9364_p4512
mc16_13TeV.364163.Sherpa_221_NNPDF30NNLO_Wmumu_MAXHTPTV140_280_CFilterBVeto.deriv.DAOD_TOPQ1.e5340_s3126_r9364_p4512
mc16_13TeV.364164.Sherpa_221_NNPDF30NNLO_Wmumu_MAXHTPTV140_280_BFilter.deriv.DAOD_TOPQ1.e5340_s3126_r9364_p4512
mc16_13TeV.364165.Sherpa_221_NNPDF30NNLO_Wmumu_MAXHTPTV280_500_CVetoBVeto.deriv.DAOD_TOPQ1.e5340_s3126_r9364_p4512
mc16_13TeV.364166.Sherpa_221_NNPDF30NNLO_Wmumu_MAXHTPTV280_500_CFilterBVeto.deriv.DAOD_TOPQ1.e5340_s3126_r9364_p4512
mc16_13TeV.364167.Sherpa_221_NNPDF30NNLO_Wmumu_MAXHTPTV280_500_BFilter.deriv.DAOD_TOPQ1.e5340_s3126_r9364_p4512
mc16_13TeV.364168.Sherpa_221_NNPDF30NNLO_Wmumu_MAXHTPTV500_1000.deriv.DAOD_TOPQ1.e5340_s3126_r9364_p4512
mc16_13TeV.364169.Sherpa_221_NNPDF30NNLO_Wmumu_MAXHTPTV1000_E_CMS.deriv.DAOD_TOPQ1.e5340_s3126_r9364_p4512
mc16_13TeV.364184.Sherpa_221_NNPDF30NNLO_Wtaunu_MAXHTPTV0_70_CVetoBVeto.deriv.DAOD_TOPQ1.e5340_s3126_r9364_p4512
mc16_13TeV.364185.Sherpa_221_NNPDF30NNLO_Wtaunu_MAXHTPTV0_70_CFilterBVeto.deriv.DAOD_TOPQ1.e5340_s3126_r9364_p4512
mc16_13TeV.364186.Sherpa_221_NNPDF30NNLO_Wtaunu_MAXHTPTV0_70_BFilter.deriv.DAOD_TOPQ1.e5340_s3126_r9364_p4512
mc16_13TeV.364187.Sherpa_221_NNPDF30NNLO_Wtaunu_MAXHTPTV70_140_CVetoBVeto.deriv.DAOD_TOPQ1.e5340_s3126_r9364_p4512
mc16_13TeV.364188.Sherpa_221_NNPDF30NNLO_Wtaunu_MAXHTPTV70_140_CFilterBVeto.deriv.DAOD_TOPQ1.e5340_s3126_r9364_p4512
mc16_13TeV.364189.Sherpa_221_NNPDF30NNLO_Wtaunu_MAXHTPTV70_140_BFilter.deriv.DAOD_TOPQ1.e5340_s3126_r9364_p4512
mc16_13TeV.364190.Sherpa_221_NNPDF30NNLO_Wtaunu_MAXHTPTV140_280_CVetoBVeto.deriv.DAOD_TOPQ1.e5340_s3126_r9364_p4512
mc16_13TeV.364191.Sherpa_221_NNPDF30NNLO_Wtaunu_MAXHTPTV140_280_CFilterBVeto.deriv.DAOD_TOPQ1.e5340_s3126_r9364_p4512
mc16_13TeV.364192.Sherpa_221_NNPDF30NNLO_Wtaunu_MAXHTPTV140_280_BFilter.deriv.DAOD_TOPQ1.e5340_s3126_r9364_p4512
mc16_13TeV.364193.Sherpa_221_NNPDF30NNLO_Wtaunu_MAXHTPTV280_500_CVetoBVeto.deriv.DAOD_TOPQ1.e5340_s3126_r9364_p4512
mc16_13TeV.364194.Sherpa_221_NNPDF30NNLO_Wtaunu_MAXHTPTV280_500_CFilterBVeto.deriv.DAOD_TOPQ1.e5340_s3126_r9364_p4512
mc16_13TeV.364195.Sherpa_221_NNPDF30NNLO_Wtaunu_MAXHTPTV280_500_BFilter.deriv.DAOD_TOPQ1.e5340_s3126_r9364_p4512
mc16_13TeV.364196.Sherpa_221_NNPDF30NNLO_Wtaunu_MAXHTPTV500_1000.deriv.DAOD_TOPQ1.e5340_s3126_r9364_p4512
mc16_13TeV.364197.Sherpa_221_NNPDF30NNLO_Wtaunu_MAXHTPTV1000_E_CMS.deriv.DAOD_TOPQ1.e5340_s3126_r9364_p4512

Table 28: TOPQ1 DAOD list for $W + \text{jets}$ sample in this analysis.

1147 A.10.2 $Z + \text{jets}$

1148 Table 29 is the TOPQ1 DAOD list for $Z + \text{jets}$ sample in this analysis.

Nominal

Table 29: TOPQ1 DAOD list for $Z + \text{jets}$ sample in this analysis.

A.11 Diboson

1149 Table 30 is the TOPQ1 DAOD list for diboson sample in this analysis.

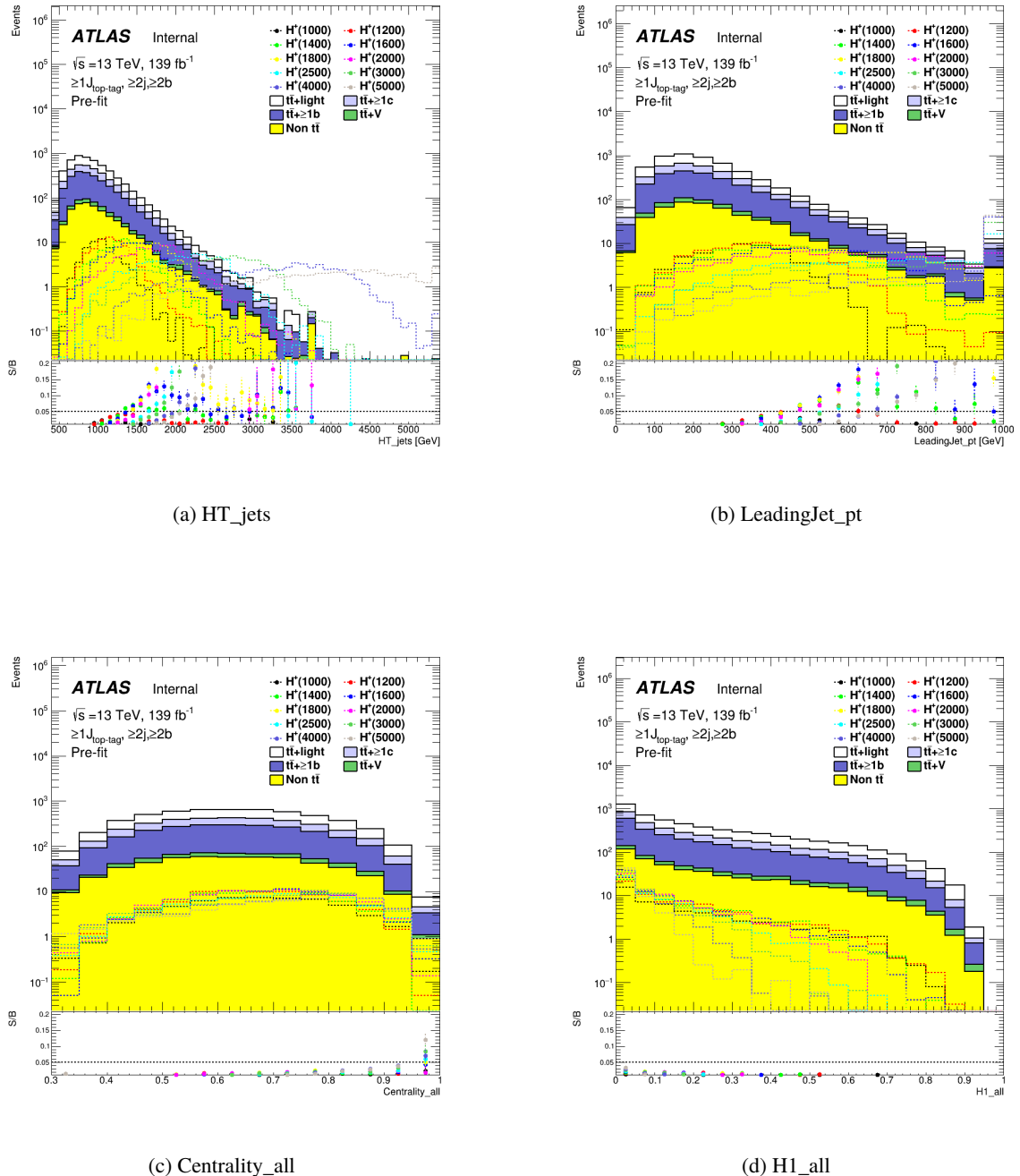
Nominal
mc16_13TeV.364250.Sherpa_222_NNPDF30NNLO_llll.deriv.DAOD_TOPQ1.e5894_s3126_r9364_p4512
mc16_13TeV.364253.Sherpa_222_NNPDF30NNLO_lllv.deriv.DAOD_TOPQ1.e5916_s3126_r9364_p4512
mc16_13TeV.364254.Sherpa_222_NNPDF30NNLO_llvv.deriv.DAOD_TOPQ1.e5916_s3126_r9364_p4512
mc16_13TeV.364255.Sherpa_222_NNPDF30NNLO_lvvv.deriv.DAOD_TOPQ1.e5916_s3126_r9364_p4512
mc16_13TeV.364288.Sherpa_222_NNPDF30NNLO_llll_lowMllPtComplement.deriv.DAOD_TOPQ1.e6096_s3126_r9364_p4512
mc16_13TeV.364289.Sherpa_222_NNPDF30NNLO_lllv_lowMllPtComplement.deriv.DAOD_TOPQ1.e6133_s3126_r9364_p4512
mc16_13TeV.364290.Sherpa_222_NNPDF30NNLO_llvv_lowMllPtComplement.deriv.DAOD_TOPQ1.e6096_s3126_r9364_p4512
mc16_13TeV.363355.Sherpa_221_NNPDF30NNLO_ZqqZv.deriv.DAOD_TOPQ1.e5525_s3126_r9364_p4512
mc16_13TeV.363356.Sherpa_221_NNPDF30NNLO_ZqqZll.deriv.DAOD_TOPQ1.e5525_s3126_r9364_p4512
mc16_13TeV.363357.Sherpa_221_NNPDF30NNLO_WqqZvv.deriv.DAOD_TOPQ1.e5525_s3126_r9364_p4512
mc16_13TeV.363358.Sherpa_221_NNPDF30NNLO_WqqZll.deriv.DAOD_TOPQ1.e5525_s3126_r9364_p4512
mc16_13TeV.363359.Sherpa_221_NNPDF30NNLO_WpqqWmlv.deriv.DAOD_TOPQ1.e5583_s3126_r9364_p4512
mc16_13TeV.363360.Sherpa_221_NNPDF30NNLO_WplvWmqq.deriv.DAOD_TOPQ1.e5983_s3126_r9364_p4512
mc16_13TeV.363489.Sherpa_221_NNPDF30NNLO_WlvZqq.deriv.DAOD_TOPQ1.e5525_s3126_r9364_p4512
mc16_13TeV.363494.Sherpa_221_NNPDF30NNLO_vvvv.deriv.DAOD_TOPQ1.e5332_s3126_r9364_p4512
mc16_13TeV.364283.Sherpa_222_NNPDF30NNLO_llljjj_EW6.deriv.DAOD_TOPQ1.e6055_s3126_r9364_p4512
mc16_13TeV.364284.Sherpa_222_NNPDF30NNLO_llvjjj_EW6.deriv.DAOD_TOPQ1.e6055_s3126_r9364_p4512
mc16_13TeV.364285.Sherpa_222_NNPDF30NNLO_llvijj_EW6.deriv.DAOD_TOPQ1.e6055_s3126_r9364_p4512
mc16_13TeV.364287.Sherpa_222_NNPDF30NNLO_llvijj_ss_EW6.deriv.DAOD_TOPQ1.e6055_s3126_r9364_p4512
mc16_13TeV.345705.Sherpa_222_NNPDF30NNLO_ggllll_0M4130.deriv.DAOD_TOPQ1.e6213_s3126_r9364_p4512
mc16_13TeV.345706.Sherpa_222_NNPDF30NNLO_ggllll_130M41.deriv.DAOD_TOPQ1.e6213_s3126_r9364_p4512
mc16_13TeV.345723.Sherpa_222_NNPDF30NNLO_ggllvvZZ.deriv.DAOD_TOPQ1.e6213_s3126_r9364_p4512

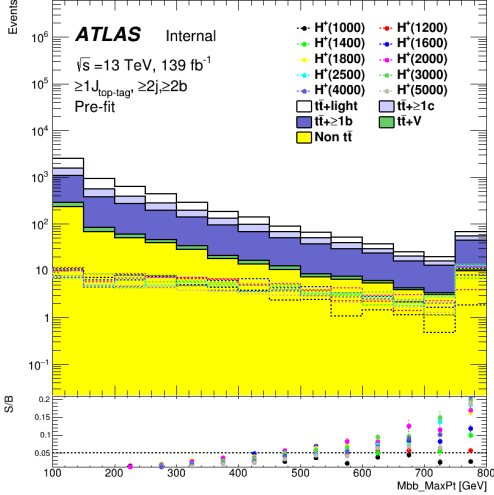
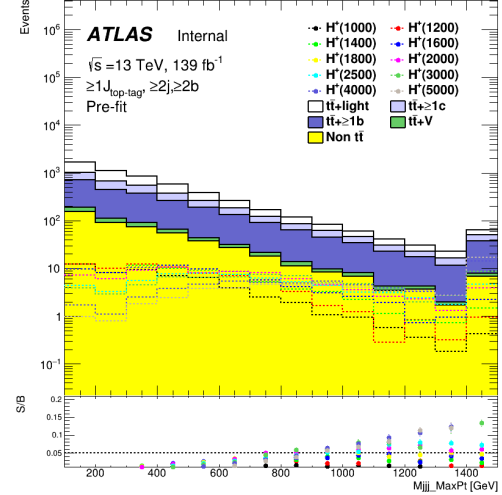
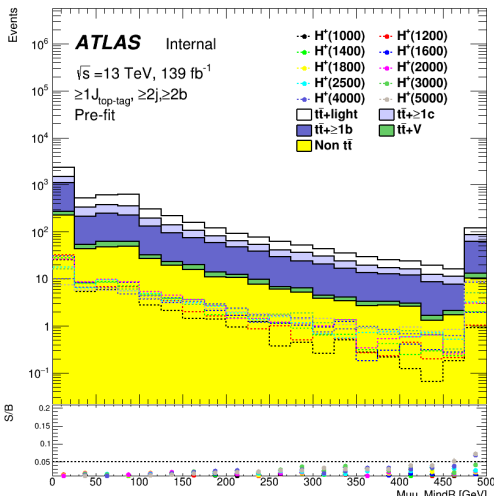
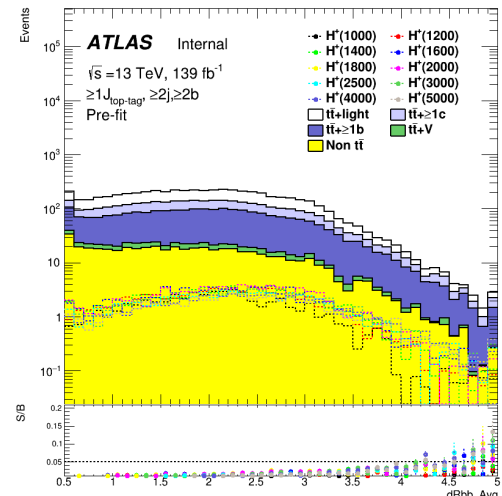
Table 30: TOPQ1 DAOD list for diboson sample in this analysis.

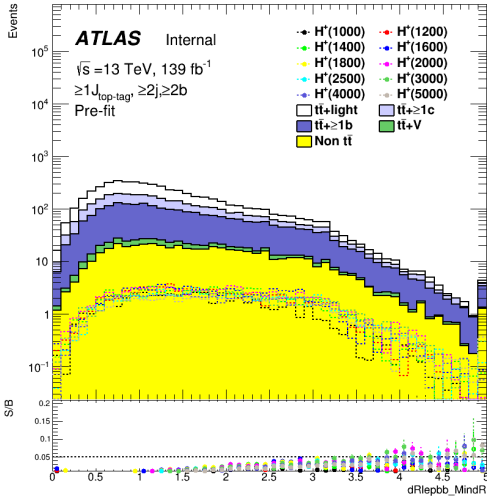
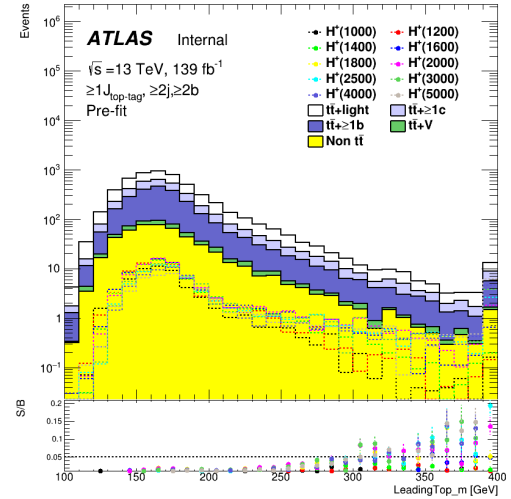
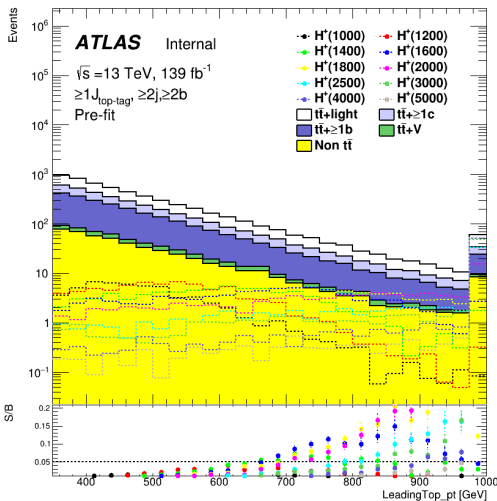
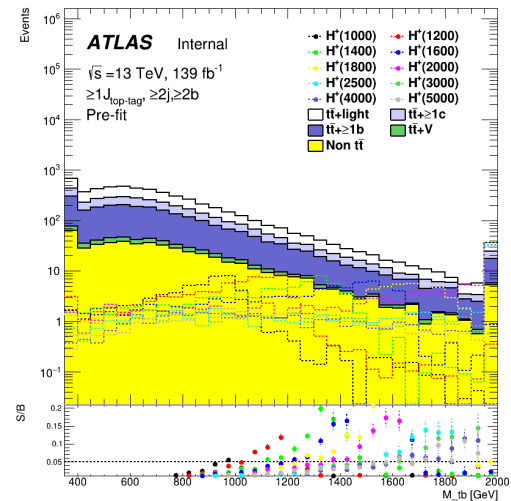
1151 B Signal/background comparisons

1152 B.1 BDT input variables

1153 Figures 145 (Figure 145) compare the shape of the variables included in the BDT for all H^+ (W') signal
 1154 masses and background.



(e) $M_{bb, \text{MaxPt}}$ (f) $M_{jjj, \text{MaxPt}}$ (g) $\mu_{uu, \text{MindR}}$ (h) $dR_{bb, \text{Avg}}$

(i) $dR_{\text{lepb_MindR}}$ (j) LeadingTop_m (k) LeadingTop_pt (l) M_{tb}

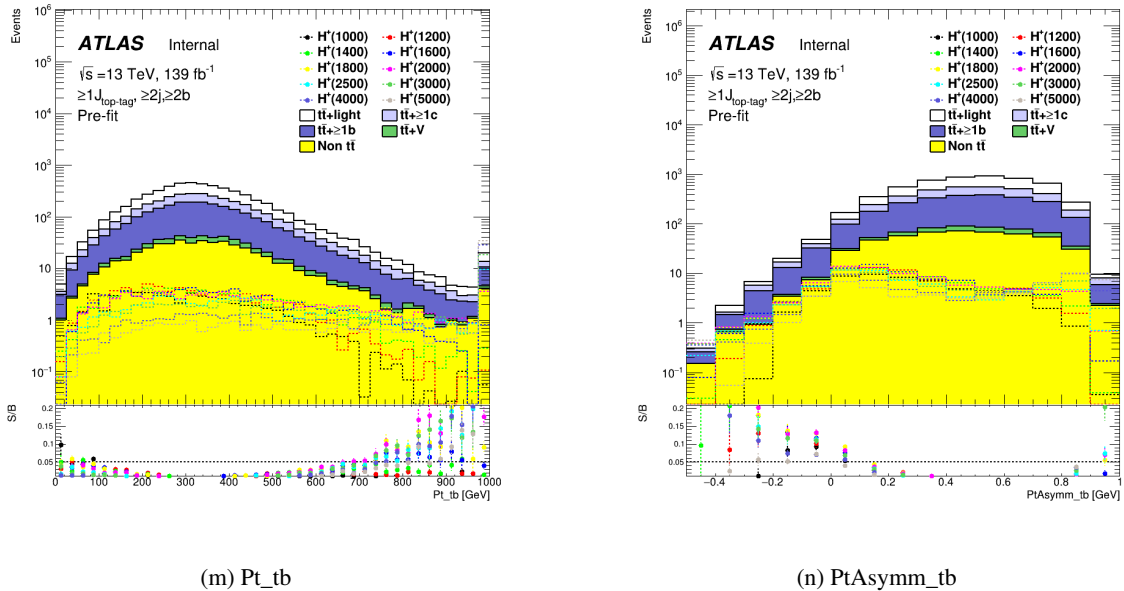


Figure 145: Comparison of the kinematic variables included in the BDT in the SR for the various H^+ signal masses between signal and background.

1155 B.2 BDT outputs

1156 B.3 Comparison using distributions with binning